



HAL
open science

Evaluation of doping in 4H-SiC by optical spectroscopies

Pawel Kwasnicki

► **To cite this version:**

Pawel Kwasnicki. Evaluation of doping in 4H-SiC by optical spectroscopies. Materials Science [cond-mat.mtrl-sci]. Université Montpellier II - Sciences et Techniques du Languedoc, 2014. English. NNT : 2014MON20145 . tel-01713581

HAL Id: tel-01713581

<https://theses.hal.science/tel-01713581>

Submitted on 20 Feb 2018

HAL is a multi-disciplinary open access archive for the deposit and dissemination of scientific research documents, whether they are published or not. The documents may come from teaching and research institutions in France or abroad, or from public or private research centers.

L'archive ouverte pluridisciplinaire **HAL**, est destinée au dépôt et à la diffusion de documents scientifiques de niveau recherche, publiés ou non, émanant des établissements d'enseignement et de recherche français ou étrangers, des laboratoires publics ou privés.

**UNIVERSITE MONTPELLIER II
SCIENCES ET TECHNIQUES DU LANGUEDOC**

THESE

pour obtenir le grade de

DOCTEUR DE L'UNIVERSITE MONTPELLIER II

Discipline : Physique

Ecole Doctorale : Information Structures Systèmes

présentée et soutenue publiquement

par

Pawel Kwasnicki

le 09 décembre 2014

**Evaluation of doping in 4H-SiC by
optical spectroscopies**

JURY

Konstantinos ZEKENTES	Principal Researcher	FORTH	Rapporteur
Marcin ZIELINSKI	Docteur ingénieur	NOVASIC	Rapporteur
Didier CHAUSSENDE	Directeur de Recherche	Université Grenoble Alpes	Examineur
Ahmed-Azmi ZAHAB	Professeur	Université Montpellier II	Examineur
Sandrine JUILLAGUET	Maître de Conférences	Université Montpellier II	Directrice de Thèse
Herve PEYRE	Maître de Conférences	Université Montpellier II	Co- Directeur
Jean CAMASSEL	Professeur	Université Montpellier II	Invité

**UNIVERSITE MONTPELLIER II
SCIENCES ET TECHNIQUES DU LANGUEDOC**

THESE

pour obtenir le grade de

DOCTEUR DE L'UNIVERSITE MONTPELLIER II

Discipline : Physique

Ecole Doctorale : Information Structures Systèmes

présentée et soutenue publiquement

par

Pawel Kwasnicki

le 09 décembre 2014

**Evaluation of doping in 4H-SiC by
optical spectroscopies**

JURY

Konstantinos ZEKENTES	Principal Researcher	FORTH	Rapporteur
Marcin ZIELINSKI	Docteur ingénieur	NOVASIC	Rapporteur
Didier CHAUSSENDE	Directeur de Recherche	Université Grenoble Alpes	Examineur
Ahmed-Azmi ZAHAB	Professeur	Université Montpellier II	Examineur
Sandrine JUILLAGUET	Maître de Conférences	Université Montpellier II	Directrice de Thèse
Herve PEYRE	Maître de Conférences	Université Montpellier II	Co- Directeur
Jean CAMASSEL	Professeur	Université Montpellier II	Invité

Acknowledgements

W

orking on the Ph.D. has been a wonderful and often overwhelming experience. Without the help of many people the overcoming the problems would not be possible. I am indebted to many people for making the time working on my Ph.D. an unforgettable experience.

First of all I would like to express my deepest appreciation to my supervisor dr. Sandrine Juillaguet as well as my co-supervisor dr. Hervé Peyre. Without their guidance, encouragement and support during the research, it would have been impossible for me to complete this thesis. They have always been ready to offer their help whenever needed. We had many lively discussions during these three years and I have learned a lot from them.

I also want to thank dr. Sylvie Contreras and dr. Leszek Konczewicz, whose help of understanding the electrical measurement aspect of my work was tremendous and whose scientific work inspired me a lot.

I would particularly like to thank dr. Leszek Konczewicz for his support and help to overcome the scientific problems as well as aid whenever I needed it.

My work has greatly benefited from discussions, suggestions and kind encouragement from materials, devices, sensors and bionanophotonics team in Laboratoire Charles Coulomb at University Montpellier 2 especially: Jean-Roch Huntzinger, Perine Landois, Antoine Tiberj and Paillet Matthieu. I would like especially thank to Prof. Jean Camassel for fruitful and interesting discussions.

I wish to thank all group members and technical staff in laboratory, especially Philippe Arcad and dr. Nina Diakonova for their help with FTIR measurements, Bernard Boyer for his help with the SIMS measurements and dr. Thierry Michel and David Maurin for their help with micro-Raman measurements.

I have been very privileged to get to know and to collaborate with many other great people from NetFiSiC project who became friends over the last three years. I learned a lot from you about life, research, how to tackle new problems and how to develop techniques to solve them. I would like to thank to Marcin Zielinski and Roxana Arvinte for fruitful collaboration, providing samples and many interesting discussions about growth aspects.

For this dissertation I would like to thank my reading committee members: Marcin Zielinski and Konstantinos Zekentes for their time, interest, and helpful comments. I would also like to thank the other three members of my oral defense committee Didier Chaussende, Ahmed-Azmi Zahab, Jean Camassel.

I will always remember the supports, and pleasant time we had with my friends from NetFiSiC grupe: dr. Kassem Al Assaad, Chamseddine Bouhafs, dr. Nikolaos Tsavdaris, Kanaparin Ariyawong, Roxana Arvinte, Tomasz Sledziewski, dr. Narendraraj Chandran, Matthieu Florentin, Aleksey Mikhaylov, dr. Marilena Vivona, Alberto Salinaro, dr. Gediminas Liaugaudas, dr. Mamour Sall, dr. Dhanasekaran Vikraman, dr. Florian Chevalier.

I'd also like to thank my former professors Igor Tralle who supported me with many advices during my master study and helped me to start my Ph.D. study.

Finally, a deep sense of appreciation goes towards all of my family for providing me with the endless love and support I needed to pursue and achieve my goals in life. I would like to thank my mom, dad, sister and brothers for their infinite support throughout everything.
Dziękuję za wsparcie pomoc i obecność.

A very special thanks goes to my wife for here love and encouragements during my work in Montpellier.

This work was supported by European Union Marie Curie project NetFiSiC.

Introduction

Today we are still working with Si and SiO₂ to produce the electronic devices. However, new materials are required for some special applications since the characteristic properties of material play a key role for the performance of the fabricated electronic devices. Silicon carbide is one of such promising materials for niche applications. Due to its extreme thermal stability, wide bandgap and high breakdown field the attention given to SiC has progressed recently.

Although SiC has been known since the first observation by J.J. Berzelius in 1842, it was in the late 1980s that SiC wafers became commercially available after the breakthrough had been made in growth technology. Up to now the material quality and the diameter of silicon carbide wafers have steadily been improved.

Due to continuous improvement in crystal growth techniques and experimental methods in the investigation of crystalline materials, as well as in theoretical work based on modern physics and high computational power, the science of semiconductors has grown to an enormous size and has reached a state of maturity. However, concerning SiC material, still many material related issues have to be solved before new alternatives can compete in the market. One of the important points is the control of doping during epitaxial growth and possibility of its evaluation. There are several options to determine the doping level in SiC, but some of them damage the epilayer or required special sample's preparation. To overcome these problems one of possible way is to use contactless and non-destructive optical measurements like Photoluminescence or Raman scattering spectroscopies.

The objective of this thesis is to investigate physical and electrical properties of 4H-SiC focusing on the evaluation of the doping / carrier concentration using non-destructive and contactless methods. This work was done in framework of NetFISiC European program (2011-2015). The main scientific objective of NetFISiC (ITN Marie Curie project) is to provide Silicon material of various polytypes with improved and adequate functional interfaces for getting a step forward in electronic devices performance. Research efforts are mostly dedicated to solve the problems faced by important devices like MOSFET and Schottky diodes. Besides, some fundamental researches are performed both on the growth aspect and on new and innovating devices. Applications of SiC in high temperature, high power and harsh environment are main targets. To this end, twelve partners are involved in the NetFISiC project, three of which are companies (INFINEON, ACREO and NOVASiC). The partners were chosen for their recognized expertise in the field of SiC material and / or specific related techniques. The consortium is divided in three technical work-packages:

- WP1 (Material growth and related aspects) is dedicated to the development of less mature polytypes than 4H (3C and 15R).

- WP2 (Characterization of material and functional interfaces) is in charge of studying the properties of the materials, surface and interfaces. This WP makes the important link between the growth (WP1) and the device manufacturing group (WP3).
- WP3 (Devices and demonstrators) is in charge of the electrical testing and fabrication of the targeted devices.

The work of these three years during the thesis has been carried out in close collaboration with many partners in the NetFISiC project. But we chose to present the study of the doping in 4H-SiC, and the main results were obtained through collaboration with NOVASiC, one of the WP1 partner.

The manuscript is divided in five chapters:

First chapter introduces the SiC material. Brief historical overview is given. Then some of the physical and electrical proprieties of several polytypes of SiC are presented and we also give a short summarized of the most common defects occurring in SiC layers. The second part of the chapter gives an overview on the growth techniques and more particularly chemical vapor deposition, since these techniques were used to make the samples investigated in this work.

In Chapter 2, the experimental techniques (as secondary ion mass spectroscopy, low temperature photoluminescence and Raman spectroscopy) used to characterize different aspects of SiC material are presented. Since this work concerns 4H-SiC we focus on application of these techniques to investigate this polytype.

The aim of Chapter 3 is to introduce the theoretical approach of evaluation of carrier concentration in n- and p-type 4H-SiC using Raman spectroscopy. First we focus on the optical part of Raman spectra. We study the differences related to the type of carrier on the LOPC mode. In the second part we focus on the acoustic range. The model of Fano-interference effect is developed, first for n-type 4H-SiC and then extends for p-type SiC. The influence of Fano-parameters used on the fitting of the FTA modes is investigated and discussed.

Chapter 4 & 5 present the main part of the experimental results obtained on n- type and p-type 4H-SiC samples, respectively. The main objective is to evaluate the doping level in non-destructive way and verify the existing calibration curves for LTPL and Raman or even create them when there is lack. For this purpose, at first, SIMS measurements were done in order to obtain the concentration of dopant: nitrogen in n-type or aluminum in p-type samples. Second, we propose to evaluate the doping level in nondestructive way. Two methods are discussed and compared: photoluminescence versus Raman. The calibration curve for p-type 4H-SiC to evaluate the carrier concentration using Raman spectroscopies will propose.

Finally the comparison of the LTPL and Raman spectroscopies in terms of evaluation of doping level in n- and p-type SiC is done. The advantages and limitations of each of method are presented and discussed. Eventually we propose a practical application.

Table of contents

Chapter 1: Background consideration.....	11
Introduction	11
1.1 Crystal structure of SiC and polytypism	12
1.1.1. Electronic structure of SiC.....	16
1.1.2. Energy bandgap (E _g).....	17
1.2 Doping in different polytypes	19
1.3 Defects	20
1.3.1 Deep center.....	21
Nitrogen:.....	21
Aluminum:	21
1.3.2 Stacking faults	22
1.3.3 Micropipes.....	23
1.3.4 Vacancies.....	24
1.3.5 Intrinsic Defects in Silicon Carbide.....	25
<i>L-center</i>	25
Z ₁ -Z ₂ defects	25
1.4 Crystal Growth techniques	26
1.4.1 Chemical Vapor Deposition (CVD).....	26
1.4.2 Doping Control	29
Bibliography.....	30
Chapter 2: Experimental techniques.....	35
Introduction	35

2.1	Secondary ion mass spectrometry (SIMS)	35
2.1.1	Ion Beam Sputtering.....	36
2.1.2	Collection of the secondary ions beam.....	38
2.1.3	Analysis of the secondary ions beam	39
2.1.4	Secondary ion detection	39
2.1.5	Relative Sensitivity Factors – Concentration calibration	40
2.1.6	RSF tables	41
2.1.7	Depth Profiling	43
2.2	Photoluminescence	45
2.2.1	Free exciton transition	45
2.2.2	Coulomb interaction.....	46
2.2.3	Doped-assisted mechanisms.....	47
2.2.3.1	Band to band transition.....	48
2.2.3.2	Free to bound transition.....	49
2.2.3.3	Donor-Acceptor Pair transition	50
2.2.4	Exciton transitions.....	52
2.2.5	Polytype identification by LTPL	56
2.2.6	Experimental setup	57
2.3	Raman scattering spectroscopy	58
2.3.1	Stokes and anti-Stokes transition.....	59
2.3.2	Selection rules	60
2.3.3	Particularity of phonons in SiC	62
2.3.4	Application: polytype identification by micro-Raman spectroscopy.....	65
2.3.5	Experimental setup	67
	Bibliography	69
	 Chapter 3: Doping level evaluation by Raman scattering spectroscopy: Fitting models for n- and p-type 4H-SiC	73
	 Introduction	73
3.1	LOPC modes	74

3.1.1	4H-SiC n-type.....	76
3.1.2	4H-SiC p-type.....	78
3.2	Fano-interference effect in SiC.	79
3.2.1	p-type SiC.....	83
3.2.2	Influence of Fano parameters on the line shape of FTA line.	84
3.3	Application of theoretical fit on experimental spectra.....	86
3.4	Conclusion.....	87
	Bibliography.....	88
	Chapter 4: Investigation of nitrogen doped 4H-SiC epilayers grown by Chemical Vapor deposition.	89
	Introduction.....	89
4.1	Samples description	89
4.2	Nitrogen doping in 4H-SiC.....	91
4.2.1	Evaluation of nitrogen content by LTPL	91
4.2.2	Experimental results and discussion	94
4.2.3	LTPL investigation-summary	97
4.3	Evaluation of free carrier concentration By Raman.....	99
4.3.1	LOPC modes.....	100
4.3.2	FTA modes.....	104
4.3.2.1	Fitting model.....	105
4.4	Discussion and conclusion	112

Bibliography.....	116
Chapter 5: Evaluation of doping concentration in p-type 4H-SiC doped with aluminum.....	117
Introduction.....	117
5.1 Sample description.....	117
5.2 Evaluation of doping concentration by non-destructive methods.....	120
5.2.1 Evaluation of aluminum by LTPL.....	120
5.2.2 Evaluation of p-doping level by Raman.....	126
5.3.2.1 LOPC mode.....	127
5.3.2.2 FTA modes.....	131
5.4 Carrier concentration by electrical measurements.....	132
5.5 Calibration curve for p-type 4H-SiC.....	135
5.6 Application for mapping of 2' wafer.....	139
5.7 Conclusion.....	141
Bibliography.....	142
General conclusions.....	143
Annex 1: Evaluation of doping in 4H-SiC by photoluminescence.....	147
Nitrogen content evaluation- theoretical approach.....	147
Aluminum contain evaluation- theoretical approach.....	152
Bibliography.....	155
Annex 2: Polytype identification, homogeneity and crystal quality investigation by LTPL& Raman for n and p-type 4H-SiC.....	157

2.1 n-type samples	157
2.1.1 LTPL investigation.....	157
2.1.2 Micro Raman	160
2.2 p-type samples.....	161
2.2.1 Optical microscopy investigation	161
2.2.2 LTPL.....	163
2.2.3 Micro-Raman.....	164
2.3 Sample 14-009.....	166
Bibliography.....	169
Annex 3: Carrier concentration evaluation by electrical measurements	171
3.1 Resistivity measurement by Van der Pauw methods :	171
3.2 Hall Effect measurement.....	172
3.3 Experimental Set-up.....	173
Bibliography.....	174

Chapter 1: Background consideration

Introduction

Silicon carbide (SiC) was predicted by Shockley to quickly “replace Si” in the early 1950s because of its excellent material properties to compare to Si. However, the difficulties in growing large-size SiC crystal had made it impossible for SiC to even take over a niche market from Si. Advanced SiC crystal growth technology developed in the 1980s has revitalized the investigation of SiC. It exists in a large number of polytypes which differ in their properties.

The main application for SiC crystals is in power electronics. Silicon is the material currently dominating the electronics industry. However, the demand for improved energy efficiency in power electronics, which can be satisfied by reducing the switching and conduction losses of devices, as well as devices capable of high temperature operation, is pushing for the power electronics technology development in wide bandgap semiconductors. In this context, SiC has been touted as a top candidate for decades. Recently, the development of modern epitaxial techniques has led to a rapid improvement in the material quality of SiC, thus leading to a constant increase in the performances of SiC based devices.

Silicon carbide (SiC) has received remarkable attention during the last decade as a promising device material for high temperature, high frequency, and high power device applications due to its high thermal conductivity and high critical field for breakdown. It exhibits higher values of thermal conductivity (3-13 times), critical electric field (4-20 times), and saturated carrier velocity (2-2.5 times) compared to the conventional semiconductor materials such as silicon and gallium arsenide [1], [2], [3]. It is also an attractive material for high temperature operating (>650 °C) gas sensors as well as solid-state transducers such as pressure sensors and accelerometers for automotive and space industry applications using micro electro mechanical systems (MEMS) [4], [5].

For high-frequency device applications, SiC devices can provide much higher speed compared to the Si devices due to the higher saturated drift velocity v_{sat} (influence the delay time $t = W/v_{sat}$) and lower permittivity ϵ_r (capacitance $C \propto \epsilon_r$). Beyond on favorable properties of SiC, the full performance of SiC devices is limited by the material quality itself. To bring SiC into real applications, it is essential to control polytypes during crystal growth. Although the potential of SiC has been recognized for a long time, difficulty in growing high-quality and large size SiC crystals without polytype mixing and defects had prevented electronic applications. An innovation in bulk crystal growth using a seeded sublimation method (a modified Lely method) for controlling polytypes [6] has changed research and development of SiC devices.

Nowadays, 4H- and 6H-SiC wafers of 3-4 inches in diameter are available commercially. Many SiC-based substrate manufacturers, as CREE, exhibited 6-inch (150mm)-diameter

wafers at the international conference on SiC-based power semiconductors, which took 2013, in Miyazaki in Japan.

In this chapter the basic approach of crystal structure of SiC is presented, focusing on the hexagonal 4H polytype. Both structural and electrical proprieties are discussed. The most common defects occurring in the crystal with their description are listed as well. The last section is devoted to the CVD growth technics using to growth the 4H-SiC layers studied in this work.

1.1 Crystal structure of SiC and polytypism

The basic building block of a silicon carbide crystal is the tetrahedron of four carbon atoms with a silicon atom in the center see in the Fig.1. 1. There also exists a second type rotated 180° with respect to the first. The distance between the carbon and silicon atom is 1.89\AA and the distance between the carbon atoms is 3.08\AA [7]. SiC crystals are constructed with these units joining at the corners.

When Acheson found the hexagonal crystals in the voids [8], he sent some of them to B.W. Frazier, a professor at Lehigh University. Professor Frazier found that although the crystals were all silicon carbide, they differed in their crystalline structure. The crystals have a polymorphic structure. When this phenomenon occurs in one dimension (i.e. when different crystal structures appear when varying only one single dimensional parameter), is called polytypism .This is the case of SiC. Frazier discovered the polytypism of SiC [9].

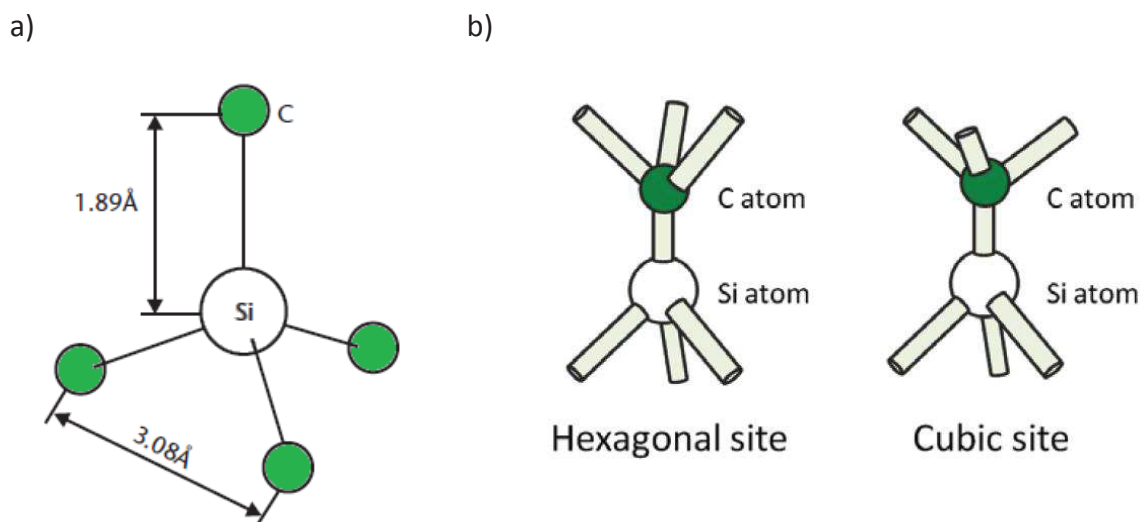


Fig.1. 1: a) The characteristic tetrahedron building block of a SiC crystal. Four carbon atoms are covalently bonded with a silicon atom in the center. Two types exist. One is rotated 180° around the c-axis with respect to the other, as shown in b) [7].

The elementary building block of the silicon carbide crystal is a covalently bonded tetrahedron structure of carbon (C) and silicon (Si) atoms as shown in Fig.1. 2. Every SiC crystal can be described by superimposed hexagonal crystal bilayers or double layers, compare to the figures in Fig.1. 1 and Fig.1. 2. The basis vectors of the hexagonal unit cell are $a_1 = (1 ; 0 ; 0) \times \alpha$ and $a_2 = (0.5 ; \sqrt{3}/2 ; 0) \times \alpha$, where $\alpha = 3.078 \text{ \AA}$ (average value). The third basis vector is $c = (0 ; 0 ; 1) \times c$ in the direction of the c-axis, where c is integer times of 2.52 \AA .

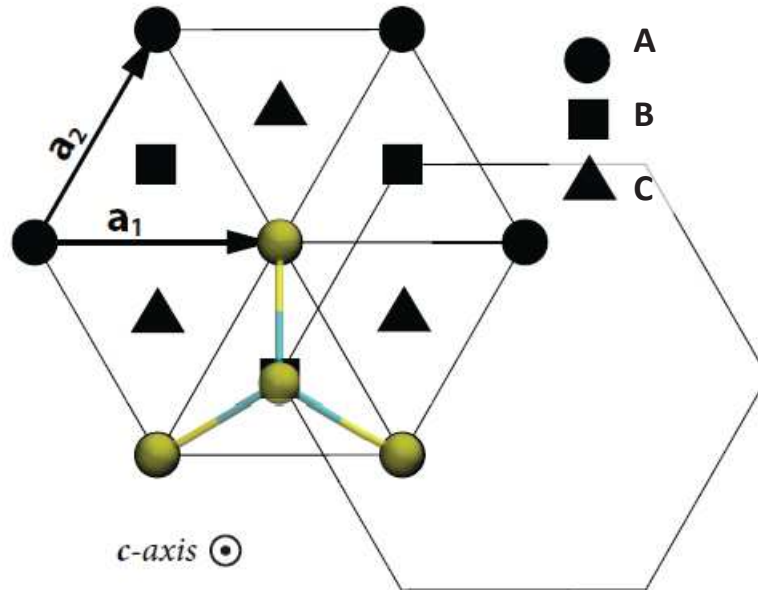


Fig.1. 2: The three possible hexagonal positions (A, B, and C) for Si and C atoms sketched schematically in a plane perpendicular to the c-axis. Symbols assigned to A, B and C letters represent Si and C atoms in bilayers of the successive hexagonal planes [9].

The polytype can be defined as the ability to crystallize in several different crystal structures by varying the packing layout of the same 2-dimensional unit cell in the direction of the c-axis. Starting from the lower (A) basal plane and starting from the A position for a vertical Si-C bond, there are two possibilities to stack the next Si-C bonds. They correspond with the two positions B or C. In both cases, the stacking of Si-C bilayers is done along the c-axis and the crystal lattice parameters in the (h_1, h_2, h_3) plane remains constant. As a consequence, different polytypes can belong to different lattice types and space groups. It is known from the beginning of the 20th century that silicon carbide has several polytypes [10], [11]. So far more than 250 SiC polytypes have been recognized [12]. The two extremes polytype are the pure cubic polytype (with zinc blende structure) and the pure hexagonal one (with wurtzite structure). All other polytypes represent hexagonal (H) or rhombohedral (R) combinations of these basic structures.

To distinguish between the different polytypes, there are different notations. Apart from the historical one that considers only the cubic polytype (referred to as β -SiC) from the complete family of hexagonal and rhombohedral polytypes (referred to as α -SiC), the simplest

notation was proposed by Ramsdell [13]. He noticed, first, the total number of Si-C bilayers in the stacking sequence and, next, indicated the crystal structure of the Bravais lattice (C for cubic, H for hexagonal and R for rhombohedral). In this way, the two simplest polytypes were noted 3C-SiC for the cubic one and 2H-SiC for the hexagonal one. In Fig.1. 3 the stacking sequences of the most common polytypes 2H, 3C, 4H and 6H are given in the Ramsdell notations.

This is the simplest notation but this is not the most accurate. An alternative way is to use the Hägg notation that described as “+” the stacking direction of bilayers A-B, B-C and C-A and “-” the stacking direction of A-C, C-B and B-A [14]. A simplification is the Zhdanov notation that gives the number of + and - consecutive sequences defined by the Hägg notation [15]. Finally, the Jagodzinski notation [16] accounts for the number of cubic (k) and hexagonal (h) non equivalent sites present in the polytype. For completeness, a summary of the different notations for the most common polytypes is given in Tab.1. 1.

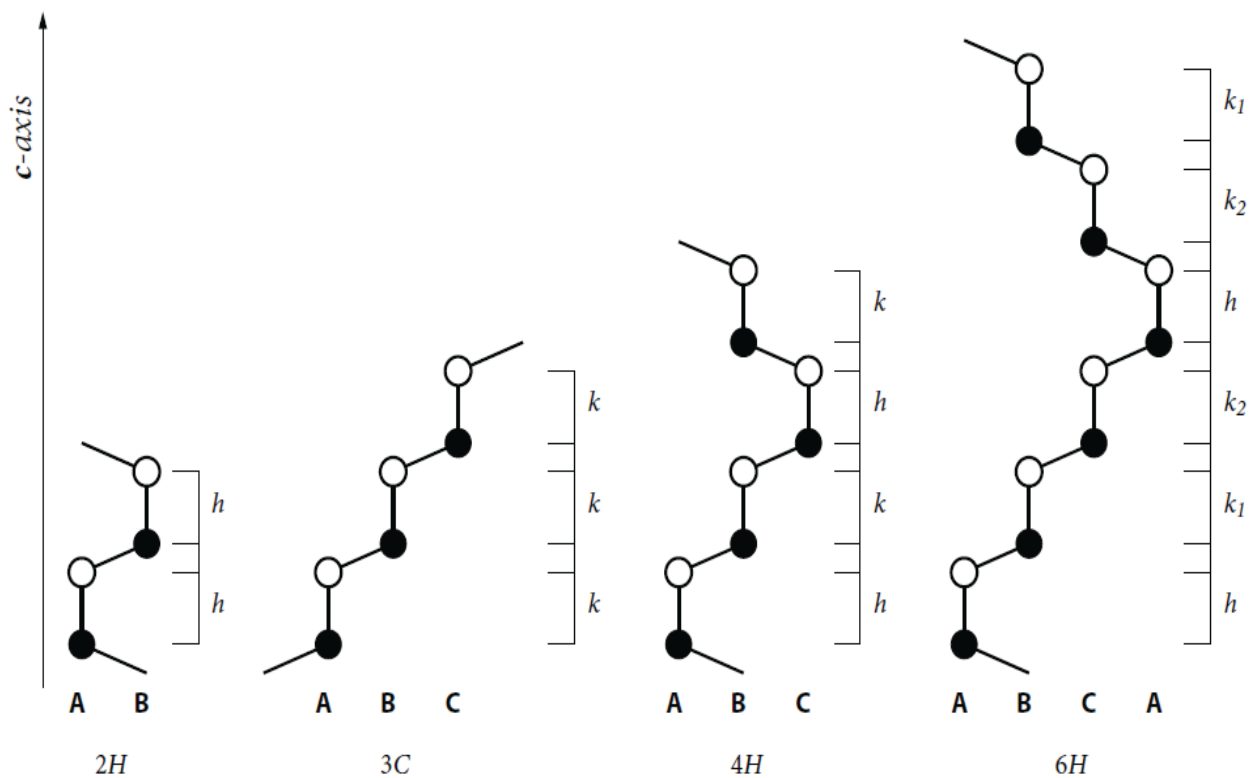


Fig.1. 3: Illustration of the primitive cells of important polytypes of SiC. It has to be noted, that in 3C-SiC, due its high T_d symmetry, the primitive cell contains only two atoms [7].

Stacking sequence	Ramsdell	Hägg	Zhdanov	Jagodzinski
ABC	3C	(+++)	(3)	K
AB	2H	(+-)	(11)	H
ABCB	4H	(++--)	(22)	Hk
ABCACB	6H	(+++---)	(33)	Hkk
ABCABACB	8H	(++++----)	(44)	Hkkk
ABCBACABACBCACB	15R	(++---) ₃	(23) ₃	Hkchk
ABCACBACBACBCABACB	21R	(+++----) ₃	(34) ₃	hkkhkkk

Tab.1. 1 : Different notations of the most common SiC polytypes.

All the polytypes of SiC are referred to a hexagonal coordinate system consisting of three a-plane coordinates a_1 , a_2 , and a_3 , and a c-axis coordinate (see Fig.1. 4). The c-axis is the direction of the stacking of hexagonally close packed layers, and the three a-plane axes are all in the plane perpendicular to c-axis as shown in Fig.1. 4, with 120-degree angle between a-planes. Commercially available SiC bulk material is generally cut and polished 2-8 degrees off-axis towards $\langle 11\bar{2}0 \rangle$ for avoiding the growth of 3C inclusions in the epitaxial layers of 4H, called step-controlled epitaxy by Matusunami et al. [17]. Two different faces perpendicular to the c-axis (Si 0001 and C 000 $\bar{1}$) exist in commonly used SiC. SiC with the silicon face is commonly used for device applications since the quality of epitaxial growth is better than that on the carbon face.

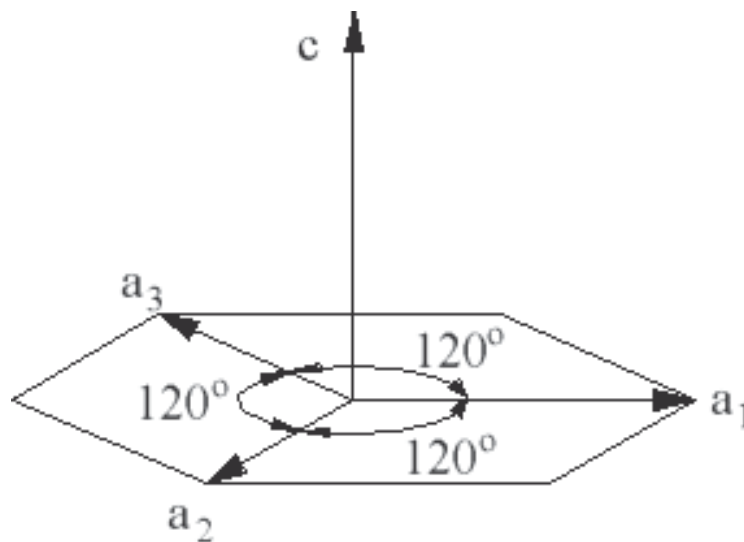


Fig.1. 4: The Miller indices describing the hexagonal structure [3].

1.1.1. Electronic structure of SiC

Different polytypes differ only in the stacking of double layers, however, this affects all electronic and optical properties of the crystal. From an application viewpoint the important polytypes are the 3C and the 6H and 4H. The latter two can be grown conveniently, unlike 3C-SiC. Let's focus on the 4H-SiC polytype. 4H-SiC has two non-equivalent positions for carbon and silicon atoms according to hexagonal (h) and cubic (k) bilayers. Properties and electronic structure of defects may vary depending on the two different places. This is called site-dependency. Polytypes with hexagonal crystal structure have hexagonal Brillouin zone (BZ). The Fig.1. 5 shows the most important points in the hexagonal Brillouin zone, as well as the M – Γ section of the calculated band structure of 4H-SiC. Silicon carbide is an indirect semiconductor. In 4H-SiC the conduction band minimum is at the M point, while the valence band maximum is at the Γ point of the BZ see Fig.1. 5. Carbon and silicon atoms are bonded by sp^3 hybrid covalent bonds. Due to the higher electronegativity of carbon atoms, bonds are slightly negatively polarized toward carbon atoms.

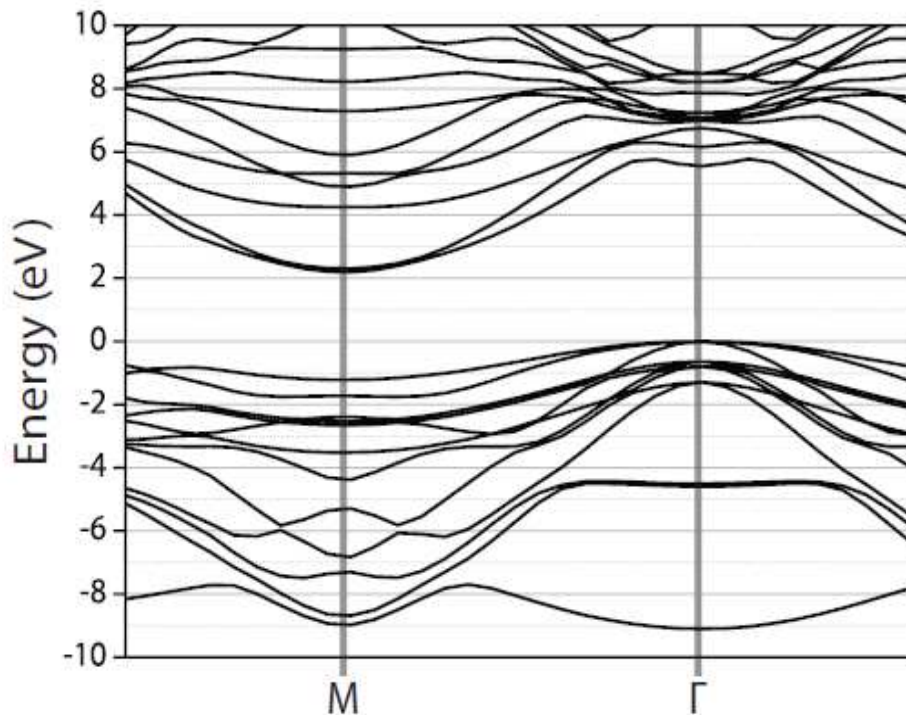


Fig.1. 5: Illustrative picture of the indirect gap of the calculated band structure of 4H-SiC

1.1.2. Energy bandgap (E_g)

The band gap in SiC polytypes is indirect. Experimentally, the band gap energy for the different polytype range from 2.39 eV for 3C-SiC, to 3.330 for 2H-SiC with 3.265 eV for 4H-SiC [18] at room temperature. The top of the valence band is at the Γ point ($k=0$) in the Brillouin zone (BZ), whereas the conduction band minima occur at the BZ boundary. The exact positions of the conduction band minima and their energy with respect to the top of the valence band (the band gap) depend on the polytype. For example, the minima are at the X points in the BZ of 3C-SiC (see Fig.1. 6), the M points in the BZ of 4H-SiC (see Fig.1. 6 b)), and along the M-L lines in the BZ of 6H-SiC (see Fig.1. 6 b)). The number of equivalent conduction band minima is therefore three, three, and six, respectively for these polytypes. Photons with the necessary energy to bridge the band gap have a very small momentum or k-vector compared with the k-vector separation between the valence and conduction band edges.

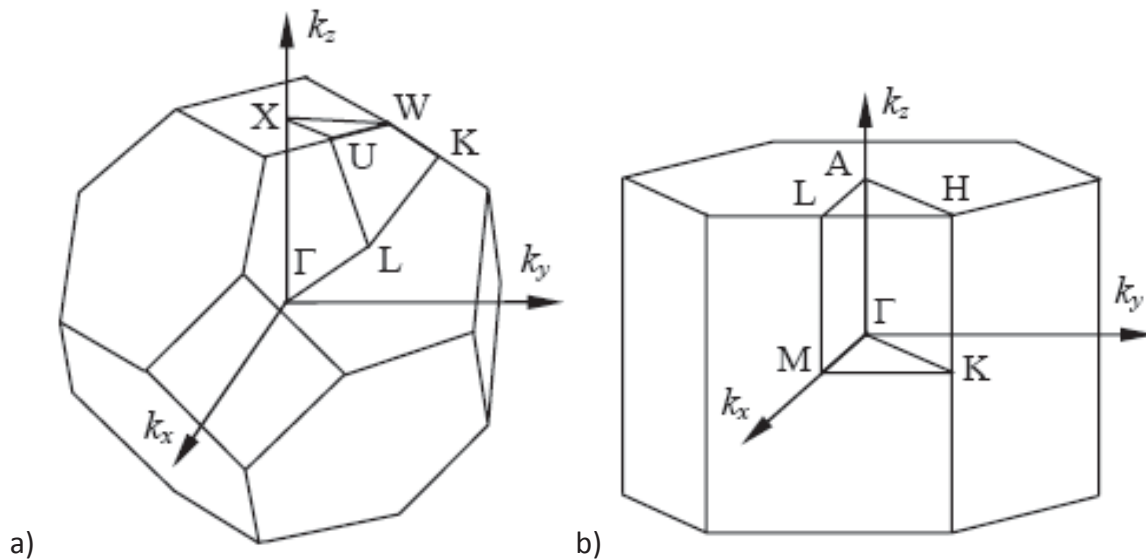


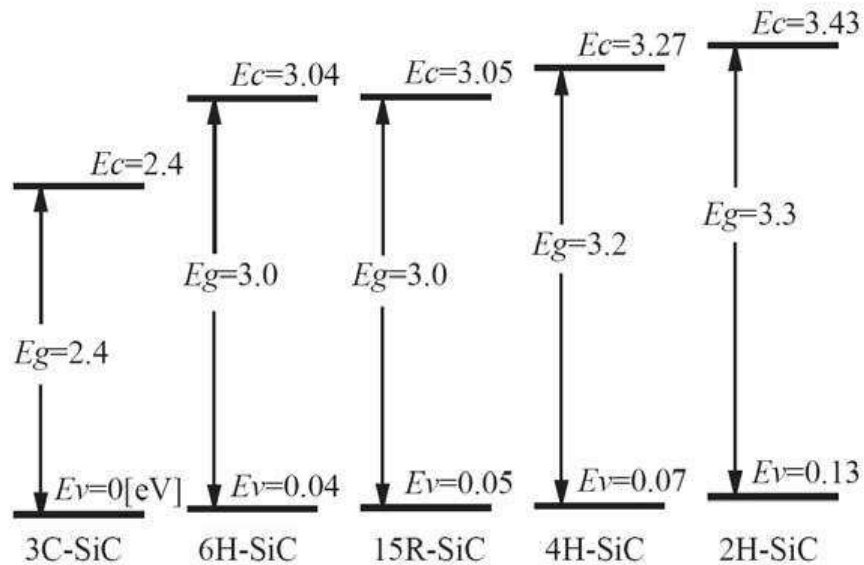
Fig.1. 6 Brillouin zones for a) cubic (3C) and b) hexagonal (4H and 6H) SiC.

The top of the valence band in SiC is P -like. The holes can thus be characterized by an orbital angular momentum $L_h=1$ and a spin $S_h=1/2$. A small splitting of the valence band states results from the spin-orbit (SO) coupling and the crystal field (CF) of the particular SiC polytype. The degeneracy of P -like states is not lifted in cubic symmetry. Therefore, in 3C-SiC the valence band edge is only split by SO coupling. The resulting states are states of total angular momentum $J_h = 3/2$ and $J_h=1/2$, the former lying uppermost. In the hexagonal and rhombohedral polytypes the CF is uniaxial, and thus the P -like states are affected.

An electron at the bottom of the conduction band in SiC behaves as a spinlike particle, that is, $L_e=0$ and $S_e=1/2$. In addition to spin degeneracy, there will also be degeneracy owing to the occurrence of several inequivalent conduction band minima. The wavefunction of the electron can be described by a linear combination of the wavefunctions belonging to the different conduction band minima. If the electron is localized at a defect, the linear

combinations will have to conform to the symmetry of the defect. Since the different possible combinations will overlap differently with the defect, they may have different energies resulting in so-called valley orbit (VO) splitting. In Fig.1.7 a) we can see a diagram of the energy band gap for the five most common SiC polytypes. The energy difference of the conduction band of the cubic polytype in respect with the hexagonal is quite large while the respective differences in the valence bands is of the order of 1/10 of the differences in the conduction bands.

a)



b)

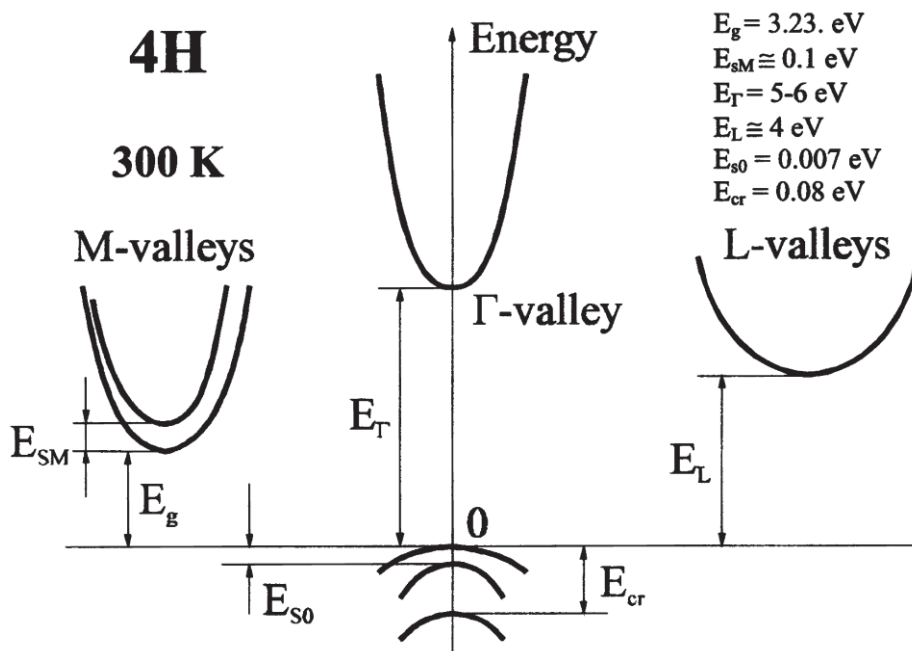


Fig.1. 7 : a) The energy diagram of five most common polytypes, b) Band structure of 4H-SiC at 300K. Important minima of the conduction band and maxima of the valence band are shown [19].

The experimentally energy band gap for 4H-SiC is 3.265 eV [18].

Fig.1. 7 b) shows the band gap structure of 4H-SiC. The wide band gap makes it possible to use SiC for very high temperature operation. Thermal ionization of electrons from the valence band to the conduction band, which is the primary limitation of Si-based devices during high temperature operation, is not a problem for SiC-based devices due to the wide band gap.

1.2 Doping in different polytypes

One of the most widely studied impurity is nitrogen as this is believed to cause the n-type character of high purity material. Boron, aluminum and gallium have received a great deal of attention as acceptors in SiC. Reports of beryllium-doping and oxygen-doping have also been made. The standard techniques of Hall measurements and photoluminescence have mainly been used to studies about different aspects of dopant.

A very striking and beautiful feature of polytypism is the behavior of impurity atoms. In Fig.1. 8 it may be seen that the sites are not equivalent in the hexagonal polytypes 4H-SiC and 6H-SiC. The difference is in the second-nearest neighbors.

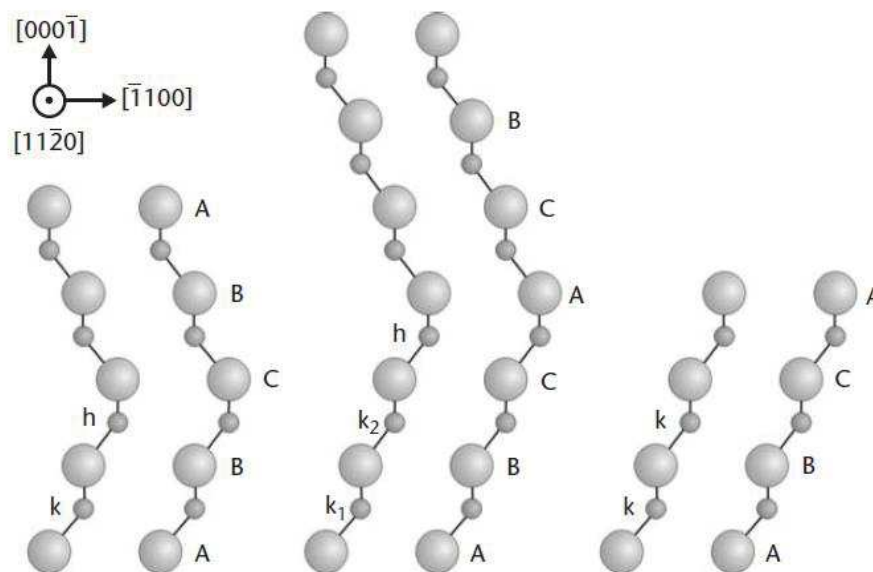


Fig.1. 8 : The three most common polytypes in SiC viewed in the $[11\bar{2}0]$ plane. 4H-SiC, 6H-SiC, and 3C-SiC respectively; k and h denote crystal symmetry points that are cubic and hexagonal, respectively [7].

Nitrogen as well as other donor impurities, such as phosphorus, occupy the carbon sites substituting a carbon atom in the lattice can either occupy a “k” site or an “h” site in 4H-SiC [20]. The k site is a lattice site that displays cubic symmetry, whereas the h site has hexagonal symmetry. The immediate vicinity of a nitrogen atom on either site is the same, but the second-nearest neighbors to the sites are different, which creates a slightly different core binding energy. Thus, 4H-SiC has two binding energies for the nitrogen donor, which has consequences when designing devices. 6H-SiC has three energy levels for nitrogen and 3C-SiC has only one. More complex polytypes such as rhombohedral (15R-SiC) has no less than five binding energies, although only four have been identified. Boron may substitute on the carbon sublattice or may occupy either the carbon or the silicon site (or both sites), in order to minimize the total free energy of the system. In the other hand aluminum atoms substitute only on the silicon sublattice [21]. The SiC polytype does not affect the site preference of these impurities, though energy levels of impurity atoms differ in the different polytypes.

Epilayer doping can be achieved by mixing e.g. nitrogen (for n-type doping) and trimethylaluminum (for p-type doping) with precursor gases during epitaxy for the most common dopant species i.e. nitrogen and aluminum. Phosphine (PH₃) and diborane (B₂H₆) can be used for less common dopant species such as phosphorus and boron. The doping concentration can be controlled by changing the silicon-carbon ratio (Si:C). This can easily be done by adjusting the amount of precursor gases.

1.3 Defects

The great advances in the development of SiC technology over the past 10–15 years have made it possible to develop almost all the basic types of semiconductor devices based on SiC, including the first integrated circuits. It is evident that further advances in the technology of SiC and the creation of new devices will, on the one hand, require studies of the parameters of deep centers in the epitaxial layers and *p-n* junctions obtained by various techniques. On the other hand, studies of the parameters of devices that have already been created can yield additional information on the properties of deep centers in them. In addition, the various methods for growing epitaxial layers and creating *p-n* junctions lead to the formation of different deep centers in the bulk of the semiconductor and on its surface, which in turn affect the characteristics of devices created from them. Thus, it is possible to determine the optimum combination of technologies for creating a given type of device with the best set of operating characteristics through studies of the parameters and distributions of deep centers. The purpose of this section is to summarize the currently available data on the parameters of deep centers in 4H-, 6H-, and 3C-SiC and to analyze their properties from

the standpoint of their possible influence on the characteristics of device structures based on SiC.

1.3.1 Deep center

Deep centers in a semiconductor have an effect on the lifetime and diffusion length of minority charge carriers, the efficiency of light-emitting diodes and photodetectors, the gain of transistors, and the magnitude of the temperature coefficient for the breakdown voltage of p-n junctions. To predict theoretically the main parameters of impurity and defect centers in the semiconductor material is impossible, the principal source of information on deep centers is experiment.

The allowed states in the band gap of semiconductors are traditionally divided into “shallow” and “deep” states. The shallow states are usually assumed to be those with ionization energies $E_i < 0.1$ eV, and deep states, those with $E_i > 0.1$ eV [22]. For SiC this division is even more arbitrary, since even the ground donor and acceptor levels have ionization energies $E_i \geq 0.1$ eV. Thus, strictly speaking, in SiC all the levels that have been studied are deep.

Nitrogen:

The residual type of SiC is n type, by nitrogen. Nitrogen has a fairly high solubility in SiC ($\approx 10^{21}$ cm⁻³) and the lowest ionization energy of all the impurity donor levels. By implanting N ions it is also possible to obtain thin, heavily doped layers of SiC for forming ohmic contacts [23], [24]. The existence of nonequivalent sites in the SiC lattice shows up most clearly in the energy position of the deep centers associated with nitrogen atoms [25], [26], [27]. In all the main polytypes of SiC, nitrogen atoms have been observed in association with both cubic (c) and hexagonal (h) lattice sites, with the ratio of the level concentrations (N_h/N_c) corresponding to the ratio of the number of hexagonal and cubic sites in the crystal lattices of the different SiC polytypes. $N_h/N_c=1:1$ for 4H, $N_h/N_c=1:2$ for 6H, and $N_h/N_c=2:3$ for 15R. According to the latest studies, the ionization energies of the nitrogen levels are [$E_c-0.081$, $E_c-0.138$, $E_c-0.142$ eV (6H)] [26]; [$E_c-0.052$, $E_c-0.092$ eV (4H)] [27], [28]. Most investigators assume that nitrogen occupies a carbon site in the SiC lattice [29], [30]. It has been reported that in the purest 4H-SiC layers the electron spin resonance (ESR) usually associated with nitrogen levels is absent [31]. This was believed to indicate a significant contribution from intrinsic defects to the conductivity of lightly doped layers of SiC. Another feature of SiC(N) samples is the formation of an exciton bound to a neutral donor level of nitrogen.

Aluminum:

The p-type silicon carbide is customarily obtained using Al which forms the shallowest acceptor levels in the lower half of the band gap and has the highest solubility ($\sim 10^{21}$ cm⁻³)

[32], [33], [34]. It has been shown [33] that when the Al concentration is raised from 10^{18} to 10^{21} cm^{-3} , its ionization energy decreases from 0.27 to 0.1 eV. Later it was shown [35] that the ionization energy of the Al levels ($E=0.24$ eV) is independent of its concentration up to 5×10^{20} cm^{-3} if the degree of compensation of the epitaxial layers is $k < 0.01$. For $k > 0.01$, the ionization energy dropped to 0.1 eV ($[\text{Al}] \sim 5 \times 10^{20}$ cm^{-3}). These results were explained in terms of percolation theory [36]; i.e., the interaction among all the forms of impurities in the compensated semiconductor gives rise to an additional potential, which reduces the ionization energy of the impurity. This explanation, however, does not rule out the formation of several types of deep centers when SiC is doped with aluminum. The doping of SiC with aluminum was the only method (until GaN light-emitting diodes were produced) for creating light-emitting diodes with peak emission in the blue region of the spectrum [37].

1.3.2 Stacking faults

Reports by Lendenmann [38] and Bergman [39] reveal that a 4H-SiC PiN diode operating under normal conditions begins to degrade. While the diode is operating, defects, which the authors interpret as stacking faults, evolve with an accompanying reduction in carrier lifetime. The defects thus act as recombination centers for the carriers. Furthermore, the stacking order has been identified as that of the 3C-SiC polytype and, according to the study by Stahlbush, an explanation to the recombinative behavior of the stacking fault is that the 3C-SiC, having a lower bandgap than 4HSiC, acts as a quantum well, thereby enhancing the recombination [40] [41]. It is a very serious materials issue that must be solved prior to the realization of commercial bipolar devices. Work is ongoing to reduce defects in SiC material. One of the concepts is the reduction of defects through epitaxial growth on porous SiC substrates [42]. This approach has clearly demonstrated a reduction in intrinsic defects, as evidenced by photoluminescence measurements. It is too early to tell whether this technique can provide a path forward for the bipolar devices but it will clearly find its applicability in several areas where SiC will have a market.

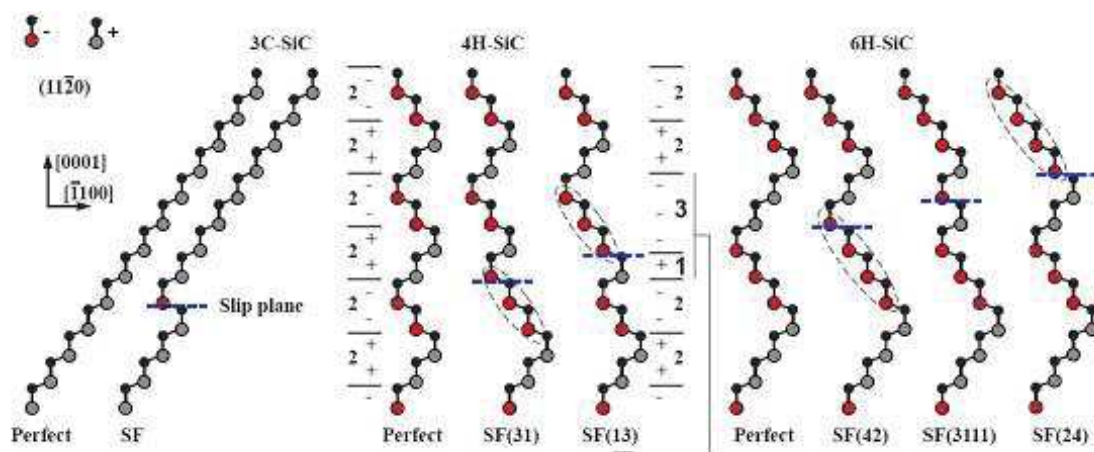


Fig.1. 9 : Simple SF on the three most known polytypes of SiC [44], [45].

The study about the SFs exhibit the behavior as quantum wells in the hexagonal polytypes were carried out in detail by J. Sun. et al. [43] [44], [45], [46]. It has been demonstrated that SFs are created or developed from the glide of partial Shockley dislocations [44], [45], [46], [47]. On the insert of Fig.1. 10 it is possible to see the separation of a perfect dislocation with a Burgers vector of $\mathbf{b}=\frac{1}{3} \langle 11\bar{2}0 \rangle$ to two partial dislocation with Burgers vectors $\mathbf{b}=\frac{1}{3} \langle 0110 \rangle$ and $\mathbf{b}=\frac{1}{3} \langle 10\bar{1}0 \rangle$. The movement and distribution of these dislocations are responsible for the creation of SFs on the 4H-SiC crystal.

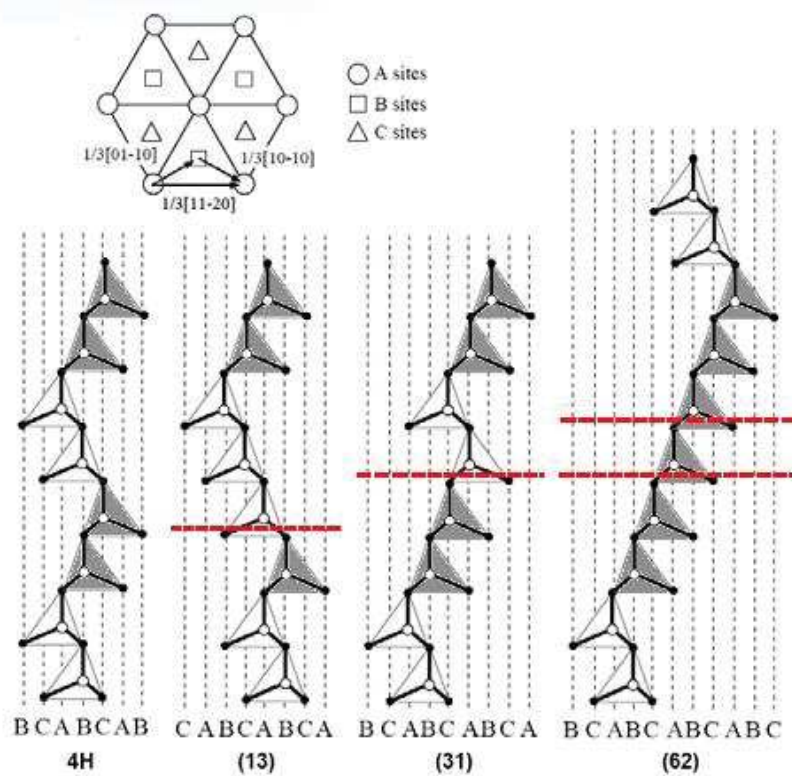


Fig.1. 10: Types of single SFs in 4H-SiC where the double SF is in the last configuration [45].

1.3.3 Micropipes

Micropipes may be caused by several screw dislocations bunching together to form a giant screw dislocation, making it energetically favorable to open up a hollow core [48]. A different way of forming micropipes may be simply by system contamination, where particles are trapped in the growing crystal, thus forming a micropipe, as described by Augustine et al. [49]. One of the way micropipes form, according to the same authors, is by vacancy condensation at a helical dislocation. Micropipes are basically a hollow core penetrating the entire wafer along the c -axis direction. Placing any device directly on top of the micropipe is bound to cause failure. These defects are particularly disturbing for large-area devices and high-power devices.

1.3.4 Vacancies

Vacancies in materials and in particular in SiC are caused by the absence of a Si (V_{Si}) or C (V_C) atom from the crystal lattice. The situation of these defects in SiC is different than other semiconductors, like Si, since the stronger chemical bond reduces the mobility of the vacancies. They are thermally stable at room temperature [50]. These defects can be electrically active and affect the electronic properties. They create energy states in the band gap and can be optically identified [50]. The two types of vacancies behave in different manners.

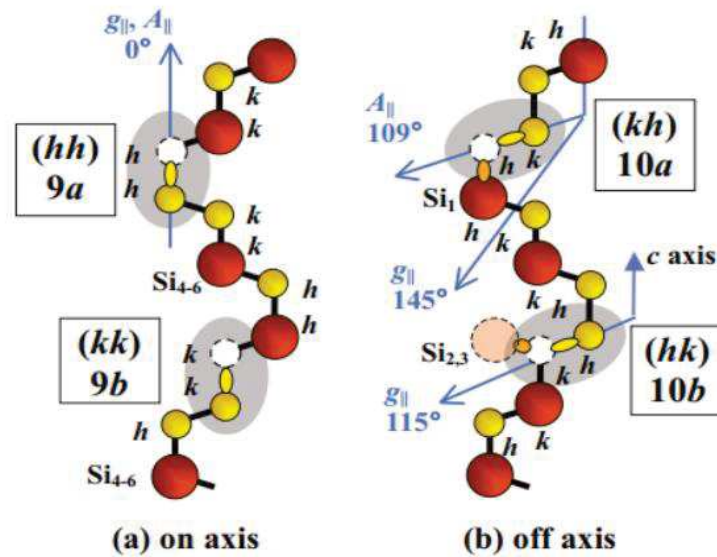


Fig.1. 11: Atomic models for four $C_{Si}V_C$ pairs in 4H-SiC. This figure shows a lattice structure in $(11\bar{2}0)$ plane of crystal. Carbon (silicon) atoms are drawn as small (large) balls, and their dangling bonds are drawn as small ovals. Open balls are carbon vacancies [51].

The dangling bonds around the V_{Si} vacancy are strongly localized at the neighboring carbon atoms due to the lack of p electrons in the carbon core. The distance of two neighboring atoms (3.09 \AA) is slightly larger than their bond length in pure silicon 2.35 \AA . This should lead to a lowering of the symmetry distortion for the carbon vacancies in SiC, like the vacancies in pure Si in order to gain energy with the formation of dimer like bonds between neighboring Si atoms [52].

1.3.5 Intrinsic Defects in Silicon Carbide

L-center

L-centers have been observed in p-n structures obtained by sublimation epitaxy (SE structures) and in several p-n structures produced by Container less Liquid Epitaxy (CLE structures). In the implantation structures their concentration increased near the metallurgical boundary of the p-n junction, while in the other types of samples there was no noticeable profile in the distribution of L-centers. The ionization energy of the L-centers was close to the data obtained by other methods for the ionization energy of an impurity Al level [33]. However, while in the case of the ID p-n structures the presence of Al atoms in the base region and a drop in their concentration far from the p-region can be explained, for the sharp CLE and SE structures, the presence of Al in the n-base at concentrations of 10^{16}cm^{-3} appears improbable. The relationship between the observed L-center and impurity Al atoms, a study was made of CLE and SE p-n structures with the n-base doped with aluminum during growth of SiC (Al) [53]. Based on studies of these samples, it was concluded [54], [55] that the L-center is a defect complex, which does not directly include an Al atom and develops after both diffusion and implantation of Al and for other reasons as well. Later, analogs of the L center were observed in 4H-SiC samples obtained by sublimation [56] and in 4H- and 6H-SiC samples obtained by CVD [57], [58].

Z_1 - Z_2 defects

Yet another double peak Z_1/Z_2 ($E_c - 0.6-0.7$ eV) has been observed [59] and subsequently also found in CVD epitaxial layers [60]. ESR was used previously to study several deep centers in 6H-SiC substrates obtained by the Lely method [61]. One of the observed centers with an energy of ~ 600 meV was associated with a Carbon vacancy (VC) – Silicon Vacancy (VSi) divacancy. It was suggested [62] that this center corresponds to the Z_1/Z_2 center observed by DLTS.

In the case of 4H-SiC, the shallower intrinsic defects were found in sublimation-grown epilayers at $E_c - (0.16-0.18)$ eV [63]. Parameters of this center were very close to parameters of radiation defects P_1/P_2 from reference [64]. More common for 4H-SiC is background level Z_1 energy $E_c - (0.63-0.68)$ eV, which was identified in materials grown by different technological methods [62], [65], [63]. According to Reference [63], the concentration of the Z_1 falls with decreasing $N_d - N_a$ value in the epilayer. For the same $N_d - N_a$ it is lower in layers with a high dislocation density.

1.4 Crystal Growth techniques

To bring SiC into real applications, it is essential to control the polytypes and the doping level during the crystal growth. Although the potential of SiC has been recognized for a long time, difficulty in growing high-quality and large size SiC crystals without polytype mixing had prevented electronic applications. An innovation in bulk crystal growth using a seeded sublimation method (a modified Lely method) for controlling polytypes has changed research and development of SiC devices [66]. Nowadays the diameter is rapidly increasing and 6-inch wafers have already been demonstrated. The increase in wafer diameter is significantly faster than that experienced for Si and GaAs, [67]. A lot of research is being conducted on the seeded sublimation growth technique. The current standard of 8° off-axis from the [0001] plane on the 4H-SiC wafers was introduced in 1995 by Cree. The trend must be to reduce the off-axis angle. Fortunately, if we look at what has happened previously in the Si and GaAs worlds, the standard was to use off-axis substrates initially, but as the material quality improved, the need for off-axis substrates was reduced and on-axis substrates are now used for epitaxy.

The source material will release excess silicon in the beginning of the growth cycle and be more carbon-rich in the end due to preferential depletion of silicon. This is a known problem and it is a matter of detailed control and an understanding of the dynamic transport mechanisms in combination with thermodynamics. Nevertheless, the result is invariably that SiC boules grown by seeded sublimation growth are Si-rich in the beginning and C-rich near the end, which creates yield issues.

There are mainly three different techniques used to grow epitaxial layers of SiC. Liquid phase epitaxy (LPE), sublimation epitaxy (SE) and chemical vapor deposition (CVD). The first two techniques are characterized by their high growth temperature (1700-2000°C) and high growth rate (from 15 $\mu\text{m}/\text{h}$ to more than 2 mm/h). Although these two techniques have shown promising results concerning the high growth rate and relative low residual doping they are not as well suited for growth of device structures as the CVD technique. The high temperature used releases unwanted impurities (like boron, titanium and aluminum) from the graphite which might be difficult to remove. The control of intentional doping for growth of device structures may also be difficult. In this work all investigated samples were grown by CVD method.

1.4.1 Chemical Vapor Deposition (CVD)

Chemical vapor deposition (CVD) is a process whereby a solid material is deposited from a vapor by a chemical reaction occurring on or in the vicinity of a normally heated substrate surface. The solid material is obtained as a coating, a powder, or as single crystals. By varying the experimental conditions—substrate material, substrate temperature, composition of the reaction gas mixture, total pressure gas flows, etc. materials with different properties can be grown. A characteristic feature of the CVD technique is its excellent throwing power,

enabling the production of coatings of uniform thickness and properties with a low porosity even on substrates of complicated shape. Another characteristic feature is the possibility of localized, or selective deposition, on patterned substrates. Other CVD applications are the preparation of high temperature materials (tungsten, ceramics, etc.) and the production of solar cells, of high temperature fiber composites, and of particles of well-defined sizes. Recently, high- T_c superconductors have also been made by this technique [68]. Since oxygen activity in the vapor can be precisely controlled during the deposition, no annealing in oxygen is needed to achieve superconductivity.

The development of SiC CVD reactors are towards rotation of the substrates which is probably necessary to obtain the high doping and thickness uniformity needed for certain devices. The precursors used for growth of SiC are usually silane (SiH_4) and propane (C_3H_8) whereas hydrogen is used as carrier gas. The gases pass over a heated graphite susceptor that is coated by SiC or tantalum carbide (TaC). The velocity of the gases is high but it is always laminar flow. Over the susceptor there will be a boundary, or stagnant, layer where the velocity gradient decreases to zero. As the gases are heated, the silane and hydrocarbon will decompose and the species will diffuse through the boundary layer to grow on the reactor walls or on the substrate. A comprehensive study of this may be found in a paper by M. Leys and H. Veenvliet [69]. The concentration of precursor gases will decrease with respect to the flow direction over the susceptor due to the consumption of growth species, which results in a tapered layer thickness. This effect is known as depletion. To compensate for the depletion it is common to taper the susceptor such that the velocity of the gases increases along the flow direction over the susceptor and thus the boundary layer will be pushed downward, resulting in a shorter diffusion for the active species to the substrate. It is sometimes not enough to taper the susceptor to achieve good homogeneity of thickness and doping, hence other more complicated measures are applied, such as rotation of the substrate as described in the literature [67]. The silicon cluster formation was first noticed and studied in detail by Rupp et al. in a single wafer Emcore reactor with a very high thermal gradient [70].

The schematic representation of hot-wall CVD reactor, and conceptual diagram of the horizontal hot-wall CVD reactor for epitaxial SiC is shown in Fig.1. 12 and Fig.1. 13 respectively. The CVD process used in this thesis is a horizontal homemade hot-wall CVD, for more details see ref. [71].

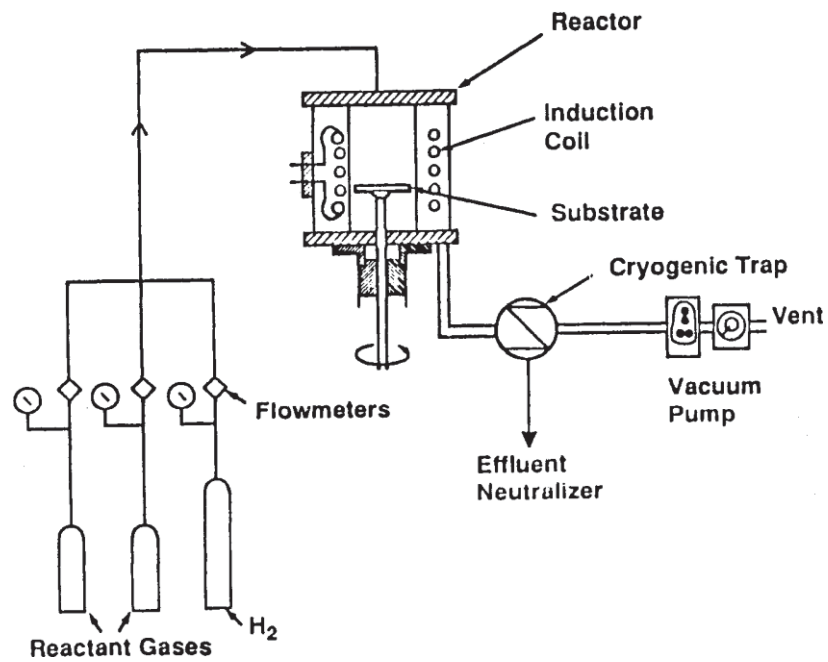


Fig.1. 12: Schematic diagram of typical CVD apparatus [72].

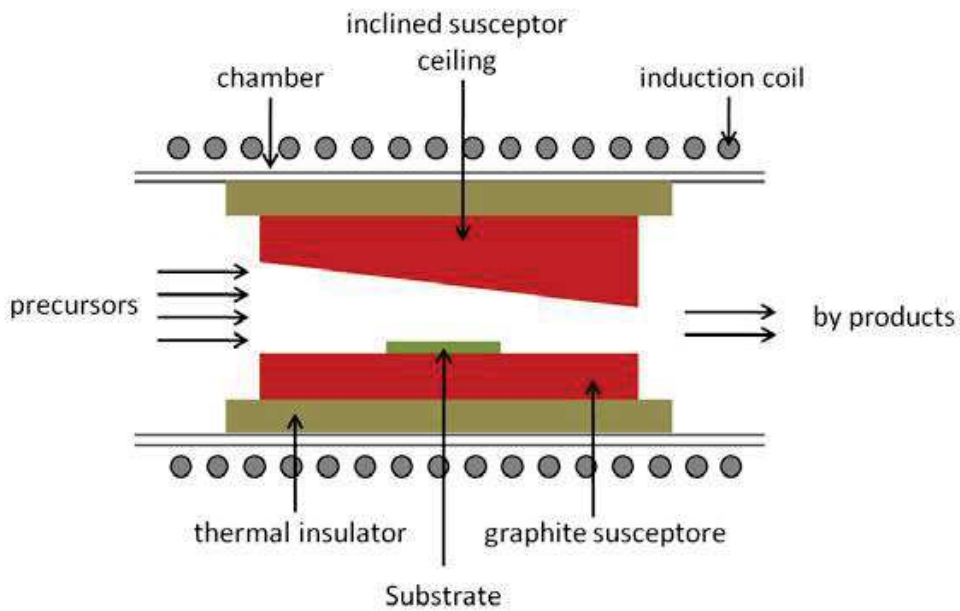


Fig.1. 13: Conceptual diagram of the horizontal hot-wall CVD reactor for epitaxial SiC [73].

1.4.2 Doping Control

Nitrogen (N_2) and Al are used as dopants to obtain n- and p-type, respectively. This can be done by introducing nitrogen for n-type and trimethylaluminum (TMA) for p-type layers. To obtain a better range of doping, it has been elegantly demonstrated that by changing the C/Si ratio of the input gases the doping concentration will change without changing the flow of nitrogen [74] or TMA. This effect is known as site competition [75]. The influence of the site competition effect has been studied in detail by R. Arvinte et al. for 4H-SiC [76]. Unfortunately, when changing the stoichiometry, the morphology is affected somewhat and it is therefore not always desirable to do this if thick layers are to be grown.

When doping is used and multiple layers are grown with different carrier type and conductivity, it is important that the doping level decreases rapidly after the source of the dopant is shut off. Otherwise one does not achieve abrupt junctions. This is known as the memory effect and it can be reduced by various tricks. For instance, one can vary the stoichiometry, provide a short purge without any dopant but continue to flow the normal precursor gases, or even perform an in-situ etch back before the next layer is grown. Although an Al memory effect was a concern in the early 1990s, this problem has been solved and it is no longer a concern.

Bibliography

- [1] R. J. Trew, «Phys. Status. Solidi.,» vol. A162, p. 409, 1997.
- [2] T. P. Chow, N. Ramungul, M. Ghezzi, "Proc. High Temperature Electronic Materials," *Devices and Sensor Conference, San Diego, p.176, USA.1998.*
- [3] C.-M. Zetterling, "Ph.D Thesis," *Department of Electronics, KTH, Royal Institute, Royal Institute of Technology, Sweden, p.15, 1997.*
- [4] P. Tobias et al., *Device Lett*, vol. 18, p. 287, 1997.
- [5] A. A. Yassen, C. A. Zorman et M. Mehregany, *J. Microelectromechanic. Sys.*, vol. 8, p. 237, 1997.
- [6] Y. M. Tairov et V. F. Tsvetkov, *J. Crystal Growth*, vol. 52, p. 146, 1981.
- [7] Stephen E. Sadow, A. Agarwal, A. House, *Advances in Silicon Carbide Processing and Applications 1 Janv.* p.8-11, 2004.
- [8] A. G. Acheson, *Engl. Patent*, p. 17911, 1892.
- [9] B. W. Frazier, J. Franklin, *Inst.*, p. 287, 1893.
- [10] R. Wang, I. B. Bath, T. P. Chow, *J. Appl. Phys*, vol. 92, p. 7587, 2002.
- [11] R. F. Adamsky, K. M. Merz et Z. Krist, vol. 111, p. 350, 1959.
- [12] G. R. Fisher et P. Barnes, *Philos. Mag. B*, vol. 61, p. 217, 1990.
- [13] L. S. Ramsdell, *Am. Mineralogist*, vol.32, p. 64, 1947.
- [14] H. G. Lundegardh, *Arkiv. fur Kemi. Mineralogi och Geologi*, vol. 1, p. 1-6, 1943.
- [15] G. Zhadanow, et al., *J. Phys. USSR*, vol. 59, pp. 422-424, 1946.
- [16] H. Jagodzinski, *Acta. Cryst.*, vol.2, p. 201, 1949.
- [17] T. Kimoto, H. Nishino, W. S. Yoo et H. Matsunami, *J. App. Phys.*, vol. 73, p. 726, 1993.
- [18] W. J. Choyke, G. Pensl, "Physical Properties of SiC", *MRS Bulletin*, 1997.
- [19] C. Persson, U. Lindefelt, *J. Appl. Phys*, vol. 11, pp. 496-5508, 1997.
- [20] H. Woodbury, G. Ludwig, *Phys. Rev. (USA)*, vol. 124, p. 1083, 1961.
- [21] Y. Tajima, W. Kingery, *Commun. Am. Ceram. Soc. (USA)*, vol. 65, p. 27, 1982.

- [22] A.A.Lebedev, Semiconductors, Deep level centers in silicon carbide: A review, vol.33, n. 2, p.107-130.
- [23] M.V.Rao, J.Gardner, O.W.Holland, M. G.Kelner, D.S.Simons et P.H.Chi, *Inst. Phys. Conf. Ser*, vol. 142, p. 521, 1996.
- [24] M.V.Rao, J.B.Tucker, M.C.Ridgway, O.W.Holland, N.Papanicolau, J.Mittereder, *J. Appl Phys*, vol. 86, p. 752, 1999.
- [25] E.N.Kolabukhova, S.N.Lukin, *Mater. Sci. Forum*, vol. 1, p. 791, 2000.
- [26] W.Suttrop, G.Pensl, W.J.Choyke, R.Steine, S. Leibenzeder, *J. Appl. Phys*, vol. 72, p. 3708, 1992.
- [27] W.Got, A.Schoner, G.Pensl, W.Suttrop, W.J.Choyke, R.Steine, S.Leibenzeder, *J. Appl. Phys*, vol. 73, p. 3332 , 1993.
- [28] C.Q.Chen, J.Zeman, F.Engelbrecht, C.Peppermuller, R.Helbig, Z.H.Chen, *J. Appl. Phys*, vol. 87, p. 3800, 2000.
- [29] M.A.Capano, J.A.Cooper, A.Saxle, *J. Appl. phys*, vol. 87, p. 8773, 2000.
- [30] T. Troffer, W.Gotz, A.Schoner, G.Pensl, R.P.Devaty, W.J.Choyke, *Inst. Phys. Conf. Ser*, vol. 137, p. 173, 1994.
- [31] Y. A.Vodakov, E.N.Kalabukhova, S.N.Lukin, A.A.Lepneva, E.N.Mokhov, *Sov. Phys. Solid State*, vol. 20, p. 258, 1978.
- [32] V.H.Daal, W.F.Knippenberg, J.D.Wassher, *J. Phys. Chem. Solids*, vol. 24, p. 109, 1963.
- [33] G.A.Lamakina, Y. A.Vodakov, E.N.Mokhov, V.G.Oding, G.F.Kholuyanov, *Sov. Phys. Solid State*, vol. 12, p. 2356, 1970.
- [34] I.V.Kodrau, V.V.Makarov, *Sov. Phys. Semicond*, vol. 11, p. 809, 1977.
- [35] A.Schoner, N.Nordell, K.Rottner, R.Helbig et G.Pensl, *Inst. Phys. Conf. Ser*, vol. 142, p. 493, 1996.
- [36] B.I.Shklovskii, A.L.Efros, *Sov. Phys. Semiconductor*, 14, 351 (1980)., vol. 14, p. 351, 1980.
- [37] L.L.Clemen, R.P.Devaty, W.J.Choyke, J.A.Powel, D.J.Larkin, J.A.Edmond, A.A.Burk, *Inst. Phys. Conf. Ser*, vol. 137, p. 297, 1994.
- [38] H. Lendenmann et al., "Proceedings of the Ultra-Low-Loss Power Device Technology workshop", p. 125-130, 2000.

-
- [39] J. P. Bergman et al., *Mat. Sci. Forum*, vol. 1, p. 299-302, 2001.
- [40] R. Stahlbush et al., *Mat. Sci. Forum*, vol. 389–393, p. 427–430, 2002.
- [41] S. Juillaguet, T. Robert, J. Camassel, “9th Expert Evaluation & Control of Compound Semiconductor Materials & Technologies”, vol. 165, p. 5, 2009.
- [42] S. E. Saddow et al., *Mat. Sci. forum*, vol. 1, p. 115–118, 2001.
- [43] J. Sun, et al., *Materials Science Forum*, vol. 717, pp. 407-720, 2012.
- [44] H. Iwata, U. Lindefelt, S. Öberg et P.R. Briddon, *J. Appl. Condens. Matter*, vol. 14, p. 12733, 2002.
- [45] H. Iwata, U. Lindefelt, S. Öberg, P. Briddon, vol.2340-342, p. 165, 2003.
- [46] H. Iwata, U. Lindefelt, S. Öberg et P. Briddon, *Microelectronics Jurnal*, p. 371, 2003.
- [47] U. Lindefelt, H. Iwata, S. Öberg, P.R. Briddon, *Phys. Rev. B*, vol. 67, 2003.
- [48] F. Frank, *Acta Crystalc*, vol. 4, pp. 497-501, 1951.
- [49] G. Augustine et al., *Phys. Stat. Sol. (b)*, vol. 202, p. 137, 1997.
- [50] H. Itoh, M. Yoshikawa, I. Nashiyama, S. Mishawa, H. Okumura, S. Yoshida, *Trans Nucl. Sci.*, vol. 37, p. 1732, 1990.
- [51] T. Umeda, J. Ishoya, “Identification of positively charged carbon antisite-vacancy pairs in 4H-SiC”, *Physev.*, vol. 75, p. 245202, 2007.
- [52] A. Zywiets, J. Furthmüller, F. Bechstedt, «*Phys. Rev. B*,» vol. 59, p. 15166, 1990.
- [53] M.M.Anikin, N.I.Kuznetsov, A.A.Lebedev, N.S.Savkina, A.L.Syrkin et V.E. Chelnokov, *Semiconductors*, vol. 28, p. 278, 1994.
- [54] M.M.Anikin, A.A.Lebedev, N.Popov, A.L.Syrkin, A.V.Suvorov, G.P.Shpynev, *Technology of Semiconductor Power Devices*, p.19 Valgus, Tallin, 1987.
- [55] N.I.Kuznetsov, A.P.Dmitriev, A.S.Fuman, *Semiconductors*, vol. 28, p. 584, 1994.
- [56] A.A.Lebedev, *Semiconductors*, vol. 33, p. 1004, 1999.
- [57] N.I.Kuznetso et J.A.Edmond, *Sov. Phys. Semicond*, vol. 31, p. 1481, 1997.
- [58] N.I.Kuznetsov, A.S.Zubrilov, *Mater. Sci. Eng. B*, vol. 29, p. 181, 1995.
- [59] H.Zhan, G.Pensl, A.Domer et S.Leibenzeder, *Ext. Abstr. Electrochem. Soc. Mtg*, p. 699-

700, 1989.

- [60] G.C.Rubicki, *J. Appl. Phys*, vol. 78, p. 2996, 1995.
- [61] A.I.Vainer, V.A.Ilin, Yu.M.Tairov, V.F.Tsvetkov, *Sov. Phys. Semicond.*, vol. 15, p. 902, 1981.
- [62] T.Dalibor, G.Pensl, H.Matsunami, T.Kimoto, W.J.Choyke, A.Schoner, N.Nordel, *Phys. Status Solidi*, vol. 162, p. 199, 1997.
- [63] A.A.Lebedev, D.V.Davydov, N.S.Savkina, A.S.Tregubova, M.P.Scheglov, R.Yakimova, M.Suvajarvi, E.Janzen, *Semiconductors*, vol. 34, p. 1183, 2000.
- [64] J.M.Langer, H.Heinrich, *Phys. Rev. Lett*, vol. 55, p. 1414, 1985.
- [65] J.P.Doyle, M.O.Adoelfotoh, B.G.Svensson, A.Schoner, N.Nordel, *Diamond Relat. Mater.*, vol. 6, p. 1388, 1997.
- [66] Y. M.Tairov, V.F.Tsvetko, *J. Crystal Growth*, vol. 52, p. 146, 1981.
- [67] A. Schöner et al., *Mat. Sci. Forum*, vol. 1, p. 187-190, 2002.
- [68] P. M. Martin, *Handbook of Deposition Technologies for Films and Coatings*, Third edition, chap.1, p. 12, 2009.
- [69] M. R. H. Leys, H. Veenliet, *J. Cryst. Growth*, vol. 55, p. 145, 1981.
- [70] R. Rupp et al., *Mat. Sci. Forum*, vol. 264–26, p. 89–96, 1998.
- [71] A. Leycuras, *Mater. Science Forum*, vol. 241, p. 338-348, 2000.
- [72] D. S. D. LeMay, *A User's Guide to Accurate Gas Flow Calibration*, 1996.
- [73] O. Kordina, C. Hallin, A. Henry, J. Bergman, *Physica Status Solidi B*, vol. 202(1), p. 321-334, 1997.
- [74] M. Zielinski, et al., *J. Cryst. growth*, vol. 310, p. 3174, 2008.
- [75] D. Larkin, *J. Phys. Stat. Sol. (b)*, vol. 202, p. 305, 1997.
- [76] R. Arvinte, et al., *Mat. Science Forum*, To be published, 2014.

Chapter 2: Experimental techniques

Introduction

After growth of an epitaxial layer there are several techniques to study its quality, particularly in term of doping level that directly determines the performances of the final device. In this chapter the principal characterization techniques used in this work will be presented along with some theoretical explanations of how they work. First Secondary Ion Mass Spectrometry (SIMS) experiment will be considered. Then, focus on non-destructive Raman and PL investigation techniques.

2.1 Secondary ion mass spectrometry (SIMS)

Secondary ion mass spectrometry (SIMS) has gained in popularity in semiconductor analysis as a tool to identify atomic species, in particular the doping concentration. SIMS is based on the observation of charged particles (Secondary Ions) ejected from the sample surface when it is bombarded by a primary beam of heavy particles (Primary Ions). Because the analyzed area is etched, SIMS is a destructive method.

The setup used in this work is a CAMECA IMF5f system, upgraded from an IMS4f base [1]. A schematic of the system is shown in Fig. 2.1

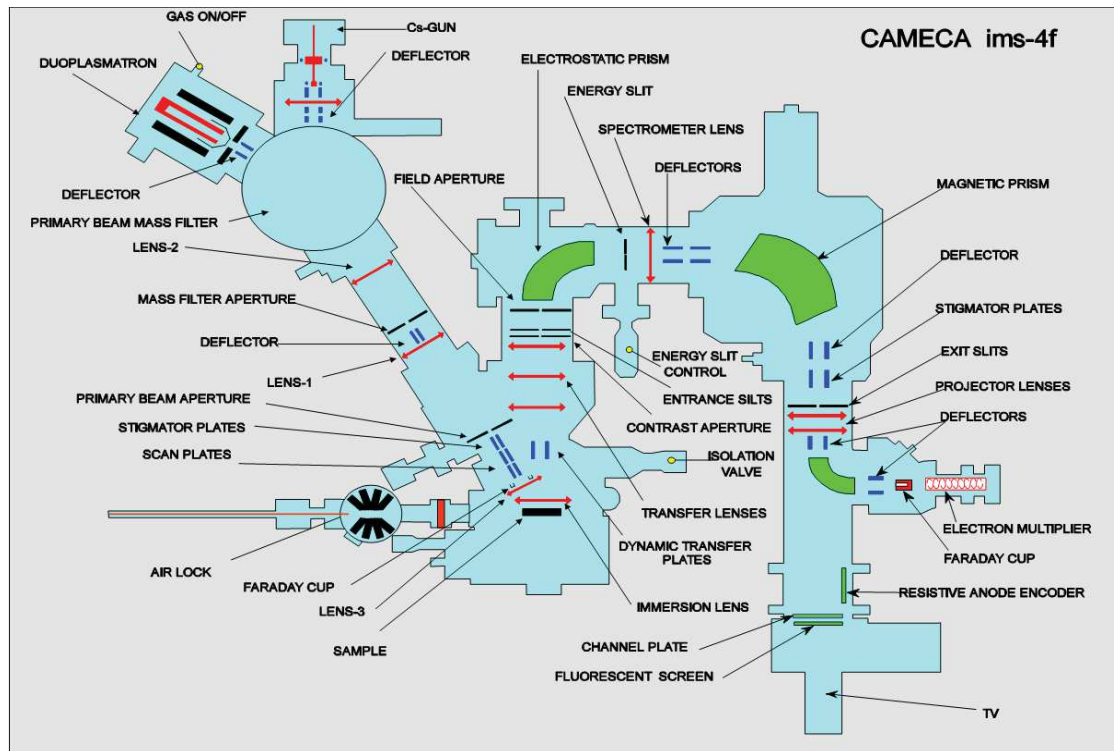


Fig.2. 1: Schematic representation of SIMS setup [2]

This SIMS setup consists of:

- A primary beam source (O_2^+ , O^- , Cs^+ or Ar^+) to supply the bombarding species
- A target or sample that must be solid and stable in a vacuum
- A secondary stage collecting and analyzing the ejected secondary ions
 - A mass analyzer to isolate the ion of interest consisting of a double focusing magnetic sector
 - An selected secondary ion detection system:
 - channel plate combined with a CCD camera for setup visualization
 - Faraday cup or electron multiplier for the signal magnitude recording.

2.1.1 Ion Beam Sputtering

The samples to study should be placed in specific holders (1 inch diameter) such as that shown in Fig. 2.2. Several holders with different analysis windows (3, 4 or 9) are available. The holders are introduced into the analysis chamber via a load-lock system to preserve Ultra High Vacuum on the whole path of the ions, i.e. since the primary ions beam sources to the secondary ions beam detectors.



Fig.2. 2: Example of typical sample holder of 1 inch diameter for Cameca IMS5f SIMS equipment

Two different primary ions sources are available on the equipment: a Cesium gun for Cs^+ ions and a duoplasmatron that generate O_2^+ , O^- and Ar^+ ions. Selected primary ions are accelerated with energies adjustable between 5 and 17 keV and mix with sample atoms to depths usually of few nanometers. The bombarding primary ion beam produces monatomic and polyatomic particles of sample material and re-sputtered primary ions, along with electrons and photons. A charge exchange in the near surface environment results in the conversion of a portion of the eroded atoms to negative or positive ions. The secondary particles carry negative and positive charges and they have kinetic energies that range from zero to several thousand eV (see Fig. 2.3).

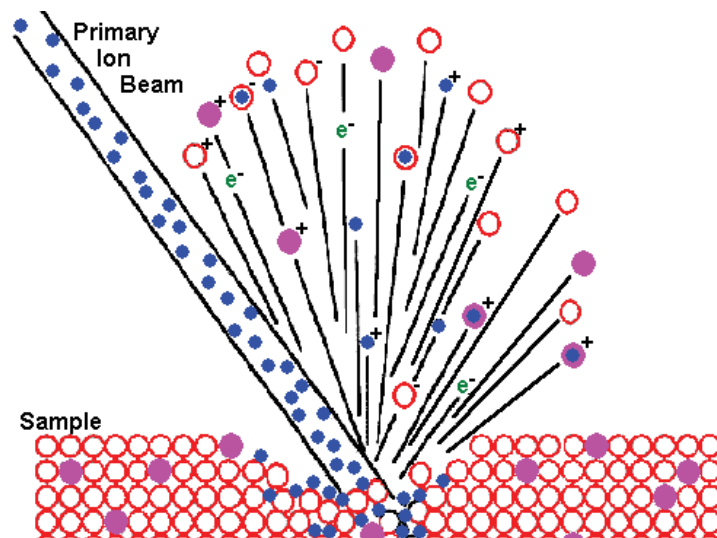


Fig.2. 3: Schematic of surface sputtering in SIMS experiment [3]

The collision cascade model has the best success at quantitatively explaining how the primary beam interacts with the sample atoms. In this model, a fast primary ion passes energy to target atoms in a series of binary collisions.

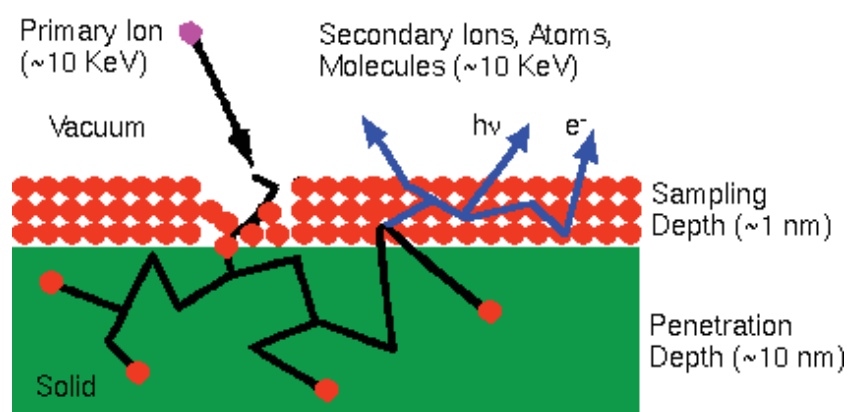


Fig.2. 4: Schematic of the SIMS sputtering mechanisms [3]

Energetic target atoms (called recoil atoms) collide with more target atoms. Target atoms that recoil back through the sample surface constitute sputtered material. Atoms from the sample's outer monolayer can be driven in about 10 nm, thus producing surface mixing. The term knock-on also applies to surface mixing. Sputtering leads to surface roughness in the sputter craters. Lattice imperfections, either already present or introduced by surface mixing, can be germs for roughness that takes the form of ribbons, furrows, ridges, cones, and agglomerations of cones. Polycrystalline materials form rough crater bottoms because of differential sputter rates that depend on crystal orientation see Fig.2.4.

Typical sputter rates for monocrystalline SiC materials vary between 0.5 and 5 nm/s, depending on primary beam intensity, sample material and crystal orientation. Typical crater size is about $150\ \mu\text{m} \times 150\ \mu\text{m}$ but only the $40\ \mu\text{m} \times 40\ \mu\text{m}$ at the center is quantitatively analyzed. The sputter yield is defined as the ratio of the number of atoms sputtered to the number of impinging primary ions.

2.1.2 Collection of the secondary ions beam

The secondary ions are extracted from the surface using an electrical potential varying between 1kV and 10kV. Notice that to prevent fluctuations on the extraction potential due to surface charge effect on high resistive samples, it is possible to use an collinear electron gun during the analyze. The ions beam is directed toward the inlet of the mass spectrometer through a series of electrostatic lens and other aperture and slits.

2.1.3 Analysis of the secondary ions beam

Mass spectrometer combined two sectors. The first one is the electrostatic analyzer which provides energy separation. The ions entering the radial electrostatic sector will follow a trajectory which depends on the ion energy and the electric field strength. Thus ions of the same energy will follow the same path. Then, the energy selected ions are focused through the second sector, the magnetic one, where they follow a trajectory which depends on the momentum of the ion and the strength of the magnetic field. Thus ions of the same mass on electric charge ratio will follow the same path and can through the physical aperture of the detector. Note that in this kind of configuration it is possible to very precisely select an ionic species to analyze by two methods: by adjustment of the energy window (Kinetic Energy Filtering) or using High Mass Resolution capability [4].

All the elements of the periodic table could be detected with sensitivity level down to 100 ppb and interferences between elements could be resolve with a resolution $m/\Delta m$ up to 25000.

2.1.4 Secondary ion detection

The IMS5f equipment has two types of devices detection of secondary ions. The first one is a channel plate combined with a CCD camera, allowing the visualization of ionic images. Notice that the magnification of the ionic microscope varies between 100 and 1000. On the other hand, for a quantitative evaluation of the ions, there are two possibilities: using the Faraday cup or using the electron multiplier, the latter being the most sensitive.

Quantitative analysis of a species in material bulk results in the classical 1D profile: ionic element (atomic or molecular) counts versus erosion time (see *Fig.2. 5*).

To obtain a more standard depth concentration profile, for example concentration in atoms by cubic centimeters versus depth in nanometers, calibrations should be applied on both axes of the graph.

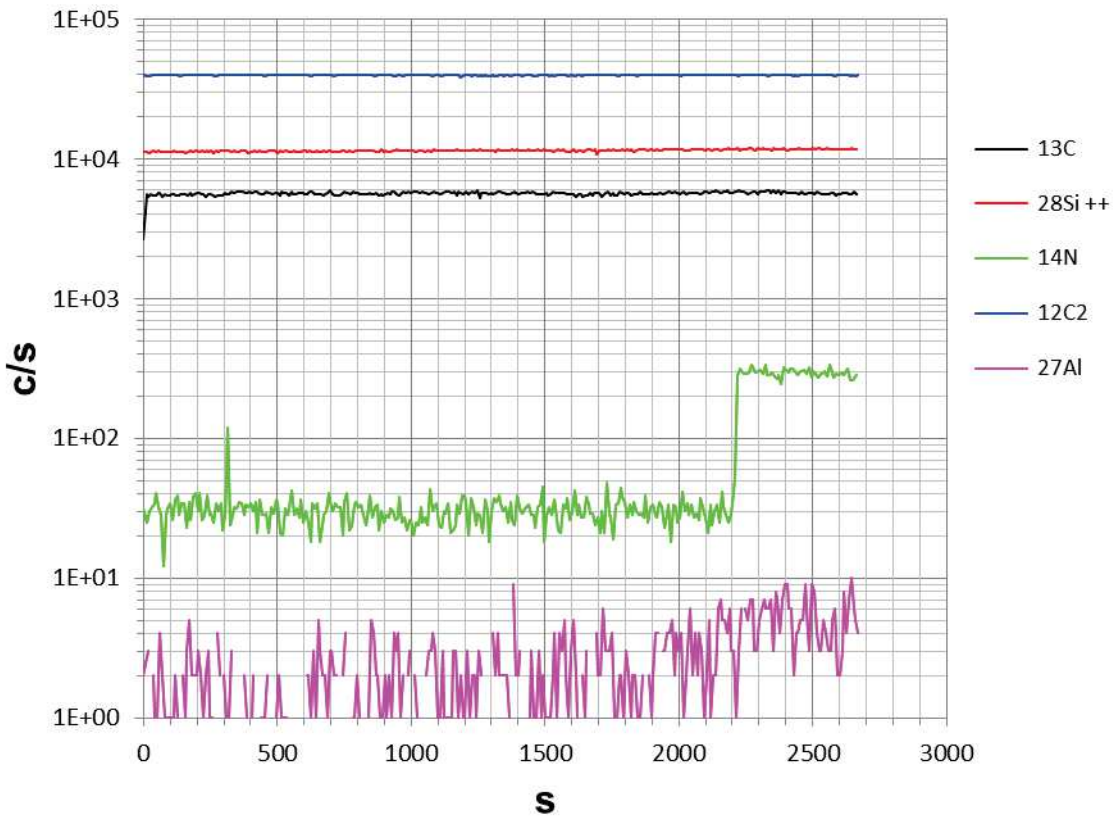


Fig.2. 5: Example of rough SIMS spectra, counts vs. erosion time.

2.1.5 Relative Sensitivity Factors – Concentration calibration

Quantitative analysis by SIMS uses relative sensitivity factors defined according to the following equation:

$$\frac{I_R}{C_R} = RSF_E \cdot \frac{I_E}{C_E} \quad 2.21$$

and RSF_E is a dimensionless Relative Sensitivity Factor for Element E, relative to the element R

where, I_E and I_R (c/s) are the secondary ion intensity for elements E and R, respectively C_R and C_E (cm^{-3}) are concentrations of the elements R and E, respectively E and R being isotope of molecular or atomic species.

The major (or matrix) element is usually chosen as the reference. Substituting M (matrix) for R (reference) and rearranging gives the following equation:

$$C_E = C_M \cdot RSF_E \cdot \frac{I_E}{I_M} \quad 2.22$$

In trace element analysis, we can assume that the matrix elemental concentration remains constant. The matrix concentration can be combined with the elemental RSF_E to give a more convenient constant, RSF :

$$RSF = C_M \cdot RSF_E \quad 2.23$$

Note that RSF has the same concentration units as C_M .

This RSF is a function of the element of interest and the sample matrix. This coefficient can be considered constant for a given matrix, i.e. when the level of impurities concentration (and that of the analyzed species in particular) remains below the percent.

In practice, the RSF is determined from a reference sample for which the level of concentration of the element E is well known. To determine the level of the same element (e.g. N or Al) in a new sample having the same matrix (e.g. SiC), simply collect the I_{ES} and I_{MS} intensities by SIMS. The C_{ES} concentration of the element E in this new material it is easily deduced from the relation below:

$$C_{ES} = RSF \cdot \frac{I_{ES}}{I_{MS}} \quad 2.24$$

where "s" subscript refers to the new analyzed sample.

2.1.6 RSF tables

The following tables of RSF values show how sensitivity depends on the element of interest. Low $RSFs$ mean high sensitivity [5]. Note that modest concentrations of high sensitivity elements can saturate electron multiplier ion detectors. In this case it is possible use Faraday cup detector to quantify the species concentration level. These $RSFs$ values have been measured for oxygen primary ion bombardment, positive secondary ions, and a silicon matrix. In the case of the SiC, there is no significant difference in terms of RSF between the 4H, 6H or 3C polytypes. Some typical values are given in *Tab.2. 1*.

Monitored ion	SiC		Si	
	RSF (atoms cm ⁻³)	DL (atoms cm ⁻³)	RSF (atoms cm ⁻³)	DL (atoms cm ⁻³)
¹ H ⁺	2.5×10 ²⁴	1.0×10 ¹⁹	6.2×10 ²⁴	2.3×10 ¹⁸
²⁸ Si ¹ H ⁺	8.7×10 ²⁴	8.5×10 ¹⁸	1.4×10 ²⁵	2.7×10 ¹⁸
⁹ Be ⁺	3.1×10 ²⁴	1.0×10 ¹⁴	3.2×10 ²²	4.7×10 ¹³
¹² C ¹¹ Be ⁺	5.8×10 ²⁴	8.0×10 ¹⁷	-	-
¹¹ B ⁺	5.6×10 ²²	1.0×10 ¹⁴	6.5×10 ²²	1.8×10 ¹⁴
²⁷ Al ⁺ (HMR) ^a	1.5×10 ²¹	3.0×10 ¹⁶	1.4×10 ²¹	7.0×10 ¹³

$^{27}\text{Al}^+$ (-100V offset) ^b	2.5×10^{23}	3.0×10^{16}	-	7.0×10^{13}
$^{27}\text{Al}^+\text{C}^{\text{+a}}$	3.5×10^{24}	1.4×10^{17}	-	-
$^{28}\text{Si}^{27}\text{Al}^{\text{+a}}$	7.5×10^{23}	4.2×10^{17}	4.8×10^{23}	7.0×10^{17}
$^{14}\text{N}^+$ (HMR) ^c	2.7×10^{24}	1.0×10^{17}	2.9×10^{25}	1.0×10^{19}

^aHMR mode with $M/\Delta M \sim 2000$.

^bthe energy bandpass was $\sim 60\text{eV}$.

^cHMR mode with $M/\Delta M \sim 2500$.

Tab.2. 1: Experimental SiC RSFs and detection limits (DLs) for positive ions measured under O_2^+ primary ions sputtering with respect to Si, the last two columns show RSFs and DLs for Si [5].

In practice, we observe some fluctuations on the RSF values determined from the same reference sample but at different date because the experimental setup is not absolutely the same. This is why the RSF determination is done systematically for each new experiment session and for each analyzed species. An example of RSF values for oxygen primary ion beam, positive secondary ions and a silicon matrix is shown in Fig.2.6

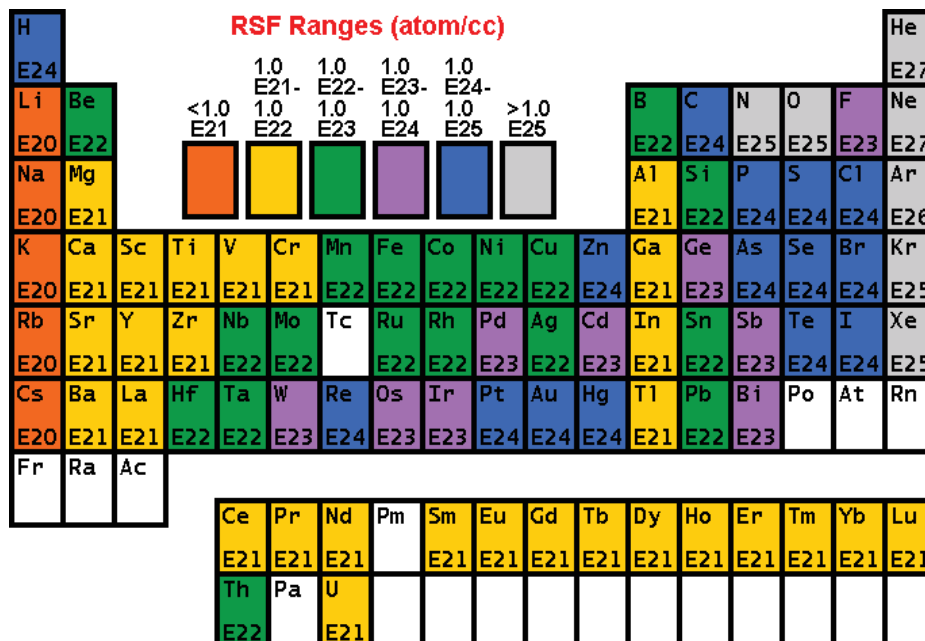


Fig.2. 6: Example of RSF values for oxygen primary ion beam, positive secondary ions and a silicon matrix [5].

2.1.7 Depth Profiling

Monitoring the secondary ion count rate of selected elements as a function of time leads to depth profiles. The following figures show the depth profile for the reference samples used to calibrate the SIMS profiles (*Fig.2. 7-* of Al, and *Fig.2. 8-* N profiles). The reference samples are the implanted ones with aluminum: ^{27}Al , 90keV, with implanted dose $\phi=12^{13}$ at/cm 2 and depth of $\sim 1000\text{\AA}$ and nitrogen: ^{14}N , 60keV with implanted dose $\phi=12^{15}$ at/cm 2 and depth of $\sim 1000\text{\AA}$.

To convert the time axis into depth, sputter crater depths are measured using a DEKTAK-150 profilometer.

Finally, it is important to recall that the concentration profiles correspond to the isotopic species selected in the mass spectrometer. It is often necessary to correct these values by applying the natural isotope ratio if we want to compare these results with those obtained by other techniques.

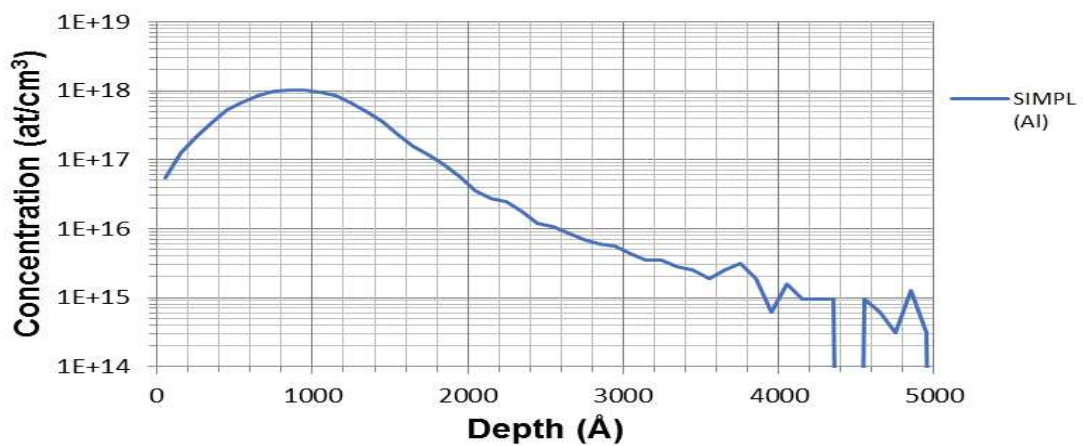


Fig.2. 7: SIMS profile of reference sample for aluminum.

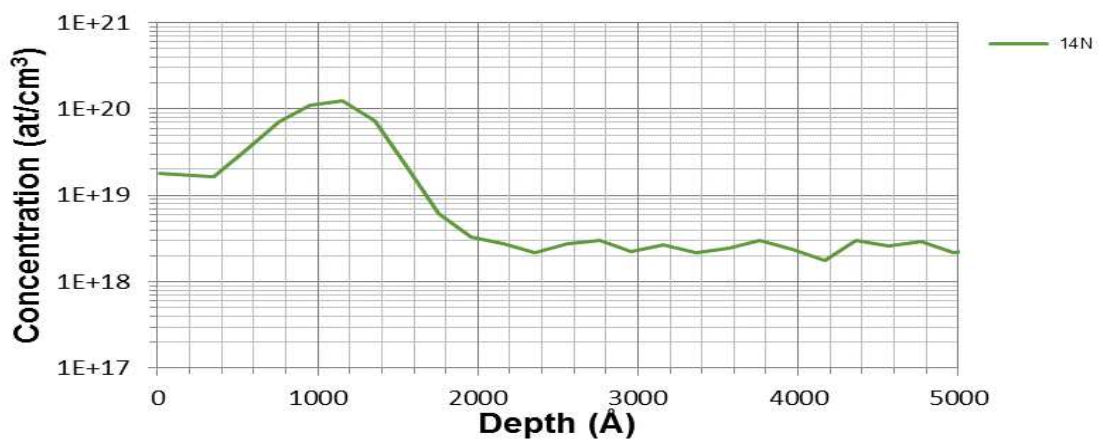


Fig.2. 8: SIMS profile of reference sample for nitrogen.

To measure nitrogen concentration and Al concentration in this work, the experimental setup was a Cameca IMS 5f spectrometer with O_2^+ as the primary ion source. The impact energy was 15 keV. The secondary beam high voltage was set on 4.5 kV and the mass resolution was fixed at $M/\Delta M = 2000$. The investigated atomic masses were: $^{13}C^+$ (matrix), $^{28}Si^{++}$ (matrix), $^{12}C_2$ (matrix), $^{14}N^+$ and $^{27}Al^+$. The size of craters was $150 \times 150 \mu m$ and their depth was measured using a Dektak 150 profile-meter. The RSFs (Relative Sensitivity Factors) used to calibrate the concentration profiles were defined from reference samples in which the concentration profiles were well known. In this work $^{12}C_2$ isotope signal as matrix reference has been used. Tab.2.2 and Tab.2.3 shows the RSFs values. Since the measurements were done in different days we have two set of RSFs value.

	$^{14}N^+ / ^{12}C_2$	$^{27}Al^+ / ^{12}C_2$
RSF	1.3×10^{21}	8.8×10^{17}

Tab.2. 2: RSF values used in O_2^+ configuration for measurements of the n-type samples

	$^{14}N^+ / ^{12}C_2$	$^{27}Al^+ / ^{12}C_2$
RSF	1.01×10^{21}	1.08×10^{18}

Tab.2. 3: RSF values used in O_2^+ configuration for measurements of the p-type samples

As it was mentioned before, because the measurements were done in different days we observe a slight differences of RSFs values.

The detection limit was found to be close to $6 \times 10^{16} \text{ cm}^{-3}$ and $3 \times 10^{13} \text{ cm}^{-3}$ for nitrogen and aluminum, respectively.

An example of nitrogen (green line) and aluminum (pink line) SIMS profiles is presented in the Fig.2.9. As we can notice, the profile corresponding to the nitrogen shows concentration value in a quite stable level of $9.5 \times 10^{17} \text{ cm}^{-3}$ up to $11.6 \mu m$ before changing significantly to the concentration value of $1 \times 10^{19} \text{ cm}^{-3}$. This change corresponds to the transition layer/substrate. When this interface is observed, we could estimate the thickness of the layer; for example: 11.6 nm in the case of the sample 13-008. Looking on the aluminum profile we can state that the concentration value is lower than the detection limit in the layer but raises to 10^{14} cm^{-3} in the substrate.

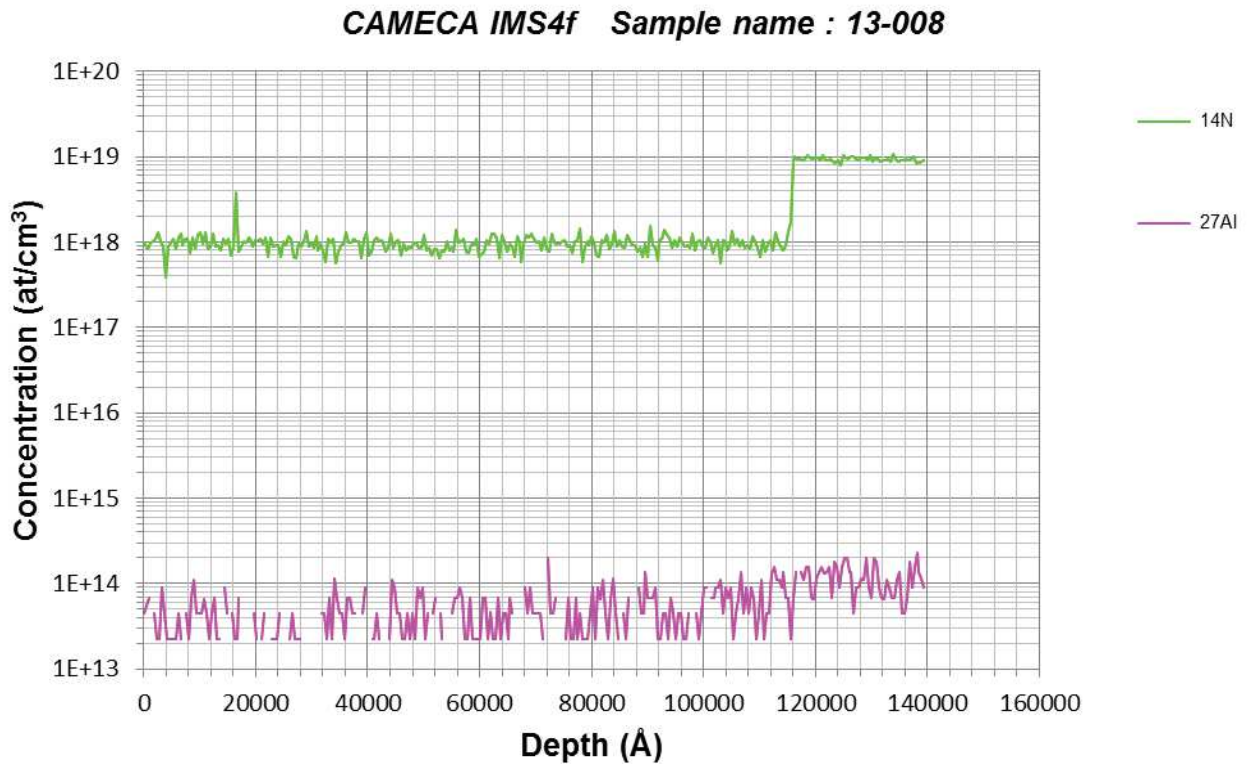


Fig. 2. 9: SIMS profiles of nitrogen and aluminum collected on the n doping sample. The values of $N = 9.5 \times 10^{17}$ and $Al \leq 3 \times 10^{13}$ (DL)

2.2 Photoluminescence

Whatever, the process of luminescence always requires a non-equilibrium carrier concentration to be achieved in the electronic bands or in the electronic states of an investigated structure. If the non-equilibrium is achieved by irradiation with light, the radiative recombination is said photoluminescence.

2.2.1 Free exciton transition

Fig.2.10 represents the energy band diagram of a two semiconductor with direct and indirect band gap. Direct semiconductors have holes and electrons positioned directly adjacent at the same momentum coordinates, so that electrons and holes can recombine relatively easily while maintaining momentum conservation. In an indirect semiconductor, the match between conduction band energy valleys and holes that would allow momentum conservation is not favorable, most of the transitions are forbidden, and the resulting radiative lifetime is long. SiC is indirect semiconductor, in which radiative recombination of

injected carriers is extremely unlikely. The radiative lifetime in such materials occurs in the range of seconds, and nearly all injected carriers recombine radiatively or non-radiatively through defects in the crystal. For a recombination event to occur in indirect gap materials, an electron must change its momentum before combining with a hole, resulting in a significantly lower recombination probability for the occurrence of a band-to-band transition.

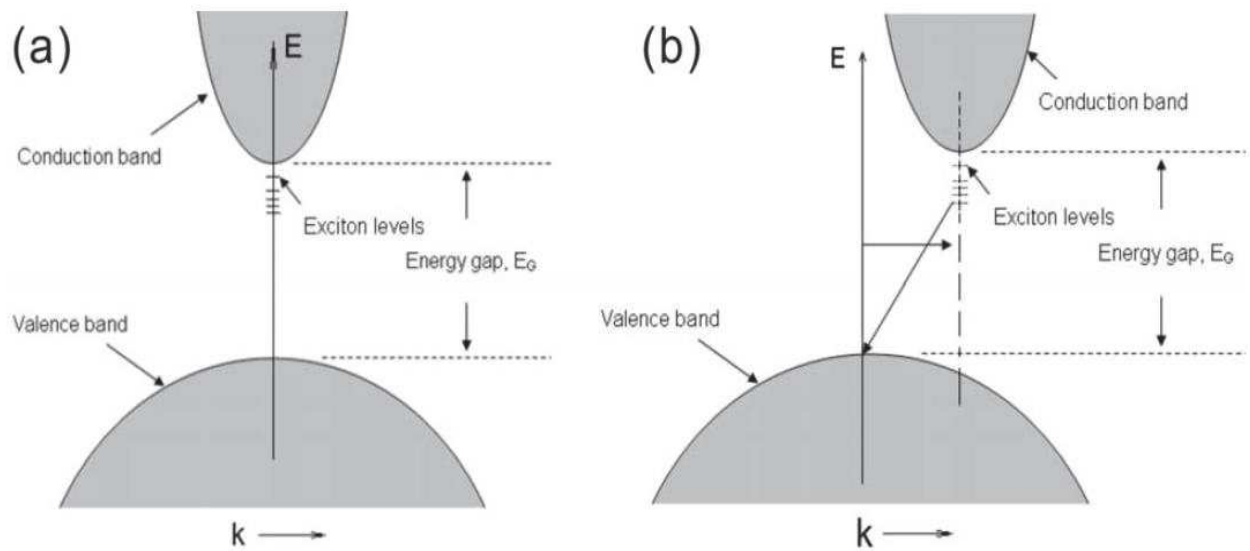


Fig.2. 10: Schematic diagram of the exciton recombination process in a direct bandgap and an indirect bandgap semiconductor [6]

2.2.2 Coulomb interaction

The electron hole interaction in the band structure of a semiconductor refers to the k-space. In the real space the electron and the hole are interacting via coulomb attraction. This bound pair of electron and hole is called an exciton. It can be calculated with the Schrödinger equation similar to a hydrogen atom because both cases represent a two particle model where one particle orbits the other particle. A characteristic size description of the smallest possible radius of the orbit is the Bohr radius:

$$a_0 = \frac{\hbar}{m_{\mu}^* c \alpha} \quad 2.1$$

with the reduced mass m_{μ}^* , the speed of light c and the fine structure constant α . Comparing the mass of the nucleus of the hydrogen atom to the much lower effective mass of the hole

in the exciton leads to a much larger Bohr radius for the exciton than for the hydrogen atom. If the exciton Bohr radius exceeds the lattice constant of the crystal the exciton is called a Mott-Wannier exciton. These excitons are weakly localized because they are electrically neutral. This gives the electron-hole pair the possibility to travel almost freely through a semiconductor [7].

2.2.3 Doped-assisted mechanisms

When a semiconductor absorbs a photon of energy greater than the bandgap, an electron is excited from the valence band into the conduction band leaving behind a hole. When the electron returns to its original state, it may do so through radiative (release of a photon) or non-radiative (no photon production) recombination. When the electron and hole recombine through radiative recombination, the energy of the emitted photon is dependent on the change in energy state of the electron-crystal system. In indirect bandgap semiconductor, photon emission requires the aid of a phonon (energy in the form of lattice vibrations) to conserve momentum within the lattice structure. With the introduction of impurities in semiconductor material discrete energy levels are formed within the semiconductor's forbidden energy gap. Shallow donor levels are defined as levels just below the conduction band, whereas, shallow acceptor levels are defined as levels just above the valence band. These donor or acceptor level traps can act as recombination centers for transitions within the bandgap. By studying the nature of these trap levels, information about the impurity or defect can be resolved. In Fig. 2. 11 several possible processes for radiative and nonradiative recombinations are illustrated.

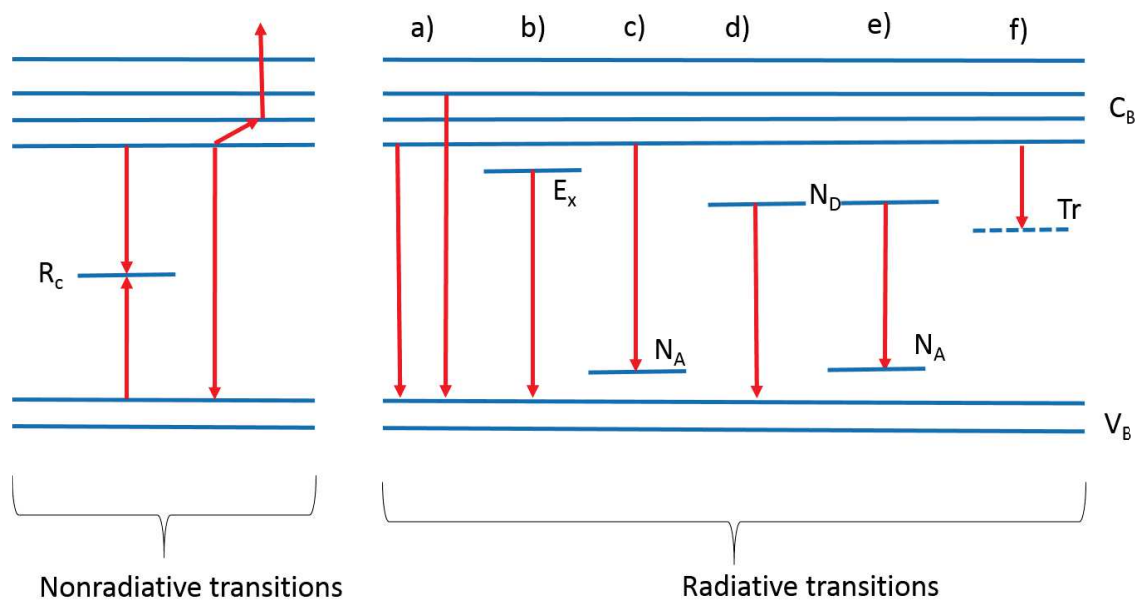


Fig.2. 11: Radiative and nonradiative recombination processes for excited electrons; (E_x : exciton, N_A : acceptor, N_D : Donors, Tr : trapping center, R_C : recombination center).

The first three radiative processes and the last non-radiative process are intrinsic, whereas for the others at least one impurity is required. Process a) are band-to-band recombinations which are usually not very efficient, process b) is the exciton luminescence. The trapping centers labeled Tr in Fig. 2. 11 can be very efficient for luminescence since they can first capture and localize an electron or hole which then strongly increases the probability of capturing the other partner for the radiative recombination.

2.2.3.1 Band to band transition

The first transitions described here are radiative band-to-band or direct recombination which dominate at room temperature and can be used to estimate the material bandgap energy (E_g). For indirect semiconductors a band-to-band recombination process is unlikely because the electrons at the bottom of the conduction band have a nonzero crystal momentum with respect to the holes at the top of the valence band. Band-to-band transition contains the recombination of free electrons and free holes. This transition occurs when an electron falls from its conduction band state into the empty valence band state associated with the hole. Band-to-band transition depends on the density of available electrons and holes and probability which is proportional to the absorption coefficient. So we can represent the recombination rate as [6]:

$$U = \alpha(np - n_{ie}^2) \quad 2. 2$$

where, α is the recombination constant, n_{ie} is the effective intrinsic concentration, n -electron and p -hole concentration.

The energy, which is equal to the energy difference between the excited and ground states, released during the process usually produces a photon and emits light in a semiconductor having a direct band gap. It is given by the equation:

$$h\nu = E_f - E_i \quad 2. 3$$

where E_f and E_i are, respectively, the final and initial state energies. In indirect semiconductors such like SiC, band-to-band recombination occurs with phonon contribution and emitted photon energy is

$$h\nu = E_f - E_i \pm h\Omega \quad 2. 4$$

where $h\Omega$ is the phonon energy [6].

2.2.3.2 Free to bound transition

At temperature for which $k_B T$ is greater than the ionization energy of shallow impurities, these impurities are ionized, hence band-to-band transition dominate. At sufficiently low temperatures the thermal energy of carriers becomes smaller than the ionization energy of the impurities. For example, in a p-type material containing N_A acceptors per unit volume, holes are trapped at the acceptor if $k_B T$ is smaller than E_A , where E_A is the ionization energy of the acceptor. Free electrons can recombine radiatively (and sometimes non-radiatively) with the holes trapped on acceptors or holes can recombine with the electrons trapped on the donors. Such transition involving free carrier (electron) and a charge (hole) bound to an impurity, are known as free-to-bound transition. The emitted photon energy is given by

$$h\nu = E_g - E_A \quad 2.5$$

where E_A is the acceptor shallow binding energy. The similar equation can be written for the transition donor to valence band substituting the energy E_A for E_D in equation (2.5). If an electron is captured at a donor site, however, it has a high probability at room temperature of being re-emitted into the conduction band before completing the remaining steps of the recombination process. A similar statement can be made for holes captured at acceptor sites. For this reason sites may be likened to extremely inefficient R-G centers (R-G centers can be special impurity atoms or lattice defects [8]), and the probability of recombination occurring via shallow levels is usually quite low at room temperature. Nevertheless, it should be noted that the largest energy step in shallow-level recombination is typically radiative and that the probability of observing shallow-level process increases with decreasing system temperature. Fig.2. 12 shows the excitonic energy gap plotted as a function of the temperature (K) [9]. One may notice that with increasing the temperature the excitonic energy gap decreases.

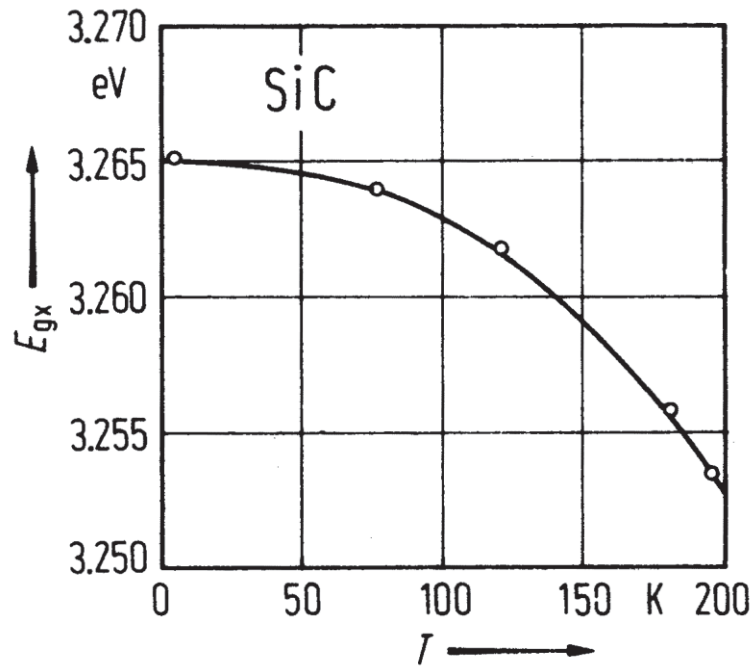


Fig.2. 12: Excitonic energy gap vs. temperature for 4H-SiC [9].

2.2.3.3 Donor-Acceptor Pair transition

When both donor and acceptor impurities are present in semiconductors, coulomb interaction between the donors and acceptors modifies the binding energy in such a way that the transition energy is distance dependent. The DAP (Donor Acceptor Pair) complex consists of four point charges like an exciton neutral impurity complex (bound exciton). The donor ion D^+ and the acceptor ion A^- are immobile point charges while the remaining two charges, an electron and a hole, are mobile. This process represented by the reaction [6]:



The recombination energy of a donor acceptor pair given by [6]

$$E(r) = E_g - (E_D + E_A) + \frac{e^2}{\epsilon r} \quad 2.7$$

where E_g is the bandgap energy, E_D and E_A are the binding energy of the donor and the acceptor respectively and the last term is the coulomb interaction of the donor-acceptor pair separated by r .

Although Al seems to be one of the most studied p-type impurity in the different polytypes, detailed PL characterizations have also been reported on material doped with B and Ga acceptors [10], [11], [12], [13], [14]. Al, B and Ga acceptor impurities are also radiative

centers in other SiC polytypes. Recently, there has been some discussion about the validity of previously reported values for the ionization energy of B in 6H-SiC. Suttrop et al. [15] have shown strong experimental evidence that the ionization energy of the isolated B acceptor is 0.32 eV. They also reported that the commonly observed yellow emission is associated with a boron-related deep center (D-center) with a 0.58 eV ionization energy. These results have been confirmed by Reinke et al. [16], who have suggested that B like Al occupies a Si site in 4H& 6H-SiC. The ionization energies of some acceptors and donors in the most common SiC polytypes are listed in *Tab.2. 4*.

polytype	Impurity					
	Al	B	Be	Ga	N	P
3C	0.257 [17]	0.735 [10]	-	0.344 [38]	0.055[21]	-
4H	0.191 [18]	0.647 [18]	-	0.267 [19]	0.061[21]	0.060[21]
6H	0.249 [18]	0.723 [18]	0.4 [20]	0.333 [18]	0.085 [21]	0.080[21]
	0.239 [18]	0.698 [18]	0.6 [20]	0.317 [18]	0.14 [21]	0.13 [21]
		0.320 [15]				
15R	0.236 [18]	0.700 [18]	-	0.320 [18]	-	
	0.230 [18]	-	-	0.311 [18]	-	
	0.223 [18]	-	-	0.305 [18]	-	
	0.221 [18]	0.666 [18]	-	0.300 [18]	-	
	0.206 [18]	-	-	0.282 [18]	-	

Tab.2. 4: Ionization energy (eV) of some acceptor and donors impurities in the most common SiC polytypes.

An example of typical (Al-N) DAP spectra for the three common SiC polytypes 4H, 6h and 3C are shown on Fig.2. 13.

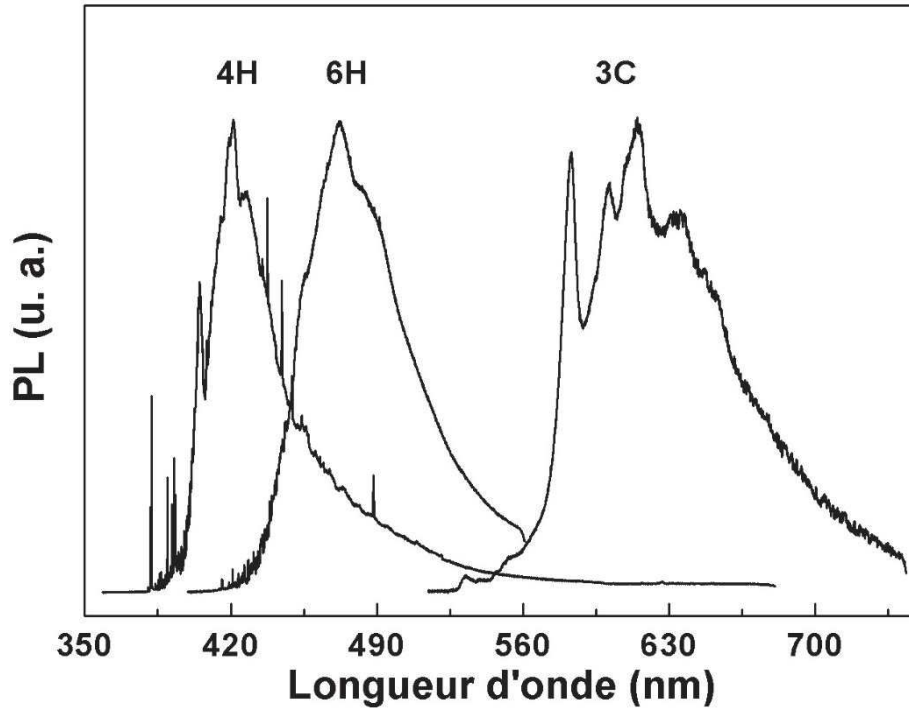


Fig.2. 13 : Example of PL spectra collected at 5K on 4H, 6H and 3C-SiC polytype materials compensated [22].

2.2.4 Exciton transitions

2.2.4.1 Free Exciton:

Excitonic recombination can occur following the generation of an electron-hole pair. Coulombic attraction leads to the formation of an excited state in which an electron and the hole remain bound to each other in a hydrogen-like state, referred to as a free exciton [6].

The energy of the emitted photon will be:

$$h\nu = E_g - E_x \quad 2.8$$

where E_g is the bandgap energy of the semiconductor and E_x is the Coulomb energy of the exciton.

Figure 2.14 shows the typical spectra of pure 4H-SiC, the intrinsic transition occurs.

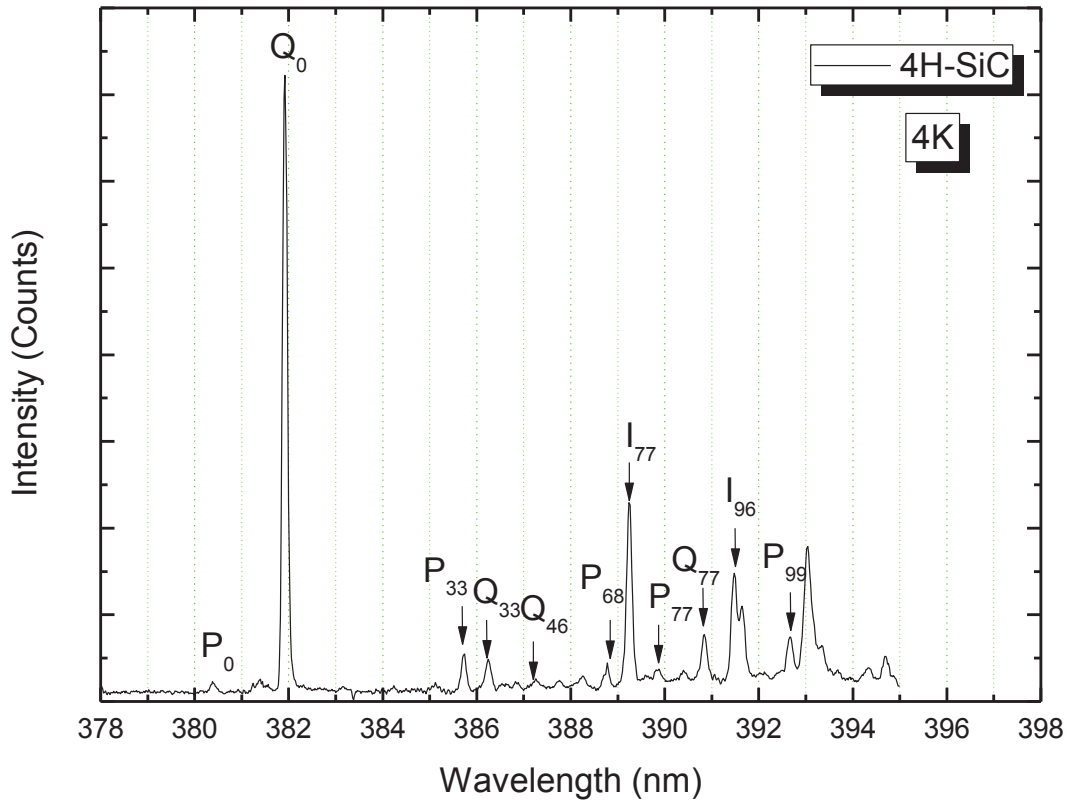


Fig.2. 14 : Example of spectra taken on 4K in a pure 4H-SiC epilayer with visible the intrinsic transition (I_{77} line) marked lines P_0 and Q_0 are due to nitrogen bound to an exciton, P_x and Q_x their phonon replicas (x stands for energetic position below P_0 or Q_0 respectively).

2.2.4.2 Bound Exciton (Exciton-Impurity Interaction):

As a matter of fact, many semiconductor materials contain small amounts of natural defects or impurities forming neutral donors and acceptors. Optically generated free excitons can interact with those impurities and may become captured by them. They are then called donor-bound or acceptor-bound excitons depending on whether the impurity that the exciton is attached to is a donor or an acceptor, respectively. Energy is the fundamental criterion that determines whether or not a free exciton can be trapped at an impurity. If the total energy of the system is reduced when the free exciton is in the vicinity of the impurity, then it is energetically favorable for the exciton to remain near the defect the exciton becomes bound to the impurity via van der Waals interaction [23]. This bound exciton can be considered as analog to the hydrogen molecules H_2 except for different binding energies. Bound exciton have much smaller binding energies (usually a few meV) because the hole mass is much smaller than that of the proton and in a medium coulomb interaction is

lowered by the square of the dielectric constant. The common nomenclature is (D^0, X) and (A^0, X) for neutral-donor bound and neutral-acceptor bound excitons, respectively. Photon being emitted following a bound exciton annihilation has the energy:

$$h\nu = E_g - E_X - E_B \quad 2.9$$

Where E_B is the binding energy of the exciton to the defect.

Momentum conservation rules require that only the free excitons which have the same k-vector as the outgoing photon can recombine radiatively. Since the photon momentum is small compared to the momentum of excitons, only excitons with virtually no kinetic energy ($K=0$) are allowed to recombine. However, this condition does not prevent the excitons from having kinetic energy. Recombination of free excitons with momentum other than the outgoing light can occur through phonon participation. Phonons provide the necessary momentum to satisfy the momentum conservation law and thereby reduce restriction on the free exciton momentum allowing of excitons finite K to annihilate. For one phonon emission the momentum and energy conservation law can be expressed as:

$$K = k + q_{ph} \quad 2.10$$

$$h\nu = E_X(K) - h\nu_{ph} \quad 2.11$$

where the subscript "ph" refers to the phonons and $E_X(K)$ is the total energy of free exciton.

Fig.2.15 shows an example of LTPL spectra collected on 4H-SiC sample with nitrogen bound to an exciton labelled P_0 and Q_0 respectively for a nitrogen hexagonal and cubic sites. Since SiC is an indirect band gap semiconductor, crystal momentum needs to be released when an exciton recombines. In the case of a band exciton, the momentum can be taken up either by lattice phonons or by the binding center itself. The phonon replicas are labeled as P_x and Q_x in Fig.2. 15 where x index is the phonon energy (meV) below P or Q lines.

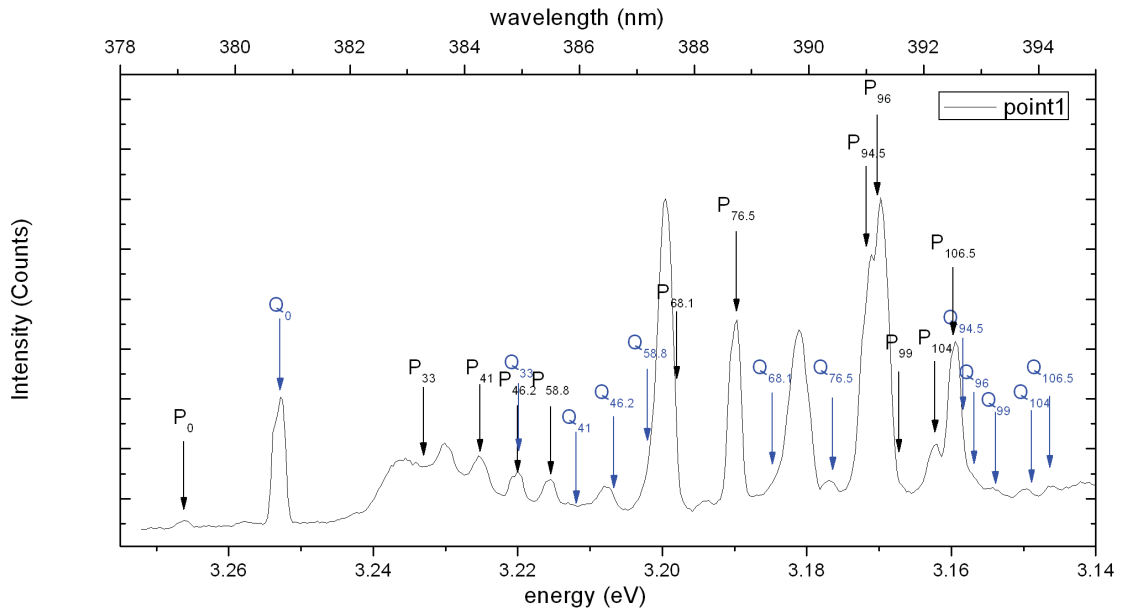


Fig.2. 15 : Example of LTPL spectra collected on 4H-SiC sample, labeled energetic positions of P_0 and Q_0 lines with their phonon replicas for nitrogen.

One may see on Fig.2. 16 the typical LTPL spectra in near band exciton range of 4H-SiC doped with aluminum with week compensation. Intense line corresponding to aluminum presence labeled as Al_0 is visible.

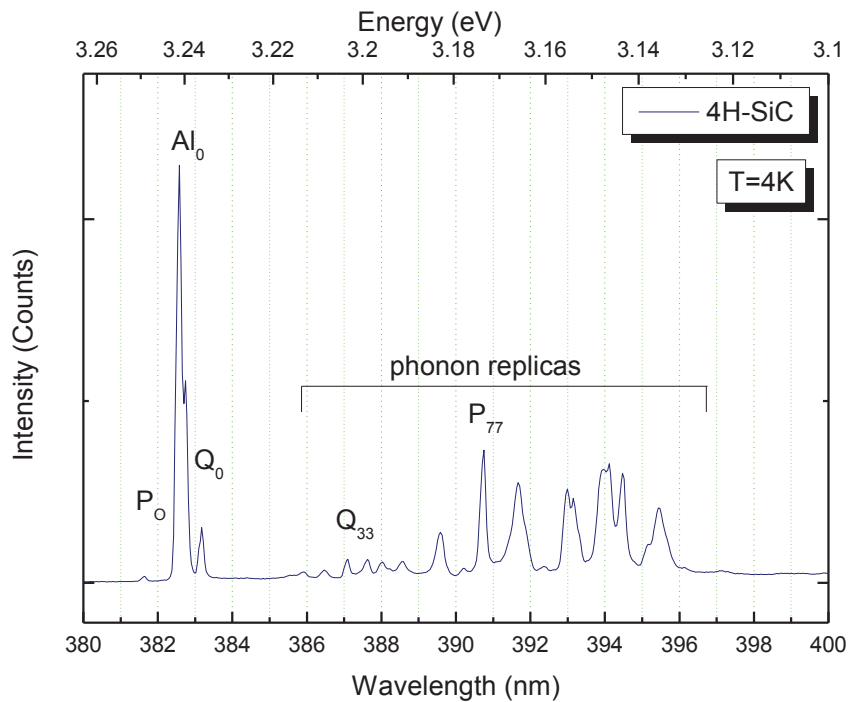


Fig.2. 16 : Example of LTPL spectra in NBE range, collected at 4K on aluminum doped 4H-SiC material. Marked Al_0 , P_0 and Q_0 and phonon replicas.

2.2.5 Polytype identification by LTPL

The identification of the polytype for SiC is quite easy due to characteristic lines in the near band edge range. The example of typical low temperature photoluminescence spectra for different polytypes is shown in *Fig.2. 17*. Due to the intrinsic n type on SiC, in the NBE nitrogen bound excitons appear at different energetic positions depending of the polytype.

At first glance one can notice the difference between the spectra corresponding to the specific polytypes. Differences in term of the number of the peaks as well as energetic position of characteristic lines are observed.

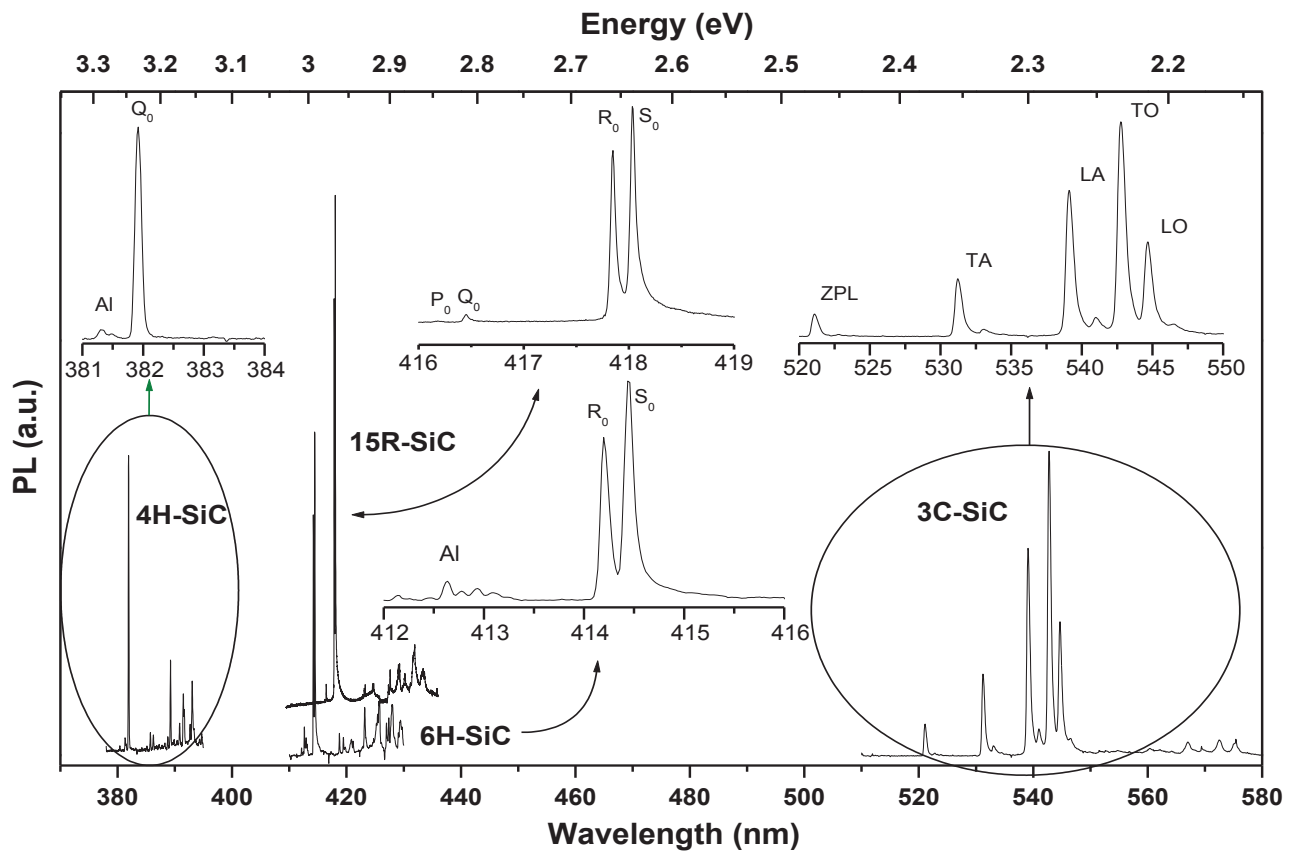


Fig.2. 17: Examples of LTPL spectra collected at 5K for the 4H, 6H, 15R and 3C-SiC polytypes [24].

Each polytype contains cubic and hexagonal sites, depending on the stacking sequence, with the exception of 3C which is purely cubic and 2H that is purely hexagonal. In the LTPL spectra of the most common polytypes that have been observed each site gives a no phonon transition of the N impurity and phonon replicas associated with them. One case that this does not apply though is for the 15R-SiC where there are four no phonon lines for the 5 sites that exist. For the four common polytypes presented in *Fig.2. 17*, this can be summarized as:

- 3C-SiC, 1 cubic site, 1 no phonon peak noted as ZPL;
- 4H-SiC, 2 sites, 1 hexagonal and 1 cubic, 2 no phonon peaks noted as P_0 and Q_0 , respectively;
- 6H-SiC, 3 sites, 1 hexagonal and 2 cubic, 3 no phonon peaks noted as P_0 , R_0 and S_0 , respectively;
- 15R-SiC, 5 sites, 2 hexagonal and 3 cubic, 4 no phonon lines noted as P_0 , Q_0 , R_0 and S_0 .

2.2.6 Experimental setup

The schematic representation of the setup used in this work is presented in *Fig.2. 18*.

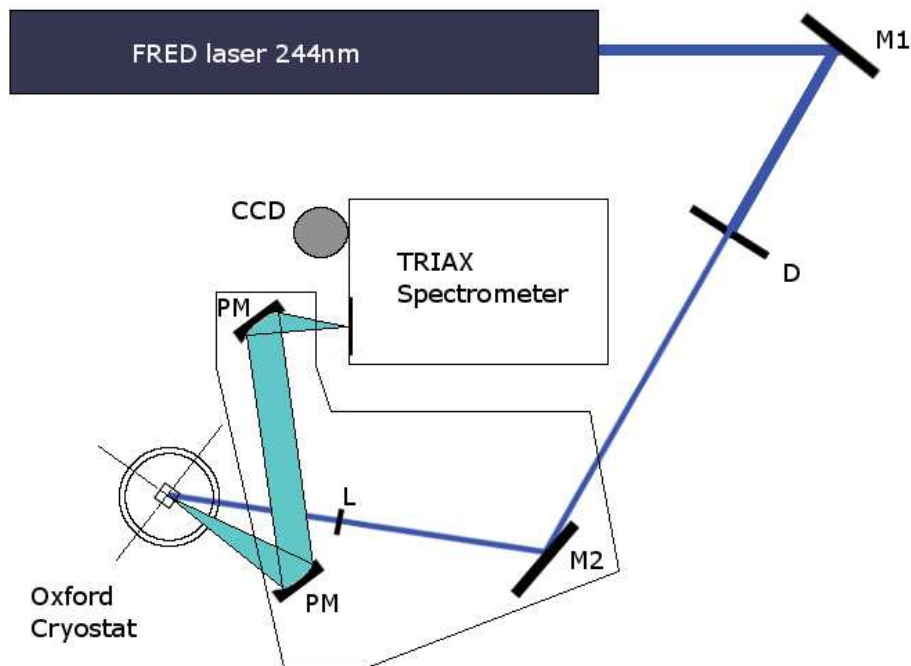


Fig.2. 18: Schematic representation of photoluminescence setup used in this work. M1 and M2 are mirrors, D is a diaphragm, L is a focusing lens and PM are the two parabolic mirrors collecting the luminescence.

The low temperature photoluminescence measurements were carried out at 4K using an Oxford He cryostat. The laser used to excite the samples is a frequency doubled argon ion (FRED) laser with a wavelength of 244 nm and a power about 30 mW. The penetration depth of the laser is about few μm at 4K for 4H-SiC, depending of the concentration values of impurities [25]. The laser beam is focused onto the sample's surface with a diameter of a few hundred micrometers. The sample is placed in an Oxford cryostat and cooled down at

4K with He liquid. The luminescence coming out from the sample passes through the Winlight system consisting of two parabolic mirrors and is finally focused onto the entrance slit of the Jobin-Yvon Horiba TRIAX 550 spectrometer with three grating (600, 1200 and 2400 gr/mm) to provide different resolution of the spectra. The 2400gr/mm can provide the resolution of 0.0125nm which is the highest resolution we can achieve with this setup. Usually, the entrance slit is about 50 μm . Finally, the spectra were collected by a Jobin-Yvon Spectrum One liquid-nitrogen cooled CCD array coupled to a CCD3500v controller and send to a computer. Further data processing is done on other computers.

2.3 Raman scattering spectroscopy

Raman scattering (RS) is one of the most commonly used techniques to study vibrational phenomena in solids [26]. The inelastic light scattering in crystals is susceptible to selection rules originating from wavevector (q) conservation [26], [27]. The magnitudes of the incident (q_i) and the scattered (q_s) radiation wavevectors are much smaller than that of a general vector (q) in the Brillouin Zone (BZ), ($q_i, q_s < q$). Hence, in order to conserve q the created (Stokes) or annihilated (anti-Stokes) phonon must have a wavevector of magnitude $q \leq 0$, i.e. near the center of the Brillouin zone (point Γ). Thus, the first order RS can investigate only phonons with $q \leq 0$. Phonons with larger q may be observed in second order (two phonons) Raman spectra. The $q \leq 0$ restriction can also be removed by introducing impurities or defects into the material or by fabricating crystals with a much larger lattice constant along the growth direction than that of the corresponding single crystals (superlattice). For Raman-scattered photons, the matter is excited into a virtual intermediate state and then relaxes to a vibrational state above the ground state. The photon transfers a certain amount of energy to the material, losing energy (Stokes shift). If the matter is already in a vibrationally excited state, inelastic scattered photons may also gain energy. The incident photon excites the material to a virtual intermediate state, which then can relax to its ground state. The scattered photon gains the energy difference, having a higher energy than before the scattering event (anti-Stokes shift). These three Raman scattering processes can be understood in a classical picture as a collision between the incident photon with matter. The Jablonski diagram in the Fig. 2. 19 shows the processes caused by incident photons. As in absorption spectroscopy the photon is absorbed and the system is excited to a higher state.

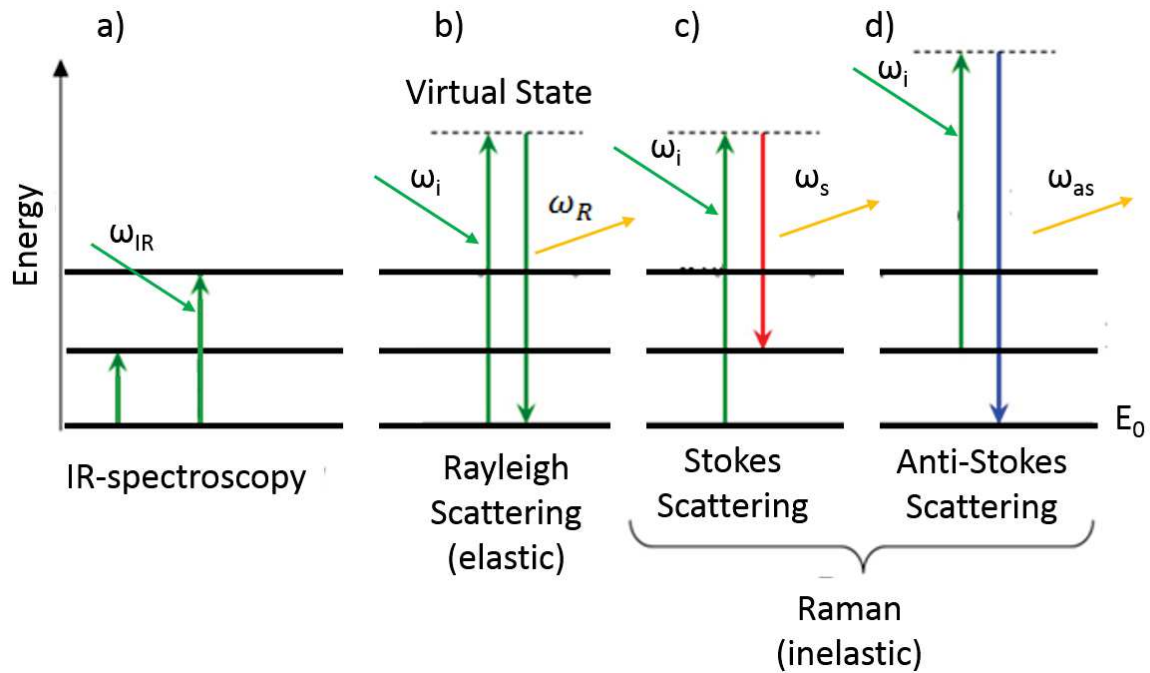


Fig.2. 19: Jablonski energy diagram of the scattering processes of light with Rayleigh scattering and Raman scattering (Stokes and anti-Stokes shifts). For comparison, an IR spectroscopy scattering scheme is shown on the left [28].

If there is no state available that can be filled by the system, scattering occurs. Three important scattering processes include [26], [28]:

- elastic scattering without energy transfer (Rayleigh scattering, 0.01%),

Fig.2. 19b) the scattered photon has the same energy as before $\hbar\omega_i = \hbar\omega_R$

- inelastic scattering with energy loss (Stokes shift, $10^{-6}\%$)

Fig.2. 19c) the scattered photon loses energy $\hbar\omega_i > \hbar\omega_s$

- inelastic scattering with energy gain (anti-Stokes shift, $10^{-6}\%$)

Fig.2. 19d) the scattered photon gains energy $\hbar\omega_i < \hbar\omega_{as}$

2.3.1 Stokes and anti-Stokes transition

As already said, Raman spectroscopy measures the energy that is transferred due to inelastic scattering. The energy transfer between both collision partners is equal to the

difference between the two involved energy levels $\hbar\omega_j$. With the energy $\hbar\omega_j$ transferred during the scattering process and the energy $\hbar\omega_i$ before scattering, the scattered photon will have the energy $\hbar\omega_{s/a}$ expressed by:

$$\hbar\omega_{s/a} = \hbar\omega_i \pm \hbar\omega_j \quad 2.12$$

The plus and minus in equation (2.12) corresponds to an energy gain (anti-Stokes shift) and an energy loss (Stokes) of the photon. The Stokes and anti-Stokes shifts are symmetric, determined by the difference of energy between the ground state and the vibrational state. For scattering on atom, the electric field of the photon affects the atom's electrons, resulting in atom distortion. The distorted atom acquires a contribution to its dipole moment μ :

$$\mu = \alpha E \quad 2.13$$

where α is a proportional constant of atom's polarisability. The polarisability corresponds to cloud electron deformation around an atom.

Vibrational Raman scattering occurs because an atom's vibration can change the polarisability. The change is described by the polarisability derivative $\frac{\partial \alpha}{\partial Q}$, where Q is the normal coordinate of the vibration. The polarisability is typically different if the field is applied parallel or perpendicular to the molecular axis or in different directions relative to the molecule. Nevertheless, for a small electric field, the polarisability is the same for the field oriented in opposite directions along the same axis ($\mu(-E) = -\mu(E)$). Thus, the distortion induced in a molecule by an applied electric field depends on the relative orientation and returns to its initial value after a rotation of 180° . The selection rules for Raman-active vibrations are linked to molecular symmetry and identify vibrations that change a molecule's polarisability. For scattering on anisotropic crystals, with the propagating phonons dependent on the crystal axis, similar dependence to the orientation of the light to the crystal axis is observed. Raman peaks were observable within the spectra, depending on the scattering geometry. The features of one phonon contributing to Raman scattering, were followed by higher order scattered peaks in the spectra, involving multiple phonons (in the second-order peaks, two phonons participate).

2.3.2 Selection rules

The selection rules allow to predict if a certain lattice vibration oscillation is Raman active or not. The selection rules for Raman scattering state that there must be a change in the permanent dipole moment μ during the vibration. Group theory methods, called nuclear site

group analysis, show that for an atomic symmetry center, the Raman-active vibrations will be silent in the infrared and vice versa [28], [29], [30], [31]. Because of the requirement of a conserved total angular momentum in the ground state of the system, only certain transitions can be induced. A basic summary and tables are given in the book by W. J. Miller [31]. The Raman intensity is proportional to the square of the change in the polarisability α :

$$I_{IR} \propto \left(\frac{\partial \mu}{\partial q} \right)_0^2, \quad I_{Raman} \propto \left(\frac{\partial \alpha}{\partial q} \right)_0^2 \quad 2.14$$

Here, q is the normal coordinate of the vibration. In the crystals, the interaction between the incident photon and a phonon is indirect. The interaction is connected to electronic interband transitions, which determine the dielectric susceptibility χ in the visible spectral range [32]. If these interband transitions are influenced by phonons, Raman scattering occurs. The normal coordinate of the phonon can be expressed by equation:

$$Q_j = A_j e^{\pm i(q_j \cdot Q_j \cdot t)} \quad 2.15$$

The vibrational influence on the susceptibility tensor can be described by expanding χ into a Taylor series with respect to the normal coordinate of the vibration Q_j :

$$\chi = \chi^{(0)} + \sum_j \chi^{(1)} Q_j + \dots = \chi_0 + \sum_j \left(\frac{\partial \chi}{\partial Q_j} \right)_0 Q_j + \dots \quad 2.16$$

The summation runs over the $3N - 3$ vibrational modes, with N as the number of atoms in the unit cell [32]. For example, for the diatomic base of silicon, the summation runs over the three optical phonons; for SiC, the summation depends on the individual polytype. If monochromatic light with the frequency ω_i illuminates a sample in the direction k_i , the associated electric field E induces an electric moment P according to

$$P = \varepsilon_0 \chi E = \varepsilon_0 \chi E_0 e^{i(k_i \cdot r - \omega_i t)} \quad 2.17$$

Combining the equation (2.16) with the equation (2.17) and we obtain:

$$P = \varepsilon_0 \chi E + \sum_j \varepsilon_0 A_j E_0 \left(\frac{\partial \chi}{\partial Q_j} \right)_0 e^{[i(k_i \pm q_j) \cdot r - i(\omega_i \pm \omega_j) t]} \quad 2.18$$

The first term represents Rayleigh scattering. The second term corresponds to Stokes and anti-Stokes scattering with the frequencies $\omega_i \pm \omega_j$. This second term can only be observed if there is a change in dielectric susceptibility $\left(\frac{\partial \chi}{\partial \omega_j}\right)_0 = \chi^{(1)} \neq 0$. Higher order terms in the Taylor expansion describe multi-phonon processes leading to higher order Raman scattering. The elements of $\chi^{(1)}$ are referred to as components of the Raman tensor determining a normal vibration Q_j as a Raman active or not [32], [33]. The exact form of the Raman tensor depends on the crystal symmetry as described by W. Hayes [34] and Rousseau et al. [35] For example, in the orthonormal coordinate system $x = [100], y = [010], z = [001]$, the Raman tensor for silicon will have the form [32], [33]:

$$R_x = \begin{pmatrix} 0 & 0 & 0 \\ 0 & 0 & d \\ 0 & d & 0 \end{pmatrix}, R_y = \begin{pmatrix} 0 & 0 & d \\ 0 & 0 & 0 \\ d & d & 0 \end{pmatrix}, R_{xz} = \begin{pmatrix} 0 & d & 0 \\ d & 0 & 0 \\ 0 & d & 0 \end{pmatrix}, \quad 2.19$$

The entire Raman scattering efficiency I is then given:

$$I = C \cdot \sum_j |e_i R_j e_s|^2 \quad 2.20$$

where e_i and e_s are the polarization vectors of the incident and scattered light, respectively, C is a constant [32], [33].

2.3.3 Particularity of phonons in SiC

Cubic SiC crystallises in the zinc blende structure (space group T_d^2) which has two atoms per unit cell, and thus three optical modes are allowed at the centre of the BZ. Since SiC is a polar crystal, the optical modes are split into one non-degenerate longitudinal optical phonon (LO) and two degenerate transverse optical phonons (TO). The first and second order RS studies of cubic SiC were discussed in detail by Olego and co-workers [36], [37]. The first and second order spectra measured as a function of hydrostatic pressure reveal the mode-Grüneisen parameters of the LO and TO modes at Γ and of several optical and acoustical phonons at the edge of the BZ [36], [37]. The data analysis also provides information about the relaxation mechanisms of the optical phonons. Information about the transverse effective charge was obtained from a study of the pressure and temperature dependences [37] of the long-wavelength optical phonons. The 2H-SiC polytype, the rarest

polytype, has the wurtzite structure and belongs to the space group C_{6v}^4 . This uniaxial crystal has four atoms per unit cell, and consequently has nine long-wavelength optical modes. Group theory predicts the following Raman active lattice phonons, near the center of the BZ: an A_1 branch with phonon polarisation in the uniaxial direction, a doubly degenerate E_1 branch with phonon polarisation in the plane perpendicular to the uniaxial direction, and two doubly degenerate E_2 branches. The A_1 and E_1 phonons are also infrared active, while E_2 is only Raman active. In uniaxial crystals, in addition to the long-range electrostatic forces responsible for the longitudinal-transverse splitting, we observe the short-range interatomic forces which exhibit the anisotropy of the force constants. The predominance of one of the two independent forces dictates the split between the different long-wavelength optical modes [27], [38].

Polytype	Group Symmetry	Atoms/unit cell	% of hexagonality
3C	T_d^2	2	0
2H	C_{6v}^4	4	100
4H	C_{6v}^4	8	50
6H	C_{6v}^4	12	33
8H	C_{6v}^4	16	25
15R	C_{3v}^5	15	40
21R	C_{3v}^5	21	29

Tab.2. 5: Space group, number of atoms by cell and hexagonality for seven the most common SiC polytypes

One of the most common and one of the most studied SiC polytypes is 4H. Like 2H and other hexagonal polytypes, 4H-SiC belongs to the space group C_{6v}^4 , and has 8 atoms per unit cell (see Tab.2. 5), leading to 21 phonon branches. Therefore the number of phonons observed by RS is greater for 4H than for 2H-SiC, resulting in an additional complication in distinguishing between several normal modes with the same symmetry. The assignment of the Raman spectra of 4H-SiC may be simplified by using the concept of a standard large zone (LZ) introduced by Patrick [39]. Since the SiC polytypes are characterized by a one-dimensional stacking sequence of planes in the axial direction (c-axis), the standard LZ for 4H-SiC extends to $4\pi/c$, where c is the unit cell axial dimension. Note that the reciprocal lattice vector is $2\pi/c$ thus we obtain pseudomomentum vectors $q=0$, $2\pi/c$, and $4\pi/c$, all equivalent to $q = 0$ in the BZ. This procedure, referred to as 'zone-folding' (or reduced zone scheme), is discussed extensively in the RS studies of superlattices [40]. Feldman et al [41] have used Raman spectroscopy to study lattice vibration in hexagonal polytypes. They define

a reduced momentum $x = q/q_{\max}$ which establishes the points in the phonon dispersion curves (for both optic and acoustic branches) accessible by RS. They observed that all long-wavelength modes are found on the LZ axis, and classified the modes in two categories, namely: (a) the strong modes at $x=0$, which show angular dependence, and (b) the weak modes, with no angular dependence, and with identification that depends upon their assignment to values of $x=q/q_{\max}$ ($x \neq 0$) in the LZ. The weak modes were conveniently classified according to their atomic motions as axial (parallel to c : extraordinary) or planar (perpendicular to c : ordinary). Feldman et al. [42] extended their RS studies to other polytypes and verified the concept of a common phonon spectrum (within 2%) for all polytypes [39]. They also were able to construct the phonon dispersion curves for SiC from their first-order RS data from various polytypes (except 3C-SiC, since this polytype is isotropic), namely: 4H, 6H, 15R and 21R. The phonon dispersion curves show discontinuities in the LZ representation (observed as doublet peaks in the Raman spectra), which result from the dependence of the force constant on the types of layers (hexagonal or cubic) in the polytype structure [43]. The lattice dynamics and phonon dispersion curves of SiC were modelled and compared with experimental data, resulting in an analytical model (bond-charge model) [44] supplemented with thermal processes like thermal vibrations and the displacement of atoms in the lattice. Fig.2. 20 shows the phonon dispersion curve and density of state for 4H-SiC polytype.

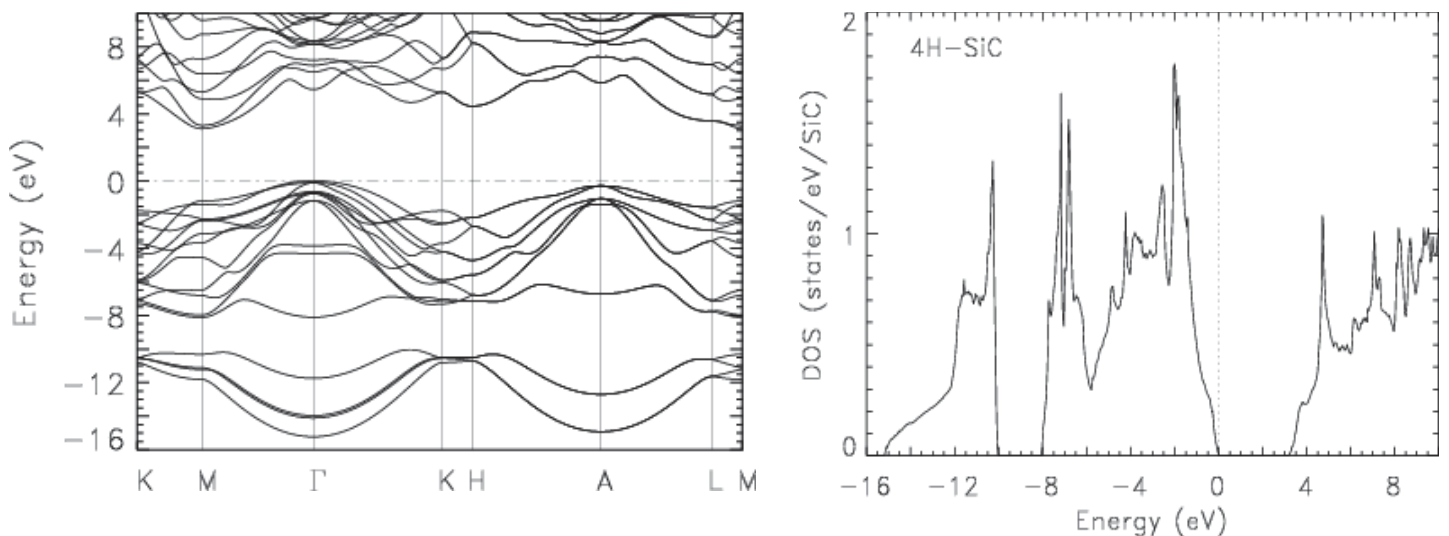


Fig.2. 20 Energetic band structure and density of states (DOS) (right graphs) for 4H-SiC, [44], [45], [46]

The acoustic and optic phonons are split into longitudinal acoustic-LA (optical- LO) and transverse acoustic-TA (optical-TO) modes [47]. This splitting originates from an additional force on the permanent dipole moment, for the longitudinal displacement only. Folded optical (FO) modes exhibited less splitting than acoustic modes [41], [48]. The polarization and geometry of the laser light to the c -axis (back- or right-angle scattering, for the a -axis swapped direction) change the measured Raman spectra, showing varying features, e.g., the

$E_1(\text{LO})$ line is only present in one direction [41], [48]. Fig. 2. 21 shows the longitudinal folding modes (FLO) for three polytypes 3C, 2H and 4H SiC and their schematic structure.

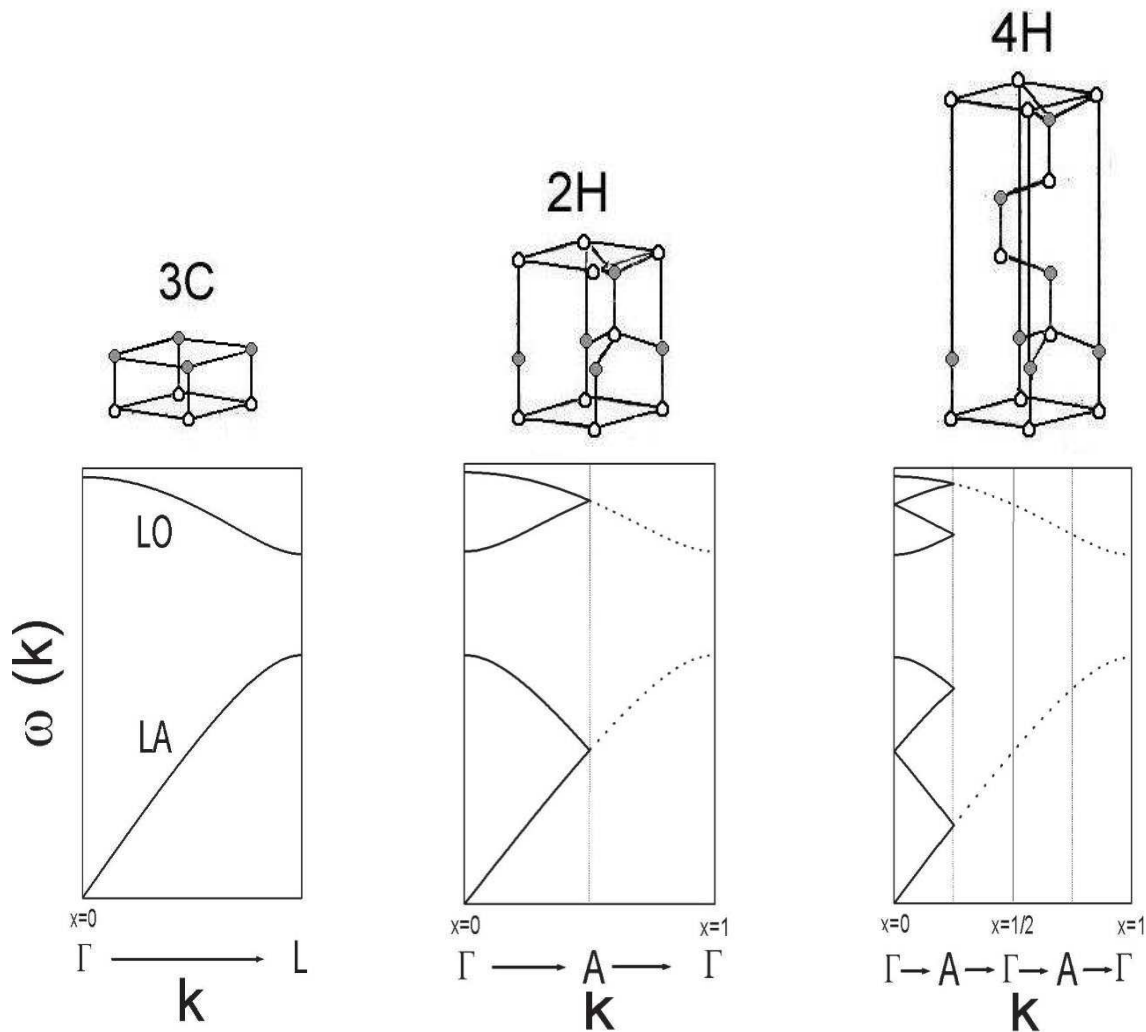


Fig.2. 21: Longitudinal folding modes for 3C, 2H and 4H SiC respectively [49]. The full lines correspond to the first Brillouin zone for each polytypes; the dotted lines correspond to the first Brillouin zone of 3C-SiC.

2.3.4 Application: polytype identification by micro-Raman spectroscopy

In the case of SiC, the Raman spectroscopy allows to easily identify the polytype. The polytypes with longer periods can be identified by the following procedures: either the period is estimated from the FTA and FTO frequencies or one can simply compare the

observed spectrum with those already calculated [50]. The identification of the common polytypes with shorter period is much easier. Already by comparing the characteristic phonon frequency position lines is possible to determine the polytype of SiC (see Fig.2. 22).

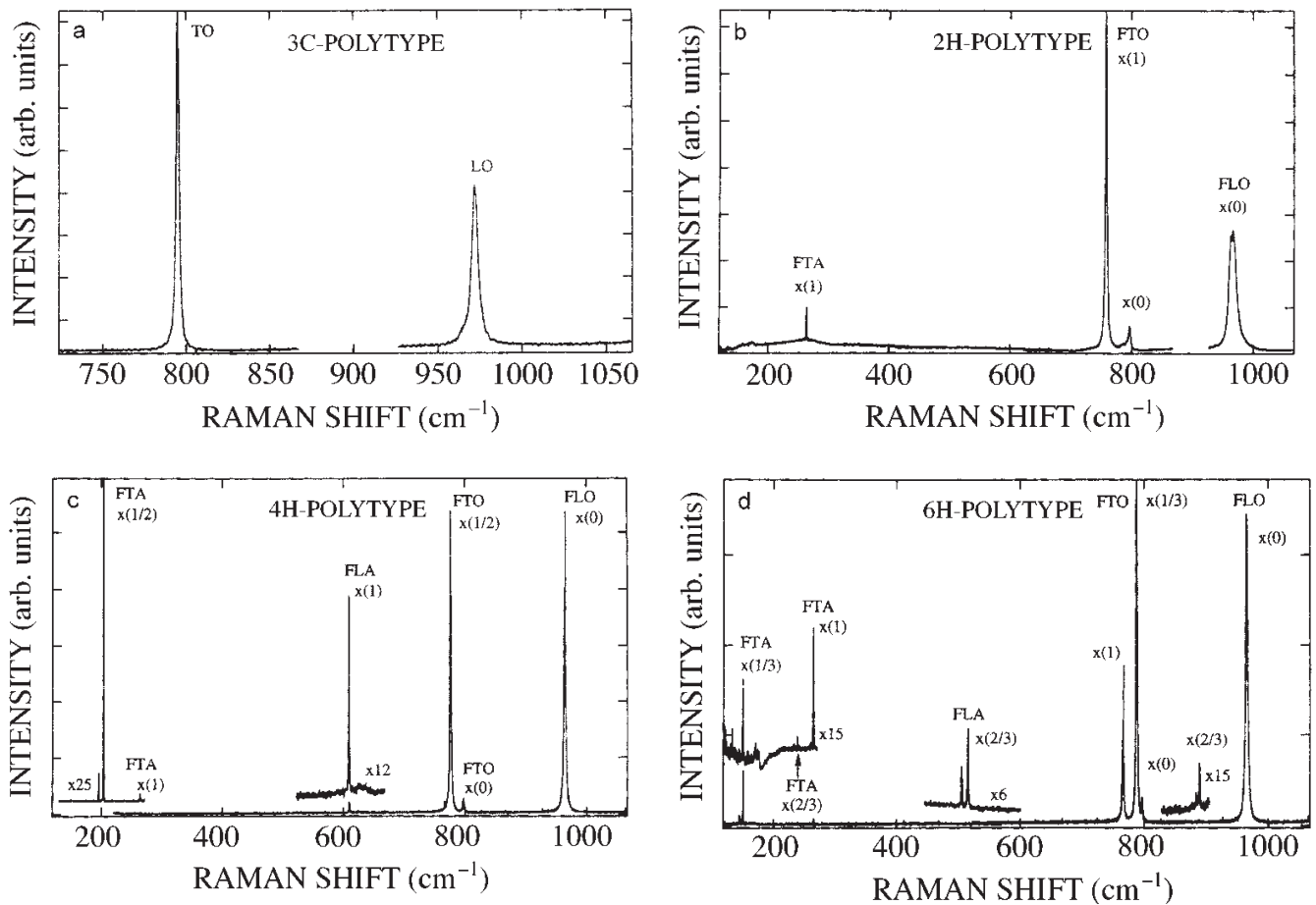


Fig.2. 22: Raman spectra of a) 3C-SiC, b) 2H-SiC, c) 4H-SiC and d)6H-SiC [51].

The observed axial-A (FL) and planer-E (FT) acoustic (A) and optic (O) modes are shown in Tab.2.6.

3C-SiC	First order (x = 0)		
FLO (cm⁻¹)	LO (972)		
FTO (cm⁻¹)	TO (796)		
FLA	ac.		
FTA	ac.		
4H-SiC	First order (x = 0)	Folded (x = 1/2)	Folded (x = 1)

FLO (cm ⁻¹)	A₁ (964)	2B₁ (-/-)	A₁ (838)	
FTO (cm ⁻¹)	E₁ (796)	2E₂ (776/-)	E₁ (-)	
FLA (cm ⁻¹)	-	2B₁ (-)	A₁ (610)	
FTA (cm ⁻¹)	-	2E₂ (196/204)	E₁ (266)	
15R-SiC	First order (x = 0)	Folded s (x = 2/5)	Folded (x = 4/5)	
FLO (cm ⁻¹)	A₁ (965)	2A₁ (932/938)	2A₁ (860/-)	
FTO (cm ⁻¹)	E (797)	2E (785/-)	2E (769/?)	
FLA (cm ⁻¹)	-	2A₁ (331/337)	2A₁ (569/577)	
FTA (cm ⁻¹)	-	2E (167/173)	2E (255/256)	
6H-SiC	First order (x = 0)	Folded (x = 1/3)	Folded (x = 2/3)	Folded (x = 1)
FLO (cm ⁻¹)	A₁ (965)	2B₁ (-/-)	2A₁ (889/-)	B₁ (-)
FTO (cm ⁻¹)	E₁ (796)	2E₂ (789/?)	2E₁ (-/-)	E₂ (767)
FLA (cm ⁻¹)	-	2B₁ (-)	2A₁ (504/514)	B₁ (-)
FTA (cm ⁻¹)	-	2E₂ (145/150)	2E₁ (236/241)	E₂ (266)

Tab.2. 6: The frequency of the folded modes for typical polytypes of SiC. The Modes A₁, E₁, and E are IR active, the modes A₁, E₁, E₂ and E are Raman active, the modes B₁ are not-active [51].

2.3.5 Experimental setup

The schematic representation of the experimental setup using to collect the data in this work is presented in Fig.2. 23. The samples are investigated by a microscope optic with possible confocal configuration. The excitation source is the Argon-Krypron laser with 647nm of wavelength. The signal is analyzed by triple monochromator with 1800 gr/mm. Next the signal is collected by CCD camera cooled with liquid nitrogen. The spatial resolution is about 1μm of diameter for the microscope's objective with apparatus number 0.92.

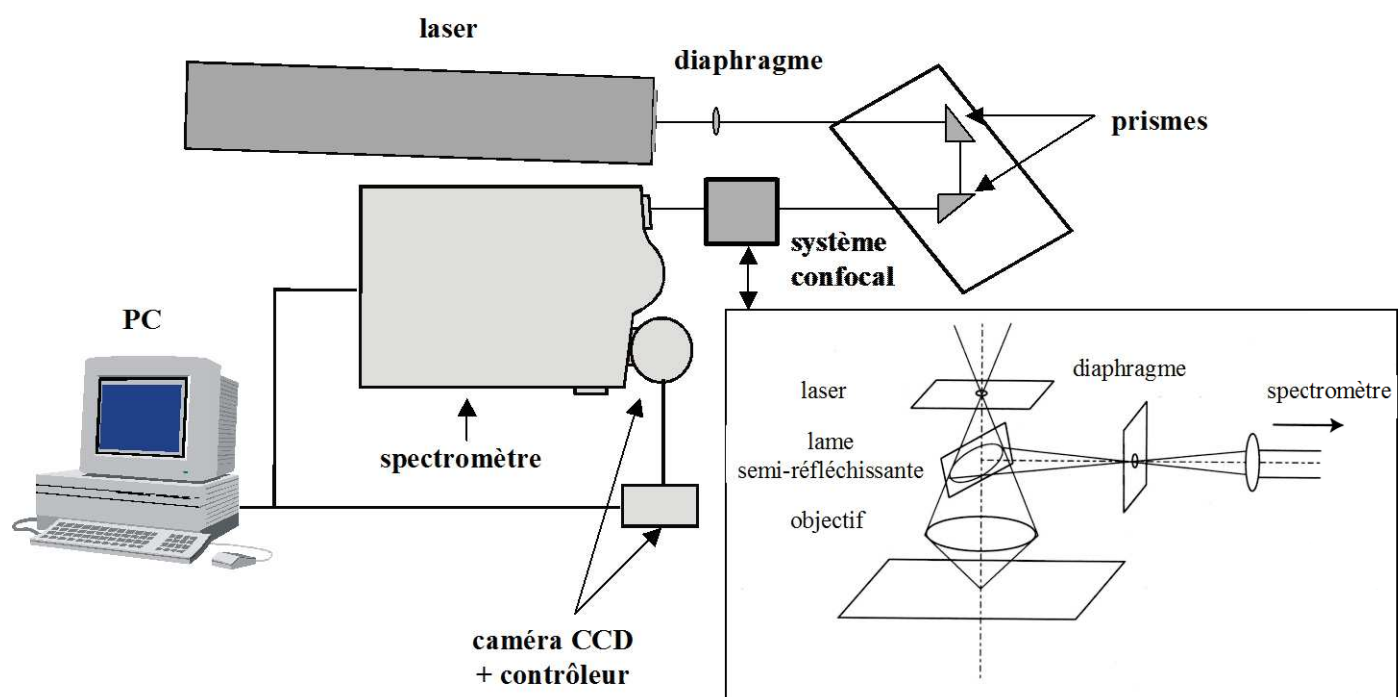


Fig.2. 23: Schematic representation of the micro-Raman setup.

Bibliography

- [1] "<http://www.gm.univ-montp2.fr/spip.php?article305>," [Online].
- [2] "<http://www.geos.ed.ac.uk/facilities/ionprobe/SIMS4.pdf>," [Online].
- [3] "<http://pprco.tripod.com/SIMS/Theory.htm>," [Online].
- [4] W. & S. Paul van der Heide, ISBN-13: 978-1-118-48048-9, 2014.
- [5] R.G. Wilson, "Int. J. Mass Spectrometry," *Ion Proc.*, vol. 43, p. 143, 1995.
- [6] H. K. Schröede, *Semiconductor Material and Device Characterization*, chap.2, p.101, New York, 1998.
- [7] H. Kuhn, *J. Chem. Phys*, p. 17, 1949.
- [8] A. H. Dessouki, "Fundamental of Solid-State Electronics," *Electronics and Communications Section*, vol. 2, pp. 1-17.
- [9] W. Choyke, D. H. L. Patrick, *Proc 7th Int. Conf. Semicond., Paris*, p. 751, 1964.
- [10] S. Yamada, H. Kuwabara, *Proc. 3rd Int. Conf. on Silicon Carbide*, vol. 12/13, p. 634-536, 1976.
- [11] H. Kuwabara, S. Yamada, *Phys. Status Solidi A (Germany)*, vol. 30, p. 739-746, 1975.
- [12] H. Kuwabara, S. Yamada, S. Tsunekawa, *J. Lumin. (Netherlands)*, vol. 12/13, p. 531-536, 1976.
- [13] H. Kuwabara, K. Yamanaka, *Phys. Status Solidi A (Germany)*, vol. 37, p. 157167, 1976.
- [14] A. Suzuki, H. Matsunami, T. Tanaka, *J. Electrochem. Soc. (USA)*, vol. 124, p. 241-246, 1977.
- [15] W. Suttrop, G. Pensl, P. Lanig, *Appl. Phys. A, Solids Surf. (Germany)*, vol. 51, p. 231-237, 1990.
- [16] J. Reinke, S. Greulich-Weber, J.-M. Spaeth, E. Kalabukhova, S. Lukin, E.N.Mokhov, *Inst. Phys. Conf. Ser. (UK)*, vol. 137, p. 211-214, 1994.
- [17] J. S. Bishop, P. N. Jr, M. Gipe, *Appl. Phys. Lett.*, vol. 52, p. 1695-1697, 1988.
- [18] M. Ikeda, H. Matsunami, T. Tanaka, *Phys. Rev. B (USA)*, vol. 22, p. 2842-2854, 1980.

-
- [19] M. Ikeda, H. Matsunami, *Phys. Status Solidi A (Germany)*, vol. 58, pp. 657-63, 1980.
- [20] Y. Maslokovets, E. Mokhov, Y. Vodakov, G. Lomakina, *Sov. Phys.-Solid State (USA)*, vol. 10, p. 634, 1968.
- [21] T. Kimoto, J. A. Cooper, *Fundamentals of Silicon Carbide Technology: Growth, Characterization, Devices and Applications*, p. 21, John Wiley & Sons, (2014).
- [22] C. Balloud, "Méthodes de caractérisation optique de SiC," p.146, *PhD thesis*, 2005.
- [23] H. B. Bebb, E. W. Williams, *Semiconductors and Semimetals*, chap.2, p. 106 1972 .
- [24] T. Robert, G. Zoulis, "Photoluminescence investigation methods of residual defects in SiC," *Physics of Advanced Materials Winter School*, p. 3, 2008.
- [25] A. Henry et al., *Materials Science and Engineering*, vol. 62, p. 234-238, 1999.
- [26] R. Krishnan, G. Chantry, R. Cowley, C. Hathaway, P. Lallemand, *The Raman Effect*, vol. 1, 1971.
- [27] R. Loudon, *Adv. Phys*, vol. 13, p. 423-482, 1964.
- [28] D. A. Long, *The Raman Effect-A Uni treatment of the Theory of Raman Scattering by Molecules*, England, chap.1 and chap. 3, p. 31-48, 2002.
- [29] M. Cardona, G. Gtinterodt, *Light Scattering In Solids VII*, Berlin Eidelberg, 2002.
- [30] W. Weber, R. Merlin, *Raman Scattering in Material Science*, Berlin, Heidelberg, 2000.
- [31] W. J. Miller, *Symmetry groups and their applications*, New Yourk, 1972.
- [32] K. Dombrowski, *Micro-Raman Investigation of Mechanical Stress in Si Device*, Dissertation, TU-Cottbus, 2000.
- [33] I. D. Wolf, "Micro-Raman spectroscopy to study local mechanical stress in silicon integrated circuits," *Semiconductor Science Technology*, vol. 11, p. 139-154, 1996.
- [34] W. Hayes, *Scattering of Light by Crystals*, New York: John Wiley & Sons Inc, 1978.
- [35] D. L. Rousseau, R. P. Bauman, S. P. S. Porto, "Normal Mode Determination in Crystals," *Journal of Raman Spectroscopy*, vol. 10, p. 253-290, 1981.
- [36] D. Olego, M. Cardona, *Phys. Rev. B (USA)*, vol. 25, p. 151-160, 1982.
- [37] D. Olego, M. Cardona, P. Vogl, *Phys. Rev. B (USA)*, vol. 25, p. 3878-88, 1982.
- [38] C. Arguello, D. Rousseau, S. Porto, *Phys. Rev. (USA)*, vol. 181, p. 1351-1361, 1969.

-
- [39] L. Patrick, *Phys. Rev. (USA)*, vol. 167 , p. 809-13, 1968.
- [40] B. Jusserand, M. Cardona, *Light Scattering in Solids V*, Topics in Applied Physics, Springer, (Berlin), Heidelberg, p. 49-152, 1989.
- [41] D. Feldman, J. P. Jr, W. C., L. Patrick, *Phys. Rev. (USA)*, vol. 170, p. 698-93, 1968.
- [42] D. Feldman, J. P. Jr, W. Choyke, L. Patrick, *Phys. Rev. (USA)*, vol. 173, p. 787-93, 1968.
- [43] C. Hodges, *Phys. Rev. (USA)* , vol. 187 , p. 994-9, 1969.
- [44] K. Karch, P. Pavone, W. Windl, O. Schutt, D. Strauch, "Ab initio calculation of structural and lattice-dynamical properties of silicon carbide," *Phys.Rev. B*, vol. 50, p. 17054-17063, 1994.
- [45] D. W. Feldma, J. H. Parker, W. J. Choyke, L. Patrick, "Phonon Dispersion Curves by Raman Scattering in SiC Polytypes 3C,4H,6H,15R,and 21R," *Phys; rev.*, vol. 173, pp. 787-793, 1968.
- [46] G. L. Zhao, D. Bagayoko, *J. Phys.*, vol. 2, p. 16, 2000.
- [47] J. C. Burton, L. Sun, M. Pophristic, S. J. Lukacs, F. H. Long, Z. C. Feng, I. T. Ferguson, "Spatial characterization of doped SiC wafers by Raman spectroscopy," *Journal of Applied Physics*, vol. 84, no. 11, p. 6268–6273, 1998.
- [48] S. Nakashima, H. Harima., "Raman investigation of SiC polytypes," *Physica Status Solidi a-Applied Recherch*, vol. 162, no. 1, p. 39-64, 1997.
- [49] H. Mutschke et al., "Infrared properties of SiC particles," *stron.Astrophys*, vol. 345, p. 187, 1999.
- [50] A. W. S. Nakashima and Z. Inoue, *J. Phys. Soc. Japan*, vol. 56, p. 3375, 1987.
- [51] H. H. S. Nakashime, "Characterization of structural and electrical in SiC by Raman spectroscopy," *Proceedings of 6th International Conference on SiC and related materials*, vol. 142, pp. 269-272, 1995.

Chapter 3: Doping level evaluation by Raman scattering spectroscopy: Fitting models for n- and p-type 4H-SiC

Introduction

Inelastic light scattering is not restricted to vibrational phenomena. Indeed Raman scattering (RS) has been used in the study of other excitations in the SiC polytype system, e.g. polaritons, plasmons, and electronic RS. In polar crystals TO phonons and photons with approximately the same energy and wave vector may couple strongly. This mixed propagating excitation, called the polariton, can no longer be described as a phonon or a photon, and its dispersion is determined by the material dielectric constant. In the case of a uniaxial crystal [1], the orientation of the electric field (E) of the incident and the scattered light with respect to the crystal axis must be taken into account. Since the crystal refractive index and the dielectric constant for the ordinary and extraordinary rays are different, the polariton is anisotropic. Azhnyuk et al. [2] carried out a detailed study of near-forward Raman scattering (inelastic scattering experiment performed at small angles with respect to the incident beam direction) in 6H-SiC. They were able to observe the extraordinary (A-branch) and the ordinary (E-branch) polaritons. They also investigated the effect of free-electrons on the polariton dispersion curve. It was observed that for nitrogen-doped (N-doped) samples the polariton shift decreased with increasing free charge carrier concentration (plasmon). The interaction between plasmon and polariton is commonly called plasmariton.

In a heavily N-doped 6H sample ($6 \times 10^{19} \text{ cm}^{-3}$) Klein et al. [3] observed an asymmetric broadening and a shift of the $A_1(\text{LO})$ phonon which were attributed to the overdamped coupling between LO phonon and plasmon modes [4]. The interaction between these two excitations occurs via their macroscopic electric fields when the frequency of oscillation of a free-carrier plasma is close to that of the LO phonon. The dependence of the LO phonon-overdamped plasmon coupled modes on carrier concentration was reported by Yugami et al [5] in 3C-SiC films, where the carrier concentrations varied from 6.9×10^{16} to $2 \times 10^{18} \text{ cm}^{-3}$. They verified that the carrier concentrations obtained from RS were in fairly good agreement with the Hall measurement values, and that the Faust-Henry coefficient [4] for the 3C-SiC ($C=+0.35$) was close to the value reported for 6H-SiC ($C = +0.39$) [3].

Low temperature Raman measurements performed on N-doped 6H-SiC show electronic transitions of E_2 symmetry at 13.0, 60.3 and 62.6 meV, which were assigned to $I_5(A_1)$ and $I_5(E)$ valley-orbit transitions at the three inequivalent N-donor sites [6] (one hexagonal and two cubics).

Room temperature Raman scattering can conveniently be used to identify a substitutional impurity (localized vibrational mode) [7] or structural defect (breaking of the translational

symmetry of the crystal) [8]. The lattice recovery under heat treatment can easily be verified by monitoring the reduction of the phonon line width and frequency shifts [8]. Although Raman scattering has been extensively used to study lattice damage and recovery in single and compound semiconductors, only a few studies have been reported in the SiC system.

A wide variety of electronic excitations in semiconductors can be studied by the Raman scattering technique [9] [10]. In the next section we will discuss the light scattering by carriers in semiconductors like SiC via a coupling of fluctuations in carrier density to the optical radiation fields. Long range Coulomb interactions are included via the random phase approximation. This leads to a discussion of scattering by plasmons and, in polar crystals like SiC, by plasmon-LO phonon coupled modes (Longitudinal Optic PC). First we will focus on the n-type SiC and then expand the equation on the p-type case. Furthermore the interaction of the free carriers with the acoustic modes will be discussed. Then we will finish to discuss the fitting model apply to the acoustic mode.

3.1 LOPC modes

The Raman line shape of the Longitudinal Optic phonon coupled (LOPC) modes is a good indicator of the structural and electrical properties of SiC. This feature has been now studied many times theoretically and experimentally [9], [11], [12]. The electronic Raman effect in semiconductors was investigated in detail by Colwell and Klein [10]. Shallow donors in the semiconductors which have their conduction band minimum at zero wave vector have a hydrogenic set of energy levels that lie just below the conduction band. These levels are described by the effective mass approximation. The line shape and frequency of the coupled modes have been calculated using dielectric analysis. In general the LOPC mode for semiconductors has two branches (L_+ and L_-), and their energies are given by the zeros of the real part of the total dielectric function. Three mechanisms generally contribute to the Raman scattering by the LOPC mode [9]:

- deformation potential (DP),
- electro-optical (EO) mechanisms and
- charge-density fluctuation (CDF)

In semiconductors, like SiC which have a large band gap and a low carrier mobility the EO and DP mechanisms dominate the scattering process. Moreover the lower-energy branch (L_-) is not observed in the Raman spectra because of the strong damping (overdamping).

The Raman scattering efficiency for the LOPC mode is given by [9]:

$$I(\omega) = SA(\omega) \text{Im}\left[-\frac{1}{\varepsilon(\omega)}\right] \quad 3.1$$

where S is proportionality constant, $\varepsilon(\omega)$ is the dielectric function and $A(\omega)$ is given by:

$$A(\omega) = 1 + \frac{2C\omega_T^2}{\Delta} [\omega_p^2 \gamma_p (\omega_T^2 - \omega^2) - \omega^2 \Gamma (\omega^2 - \gamma_p^2 - \omega_p^2)] + \left(\frac{C^2 \omega_T^4}{\Delta (\omega_L^2 - \omega_T^2)} \right) \{ \omega_p^2 [\gamma_p (\omega_L^2 - \omega_T^2) + \Gamma (\omega_p^2 - 2\omega^2)] + \omega^2 \Gamma (\omega^2 + \gamma_p^2) \} \quad 3.2$$

Here ω is the exciter frequency, ω_L , ω_T are the vibration frequency of the longitudinal and transvers optic modes respectively. ω_p is the vibration frequency of the free carriers. γ_p is the plasma damping constant. C is the so-called Faust-Henry coefficient [13]. Γ is the phonon damping constant and Δ is defined by:

$$\Delta = \omega_p^2 \gamma_p [(\omega_T^2 - \omega^2)^2 + \omega^2 \Gamma^2] + \omega^2 \Gamma (\omega_L^2 - \omega_T^2) (\omega^2 + \gamma_p^2) \quad 3.3$$

Finally the dielectric function $\varepsilon(\omega)$ is given by the contributions from phonon and plasmon with this expression:

$$\varepsilon(\omega) = \varepsilon_\infty \left(1 + \frac{\omega_L^2 - \omega_T^2}{\omega_T^2 - \omega^2 - i\omega\Gamma} - \frac{\omega_p^2}{\omega(\omega + i\gamma_p)} \right) \quad 3.4$$

When a polar semiconductor is doped to degeneracy a plasma is obtained. The plasma oscillation is a long-wavelength electron-density oscillation, a longitudinal "vibrational mode" of the electron gas, and it can couple to the electric field of the long wavelength LO phonon. The resulting mixed modes were first discussed by Varga [14] and may be found from the zeros of the real part of the total dielectric function. The plasma frequency is given in terms of the electron density by:

$$\omega_p^2 = \frac{4\pi n e^2}{\varepsilon_0 \varepsilon_\infty m^*} \quad 3.5$$

Here ε_∞ is the optical dielectric constant, n the carrier density and m^* is the electron effective mass. The plasmon damping constant is expressed as a function of the carrier mobility by the following equation

$$\gamma_p = \frac{e}{m^* \mu} \quad 3.6$$

In this equation μ is the carrier mobility. Now if we take ω_p, γ_p as adjustable parameters, one can calculate n and μ from the fit LOPC mode. In Fig. 3. 1 the variation of the theoretical line shape of the LOPC modes is shown for different value of the mobility in two cases for low electron density (a) and for high electron density (b), from the work of ref. [15]. For the low electron concentration the LOPC mode shape is almost independent of the plasmon damping constant, whereas for the high electron concentration the LOPC mode exhibits a strong dependence on the plasmon damping constant and thus on the mobility.

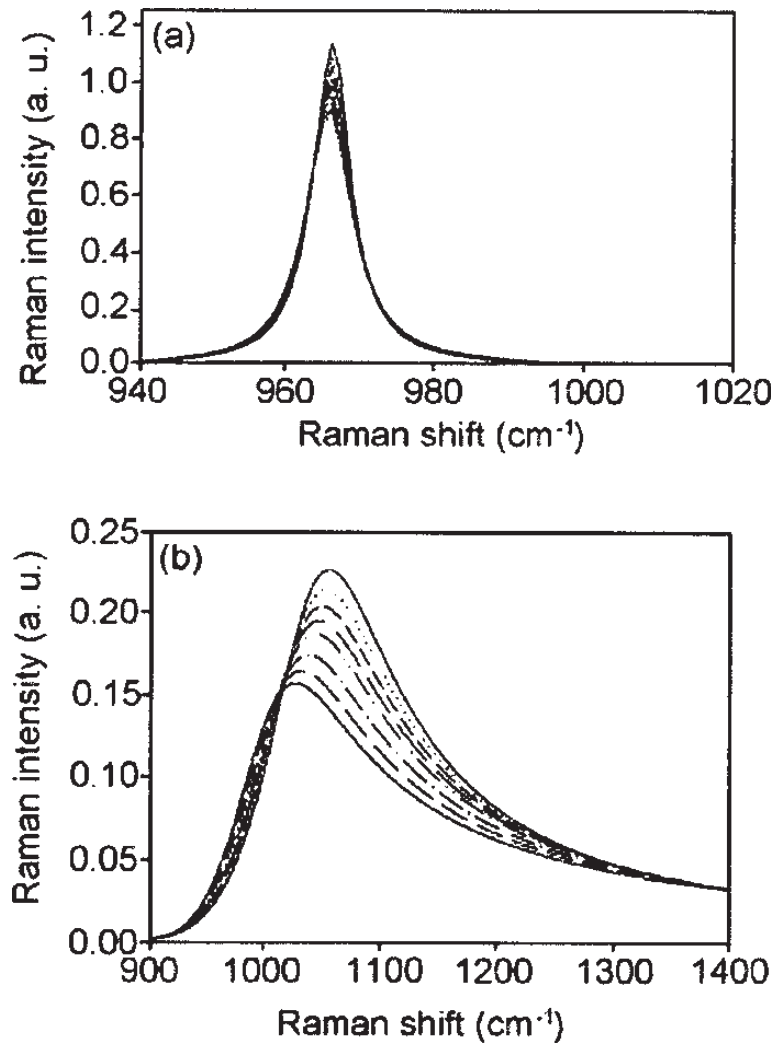


Fig.3. 1: Variation of the theoretical line shape of the LOPC modes for different plasmon damping constants at (a) low ($n=4.9 \times 10^{17} \text{ cm}^{-3}$) and b) high ($n=1.1 \times 10^{19} \text{ cm}^{-3}$) electron concentrations [15].

3.1.1 4H-SiC n-type

The equation (3.4) is very useful to determine the free carrier concentration for n-type 4H-SiC. In this way one can calculate the value of carrier concentration using the position and

the shape of the $\text{FLO}_{x(0)}$ (Folded Longitudinal Optic) line. Analyzing the Raman spectra one notices that with increasing the carrier concentration the shift to the higher energy as well as the change in the intensity of the LOPC line appears. This was observed for the n-type samples by T. Hon et al. [16]. The Fig.3. 2 shows the variation of the LOPC mode in 4H-SiC for five electron concentrations from $n=1 \times 10^{15} \text{ cm}^{-3}$, to $n=51 \times 10^{18} \text{ cm}^{-3}$. For higher electron concentrations: higher than $5 \times 10^{18} \text{ cm}^{-3}$ the LOPC modes could not be fitted because at such high concentrations the contribution by excitations out of the Brillouin zone center and the non-parabolicity of the bands have to be considered [15].

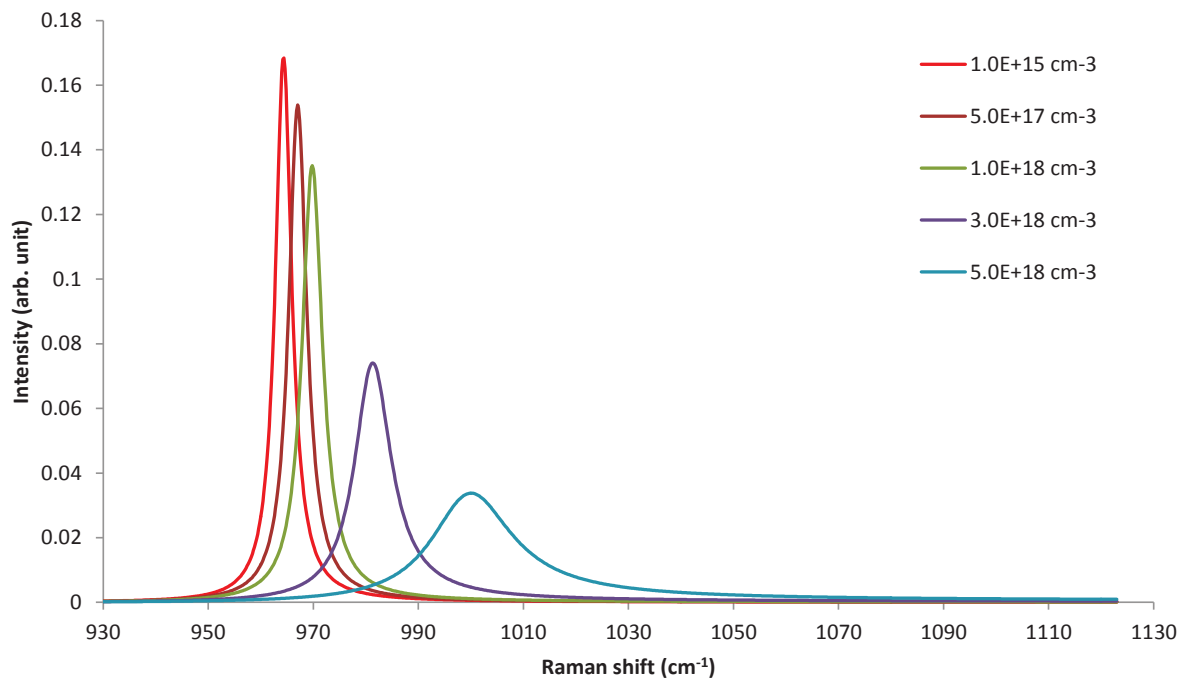


Fig.3. 2: LOPC mode in 4H-SiC for several electron concentrations. The LOPC mode shifts to the high frequency side and broadens as the free carrier concentration increases. The lines correspond to fits to equation (3.1).

The deep studies of the limitation of usability of LOPC modes to determine the carrier concentration was carried out by M. Chafai et al. [15]. They showed that for low carrier concentration— low ω_p correspond to only one well-defined ω_{LOPC} Raman shift. This cannot be maintained for increasing ω_p for which more than one value of ω_{LOPC} is possible. The upper and lower lines in Fig.3. 3 represent the upper and lower limits of the Raman shift for the values of the plasmon damping constant γ_p . The vertical bars correspond to the set of Raman shifts calculated within the range of the selected plasmon damping constants for each ω_p . The parallel bars give the error in the ω_p (free electron concentration) from a

Raman shift ω_{LOPC} . These errors increase with ω_p and can be estimated as 1% for the concentration of $2 \times 10^{18} \text{ cm}^{-3}$, 13% for concentration $5 \times 10^{18} \text{ cm}^{-3}$ and finally 20% for carrier concentration $1 \times 10^{19} \text{ cm}^{-3}$ [15].

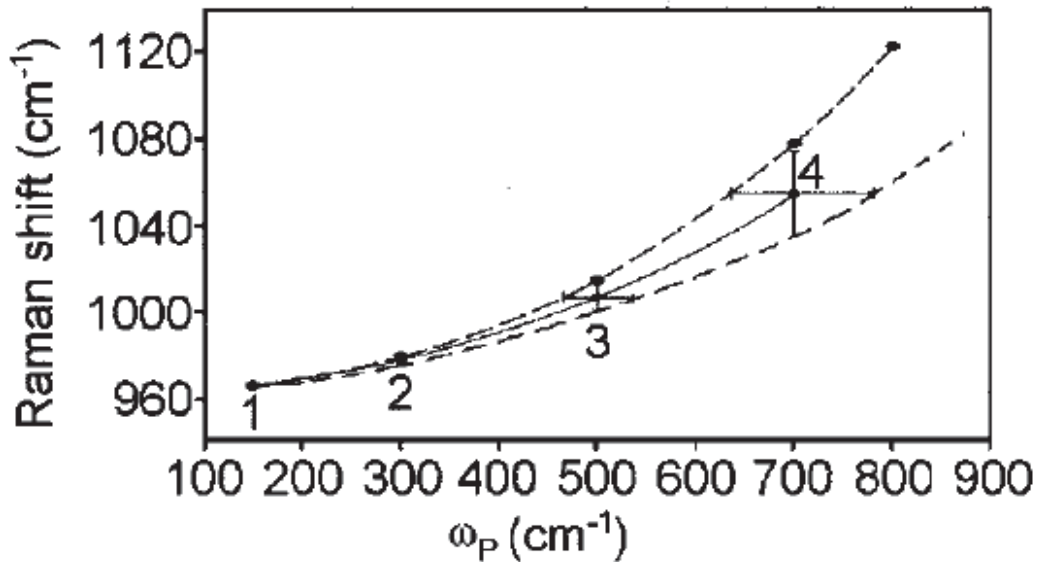


Fig.3. 3 Raman shift of the LOPC mode vs. plasma frequency for different plasmon damping constant [15].

3.1.2 4H-SiC p-type

In case of p-type SiC the equation (3.1) still can be used to fit the FLO, with consideration the effective mass of holes instead of electron. Nonetheless, the situation is quite different. The FLO line, because of weak coupling of LO-phonon-hole-plasmon-coupled mode does not exhibit significant shift to compare with n-type (see Fig.3. 4). Such a weak coupling is explained by an objectively large carrier damping rates of hole, in the other words low carrier mobility in p-type SiC [17]. Even if variations in LOPC mode intensities and broadening are perceived, there is no clear correlation with the acceptor concentration. Notice that the same behavior is observed for p-type in 6H-SiC [18]. These features strongly complicate the estimation of the carrier concentration in p-type SiC. Nonetheless knowing that there is no significant shift could be a good indicator when about determine the type of carrier. For n-type as it was shown before clear shift appears while FTLO line for p-type SiC remains in this same position regardless the doping level.

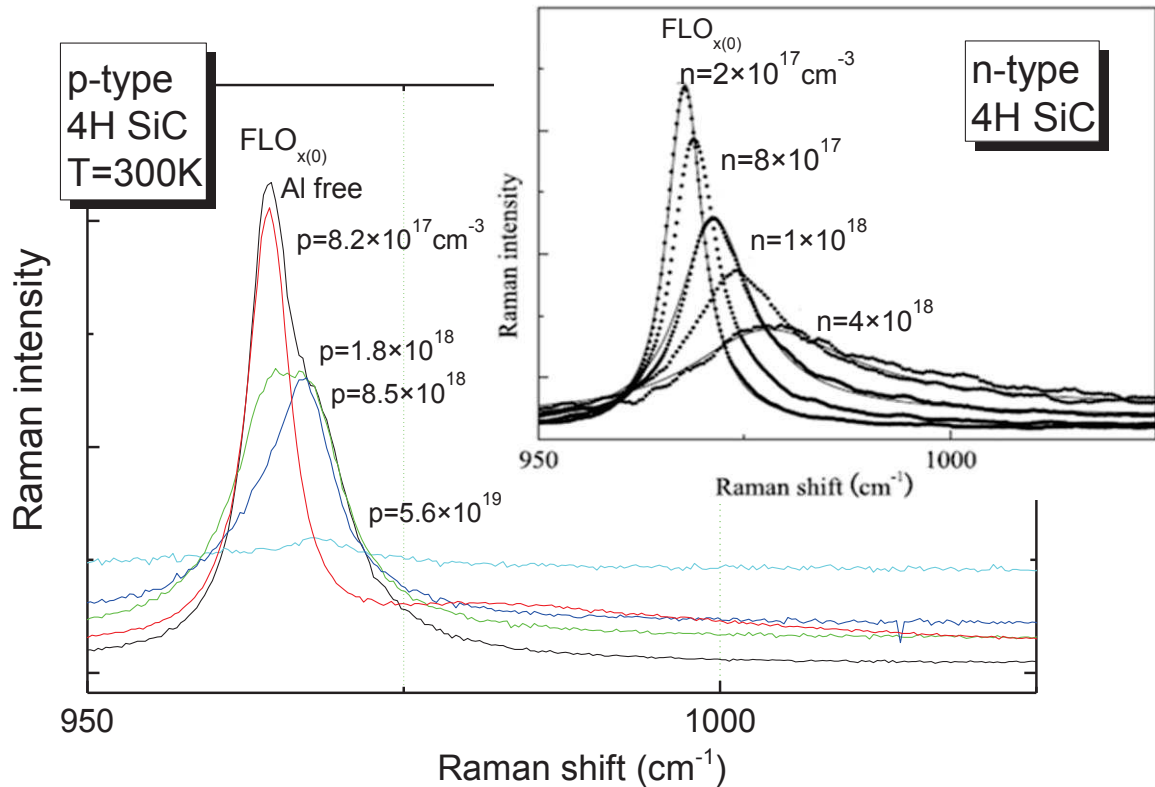


Fig.3. 4 Raman shift of the $FLO_{x(0)}$ mode observed on 4H-SiC as a function of the doping level in the case of p-type. A comparison with n-type is shown in insert [12].

The low energy part of the Raman spectra- FTA (Folded Transvers Acoustic) modes also is affect by the carrier concentration. In the next section the theoretical approach of investigation of FTA modes is developed.

3.2 Fano-interference effect in SiC.

In this section we are giving a theoretical approach for the way how the low energy part of the Raman spectrum can be used to determine the carrier concentration first for n-type and then we will extend for p-type SiC.

Let's consider an unperturbed system with a ground state $|g\rangle$, an excited electronic state $|e\rangle$, with excitation energy E_e , and a one-phonon excited state $|p\rangle$, with energy $E_0 = \hbar\omega_0$.

In this same time we neglected higher phonon oscillator states. Transitions to the states $|e\rangle$ and $|p\rangle$ are Raman-active. The Raman matrix elements connecting them to the ground state are T_e and T_p . Electron phonon coupling is assumed to be present in the form of a matrix element V between $|e\rangle$ and $|p\rangle$ as shown in Fig.3. 5. This produces a mutual repulsion of the levels E_e and E_0 to position E_{\pm} which are the roots of the secular equation:

$(E_0 - E)(E_e - E) - V^2 = 0$ in this equation V is assumed to be real.

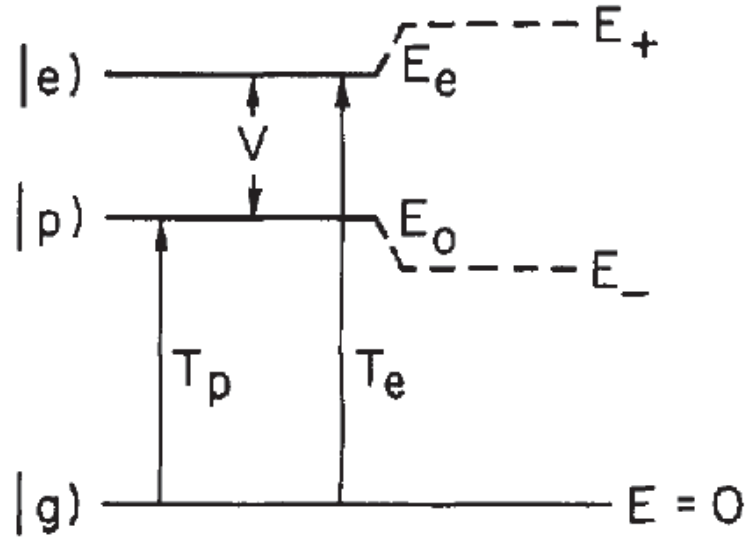


Fig.3. 5 System with two excited states coupled by a matrix element V [9]

It is more convenient to use the Green's function operator rather than deal with the proper eigenstates \pm to calculate the intensity.

$$G(z) = (\mathcal{H} - z)^{-1} = \begin{pmatrix} E_0 - z & V \\ V & E_e - z \end{pmatrix}^{-1} \quad 3.7$$

The intensity of Raman spectrum is proportional to

$$\begin{aligned} I(E) &= \pi \sum_{u=\pm} |(g|T|a)|^2 \delta(E_a - E) \\ &= \text{Im} \left\{ \sum_{i,j=e,p} T_i(i|G(z)|j)T_j \right\} \\ & \quad z = E + i0^+ \end{aligned} \quad 3.8$$

In this equation T_e and T_p are assumed to be real. The matrix inversion in equation (3.7) can be performed and finally from (3.8) we will get:

$$I(E) = \text{Im} \left\{ \frac{T_e^2(E_0 - z) - 2VT_eT_p + T_p^2(E_e - z)}{(E_0 - z)(E_e - z) - V^2} \right\} \quad 3.9$$

The poles in the denominator of (3.9) at $E = E_{\pm}$ lead to delta function. The spectrum can be written in various ways, one of which is

$$I(E) = \pi(E_+ - E_-)^{-1} [\delta(E - E_+) + \delta(E - E_-)] \\ |E_0 - E| [T_e + T_p(E - E_0)^{-1}V]^2 \quad 3.10$$

The last factor in (3.10) shows that an interference exists between two Raman amplitudes for the $g \rightarrow e$ transition, namely between the direct, first-order, transition with amplitude T_e , and the indirect, second-order, transition $g \rightarrow p \rightarrow e$ with amplitude $T_p(E - E_0)^{-1}V$. This interaction of a sharp (phonon) level p with a (n) (electronic) continuum was considered first by Fano [19] and then by many other authors. We assume for simplicity that each level e in the continuum couples to the ground state with a constant Raman matrix element T_e and to the excited phonon state with a constant matrix element V . Now replace $(E_e - z) \rightarrow 1/g(z)$ in equation (3.9). Where $g(z) = \sum_e (E_e - z)^{-1}$ is the unperturbed Green's function for the electronic continuum. The quantity:

$$q(E) = \pi^{-1} \text{Im}\{g(R + i0^+)\} \quad 3.11$$

is the number of electronic excitations per unit energy interval. Its Hilbert transform is:

$$R(E) = -\text{Re}\{g(R + i0^+)\} = P \sum_e (E - E_e)^{-1} = P \int q(E')(E - e')^{-1} dE \quad 3.12$$

where P stands for "principal value".

After these changes are done in (3.9) one takes the imaginary part and obtains:

$$I(E) = \frac{\pi q(E) T_e^2 (E_0 - E - VT_p/T_e)^2}{[E_0 - E + V^2 R(E)]^2 + \pi^2 V^4 q(E)^2} \quad 3.13$$

The denominator of (3.13) states that the interaction V has produced a width $2\pi V^2 q(E)$ to the phonon excitation, which has been shifted due to the interaction and now has maximum response at $E = E_0 + V^2 R(E)$. The equation (3.13) can be also written in simplest way given by Fano [19]:

$$I(E) = \frac{\pi q(E) T_e^2 (q + \varepsilon)^2}{(1 + \varepsilon^2)} \quad 3.14$$

where

$$\varepsilon = \frac{E - E_0 - \delta\Omega}{\pi V^2 q(E)}$$

$$q = \frac{V \frac{T_p}{T_e} + V^2 R(E)}{\Gamma}$$

$$\Gamma = \pi V^2 q(E) \quad 3.15$$

and

$$\delta\Omega = V^2 R(E)$$

In equation (3.13) and (3.14) the density of the state $q(E)$ has been included, what differs these equations from known form presented in Fano's paper [19]. In our case the quasi continuum wave functions $|e\rangle$ are normalized to unity, what differs from Fano's paper, whereas his are given a delta-function energy normalization [20]. The line shape given in (3.13) is particularly useful when the continuum is broad so that the energy dependence of q and R can be neglected. Then q is a constant, and ε is a scaled energy variable.

Mitani et al. [12] showed that the q parameter was directly related to the electron carrier concentration N_e and can be written with approximation as:

$$q = \left(\frac{1}{\pi \rho(\omega)} \right) \left(\frac{1}{V} \right) \left(\frac{T_p}{T_e} \right) \propto 1/N_e \quad 3.16$$

3.2.1 p-type SiC

In the previous section, to simplify, we considered n-type SiC. Let's now extend the approach to p-type SiC. Cerdiera et al. studied the Fano-effect in detail for p-type Si and various SiC polytypes [20], [21]. They noted that there is scattering present from a continuum and a Fano-type interference between the FTA phonon lines.

The continuum is caused by nearly vertical transitions between occupied light-hole valence band states and unoccupied heavy-hole states [20]. Given a Fermi level about 100 meV below the top of the valence band, appropriate for 10^{20} holes/cm³, and with the large known directional anisotropy in the separation between the two bands, one can explain the existence of a very broad electronic continuum from almost zero energy almost to the Fermi energy [20]. Cerdiera et al. have given a rough derivation of the width parameter Γ and asymmetry parameter q (see equation 3.15), where the matrix element in case of p-type will be expressed as:

$$V = (e|E_{el-ph}|p) \quad 3.17$$

We can write the matrix element in equation (3.17) with approximation as:

$$V = d_0(g|u|p)/a \quad 3.18$$

Where d_0 is the valence band deformation potential, u is the phonon coordinate and a is the lattice constant.

At low temperature we have:

$$|(g|u|p)|^2 = \hbar(2MN\omega_1)^{-1} \quad 3.19$$

where $\hbar\omega_1 = E_0$, M is the reduced mass per unit cell and N is the number of unit cells.

The density of states can be roughly written as:

$$q \sim (N_h - N_l)/\xi \quad 3.20$$

here N_h, N_l are the number of holes in the upper and lower valence bands respectively, ξ is the Fermi energy. Taking into account the equations (3.18), (3.19) and (3.20) the broadening parameter Γ for p-type can be expressed as:

$$\Gamma = \pi V^2 q(E) \sim \pi \frac{d_0^2}{\xi} \left(\frac{\hbar}{2M\omega_1 a^2} \right) \left(\frac{N_h - N_l}{N} \right) \quad 3.21$$

Notice that the Γ parameter for p-type is different than for n-type. Since this parameter is in denominator of q parameter, the value of q for n-type also differs from p-type. Thus for this

same value of carrier concentration the Fano-parameters of n- and p- type samples are different.

3.2.2 Influence of Fano parameters on the line shape of FTA line.

In this work the Fano-interference profiles of the FTA doublet modes was computer-fitted with Fano-formulas, in which each FTA doublet component was assumed to interfere with the electronic continuum independently of the other. Since 4H-SiC has two peaks FTA₊ and FTA₋ the intensity profile for these modes can then be expressed as a sum of two contributions, I₍₋₎ and I₍₊₎. This gives for the Raman intensities of the FTA doublet modes

$$I(E) = I^+(E) + I^-(E) = \frac{(q_+ + \varepsilon_+)^2}{(1 + \varepsilon_+^2)} + \frac{(q_- + \varepsilon_-)^2}{(1 + \varepsilon_-^2)} \quad 3.22$$

In this equation:

are the so-called asymmetry parameters, ε_{\pm} are the dimensionless frequency defined by:

$$\varepsilon_{\pm} = \frac{(\omega - \Omega_{0\pm} - \delta\Omega_{\pm})}{\Gamma_{\pm}}, \quad 3.22a$$

$\Omega_{0\pm}$ are the Raman shift of the phonon frequency without interference and $\delta\Omega_{\pm}$ and Γ_{\pm} are the peak shift and the broadening due to the interference effect, respectively.

All parameters with subscripts (+) and (-) correspond to the Fano-parameters for FTA(+) and FTA(-), respectively, which can be written as:

$$\delta\Omega_{\pm} = V_{\pm}^2 R(E)$$

$$\Gamma_{\pm} = \pi V_{\pm}^2 q(E) \quad 3.22b$$

$$q_{\pm} = (V_{\pm} \frac{T_p}{T_e} + \delta\Omega_{\pm}) / \Gamma_{\pm}$$

As it was mentioned before, because $q(E)$ and $R(E)$ generally depend on electron energy, these can be treated as constants for heavily doped 4H-SiC exhibiting a broad electronic continuum band [11]. In this case, the Fano-parameters $\delta\Omega$, Γ , and q are treated as adjustable parameters.

Let's first study influence of the Fano-parameters on the acoustic modes (FTA lines). To simplify the analyses we consider only one peak. Focus first on the broadening parameter Γ expressed by equation (3.15). The Fig.3. 6 shows the changes of the FTA line for five different values of broadening parameters from $\Gamma=0.1$ to $\Gamma=10$. In this case we took the asymmetry parameter $q = -1$ and Raman shift $\delta\Omega=0$. Increasing Γ the line is getting broader and the maximum of the peak position changes. For the Γ parameters higher than ten the line's shape is so broad that the FTA peak vanishes.

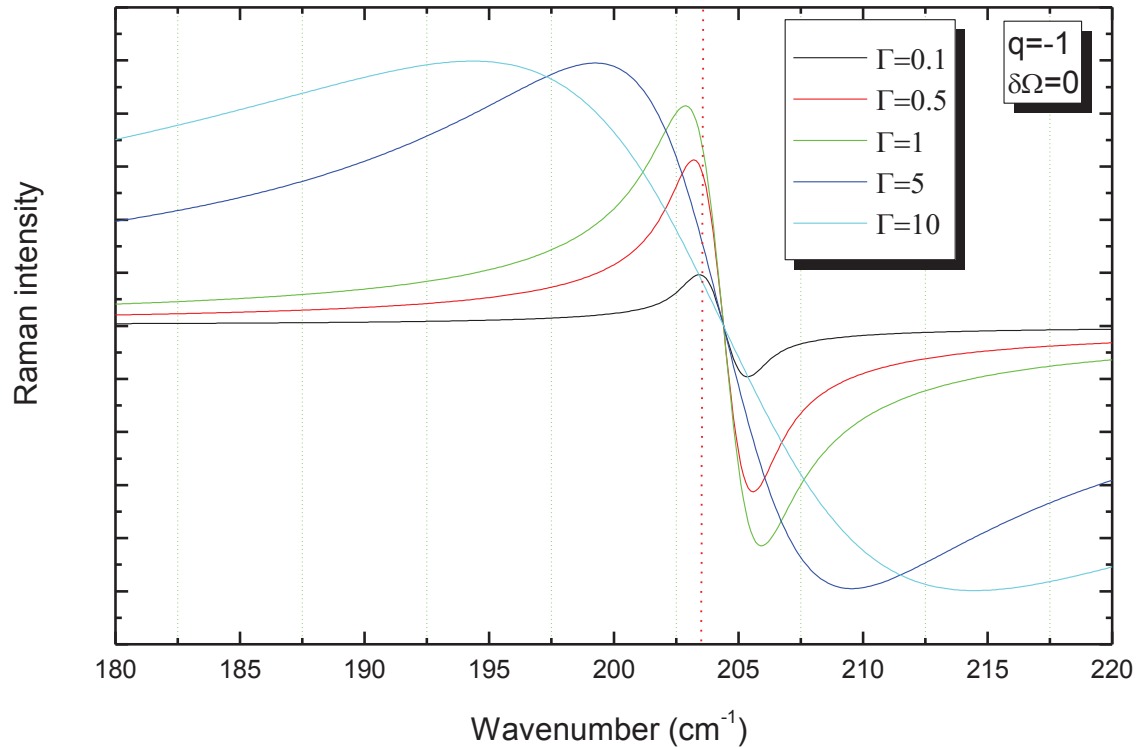


Fig.3. 6: Relative intensity of FTA line vs. wavenumber for different values of the broadening parameters Γ

Next focus on asymmetry parameter q . The Fig.3. 7 presents the changes of FTA line for seven different values of q parameter. To simplify the image we took broadening parameter $\Gamma=0.1$ and shift $\delta\Omega=0$. At first one may notice that q parameter does not influence as much as broadening parameter the position of the peak. Asymmetry parameters vary from -0.2 to -20 . For this the maximum of the FTA line shifts to the higher energy at about 0.9 cm^{-1} , while for broadening parameter changed from 0.1 to 10 we observe the shift to the lower energy of about 8.2 cm^{-1} . In general the asymmetry parameter for both n- and p- type 4H-SiC varies from ~ 1 to ~ 30 . Above 30 what is the case of low doped samples one does not observe Fano-interference in low energy region of Raman spectra.

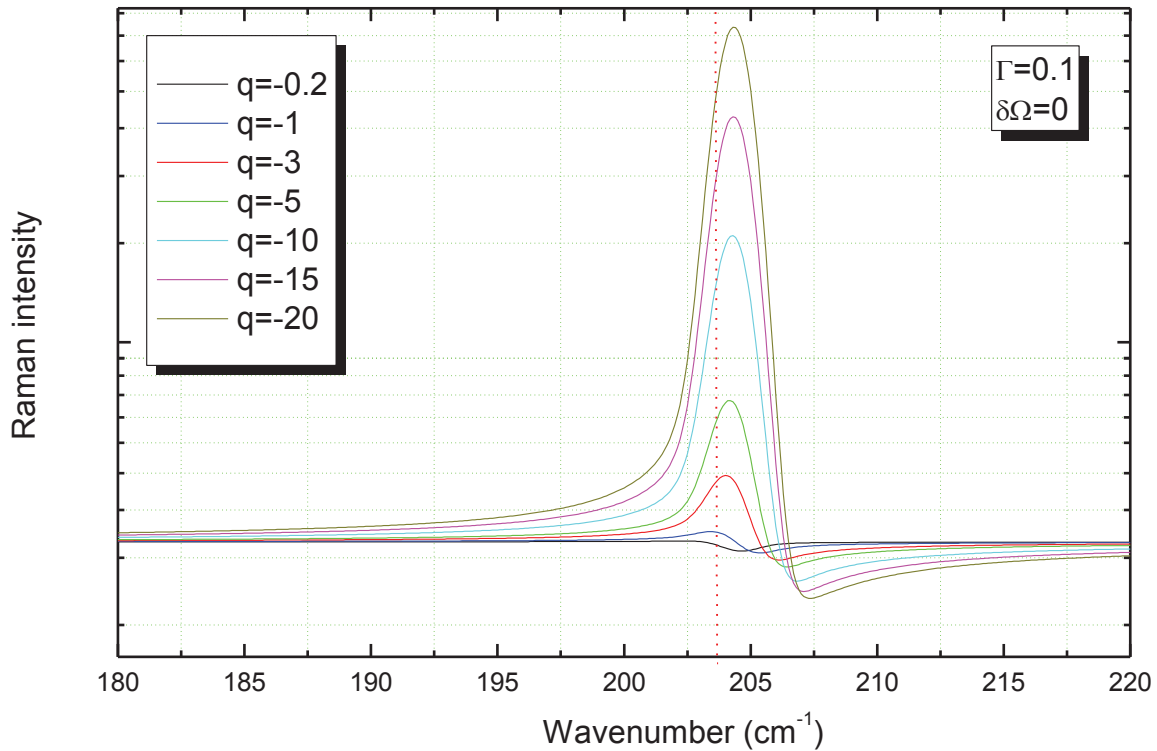


Fig.3. 7: Relative intensity of FTA line vs. wavenumber for seven different values of asymmetry parameters q

Although looking on the Fig.3. 6 and the Fig.3. 7 it seems that the asymmetry parameter has less influence on the FTA line's shape we need to keep in mind that parameter q in his denominator contains parameter Γ , what complicates the issue. We assume Γ to be constant in Fig.3. 7 but in reality it's newer the case. Both parameters are linked and have to be considered together, as is the case of Fano-formula equation (3.22). The changes of one of them drove the necessity of changes of the others what makes the fit process complicated.

3.3 Application of theoretical fit on experimental spectra

Before fitting the experimental data using Fano-function (equation (3.22)) the background from the broad electronic continuum band was subtracted. In this way, we found that the Fano-formula (3.22) reproduced the measured Raman spectra quite well. The example of theoretical fit using the Fano-formula for three samples with different aluminum concentration is shown in Fig.3. 8. In the boxes are done the Fano-parameters used to fit the experimental data. Clear differences related to the different carrier concentration can be seen between the shapes of the FTA lines corresponding to different samples. As a results the Fano-parameters q , Γ , $\delta\Omega$ differ meaningly.

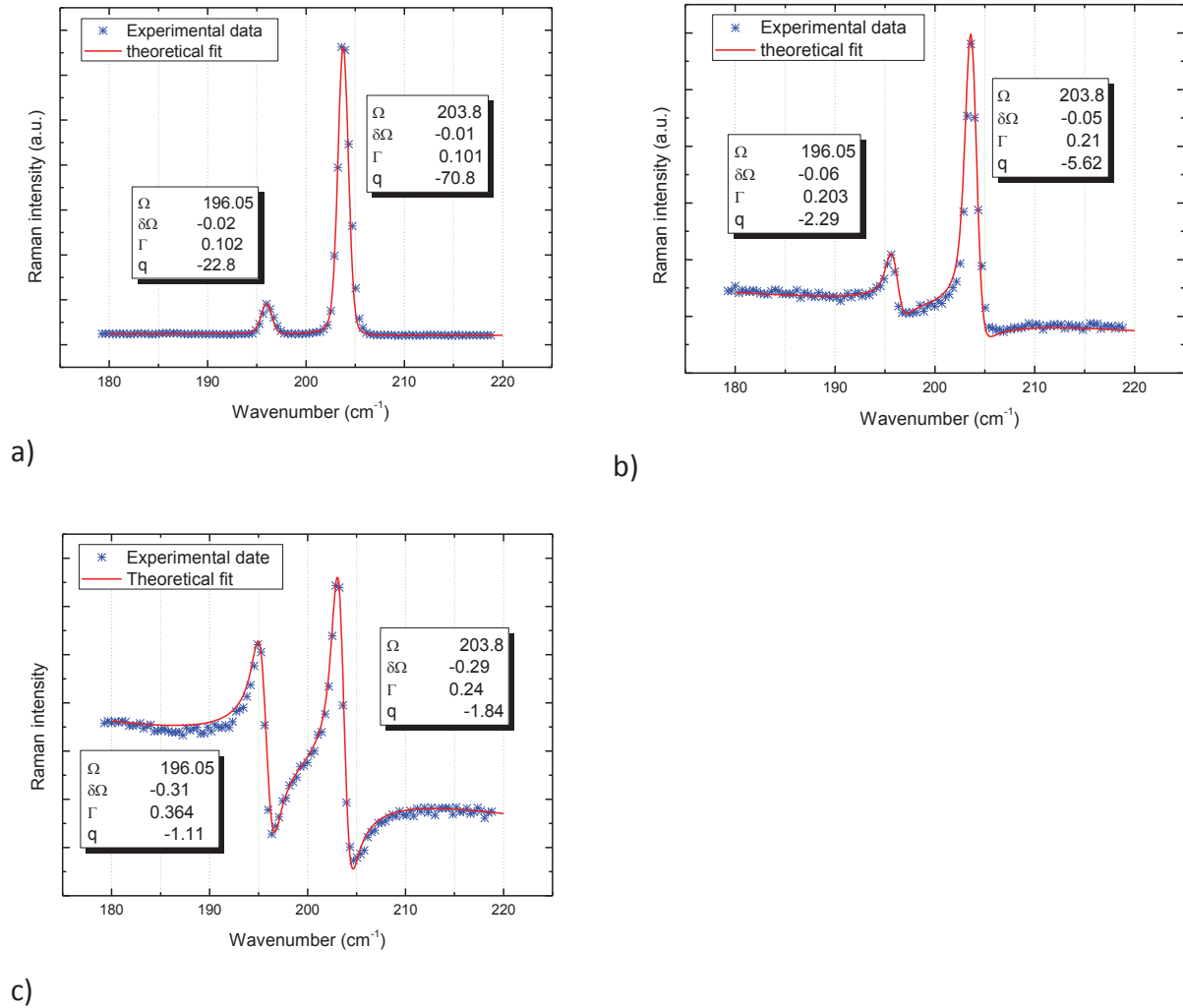


Fig.3. 8: Example of theoretical fit using Fano-formula for three differently p-doped samples with AlSiMS concentration: a) 10^{17} cm^{-3} , b) $5 \times 10^{18} \text{ cm}^{-3}$, c) $8.4 \times 10^{19} \text{ cm}^{-3}$.

3.4 Conclusion

The influence of carrier concentration on the LOPC mode of Raman spectra for both n- and p-type were studied. We showed the difference related to the type of carrier and showed that in case of low doped n-type 4H-SiC LOPC mode can be used to determine carrier concentration. Since for high doped n-type and p-type sample LOPC mode can not be used to evaluate carrier concentration we focused on low energy part of Raman spectra. We showed first the theoretical model explaining the Fano-interference effect observed by Raman scattering measurements, for n and then for p-type carrier. Finally a study of the Fano parameters to apply this fitting model was discussed to evaluate carrier concentration was presented.

In the next section we will use the Raman spectra and Fano-function to evaluate the doping level for p- and n-type 4H-SiC.

Bibliography

- [1] H. Kon, B. Jiang, J. Glass, G. Rozgonyi, K. More, J. Appl. Phys. (USA), vol. 63, p. 2645, 1988.
- [2] Y. Azhnyuk, V. Artamonov, M. Valakh, A. Litvinchuk, Phys. Status Solidi B (Germany), vol. 135, p. 75-84, 1986.
- [3] M. Klein, B. Ganguly, P. Colwell, Phys. Rev. B (USA), vol. 6, p. 2380-2388, 1972.
- [4] W. Faust, C. Henry, Phys. Rev. Lett. (USA), vol. 17, p. 1265, 1966.
- [5] H. Yugami et al., J. Appl. Phys. (USA), vol. 61, p. 354-358, 1987.
- [6] P. Colwell, M. Klein, Phys. Rev. B (USA), vol. 6, p. 498-515, 1972.
- [7] R. Nemanich, Mater. Res. Soc. Symp. Proc. (USA), vol. 69, p. 23-37, 1986.
- [8] G. Burns, F. Dacol, C. Wie, E. Burstein, M. Cardona, Solid State Commun, vol. 62, p. 449-454, 1987.
- [9] M. V. Klein, Light Scattering in Solids, edited by M. Cardona, (Berlin), 1975.
- [10] P. J. Colwell, M. V. Klein, Phys. Rev, vol. 6, p. 498, 1972.
- [11] H. Harima, T. Hosoda, S. Nakashima, Mater. Sci. Forum, vol. 449, pp. 264-268, 1998.
- [12] T. Mitani, S. Nakashima, K. Kojima, T. Kato, J. Appl. Phys, p. 112, 2012.
- [13] C. Henry, J. Hopfield, L. Luther, Phys. Rev. Letters, vol. 17, p. 1178, 1966.
- [14] B. B. Varga, Phys. Bev., vol. 135, p. A1896, 1965.
- [15] P. Chafai, et al., J. Appl. Phys., vol. 90, p. 5211, 2001.
- [16] T. Hon, W. L. Faust, J. Appl. Phys., vol. 1, p. 241, 1973.
- [17] H. Harima, S. Nakashima, T. Uemura, J. Appl. Phys., 78 1995, p. 78, 1995.
- [18] H. Harima, T. Hosoda, S. Nakashima, Mater. Science Forum, vol. 607, p. 338-342, 2000.
- [19] U. Fano, Phys; Rev, vol. 124, p. 1866-1878, 1961.
- [20] F. Cerdiera, T. Fjeldly, M. Cardona, Phys. Rev. B, vol. 8, p. 4734, 1973.
- [21] F. Cerdiera, T. Fjeldly, M. Cardona, Sol. State Commun, vol. 325, p. 13, 1973.

Chapter 4: Investigation of nitrogen doped 4H-SiC epilayers grown by Chemical Vapor deposition.

Introduction

As mentioned previously, the control of the doping concentration is important and permits to fabricate low or high resistivity SiC layers. Nitrogen is well known to be the n-type dopant in SiC. It becomes possible to control wide range doping concentration in SiC crystal by clarifying the mechanism of nitrogen incorporation. In SiC, nitrogen dopant substitutes on the C site and forms a shallow donor level as speculated on the basis of first-principles calculations [1]. Most desirable is possibility of verifying several aspects in non-destructive and the easiest possible way. Since the verification of doping level by electrical measurements requires in several cases special preparation of the samples the possible ways to overcome this problem can be optical and vibrational investigation.

In this chapter we are going to study the carrier and/or nitrogen concentration in n-type 4H-SiC layers by using different methods: vibrational and optical like Raman and Photoluminescence spectroscopy as well as structural such as SIMS.

The objective of this chapter is to compare the nitrogen concentration values obtained using different methods to check the validity of them. We will also verify for each of the applied methods the valid domain of doping ranges where it can be used in order to determine the nitrogen concentration.

All investigated samples were made by CVD method by Marcin Zielinski and Roxana Arvinte in NOVASiC in the framework of NetFiSiC project.

4.1 Samples description

A series of n-type 4H-SiC layers were grown on n-type heavily doped 4H-SiC 4° off (0001) substrates. The Chemical Vapor Deposition (CVD) of the epilayers was performed in a horizontal, hot wall, resistively heated, using hydrogen as a carrier gas and silane/propane as Si/C precursors respectively. Detailed information about the CVD technics are given in chapter 1. Growth temperature was fixed at 1780°C and the growth pressure was between 100-400 mbar. The detailed information about samples and growth parameters are given in Tab.4. 1:

Samples	N ₂	Pressure (mbar)	Face	C/Si ratio	C-V (cm ⁻³)	Growth time (min)	Thickness (μm) SIMS
13-006	1.0	250	Si	1.5	10 ¹⁶	~150	16 (FTIR)
13-007	16	150	Si	1.5	8×10 ¹⁶	~150	12.8 (FTIR)
13-008	200	100	Si	1.5	~10 ¹⁸	~150	11.6
13-010	1000	250	Si	1.5	~10 ¹⁹	~150	15.8
13-011	1000	400	Si	1	~10 ²⁰	~150	14.7

Tab.4. 1: Samples descriptions, thickness was determined by SIMS for samples 13-008,-010,-011 and by FTIR for samples 13-006&7.

All samples were grown on the Si-face 4H-SiC substrate. The ratio carbon to silicon is 1.5, except for the samples with the highest expected nitrogen concentration where the C/SiC ratio is 1. All the substrates used for the growth were n-type. They were measured by C-V and the doping level was found to be close to 10¹⁹ cm⁻³ and as the rotating susceptor was used, we will expect, that the grown layers are homogeneous. When it was possible, i.e. when the substrate and the layer have substantially different levels of carrier concentration, the growers have measured the thicknesses of the epilayer by Fourier transform infrared spectroscopy (FTIR) measurements, from the period of the interference fringes. Otherwise (samples 13-008 13-010, 13-011) the thicknesses of the layers could not be estimated only from the difference in weight of the samples.

The very first issue was to check whether the grown layers contain different nitrogen concentration as it was expected according to the applied growth parameters using SIMS (Secondary Ion Mass Spectroscopy) measurements. Each of the samples was measured on one specific position (one per sample). For each measurement with checking the nitrogen concentration the aluminum concentration and the thickness were also verified. Detailed description and experimentally conditions about this method is given in chapter 2. The dopant concentrations and the average thickness of the epitaxial layer found by SIMS for the samples studied in this section are summarized in Tab.4. 2

Samples	SIMS concentration (cm ⁻³)		Top layer depth (μm)
	[¹⁴ N ⁺]	[²⁷ Al ⁺]	
13-006	<6×10 ¹⁶ (DL)	≤3×10 ¹³ (DL)	
13-007	~8×10 ¹⁶ (DL)	≤3×10 ¹³ (DL)	
13-008	9.5×10 ¹⁷	≤3×10 ¹³ (DL)	11.6
13-010	8.6×10 ¹⁸	≤3×10 ¹³ (DL)	15.8
13-011	3.8×10 ¹⁹	≤3×10 ¹³ (DL)	14.7

Tab.4. 2 : Values of nitrogen and aluminum concentrations along with thickness determined by SIMS measurements.

However, the main drawback is the relatively high value of the detection limit of the nitrogen found by this technique (few 10¹⁶ cm⁻³), combined with the fact that the samples are damaged during the experiment. This is the main limitation of the SIMS technique in

terms of determination of nitrogen concentration in SiC materials. In order to overcome this problem the possible means of investigation are nondestructive measurements such like Photoluminescence and Raman.

4.2 Nitrogen doping in 4H-SiC

In this work, this doping species was intentionally introduced into the epitaxial layer of all the investigated samples, each time with a different N_2 value. We will see how the nitrogen content influences the PL or Raman spectrum and finally determine, using calibration curves, the value of nitrogen doping in the epilayers using two different ways: first LTPL and then Raman spectroscopies.

4.2.1 Evaluation of nitrogen content by LTPL

The basic information about PL technique and the description of experimental setup is presented in Chapter 2.

Camassel et al. showed that the LTPL measurement is a very good way to determine the concentration of impurities as nitrogen and aluminum for different polytype of SiC [2]. We have used this technique on all our 4H-SiC samples intentionally doped with nitrogen. Full range LTPL spectra (350-700nm) collected at 4K in the middle of each sample are showed in Fig.4. 1. In this present study the main interesting part of the spectra being the Near Band Edge (NBE) one, a zoom on this spectral range is presented in Fig.4. 2.

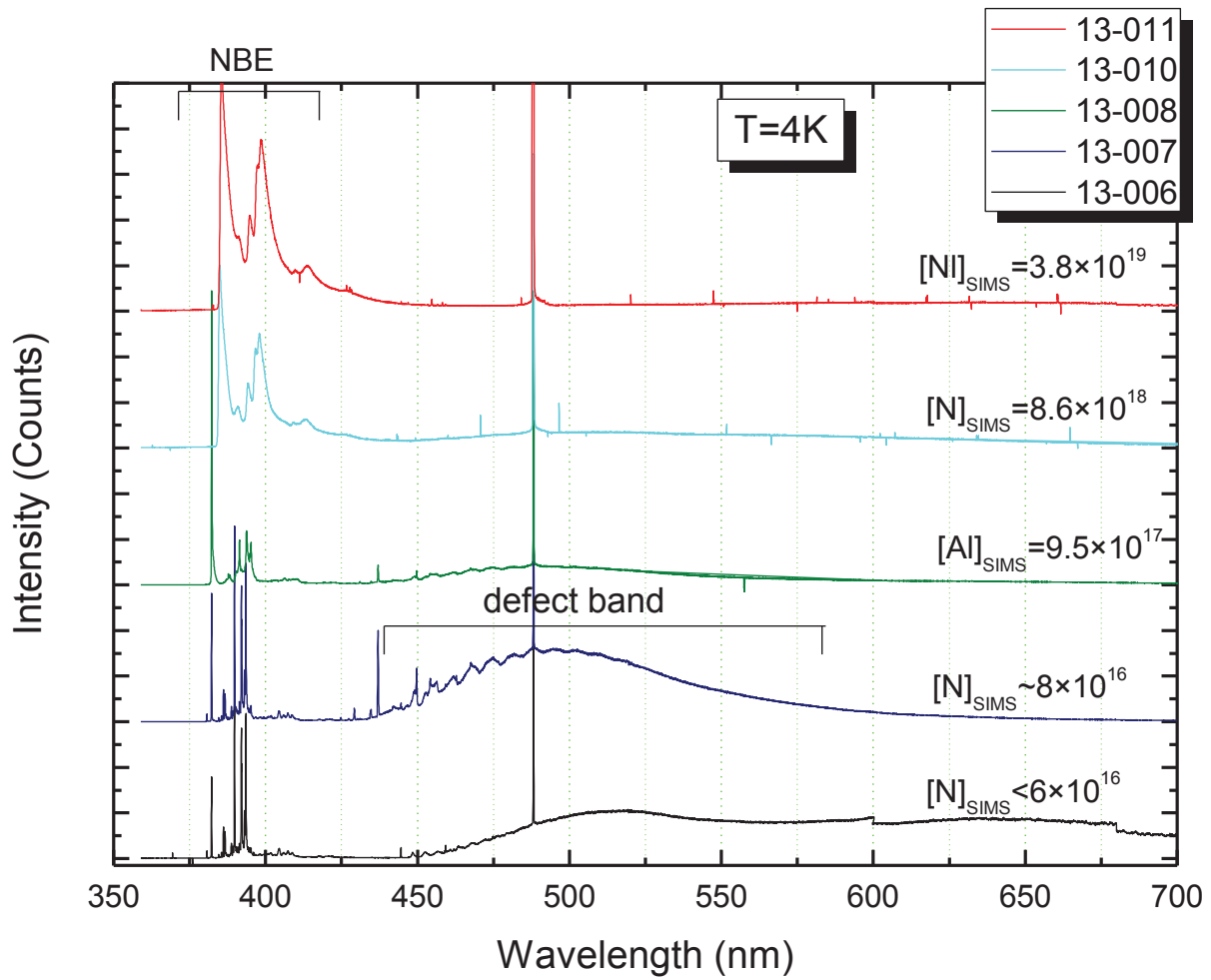


Fig.4. 1: Full range LTPL spectra (350-700nm) collected at 4K in the middle of each samples of the investigated series.

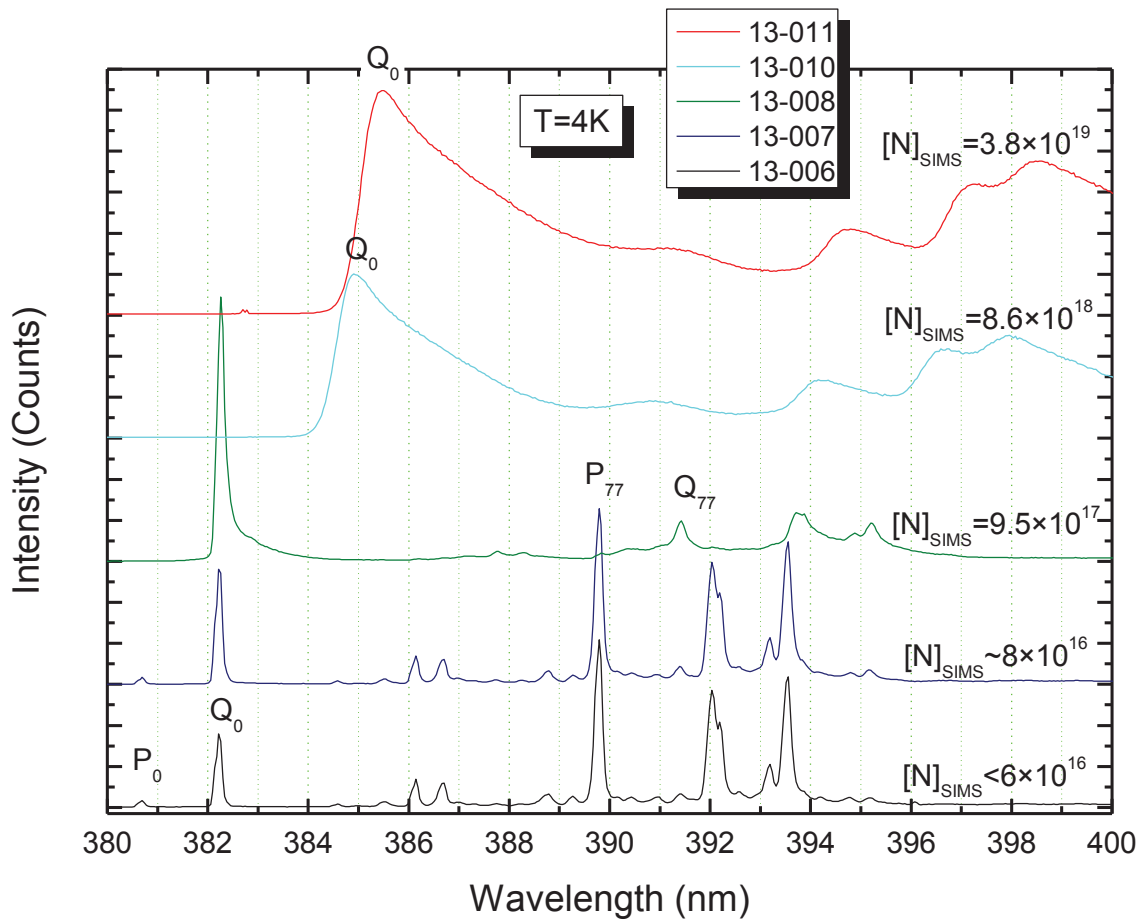


Fig.4. 2: NBE range of the LTPL spectra taken in the middle of each samples with marked characteristic phonon positions.

Fig.4. 2 shows the NBE range spectra of all investigated samples taken in the middle of each of them. We can notice P_0 and Q_0 lines as well as their phonon replicas. Remember that P_0 and Q_0 are the zero phonon line of the nitrogen bound exciton, if the nitrogen is respectively in hexagonal and cubic site.

Looking closer one of the spectra in Fig.4. 2 one may notice that the line Q_0 is much stronger than the line P_0 . However, in general the spectrum is dominated by the phonon replicas from the P related center and the total area under P_0 and its phonon replicas is several times greater than the area under Q_0 . In 4H-SiC, the exciton binding energy of P_0 is smaller than that of Q_0 . That means the exciton bound to nitrogen at the Q_0 position is more localized. Therefore, the wave functions of the electron and hole can have bigger overlap in k space. The direct no phonon transition is favored for this site. So we see a strong no phonon line Q_0 . Again, the exciton binding energy of P_0 is smaller than that of Q_0 , therefore the electron wave function radius is bigger for P_0 position. A bigger radius results in a bigger capture cross section. So overall the spectrum is dominated by the phonon replicas of the P line, although P_0 itself is smaller compared to Q_0 . As the nitrogen doping increases the P_0 line and its

phonon replica relatively to the Q_0 decrease in intensity and disappear at doping higher than $8 \times 10^{17} \text{ cm}^{-3}$. For donor concentrations above 10^{17} cm^{-3} , the interaction between donors becomes important due to the short distance between them. A relaxation of the excitons from the P site to the deeper Q donor could explain the decrease in intensity of the P-line relatively to the Q line. In addition to the decrease in intensity of the P lines, a new feature appears on the LTPL spectra as a broad background of the Q_0 line accompanied with its phonon replicas see Fig.4. 2. This gives rise to a non-symmetric shape of the Q_0 and its shift to lower energy [3], [4].

Remark: It is worth to clarify here that the substrate can be visible on the NBE of luminescence spectrum for the epitaxial layer with high quality and low doped when using 244nm line as excitation [5]. Nonetheless the spectra shown in Fig.4. 2 illustrate that even in case of low doped samples no broad band related to high doped substrate is visible in NBE range. The penetration depth of the exciton line of 244nm is about few microns [6] and decreases with increasing doping level, thus for the high doped samples, exciton diffusion to the substrate is not expected to occur.

4.2.2 Experimental results and discussion

According to the calibration curves from ref. [2], [4], showing in Fig.4. 3 we investigate the samples to evaluate nitrogen doping. Three different calibration curves corresponding to three different nitrogen concentration ranges were used.

Let's start first by the low doped samples where the P_{77} line is strong in intensity and one does not observe a significant shift of Q_0 peak. For these samples (13-006 & 13-007) since the nitrogen concentration, checked by SIMS, in the epilayer is low, the intrinsic transition should be notable (the line I_{77} should be visible). Despite the fact that these two samples are low doped we do not observe clear signature of I_{77} line. The reason of that could be to low resolution of LTPL measurements or possibly some non-radiative defects. Since there is no I_{77} line the quantification of nitrogen doping for samples 13-006 is not possible. We conclude that the nitrogen concentration is lower than 10^{16} cm^{-3} for sample 13-006.

For medium doped samples the ratio of area Q_0/P_{77} is used (see in Fig.4. 3 b). To find the value of the ratio of the Q_0 line divided by the P_{77} line for nitrogen concentration in range 10^{16} up to 10^{18} cm^{-3} , these two lines were fitted by Gaussian function. An example of the theoretical fit for the sample 13-007 is presented in Fig.4. 4.

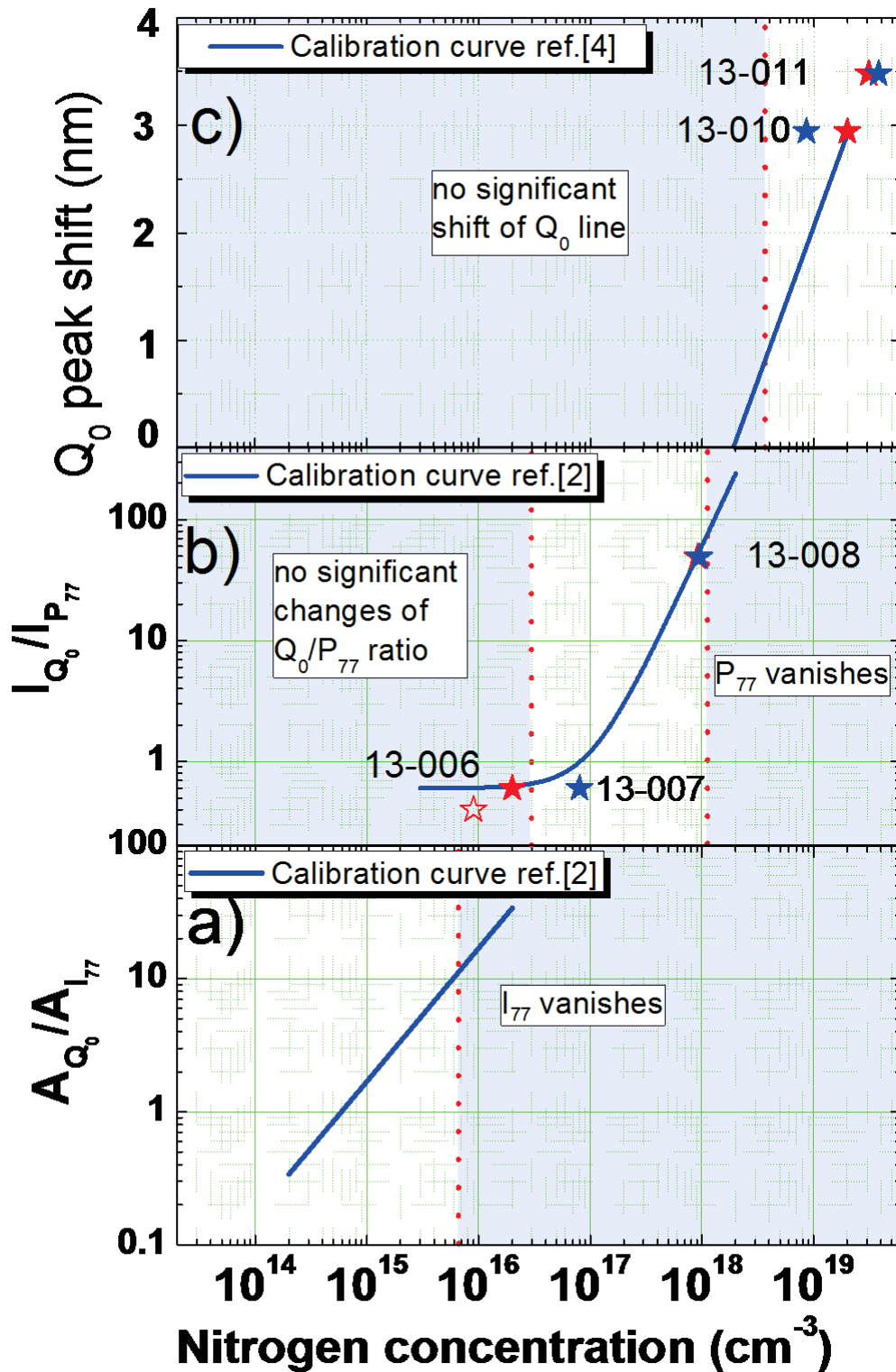


Fig.4. 3: Calibration curves of nitrogen concentration for three different doping ranges for 4H-SiC [2], [4]. Red stars are the calculated parameters for investigated samples, blue correspond to nitrogen evaluated by SIMS (here A_x stands for area, I_x for intensity).

Finally for the concentration value higher than 10^{18} cm^{-3} where the phonon replicas P_{77} is no longer notable (samples 13-010&13-011 Fig.4. 2) the only way to determine the nitrogen concentration is to use the energetic position of the Q_0 line and the calibration curve presented on the top of Fig.4. 3. All the results are plotted on Figure 4.4 as red stars.

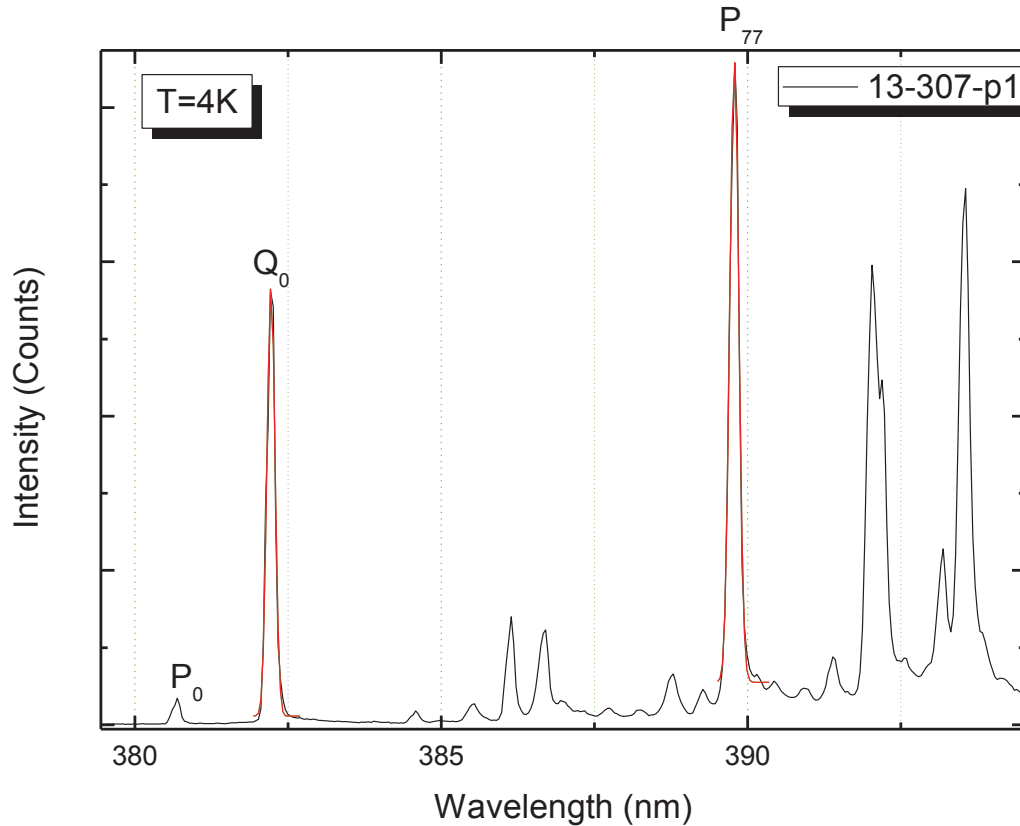


Fig.4. 4: Example of theoretical fit of the lines Q_0 , and P_0 for the sample 13-007. To fit the experimental data the Gaussian function was used.

The limitation of the method appears at the interface of the three calibration curves marked by red dotted line on the Fig.4. 3. In this part the evaluation on the nitrogen concentration could be difficult.

Focus first on figure 4.3 a). According to Henry et al. [4] the free exciton lines (related to intrinsic property of the material) are only visible when the nitrogen doping is below $2 \times 10^{16} \text{ cm}^{-3}$. For low doped samples where one uses the ratio of area of Q_0/I_{77} lines, the difficulties appear for concentration range higher than about 10^{16} cm^{-3} . The intrinsic transition weakens and as a result the line I_{77} is lower in intensity or vanishes. In this same time the interaction between donors becomes important due to the short distance between them. A relaxation of the excitons from the P site to the deeper Q donor explains the decrease in intensity of the P-line relatively to the Q line. But for the concentration range $\sim 10^{16}$ to about 10^{17} cm^{-3} no significant changes in term of intensity of the P_{77} line are notable yet Fig. 4.3 b). The only

way to evaluate the nitrogen contain in this case is to use the ratio Q_0/I_{77} . But as it was mentioned before, in this concentration range I_{77} line is very weak or vanishes and the theoretical fit could be imprecise or impossible. Since the I_{77} line is no clearly visible for doping range about 10^{16} cm^{-3} and the SIMS is not appropriate technique for determination nitrogen for low doped samples (lower than few 10^{16} cm^{-3}) the quantification of nitrogen doping in this range is very difficult or impossible at this time. Thus for sample 13-006 neither SIMS nor LTPL allow us to quantify the nitrogen doping. One of possible way to evaluate the doping level for low doped layers rests C-V measurement.

For the medium concentration (see figure 4.3 b). One may suppose that, for example using the ratio Q_0/P_{77} and calibration curve which ends at $2 \times 10^{18} \text{ cm}^{-3}$ on may determine the nitrogen doping up to this value, but in reality the evaluation of nitrogen doping higher that about 10^{18} cm^{-3} is very difficult or impossible because P_{77} line is hardly notable.

Since there are a lot of factors like quality of crystal, non-radiative defects or low resolution of PL setup, the limitation of LTPL measurements in terms of evaluation of the doping level varies for measured samples. The calibration curves therefore show the maximum possible value that can be determined using the LTPL spectrum. The shaded areas correspond to the ranges where, despite the fact the calibration curves exist, the evaluation of nitrogen doping is very difficult or in some cases impossible.

4.2.3 LTPL investigation-summary

For all investigated samples specific parameters were found, for low, middle and high doping level, using three different calibration curves. One can successfully determine the nitrogen concentration in a very large scale from $\sim 10^{16}$ up to $\sim 10^{19} \text{ cm}^{-3}$. Tab.4. 3 summarizes the values of nitrogen concentration for different samples. The targeted value of nitrogen and the nitrogen concentration values evaluated by SIMS are also mentioned to compare.

SAMPLE	TARGETED CONCENTRATION (CM^{-3})	NITROGEN CONCENTRATION ACCORDING TO SIMS (CM^{-3})	NITROGEN CONCENTRATION DUE TO LTPL (CM^{-3})
13-006	10^{16}	$<6 \times 10^{16}(\text{DL})$	$<10^{16}$
13-007	10^{17}	$\sim 8 \times 10^{16}(\text{DL})$	2×10^{16}
13-008	10^{18}	9.5×10^{17}	9.2×10^{17}
13-010	10^{19}	8.6×10^{18}	2×10^{19}
13-011	$\geq 5 \times 10^{19}$	3.8×10^{19}	$> 2 \times 10^{19}$

Tab.4. 3: Nitrogen concentration's values evaluated by LTPL and SIMS along with targeted during growth process values

The evaluated, using LTPL measurements, values of nitrogen concentration is for all samples lower than the targeted and also lower than the nitrogen contain evaluated by SIMS, except for sample 13-008. For this sample LTPL and SIMS give very similar values. The results are plotted in Fig.4. 5. For low doped samples with concentration up to few 10^{16} cm^{-3} better and more accurate method to evaluate nitrogen content seems to be LTPL since SIMS has its limitation related to detection limit. For the medium and high doped epilayers both method SIMS and LTPL give similar values. Also, the SIMS measurements show that the value of nitrogen is slightly lower than targeted.

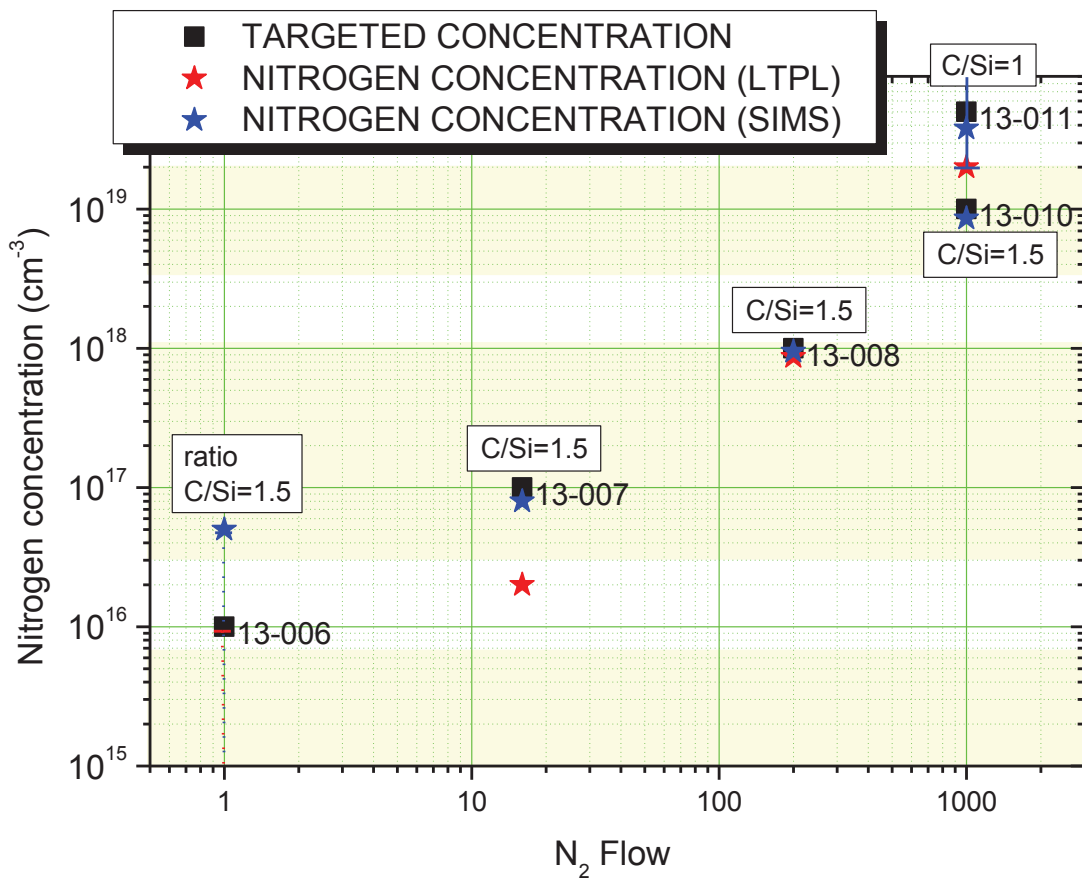


Fig.4. 5: Targeted and evaluated by SIMS and PL nitrogen concentration as a function of nitrogen flow. Yellow areas show the regions of the best validity of calibration curves.

For low doped samples, lower than few 10^{16} cm^{-3} the SIMS measurements, because of the detection limit of $\sim 6 \times 10^{16}$ cm^{-3} do not provide accurate enough results one may state that the only way to determine the nitrogen concentration value is evaluation by LTPL. Nonetheless as we could see in case of investigated samples neither LTPL allows us to evaluate value of nitrogen doping for doping range about 10^{16} cm^{-3} . Considering the highest

doped samples one may notice that the calibration curve given by Camassel et al. and Henry et al. [2], [4] finishes on value $2 \times 10^{19} \text{ cm}^{-3}$. Our evaluation of nitrogen for high doped samples could be made by prolongation of this curve. The targeted concentration, SIMS and LTPL values are in quite good agreement.

To confirm the results obtained due to LTPL measurements and obtain by a non-destructive result for high doping level we will investigate the n-type doping using Raman spectroscopy.

4.3 Evaluation of free carrier concentration By Raman

In this work for all scans the Raman spectra were collected using the experimental setup and experimental conditions described in Chapter 2.

Fig.4. 6 presents the full range spectra ($100\text{-}1100 \text{ cm}^{-1}$) collected at the center of all the investigated samples. We can notice both acoustic and optical phonon branches and the lines corresponding to different phonon and their folded modes.

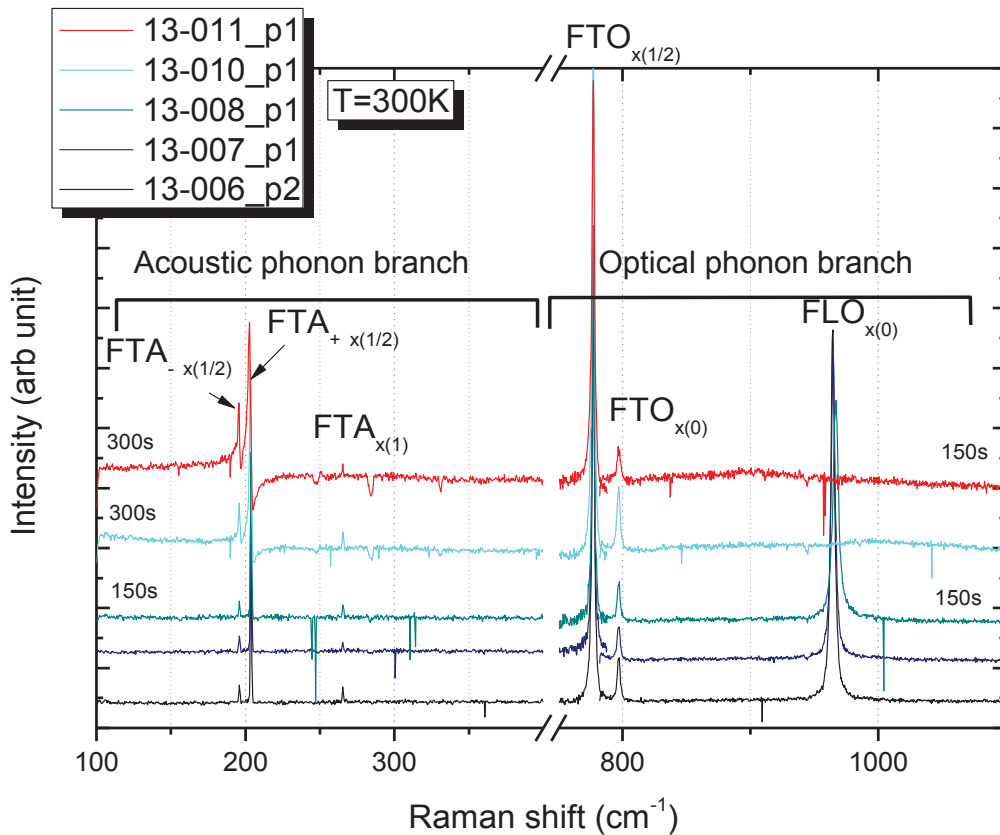


Fig.4. 6: Full range Raman spectra collected at room temperature in the middle of the investigated samples with marked phonon position.

To find out about the carrier concentration using micro-Raman spectroscopy one may use both low energy (acoustic) and high energy (optic) part of the Raman spectra (see Fig.4. 6). First, we focus on the optical modes at high energy.

4.3.1 LOPC modes

Fig.4. 7 presents the folded longitudinal optic ($FLO_{x(0)}$) mode for all investigated samples. As it has been already shown due to SIMS and LTPL measurements the sample 13-006 is the lowest doped and the sample 13-011 the highest doped with nitrogen. Fig.4. 7 presents therefore the spectra corresponding to the samples from the lowest doped in the bottom to the highest doped in the top, according to the SIMS measurements. In this way we can clearly see the changes of the FLO line related to the increase of carrier concentration.

Since 4H-SiC are uniaxial crystals, LOPC has anisotropy between the mode with the atomic displacement parallel to the c-axis (axial mode) and that with the atomic displacement perpendicular to the c-axis (planar mode). The peak intensity, FWHM and frequency position will though change with changing the carrier density [7]. The change in LOPC mode have been discussed in detail in chapter 3.

Let's first focus on the shift of the $FLO_{x(0)}$. A clear shift to the higher energy is observed for sample 13-008 (see Fig.4. 7). The relative frequency shift of LOPC is plotted in Fig.4. 8 (bottom), where solid line is the calibration curve taken from [7]. In this way, we were able to estimate a carrier concentration value of $3.3 \times 10^{17} \text{ cm}^{-3}$ for sample 13-008. The peak shift is measured from the peak positions observed in the undoped reference sample. The relative shift calculated for sample 13-006, 13-007 and 13-008 are 0.06 cm^{-1} (DL), 0.12 cm^{-1} and 2.12 cm^{-1} , respectively. The results are plotted as red stars on the Fig.4. 8. For sample 13-006&007 because no significant changes of the position are observed we deduced carrier concentration to be lower than $\sim 3 \times 10^{16} \text{ cm}^{-3}$. In the other hand for the samples 13-010 & 13-011 the FLO line is not clearly visible. Generally, this method is used to determine carrier concentration in a range of few 10^{17} cm^{-3} to few 10^{18} cm^{-3} .

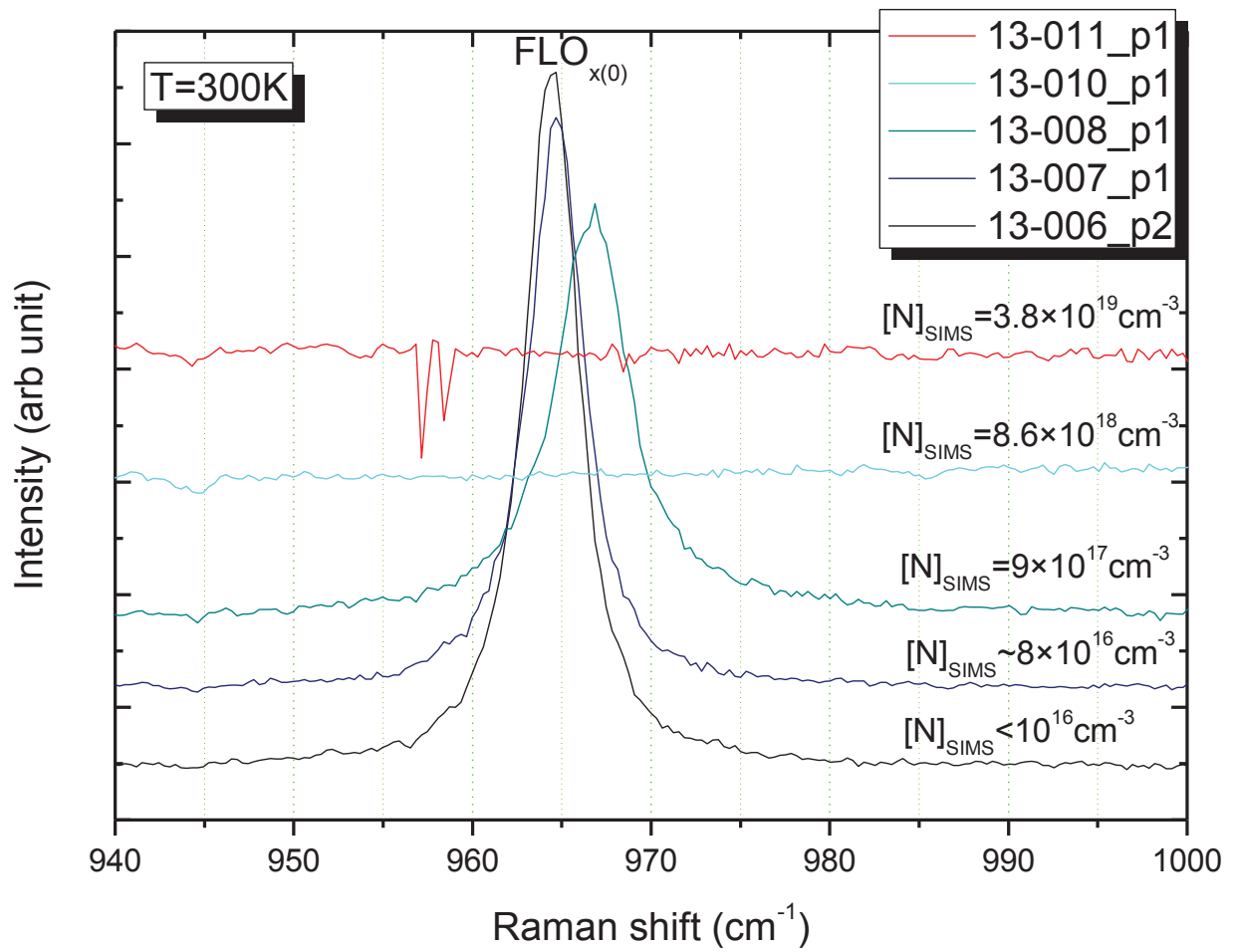


Fig.4. 7: LOPC profile for n-type 4H-SiC for all samples investigated in this work.

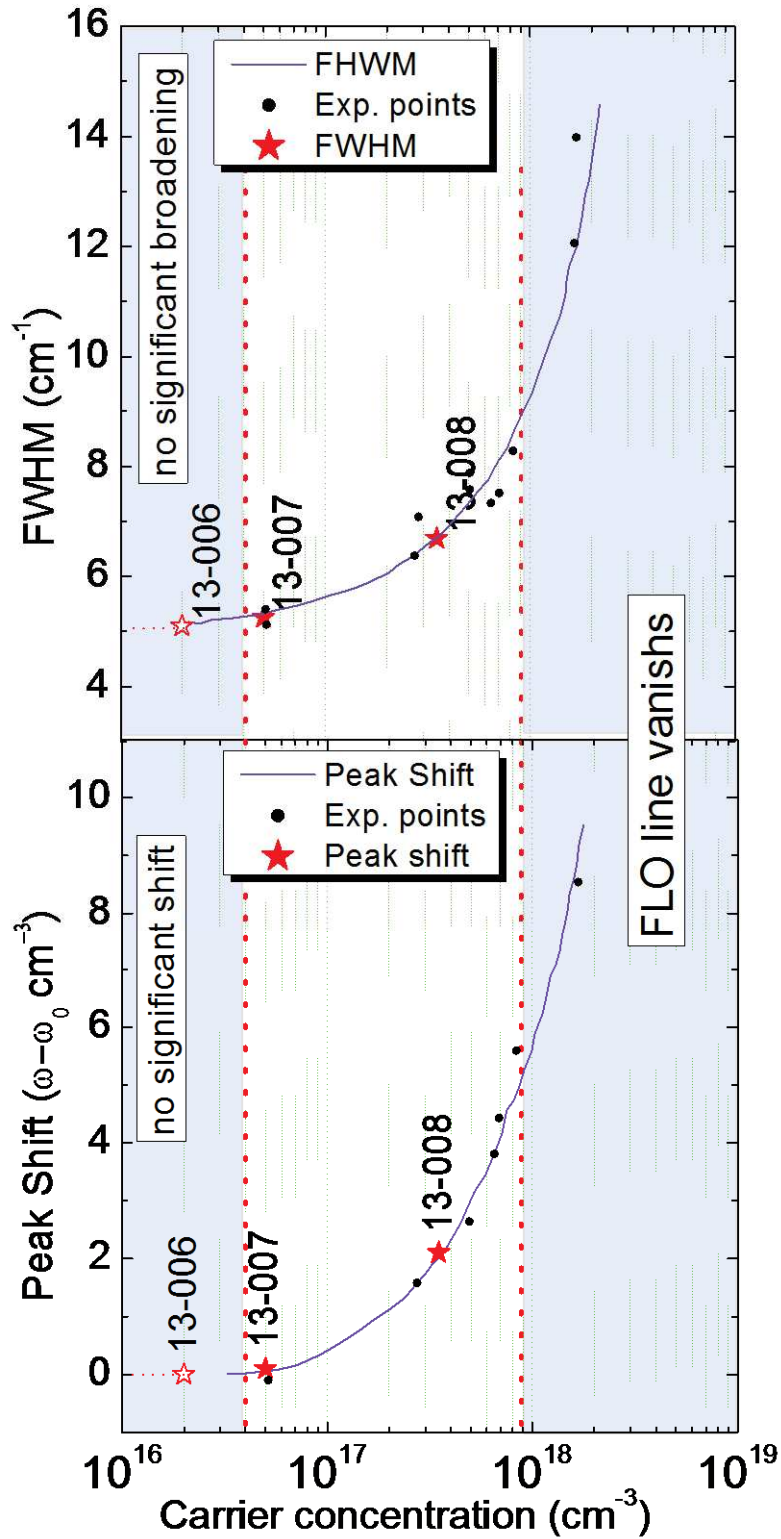


Fig.4. 8 : FWHM and relative Raman shift of LOPC mode (solid lines are the calibration curves and dots are the experimental points from [7]), red dotted lines show the limits of usability of the calibration curves.

We propose to determine carrier concentration using the FWHM (Full Width at Half Maximum). To evaluate the carrier concentration, each spectrum was fitted by Gaussian function and then the FWHM values were found for samples 13-006, 13-007 & 13-008. Example of theoretical fit for sample 13-007 is shown in Fig.4. 9 in the boxes are presented the values obtained due to theoretical fit.

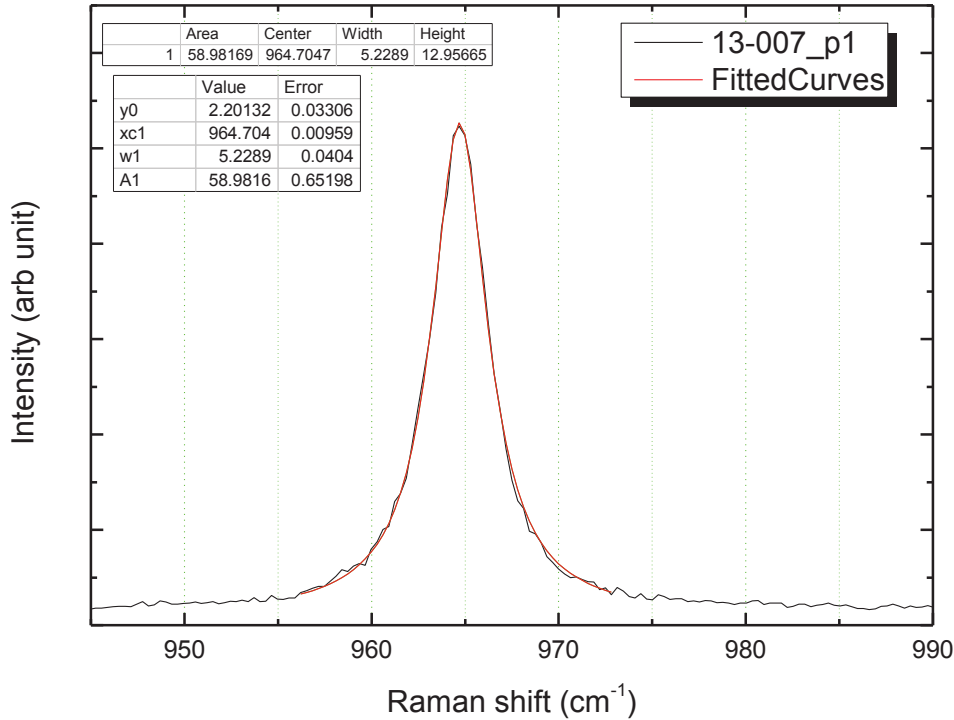


Fig.4. 9: Example of theoretical fit using Gaussian function. In the boxes the parameters of fit are shown.

The FWHM evaluated for samples 13-007 and 13-008 are 5.23 cm^{-1} and 6.41 cm^{-1} , respectively, while the lowest doped sample 13-006 has a FWHM in value of 5.09 cm^{-1} . One may see that by this way the evaluation of the carrier concentration for low doped samples is difficult. In addition the calibration curve of FWHM starts at about $2.5 \times 10^{16} \text{ cm}^{-3}$. So regarding the evaluation of the carrier concentration for sample 13-006 the only thing we can state is that the carrier concentration is lower than $2.5 \times 10^{16} \text{ cm}^{-3}$. For samples 13-010 and 13-011 with the highest carrier concentration, again, because of the contribution of the excitations out of the Brillouin zone center and the non-parabolicity of the bands we do not see clearly the FLO line and we could not estimate any FWHM.

Using the calibration curve from [7], (see Fig.4. 8 top) one can deduce the carrier concentration from the FWHM parameter of the FLO peaks. According to the FWHM of the FLO peaks, the carrier concentration is found to be lower than $2.5 \times 10^{16} \text{ cm}^{-3}$ for samples 13-006, $\sim 5 \times 10^{16} \text{ cm}^{-3}$ for 13-007 and about $3.5 \times 10^{17} \text{ cm}^{-3}$ for the sample 13-008.

This method allows determining the carrier concentration for samples with carrier concentration in range few 10^{16} cm^{-3} up to $\sim 10^{18} \text{ cm}^{-3}$. For concentration lower than 10^{16} cm^{-3} no significant changes of FTO line are notable. In the other hand for carrier concentration higher than 10^{18} cm^{-3} a drastically decreasing in the intensity and vanishing of the LOPC mode is observe. The evaluation of carrier density using LOPC in not possible for high doped samples and the only way is to use the FTA modes.

Remark: For thin and low doped samples a contribution from the substrate as an additional line or broadening of the FLO line can perturb the shape of the $\text{FLO}_{\times(0)}$ peak, when manifests. Thus when using the FLO line as an indicator of the carrier concentration, one has to be sure that the FLO line is not distorted.

In order to find the high carrier concentration (samples 13-010&11), an analysis of the acoustic mode is necessary.

4.3.2 FTA modes

Let's focus now on the acoustic part of the Raman spectra ($100 - \sim 600 \text{ cm}^{-1}$). For the high doped samples, a change of the FTA line ($\sim 200 \text{ cm}^{-1}$) is clearly visible and assigned in literature as Fano-interference effect. Fano-interference have been observed between the zone-folded transverse acoustic (FTA) phonon modes and the electronic continuum in n- and p-type SiC [7], [8], [9] This effect is clearly observed for carrier concentrations higher than 10^{19} cm^{-3} and, thus, can be used as a more suitable measurement of the free electron concentration in heavily doped n-type 4H-SiC. Distortion and asymmetry of Raman bands occur when a discrete phonon state overlaps with a broad electronic state and their symmetries coincide with each other [11]. This effect was observed in SiC and studied in detail for different polytypes by Colwell and Klein [11]. The asymmetric profiles vary with polytype and carrier density.

In this work the Fano-interference profiles of the FTA doublet modes were computer-fitted with Fano-formulas, in which each FTA doublet component was assumed to interfere with the electronic continuum independently of the other. The theoretical approach of Fano-interference effect is given in chapter 3. In order to determine the carrier concentration first we need to extract as called Fano-parameters (see Chapter 3). Next section shows the detailed investigation of FTA modes using Fano-formula and theoretical fitting model.

4.3.2.1 Fitting model

Let's look closer to the low energy part of spectra. Fig. 4. 10 presents the Raman spectra collected on investigated samples in range $160\text{-}240\text{ cm}^{-1}$ compared to the (undoped) reference sample 175c. One can notice that with increasing the nitrogen content the changes in the shape and position manifest. For low doped samples (13-006, 13-007, 13-008) no significant changes were noticed. The peaks appear in the same position as for the reference sample and we do not observe any distortion of the shape of these lines. Only two samples (13-010 and 13-011), with the highest carrier concentration exhibit significant changes. The nitrogen doping level for those samples checked by SIMS was $8.6 \times 10^{18}\text{ cm}^{-3}$ and $3.8 \times 10^{19}\text{ cm}^{-3}$ for 13-010 and 13-011, respectively. Harima et al. [12] observed previously similar Fano-interference in the FTA mode of n-type 4H-SiC with carrier concentrations from 1×10^{18} to $2 \times 10^{19}\text{ cm}^{-3}$.

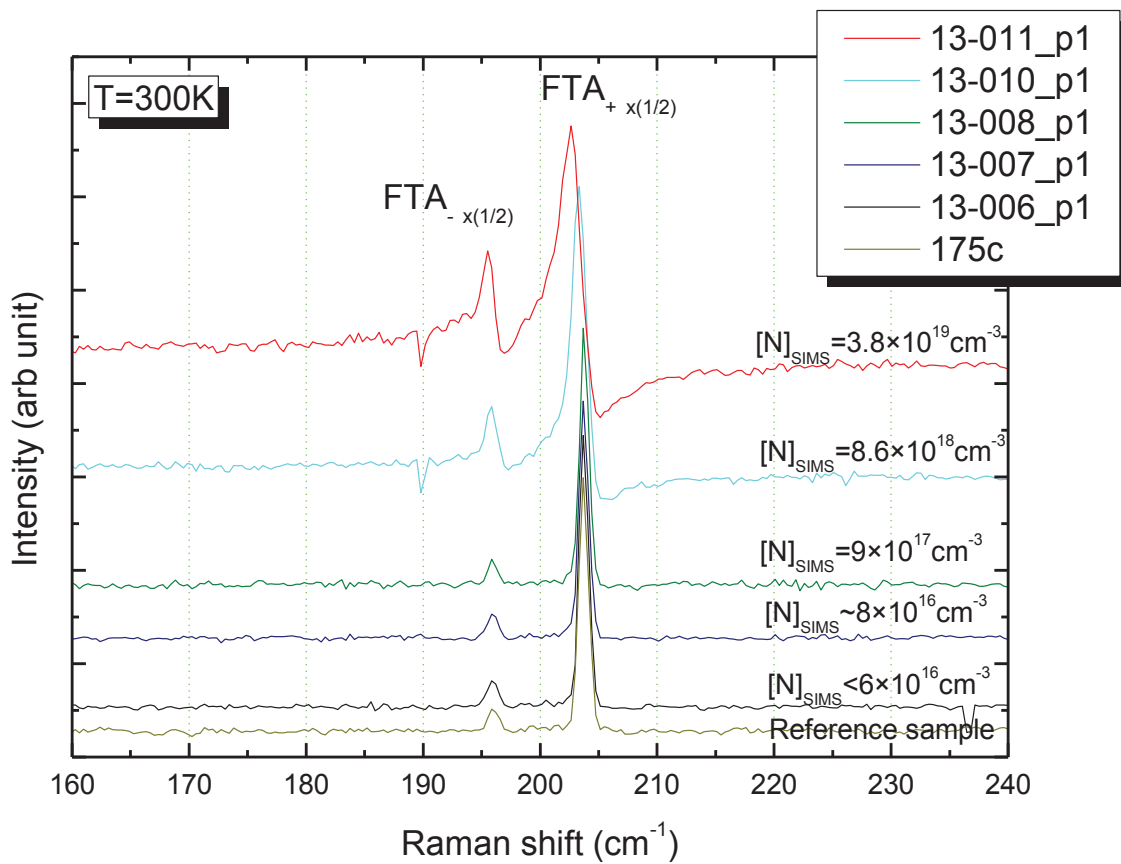


Fig.4. 10: Raman spectra collected on investigated samples in range $160\text{-}240\text{ cm}^{-1}$ compared to the (low doped) reference sample 175c. Doubled transverse acoustic phonon modes (FTA) are called $\text{FTA}_{\pm x(1/2)}$

Using Fano-formula described in chapter III one can find so-called Fano-parameters. For this we need to fit theoretically the experimental spectra. First the subtraction of the background for each spectrum was done. Secondly by using our home made computer

program with three adjustable parameters per mode described in chapter 3 (q , Γ , $\delta\Omega$) the theoretical fit for each spectrum was made. As a result of the theoretic fit we have obtained six Fano-parameters which in turn, were used as an indicators of carrier concentration. The typical examples of the fit for three differently doped samples with marked Fano-parameters values are presented in Fig.4. 11. The red stars are the experimental data and the blue lines are the theoretic fit. At first glance we can notice differences in the shape between these three spectra. Sample 13-008 which contains low value of nitrogen does not exhibit any significant changes related to the interference effect. Both FTA- and FTA+ are rather symmetric without any distortion. For samples 13-010 and 13-011 the Fano-effect manifests clearly. The lines are not symmetric anymore and we can also notice the shift. It has been demonstrated that the Fano analysis can determine carrier concentration ranging from $\sim 3 \times 10^{18}$ to $1 \times 10^{20} \text{ cm}^{-3}$ [13].

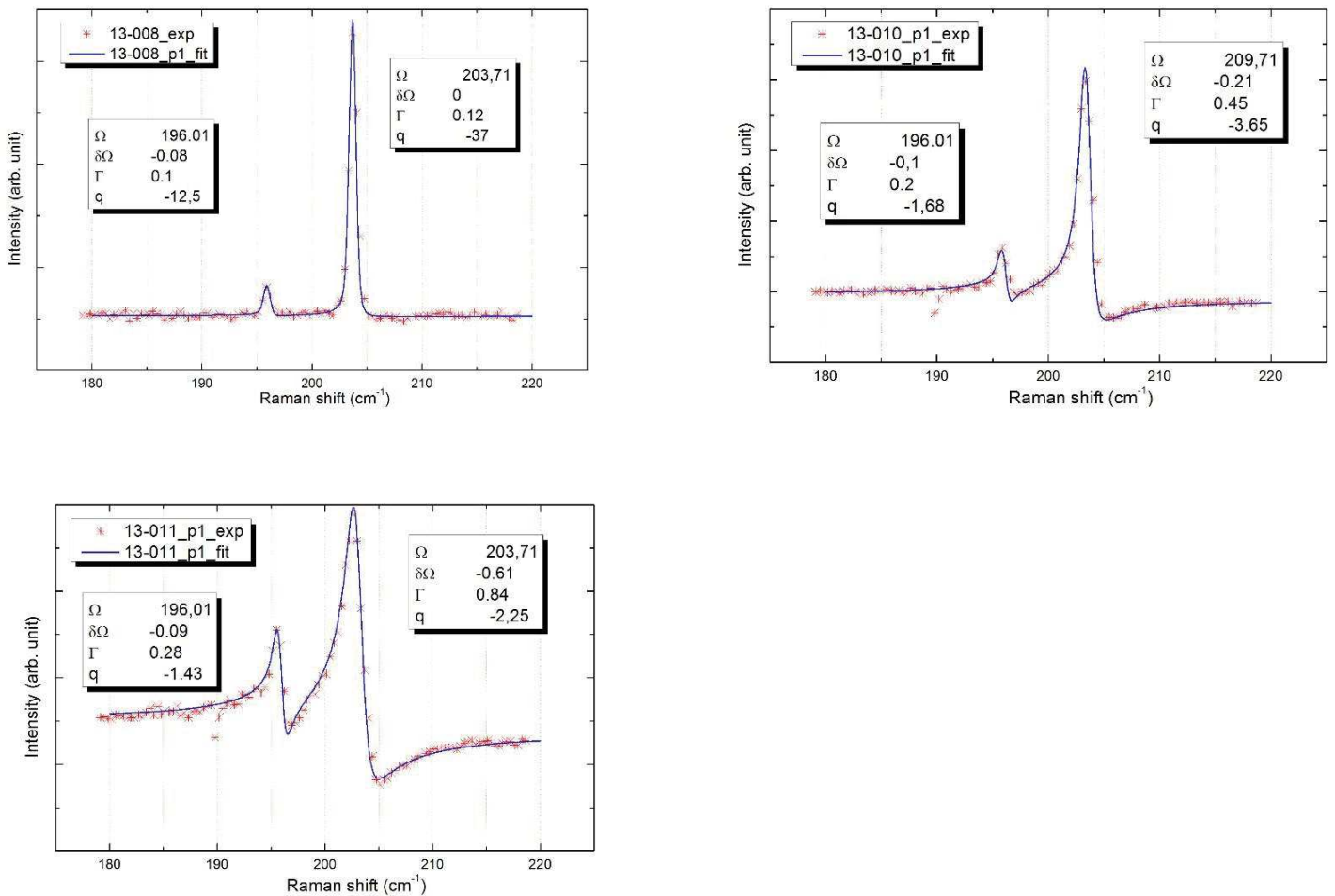


Fig.4. 11: Theoretical fits for three investigated samples 13-008, 13-010, 13-011. In the boxes the values found for the Fano-parameters. The red stars are the experimental data and blue line is the theoretic fit using Fano-formula.

In order to use the calibration curve [13], focus on the position of the FTA_{+/-} peaks. For undoped 4H-SiC crystals, the FTA_{±x(1/2)} modes are observed at 196.4 cm⁻¹ and 204.1 cm⁻¹ [14], where the fraction enclosed in parenthesis indicates the reduced wavevector (k/k_B) in the basic Brillouin zone of cubic 3C-SiC in the <111>direction. Here, k is the wavevector of the corresponding phonon in the basic Brillouin zone and k_B is the wavevector at the zone edge in the basic Brillouin zone. With increasing the carrier concentration the distance between FTA₊ and FTA₋ decreases and the peaks shift to the lower energy. This fact was shown by Mitani et al. [13].

Fig.4. 12 shows the calibration curve [13] used to estimate the carrier concentration. For carrier concentration lower than $\sim 10^{18}$ cm⁻³ no variation in the distance $\Delta\omega$ between the FTA₊ and FTA₋ is observed and it is impossible to quantify the carrier concentration values in this range. One can conclude that the determination of the carrier concentration by using the distance between FTA₊ and FTA₋ modes is only possible for the samples with carrier concentration range about 10^{18} cm⁻³ up to 10^{20} cm⁻³. For the low doped samples 13-006, 13-007 and 13-008 the distance $\Delta\omega$ between the FTA₊ and FTA₋ is found to be 7.83, 7.83 and 7.84 cm⁻¹, respectively. The blue line shows the range of carrier concentration corresponding to these values of $\Delta\omega$, thus one may only state that the carrier concentration value of samples 13-006,7&8 is lower than $\sim 10^{18}$ cm⁻³.

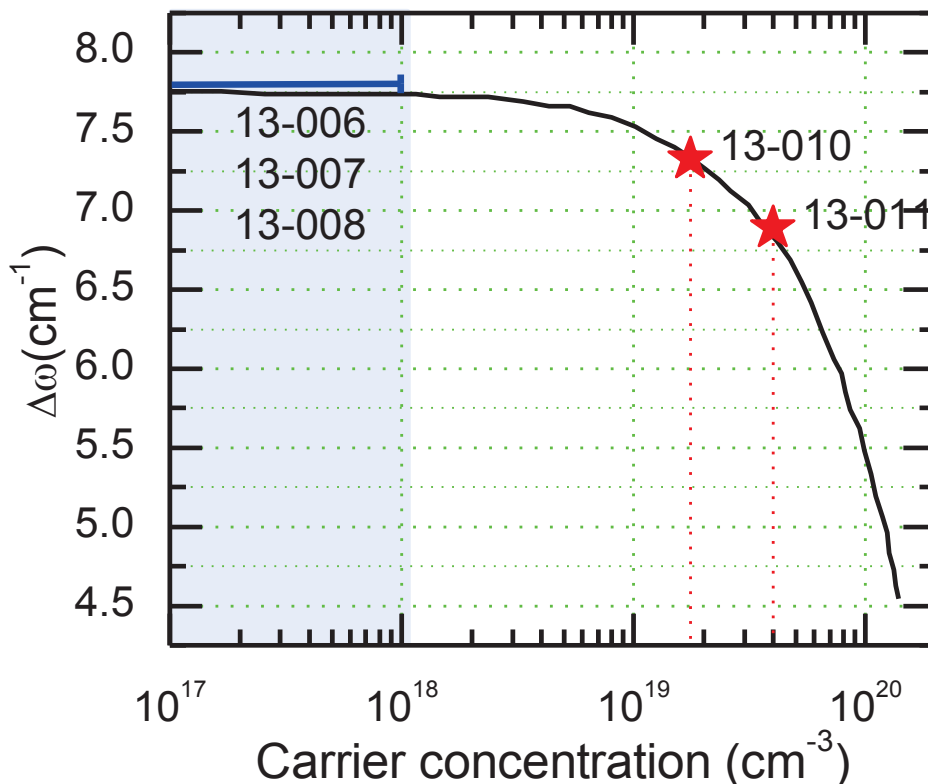


Fig.4. 12: The variation of the frequency separation between the FTA doublet modes as a function of carrier concentration [13]. Red stars are the $\Delta\omega$ values of investigated samples.

The distance $\Delta\omega$ between the FTA₊ and FTA₋ decreases drastically for the carrier concentration higher than 10^{19} cm^{-3} . One could determine the carrier concentration to be $1.8 \times 10^{19} \text{ cm}^{-3}$ for sample 13-010 and $4 \times 10^{19} \text{ cm}^{-3}$ for sample 13-011. This is in good agreement with the results of LTPL measurements (see Tab.4. 3). To evaluate the carrier concentration from Raman measurements, $\Delta\omega$ is a one of possible ways, nonetheless, it can be determined more accurately and in a wider range by using two more parameters extracted from theoretical fit.

Fig.4. 13 shows the absolute values of q versus carrier concentration. For n-type 4H-SiC, the asymmetric parameter q is negative and $|q|$ decreases as the distortion in the FTA mode increases. As it was shown in chapter 3 the parameter q is proportional to the carrier concentration.

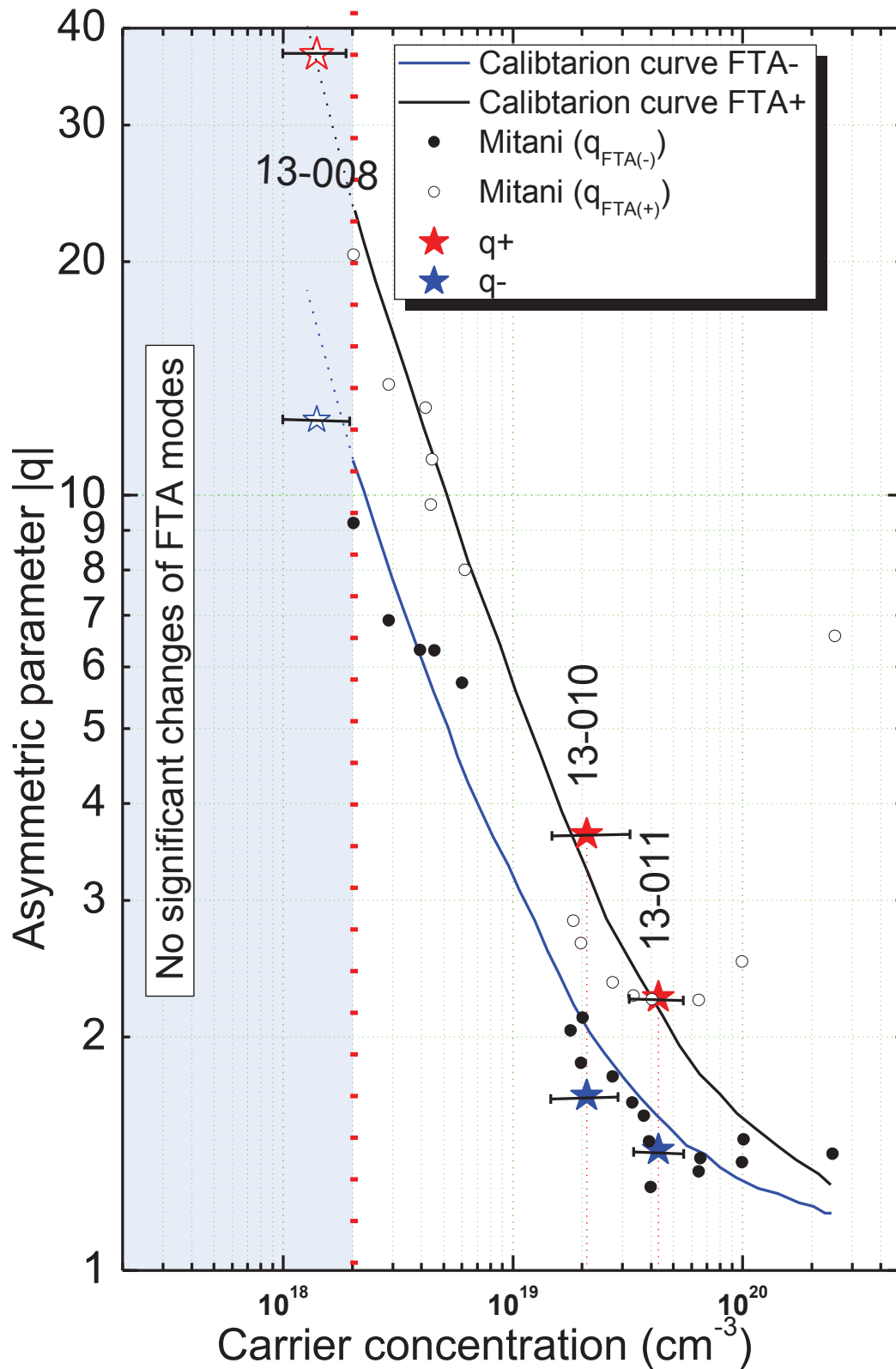


Fig.4. 13: Asymmetry parameters vs. carrier concentration, the lines are the calibration curves drawn from literature [13], blue correspond to FTA- and black to FTA+, the stars are the q parameters found due to theoretical fit obtained on investigated samples. Full and empty points are the experimental data from [13].

Then using the calibration curves from literature [13] we could successfully estimate the carrier concentration in investigated samples. Fig.4. 13 & Fig.4. 14 show Fano-parameters (asymmetric parameters and broadening respectively) plotted versus carrier concentration. The horizontal black lines plotted in Fig.4. 13 represent the errors band. One can notice that the maximum errors made evaluating the carrier concentration by using the asymmetry parameters is in range of 16%. Now using the asymmetric parameters one found the carrier concentration values to be $2.1 \times 10^{19} \text{ cm}^{-3}$ and $4.2 \times 10^{19} \text{ cm}^{-3}$ for 13-010 and 13-011 respectively. Since the calibration curve starts from carrier concentration value of $2 \times 10^{18} \text{ cm}^{-3}$, to estimate carrier concentration for sample 13-008 we assumed this same behavior for lower carrier concentration value. By prolonging the curves marked by dotted lines one estimated the carrier concentration for 13-008 to be $\sim 1.5 \times 10^{18} \text{ cm}^{-3}$. This method can be applied to calculate the carrier concentration in range $2 \times 10^{18} \text{ cm}^{-3}$ up to about $2 \times 10^{20} \text{ cm}^{-3}$ according to the calibration curves.

Limit of this method: The darken region marked on Fig.4. 13 corresponds to carrier concentration range where the q parameter as an indication of carrier concentration is not reliable or not enough precise.

Another possible way to find out the carrier concentration level in 4H-SiC n-type is to use the broadening parameter Γ . Fig.4. 14 shows the broadening parameter plotted vs. carrier concentration. The lines, full and empty circles are the calibration curve and experimental data respectively from literature [13]. The blue and red stars are the Γ parameters found due to Fano-formula and theoretical fit of FTA- and FTA+ modes, respectively. This calibration curve is useful for the samples with doping level between few 10^{18} cm^{-3} up to about few 10^{20} cm^{-3} . The errors of evaluating the carrier concentration marked in the Fig.4. 14 is lower than 7%. The values of carrier concentration obtained due to broadening parameters are $1.7 \times 10^{19} \text{ cm}^{-3}$ and $4.1 \times 10^{19} \text{ cm}^{-3}$ for 13-010 and 13-011, respectively. Nevertheless it was impossible to estimate the carrier concentration for sample 13-008. Since the calibration curves are flat in range up to about $2 \times 10^{18} \text{ cm}^{-3}$, the only thing one can say is that the carrier concentration in case of sample 13-008 is lower than $\sim 2 \times 10^{18} \text{ cm}^{-3}$, what is marked by vertical blue line in Fig.4. 14.

Limits of this method: Again darken area shows the range where the usage of broadening parameter to evaluate the carrier concentration is impossible because there is no clear correlation between broadening of FTA lines and carrier density.

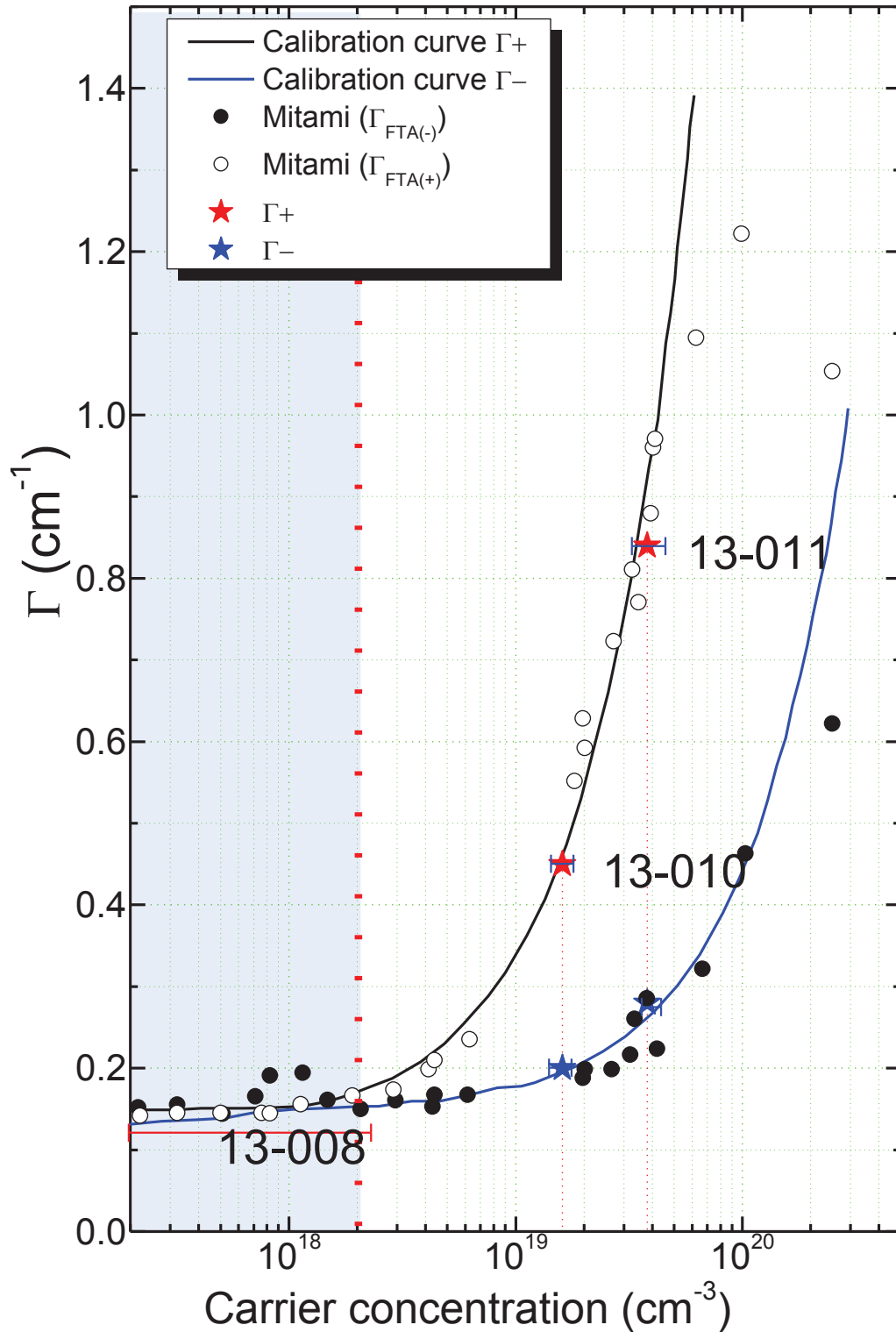


Fig.4. 14: Broadening parameters vs. carrier concentration, the lines are the calibration curves down from literature [13], blue correspond to FTA- and black to FTA+, the stars are Γ parameters found due to theoretical fit obtained on investigated samples. Full and empty points are the experimental data from [13].

Tab.4. 4 summarizes the results of evaluation of the carrier concentration due FTA modes and theoretical fit using Fano-formula. One may notice that the values obtained due to the three parameters $\Delta\omega$, q and Γ are in good agreement.

Fano-parameters	Carrier concentration (cm^{-3})		
	13-008	13-010	13-011
$\Delta\omega$	-	1.8×10^{19}	4×10^{19}
q	$\sim 10^{18}$	2.1×10^{19} ($\pm 16\%$)	4.2×10^{19} ($\pm 16\%$)
Γ	-	1.7×10^{19} ($\pm 7\%$)	3.9×10^{19} ($\pm 7\%$)

Tab.4. 4 : Carrier concentration estimated using Fano-parameters

The difference between the carrier concentrations values obtained due to Γ parameters and q and $\Delta\omega$ is $\sim 10\%$. Because Γ parameter is only related to the matrix element of electron-phonon interaction and the density of state, which for heavily doped 4H-SiC is treated as constant, for high doped samples (higher than few 10^{19} cm^{-3}) Γ is more reliable when evaluating carrier concentration. In the other hand for the carrier concentration ranging from $\sim 10^{18}$ up to $\sim 10^{19} \text{ cm}^{-3}$ since we do not observe yet any significant changes of Γ parameters, better way seems to use the asymmetric parameter q .

4.4 Discussion and conclusion

In this chapter, a series of five n-type 4H-SiC samples with different nitrogen doping concentration was investigated. The samples were grown by CVD on highly doped 4H-SiC n-type substrate (0001). For all of them the polytype, homogeneity and crystal quality were verified by LTPL and Raman spectroscopy (see annex 2). The epilayers were found to be 4H-SiC polytype and no inclusion of any other polytype was observed. The crystal quality of the layers is good, without any defects, and all investigated layers are homogeneous in terms of thickness and doping concentration.

First the nitrogen contain for all samples was found using SIMS measurements. No significant trace of aluminum was observed. Notice that the detection limit is about $6 \times 10^{16} \text{ cm}^{-3}$ for nitrogen. Since the epilayer and substrate are n-type 4H-SiC the determination of the thickness was done by measuring the depth of the SIMS crates. Due to the damage done by SIMS measurement non-destructive ways to evaluate the nitrogen and carrier concentration were studied. Optical LTPL and Raman measurements in a very large scale of doping few 10^{15} cm^{-3} up to 10^{19} cm^{-3} were proposed.

LTPL was found to be a good method to determine the type of the carrier in the layer and the compensation (if any). The nitrogen concentration was calculated using three different

calibration curves for three different doping ranges (10^{15} up to 10^{19} cm^{-3}). A limit for the highest doped samples appears at about 2×10^{19} cm^{-3} . Further investigation was necessary to do and for this we used micro-Raman spectroscopy.

Micro-Raman spectra identify the polytype, check the crystal quality and give information about doping level. However this method does not provide any information about possible compensation. Two different parts of the Raman spectra were studied:

- the optic LOPC modes for low doped samples with carrier concentration in range few 10^{16} cm^{-3} up to about 10^{18} cm^{-3} , and
- acoustic modes at low energy part of Raman spectra to determine the value of higher carrier concentration, higher than few 10^{18} cm^{-3} .

Combining the LOPC and FTA modes it's possible to evaluate the carrier concentration in case of n-type 4H-SiC in a wide range from 10^{16} cm^{-3} up to about 10^{20} cm^{-3} .

Both LTPL and Raman spectroscopies can give information about the polytype, crystal quality and carrier concentration. Considering the complementary in these both methods permit to obtain information about nitrogen doping in a very large range. Tab.4. 5 summarizes the data obtained for all investigated samples. The nitrogen concentration determined using different methods show slight differences. For low doped samples since the LOPC & FTA modes of Raman spectra do not exhibit any significant changes the best ways seems to be LTPL measurements. For the highest doped samples notice the advantage of Raman which allows to determine the carrier concentration up to 10^{20} cm^{-3} . In the middle range few 10^{16} up to about 10^{18} cm^{-3} both methods can be used.

Sample	Targeted concentration (cm^{-3})	C-V (cm^{-3})	Raman (carrier concentration cm^{-3})				PL (cm^{-3})	SIMS (cm^{-3})
			LOPC		FTA			
			$\omega - \omega_0$	FWHM	$\Delta\omega$	Γ		
13-006	10^{16}	1.06×10^{16}	$< 10^{17}$	$\leq 2.5 \times 10^{16}$			$< 10^{16}$	$< 6 \times 10^{16}$ (DL)
13-007	10^{17}	8×10^{16}	5×10^{16}	5×10^{16}			2×10^{12}	$\sim 8 \times 10^{16}$ (DL)
13-008	10^{18}	8.9×10^{18}	3.3×10^{17}	3.3×10^{17}			9.2×10^{17}	9.5×10^{17}
13-010	10^{19}	3×10^{19}			1.8×10^{19}	1.7×10^{19} ($\pm 7\%$)	2×10^{19}	8.6×10^{18}

13-011	$\geq 5 \times 10^{19}$				4×10^{19}	3.9×10^{19} ($\pm 7\%$)	$> 2 \times 10^{18}$	3.8×10^{19}
--------	-------------------------	--	--	--	--------------------	---------------------------------------	----------------------	----------------------

Tab.4. 5: Nitrogen concentrations determined by different methods in the samples studied in this work.

The limits of these two methods are shown in Fig.4. 15. The red color corresponds to the LTPL and blue to Raman. The lighter color corresponds to the limit of the used methods. In theory one using the LTPL is able to determine the carrier concentration for 4H-SiC in range 10^{15} up to 10^{19} cm^{-3} . In practice the transition region of calibration curves appear as a limitation to apply this technics (see Fig.4. 3). In the other hand micro-Raman is useful for samples with carrier concentration in range few 10^{16} up to about 10^{20} cm^{-3} . This lighter area correspond to the zone where the LOPC mode is no clearly visible any more, and at the same time the fano-effect does not manifest strongly enough so one can notice changes of the FTA modes.

On the diagonal the overlapping of these two methods is showed. Illustrating the ranges where one or another method is more appropriate to use in order to determine the nitrogen doping. In the range from 10^{15} to few 10^{16} cm^{-3} only LTPL can provide the information about the doping level. Then in range few 10^{16} up to few 10^{18} cm^{-3} both techniques can be used. Finally for high doped samples from few 10^{18} up to 10^{20} cm^{-3} only the Raman gives the information about doping level, nonetheless in range few 10^{18} to $\sim 10^{19}$ cm^{-3} the LTPL can also be used. The black circles show the ranges where in not always possible to determine the doping level neither by LTPL nor Raman.

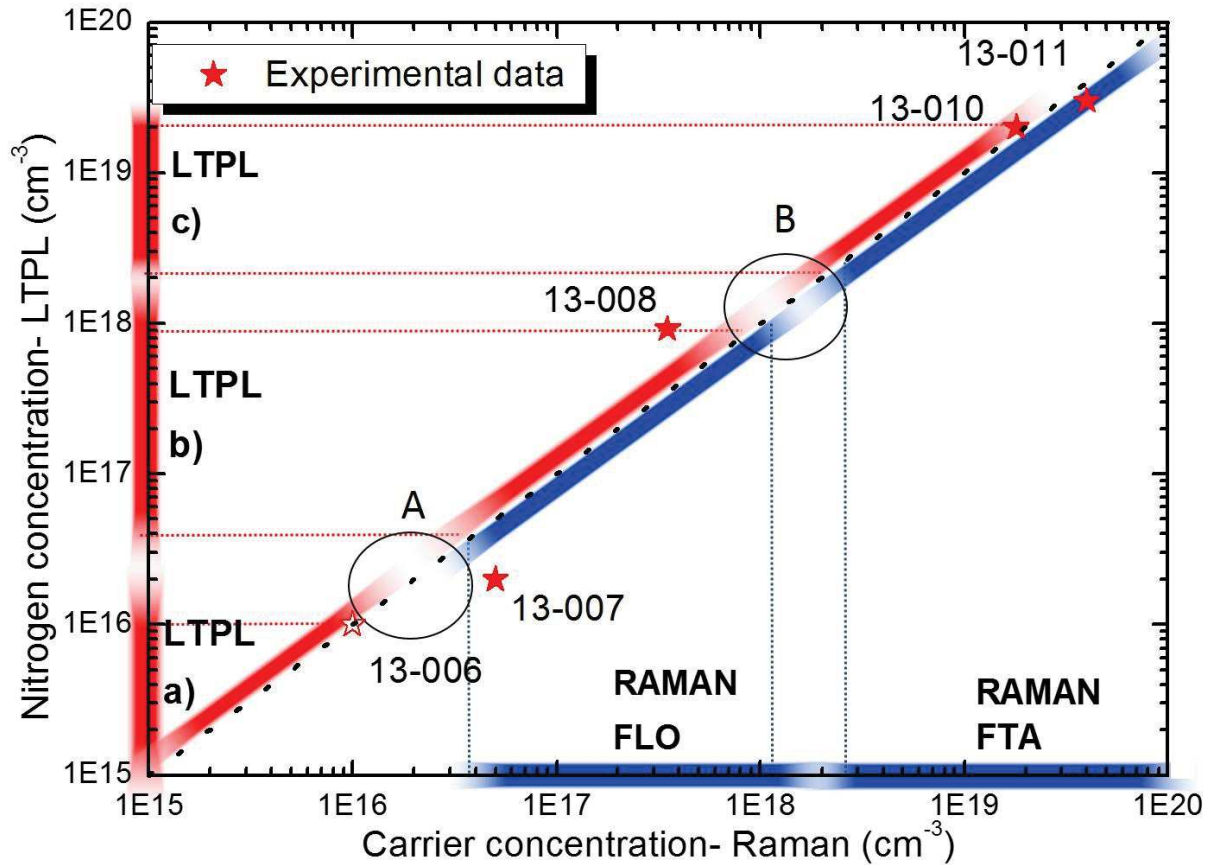


Fig.4. 15: Comparison between LTPL and Raman spectroscopies technics to determine carrier concentration in Nitrogen doped 4H-SiC materials. Blue color corresponds to Raman, red to LTPL.

Summarizing, combining both methods one can evaluate the type of carrier (electron or hole by LTPL) verify the compensation, check the polytype and the doping concentration level in a nondestructive way in a very large scale from 10^{15} up to few 10^{20} cm^{-3} .

Bibliography

- [1] A. Fukumoto, *Phys. Stat. Sol.*, vol. 220, p. 125, 1997.
- [2] J. Camassel, S. Juillaguet, M. Zielinski, C. Balloud, *Chem. Vap. Deposition*, vol. 12, p. 549, 2006.
- [3] U. Forsberg, A. Henry, M. K. Linnarsson, E. Janzén, *Mat. Sc. Forums*, vol. 338, p. 619, 2000.
- [4] A. Henry, U. Forsberg, M. K. Linnarsson et E. Janzen, *Physica Scripta*, vol. 72, p. 254-257, 2005.
- [5] A. Henry et al., *Materials Science and Engineering* , vol. 62, p. 234-238, 1999.
- [6] S. Sridhara et al., *J. App. Phys*, vol. 84, p. 2963, 1998.
- [7] H. Harima, S. Nakashima, T. Uemura, *J. Appl. Phys*, p. 78, 1995.
- [8] H. Harima, S. Nakashima, *Inst. Phys. Conf. Ser.*, vol. 365, p. 142, 1996.
- [9] H. Harima, T. Hosoda, S. Nakashima, *Mater. Sci. Forum*, vol. 607, p. 338-342, 2000.
- [10] U. Fano, "Effects of Configuration Interaction on Intensities and Phases shifts" *Phys. Rev*, vol. 124, p. 1866-1878, 1961.
- [11] P. J. Colwell, M. V. Klein, *Phys. Rev*, vol. 6, p. 498, 1972.
- [12] H. Harima, S. Nakashima, *Inst. Phys. Conf. Ser*, vol. 142, p. 165, 1996.
- [13] T. Mitani, S. Nakashima, *J. Appl. Phys*, vol. 043514 , p. 112, 2012.
- [14] S. Nakashima, H. Harima, *Phys. Stat; sol (a)*, vol. 162, p. 39, 1997.

Chapter 5: Evaluation of doping concentration in p-type 4H-SiC doped with aluminum

Introduction

In this chapter we will study the p-type 4H-SiC doped with aluminum. The aluminum and carrier concentration will be evaluated using different methods as LTPL and Raman. The objective is to verify the validity of the well-known calibration curves of LTPL to determine aluminum concentration and the usability of optical part of Raman spectra to evaluate the carrier concentration. Finally, combining the results of Hall Effect with Raman spectra we will propose a new calibration curve to determine the hole concentration in p-type 4H-SiC. In addition we will compare the two optical investigation methods: LTPL and Raman to see which one is more appropriate to characterize the p-type 4H-SiC epilayer. The advantages and disadvantages, as well as the limitation in terms of doping level evaluation of each of these methods will be shown and discussed. At the end we will present, as an application, a doping mapping of 2 inch p 4H-SiC sample.

The samples under consideration are made by CVD growth process by R. Arvinte and M. Zielinski from NOVASIC in the framework of NetFiSiC project.

5.1 Sample description

In this work we considered 18 different 4H-SiC epilayers intentionally doped with aluminum. The samples were made by M. Zielinski and R. Arvinte in NOVASIC by Chemical Vapour Deposition (CVD) on 4H-SiC 8° off axis substrate. The epitaxial growth was performed in a horizontal, hot wall, resistively heated, using hydrogen as a carrier gas, silane (SiH₄) and propane (C₃H₈) as precursors. For few of the substrates used for epigrowth the carrier concentration was verified by C-V measurements and found to be in range of 10¹⁸ cm⁻³. The epilayer carrier concentration was checked for several samples by C-V measurements and the thickness of each sample was determined by FTIR and/or weight measurements. The temperature was set on 1650°C and pressure between 120 and 200mbar, H₂=14 slm, Ar_{res}=2 slm, SiH₄= 10sccm, C₃H₈= 3.3 sccm, C/Si ratio=1 for each samples. Different aluminum doping concentrations was achieved by changing of the TMA flow. Note a reference sample with Al free (175c) was used for comparison.

More detail about the growth conditions are given in Tab.5. 1.

Sample	C-V concentration (cm ⁻³)	TMA (H ₂ dilution (slm)/ H ₂ bubbler (sccm)/ H ₂ +Al mix to reactor (sccm))	Pressure (mbar)	Thickness (μm)		Growth time (min)
				FTIR	weight	
175c	Al free	0	200	4.8		
14-012	2.2×10 ¹⁶	0	120	14.75		66
14-015	8×10 ¹⁶	2slm/40sccm/5sccm	200		13.8	66
13-331	1.8×10 ¹⁷	1/20/5	120	10	12.3	60
14-003	1.5×10 ¹⁸	1/40/20	120	11.7	12.4	65
192c	2×10 ¹⁸		200	4.6		
192m	2×10 ¹⁸		200	4.4		
14-004	5×10 ¹⁸	1/40/100	120	10.4	13	65
14-005	8×10 ¹⁸	0.5/40/100	120	10.3	11.9	60
192b	2×10 ¹⁸		200	3.5		
14-007	1×10 ¹⁹	0.15/50/100	120		12.4	67
181m	10 ¹⁹		200		3.5	
181b	1×10 ¹⁹		200	3.5		
12-308C	-		200	9.7		
12-308D	-		200	9.6		
12-308B	-		200	8.4		
12-308 E	8×10 ¹⁹		200	8.7		
12-308A	-		200	7.4		
14-009	>5×10 ¹⁹	0.15/50/100	120		14.8	67

Tab.5. 1: Sample description with detailed growth parameters and results of C-V measured and thickness of the epilayers.

For each sample the Al concentration was measured by SIMS and the check of the nitrogen concentration was done in the same time. The nitrogen contain was found to be lower than 2×10¹⁷ cm⁻³. Average doping concentrations of aluminum and nitrogen determined by SIMS are summarized in Tab.5. 2.

SAMPLE	SIMS (CM ⁻³)	
	N	Al
175C	≤10 ¹⁷ (DL)	Al-free
14-012	≤10 ¹⁷ (DL)	2.3×10 ¹⁶
14-015	≤10 ¹⁷ (DL)	6.2×10 ¹⁶
13-331	<DL	1.4×10 ¹⁷
14-003	<DL	9.1×10 ¹⁷
192C	≤2×10 ¹⁷	2 ×10 ¹⁸
192M	≤2×10 ¹⁷	4×10 ¹⁸
14-004	<DL	3.1×10 ¹⁸
14-005	<DL	6.8×10 ¹⁸
192B	≤10 ¹⁷	10 ¹⁹
14-007	<DL	1.7×10 ¹⁹
181M	<DL	2.3×10 ¹⁹
181B	<DL	5×10 ¹⁹
12-308C		6.2×10 ¹⁹
12-308D		6.4×10 ¹⁹
12-308B		7.1×10 ¹⁹
12-308E	<DL	7.1×10 ¹⁹
12-308A		8.4×10 ¹⁹
14-009	<DL	7.6×10 ¹⁹

Tab.5. 2: Aluminum and nitrogen concentration values obtained by SIMS measurements, the detection limit (DL) for nitrogen was: $\sim 2 \times 10^{17} \text{ cm}^{-3}$.

After the growth process the surface of several samples was investigated using standard optical microscopy. The measurements were done in NOVASIC by R. Arvinte. This allows us to see the quality of the surface and the effect of the increasing of the aluminum contain. These images are presented and comment in annex 2. Note that for all samples except the 14-009 (with higher doping level) the surface seems to be rather smooth without any defects. For sample 14-009 the surface differs drastically. Thus this sample will be comment separately in annex 2.

5.2 Evaluation of doping concentration by non-destructive methods

To evaluate the doping concentration in p-type 4H-SiC one can use both LTPL and Raman measurements, two non-destructive methods.

5.2.1 Evaluation of aluminum by LTPL

Starting by LTPL measurements, the experimental setup of LTPL used to collect the data has been already described in Chapter 2. These measurements were done at the temperature of about 4K in the range 380-750nm. The incorporation of Al modify the LTPL spectrum. The Fig.5. 1 & Fig.5. 2 show the LTPL spectra for several samples in range 380-475nm and zoom on the near band edge in the range of 390-395nm respectively, from the lowest doped on the bottom to the high doped sample on the top.

In low energy range of the spectra the typical signature of 4H-SiC is visible. For high doped samples (higher than few 10^{18} cm^{-3}) broad band labelled donor acceptor pair (DAP) Al-N appears. Focus first on the low and medium doping level of Al. In Fig.5. 2, to simplify the figure, all the Al lines labelled Al_0 are normalized to 1 except sample 175 in which this line is very weak (in this case the Q_0 line is normalized to 1 to simplify the graph). The evaluation of the Al concentration by LTPL is well known [1], [2] in the range of few 10^{13} up to few 10^{18} cm^{-3} . The authors shown that the intensity of the ratio of Al zero phonon line divided by Q_0 line varies as a function of aluminum concentration [1], [2]. The detailed information about evaluation of aluminum doping in p-type 4H-SiC layer are given in Annex 1.

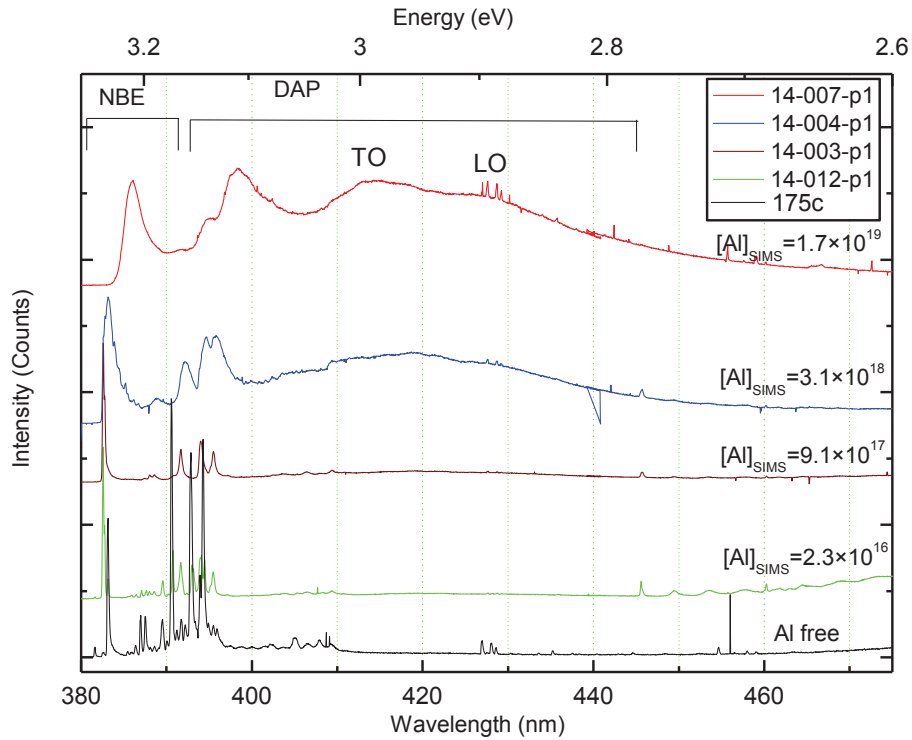


Fig.5. 1: Example of LTPL spectra in Range 380-475nm taken at 4K on four investigated samples with different Al concentration compared to the Al free samples (on the bottom).

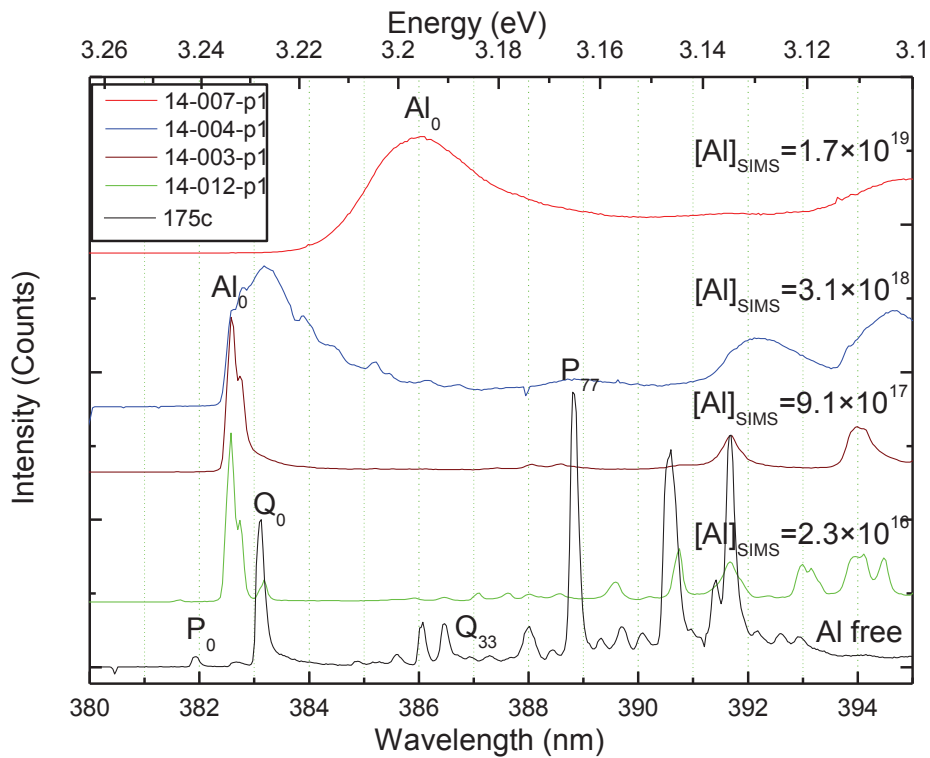


Fig.5. 2: Example of LTPL spectra in Range 380-395nm taken at 4K on four investigated samples with different Al concentration compared to the Al free samples (on the bottom)

As is shown on the Fig.5. 2, increasing the Al concentration a shift and broadening of the Al_0 line appear. The Q_0 line related to a nitrogen bound exciton vanishes at the same time. The calibration curves from ref [1], could be used for samples (175c, 14-012, 14-015 and 13-331), for the other samples no Q_0 line is solved. Fitting the LTPL spectra with the Gaussian curve, we could calculate the intensity ratios for each sample and using the formula:

$$R = \frac{I(Al_0)}{I(Q_0)}$$

In this equation $I(Al_0)$ is the intensity of the Al_0 lines and $I(Q_0)$ the intensity of the Q_0 line.

An example of theoretical fit done for sample 14-012 is shown in Fig.5. 3. Since Al_0 line consists theoretically four peaks, the fit was done for two peaks separately solved of the spectrum. Our experimental setup solved only two peaks in the Al_0 line. Fig.5. 3 shows also Gaussian fit done on Q_0 line.

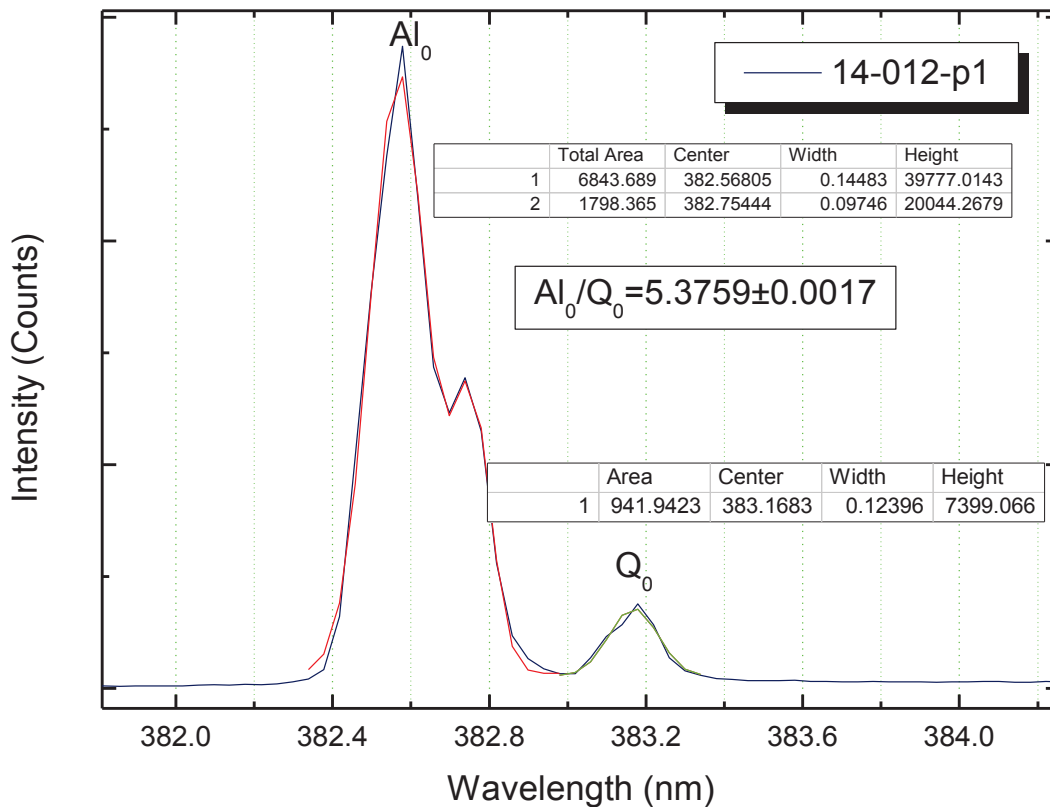


Fig.5. 3: Example of theoretical fit using Gaussian function done on sample 14-012. In the boxes the fit values.

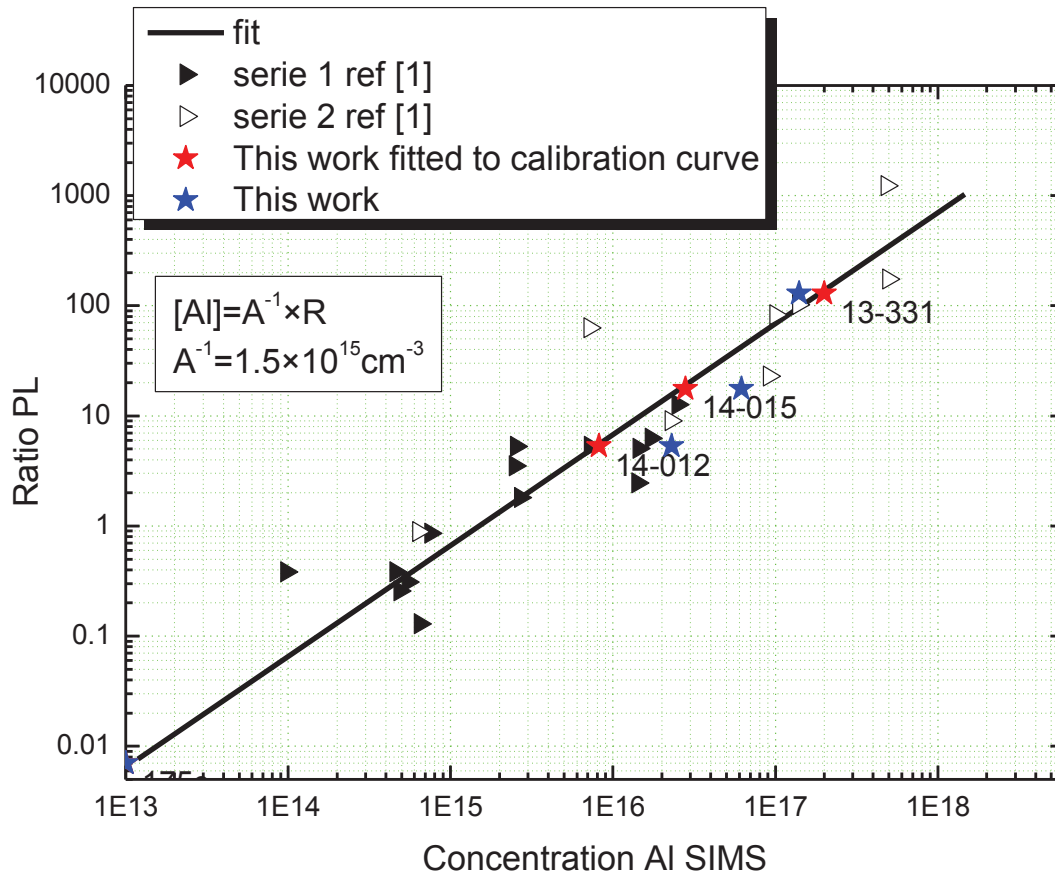


Fig.5. 4: Photoluminescence intensity ratio of the $I(\text{Al}_0)/I(\text{Q}_0)$ lines as a function of aluminum concentration measured by SIMS for 4H-SiC samples, the triangles are the data from literature [1], red stars the data of this work fitted on the curve and blue stars calculated ratio vs. SIMS values measured in this work.

The calibration curve presented in Fig.5. 4 marked by full black line [1] corresponds to an aluminum contain in range 10^{14} up to few 10^{18} cm^{-3} for a nitrogen concentration equal to $1.5 \times 10^{17} \text{ cm}^{-3}$. Fig.5. 4 presents four series of data. Two of them from literature [1] (series 1&2) and two corresponding to samples measured in this work (red and blue stars). First we found the ratio $I(\text{Al}_0)/I(\text{Q}_0)$ and fitted these values to the calibration curve to find the Al concentration (red stars). Since the investigated samples were also measured by SIMS we plotted on the Fig.5. 4 this same ratio but this time vs. SIMS results (blue stars). Two samples are placed below the calibration curve.

Notice that because we use ratio of intensity of Al_0/Q_0 , we normalize all data to the intensity of the Q_0 line, the residual nitrogen concentration should not vary from sample to sample. Of course, changing the residual N concentration should not change the slope parameter, but, simply, shift the ratio. This is explained in the ref. [1] and/or in annex 1. This shift between the two results red and blue stars could be explain by a small different in the nitrogen concentration.

Although the calibration curve in the Fig.5. 4 seems to be useful up to 10^{18} cm^{-3} , in several cases, because of strong compensation the NBE range is distorted/overlapped by DAP line and the evaluation of aluminum contain becomes impossible. Table 5.3 summarizes the value of aluminum and nitrogen evaluated by LPTL compared to SIMS results.

SAMPLE	AL (CM^{-3})	N (CM^{-3})	AL _{SIMS} (CM^{-3})
175C	$<10^{13}$	3×10^{17}	Al-free
14-012	8.2×10^{15}	6.8×10^{14}	2.3×10^{16}
14-015	2.8×10^{16}	1.5×10^{15}	6.2×10^{16}
13-331	$\sim 2 \times 10^{17}$	-	1.4×10^{17}

Tab.5. 3: Aluminum and nitrogen values calculated due to PL spectra compared to SIMS results $[\text{Al}]_{\text{SIMS}}$

Increasing the Al concentration, the authors from ref. [3] use the FWHM or shift of Al_0 line. Let's now look closer on the Al_0 lines. Taking into consideration the FWHM of Al_0 lines one can notice that increasing the aluminum doping this value increases see Fig.5. 5.

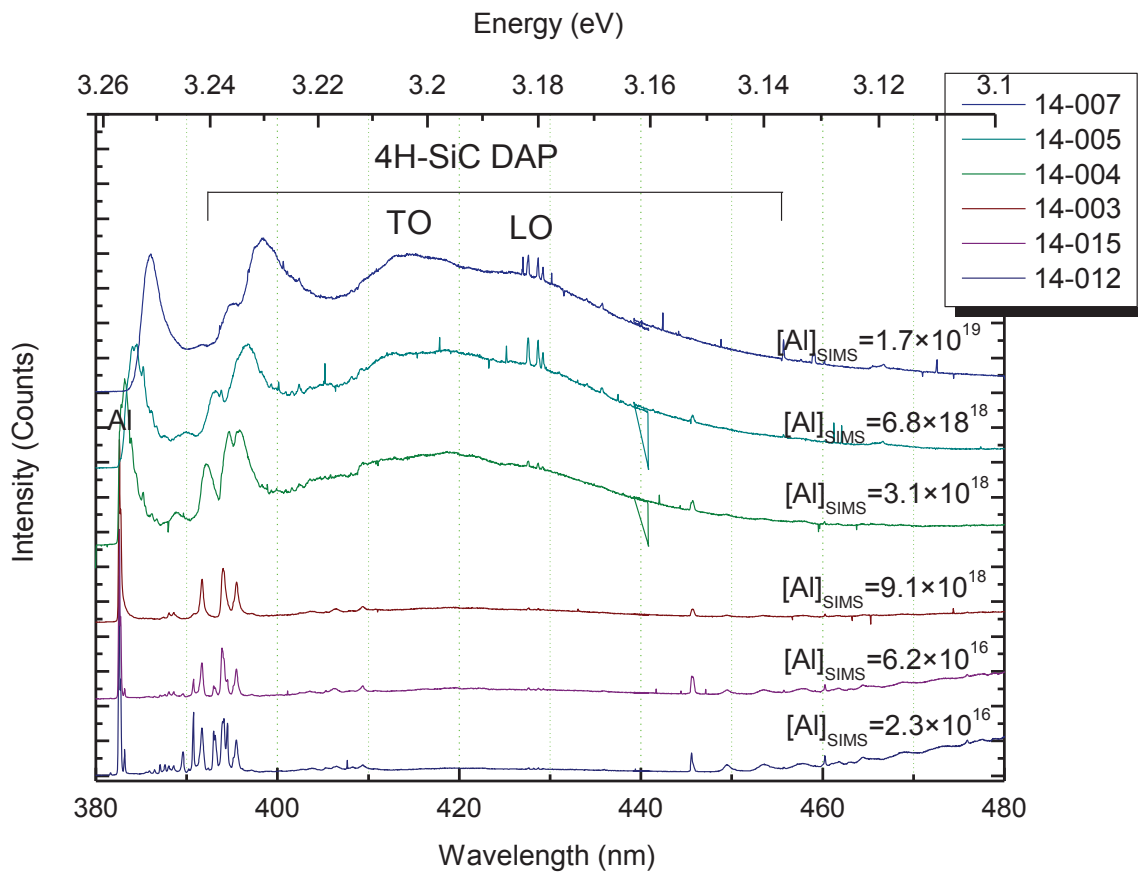


Fig.5. 5: LTPL spectra of several of investigated layers in range 380-480 with marked TO and LO phonon lines of aluminum 4H-SiC DAP

Clear correlation between FWHM and doping level was found for the samples with Al concentration higher than 10^{18} cm^{-3} . For lower doped samples no changes of width of Al_0 line are notice. The

Fig.5. 6 shows the FWHM of Al_0 line plotted vs. SIMS concentration from ref [3]. Using this calibration curve we found the aluminum values for investigated samples (reds stars). Note that this calibration curve is flat up to Al concentration few 10^{17} cm^{-3} . Thus for low doped samples (14-015,-012, 13-331) this method to evaluate Al concentration is not appropriate. Blue stars are the value of FWHM plotted versus Al measured by SIMS. Again, differences between the Al concentration measured by SIMS and evaluated due to FWHM and calibration curve was found. More experimental points have to be added to curve in Fig.5. 6 to increase its accuracy.

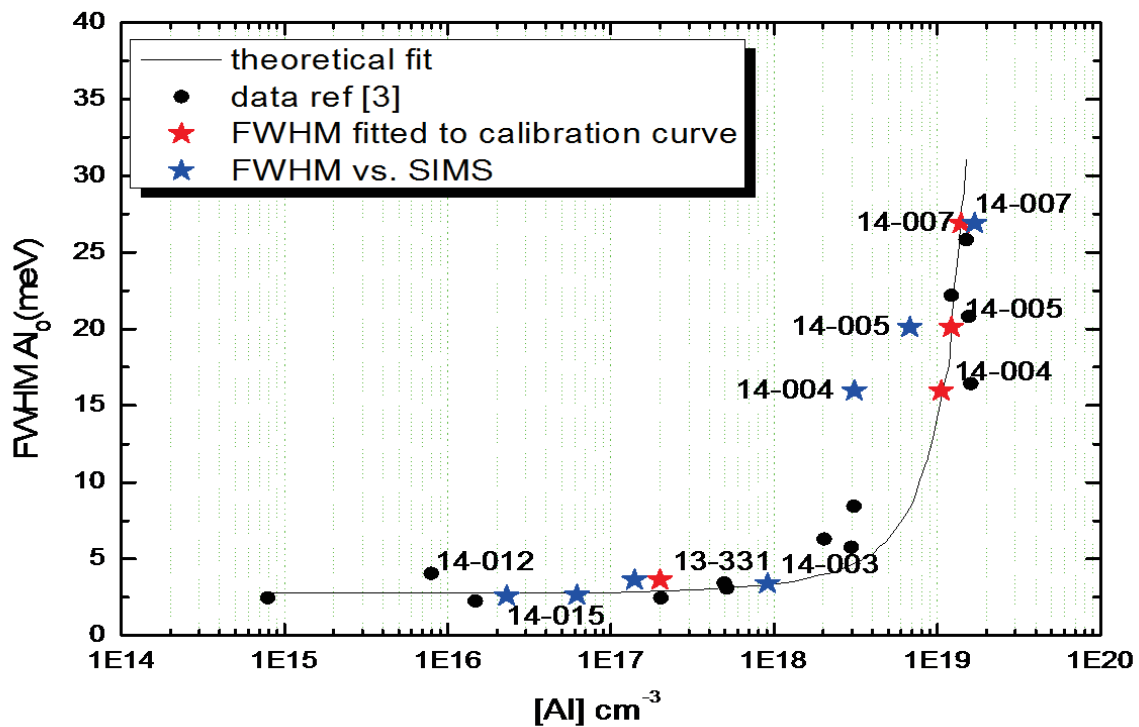


Fig.5. 6: FWHM of Al_0 line vs. SIMS concentration. The black line and circles are the data from literature [3], red stars the data of this work fitted on the curve and blue stars FWHM vs. SIMS values measured in this work.

The *Tab.5. 4* shows the value of Al determined using the calibration curve from ref. [3] and compared to the values determined by SIMS. The difference between the values obtained by SIMS and PL measurement for sample 14-004 is about one magnitude of order. The valid range when evaluating Al doping using FWHM of Al_0 line and calibration curve is from $\sim 10^{18}$ up to $\sim 10^{19} \text{ cm}^{-3}$.

SAMPLE	[AL] (CM ⁻³)	[AL] SIMS (CM ⁻³)
14-015	<3×10 ¹⁷	6.2×10 ¹⁶
14-012	<3×10 ¹⁷	2.3×10 ¹⁶
13-331	<3×10 ¹⁷	1.4×10 ¹⁷
14-003	9.1×10 ¹⁷	9.1×10 ¹⁷
14-004	1.06×10 ¹⁹	3.1×10 ¹⁸
14-005	1.22×10 ¹⁹	6.8×10 ¹⁸
14-007	1.4×10 ¹⁹	1.7×10 ¹⁹

Tab.5. 4: Aluminum concentration evaluated using FWHM of Al₀ lien and calibration curve from ref. [3]

Quite important disagreement between the values evaluated using SIMS and LTPL was found. Because Al concentration values evaluated using LTPL and calibration curve cannot be higher than values found by SIMS the general verification of used calibration curve must be considered.

5.2.2 Evaluation of p-doping level by Raman

In heavily doped p-type SiC the Raman-active LO phonon line is strongly broadened and distorted by interactions with free holes [4]. This same behavior was noted by S. Nakashima and H. Harima [5]. Also in the low frequency range one observe changes of the Raman spectrum. The FTAs lines change the shape and shift and a continuum band appears. The nature of the electronic continuum band has been studied in detail theoretically by Mils et al. [6] and experimentally by Wright and Balkanski [7]. The continuum is thought to be caused by nearly vertical transitions between occupied light-hole valence band states and unoccupied heavy-hole states [8]. Given a Fermi level about 100 meV below the top of the valence band, appropriate for 10²⁰ holes/cm³, and with the large known directional anisotropy in the separation between the two bands, one can explain the existence of a very broad electronic continuum from almost zero energy to almost the Fermi energy [8]. This is a pure electronic effect, in which a virtual electron-hole pair is created by an incoming photon. During excitation, the hole scatters to some empty state in the topmost valence band and the electron-hole pair recombines with a different energy as previously observed on p-type silicon [8].

5.3.2.1 LOPC mode

As it was explained in chapter 3.1 in a polar semiconductor collective excitation of free carriers (plasmon) interacts with the longitudinal optical (LO) phonon via their macroscopic electric fields, to form the LO phonon-plasmon coupled (LOPC) mode. The Raman line shape of the LOPC mode changes sensitively with the free carrier density. It can be seen clearly from Eq. (3.1) that free carrier concentration, for n-type, can be calculated from the ω_p data obtained from the fit of this equation by taking ω_p as the adjustable parameters. This is a good way to determine carrier density up to few 10^{18} cm^{-3} in case of n-type 4H-SiC, nonetheless for p-type 4H-SiC situation is quite different.

At first there is no significant shift as it was noticed in case of n-type 4H SiC. Typically, a variation of the n-type doping level of one order of magnitude would correspond to about 8 cm^{-1} difference in Raman shift. In the case of p-type doping it is not the case. Secondly the FLO line in crystal containing defects is distorted. Nonetheless the LOPC modes can be used as an indicator of carrier concentration in p-type 4H-SiC.

Let's look now on the optical part of Raman spectra. The spectra for several of investigated sample in range $955\text{-}975 \text{ cm}^{-1}$ are presented in the Fig.5. 7. The only clear difference between the spectra is the intensity of the FLO peak. We can also notice slight difference concerning the position, but the relation to the carrier concentration is not clear. In chapter 4 we showed that increasing doping level in n-type 4H-SiC the shift of FLO line appears, but it's not the case in p-type 4H-SiC. Knowing that, no shift of LOPC mode occurs in case of p-type 4H-SiC, one can distinguish the series of investigated samples between p-or n-type of 4H-SiC.

For each sample the LOPC mode was fitted by Gaussian function in order to obtain values of FWHM, area, intensity and wavenumber position of the peak. The Fig.5. 7 shows the analyzes of the changes of area, line positions (compared with the samples with low Al concentration) and FWHM and intensity of $\text{FLO}_{x(0)}$ line versus SIMS measurements.

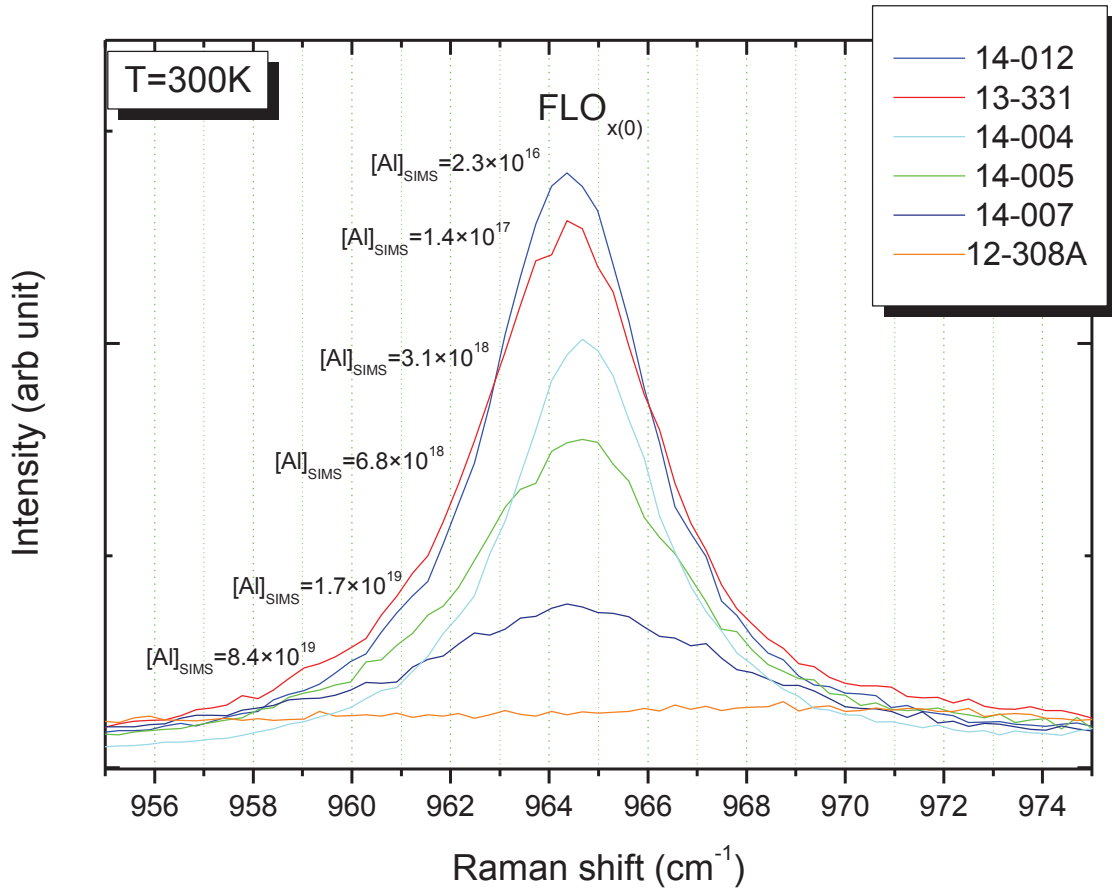


Fig.5. 7: Example of the Raman spectra collected at RT on investigated samples in range 955-975 cm^{-1} , the $\text{FLO}_{x(0)}$ line is visible.

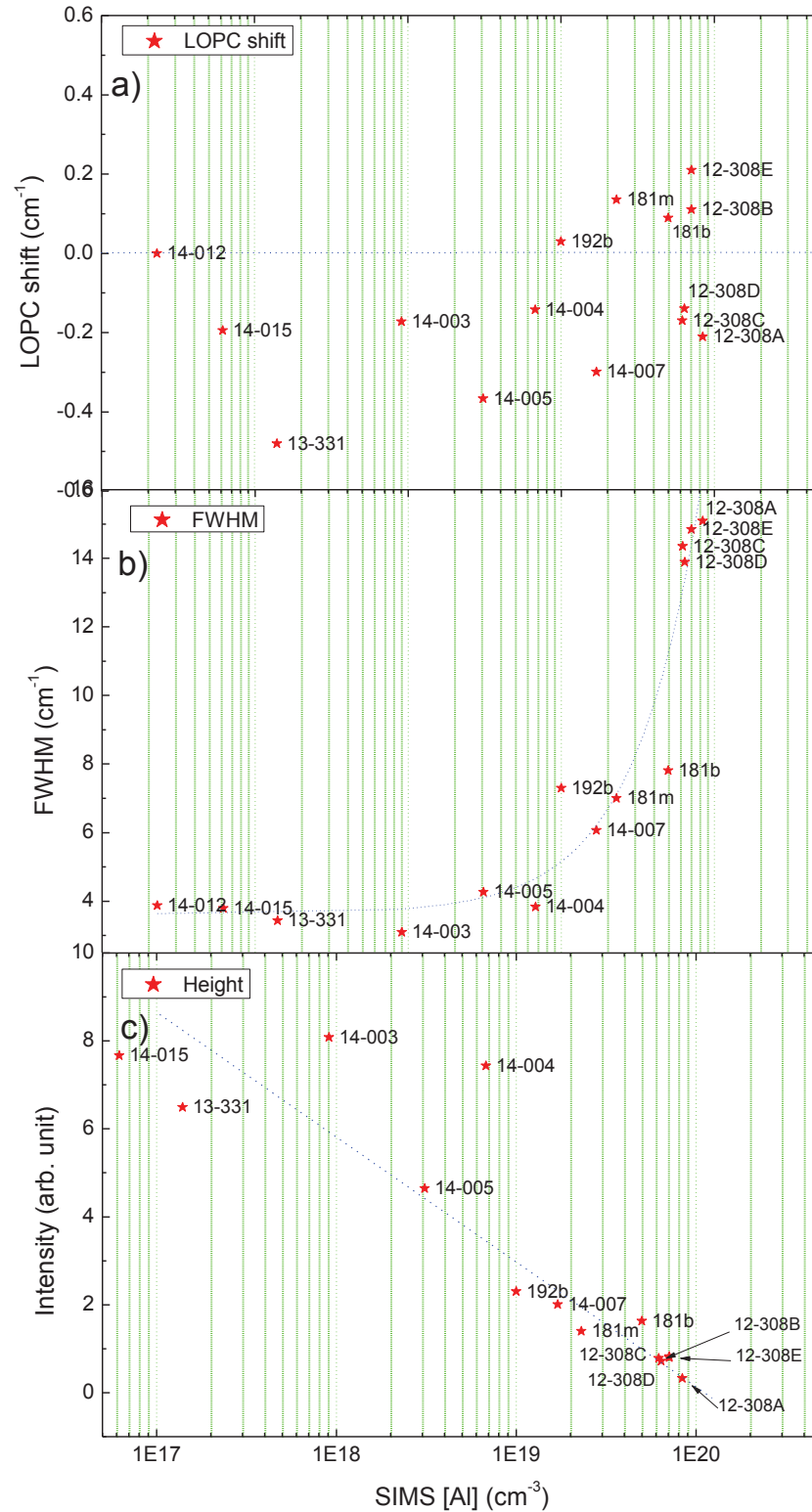


Fig.5. 8: Analyzes of LOPC mode, a) LOPC shift, b) FWHM, c) peak's intensity versus SIMS measurements for several samples. Blue dotted lines are guides for eyes.

The Fig.5. 8 a), confirms that no clear correlation between Al doping level and the position of the peak was found. No real shift appears increasing the Al concentration. Next issue is the FWHM of FLO line see Fig.5. 8 b). Here we can observe that for high doped samples (higher than 10^{18} cm^{-3}) the FWHM increases when increasing the carrier concentration. The Fig.5. 8 c) shows the variation of the relative intensity of the FLO peak. Again only for height doped samples with aluminum contain higher than 10^{18} cm^{-3} one can see that with increasing the aluminum doping the relative intensity decreases. Due to a different behavior comparing to n type samples, all these features could be used to indicate the type of carrier in this case p type in 4H-SiC.

Nonetheless, one has to keep in mind that FLO line can strongly depend on the crystal quality and could be distorted by contribution from the substrate in case of thin or low doped layers. Fig.5. 9 a) shows the Raman spectra in range $955\text{-}975 \text{ cm}^{-1}$ for samples with different Al concentration. The thickness of the samples is in range 3.5 up to $4.6 \mu\text{m}$ and aluminum varies from Al free to $5 \times 10^{19} \text{ cm}^{-3}$. Clear contribution of the substrate manifests as an addition peak and/or overlapped by $\text{FLO}_{\text{x}(0)}$ line for samples with concentration up to few 10^{17} cm^{-3} . Fig.5. 9 b) shows that in case of very low doped samples $\sim 10^{16} \text{ cm}^{-3}$ the contribution of the substrate can be seen even for thick samples.

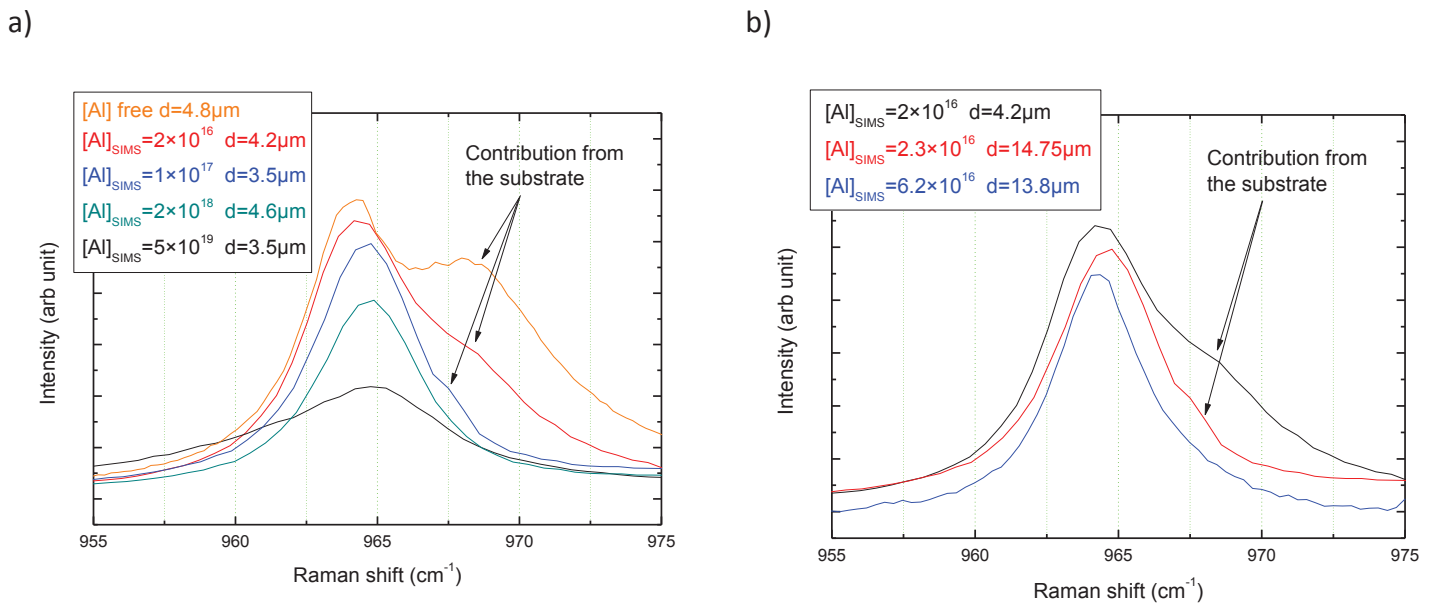


Fig.5. 9: Example of Raman spectra in range $945\text{-}980 \text{ cm}^{-1}$ for samples with different carrier concentration -a) and different thickness of the layer -b).

If the epilayer contains some defects the changes of the shape, wide and intensity could be also related to the defects and not only to the impurity content. This fact is remarkably important if we have to evaluate the carrier concentration. Better way to confirm and quantify the doping level for p-type 4H-SiC seems to be low energy range of the Raman spectrum the FTA modes.

5.3.2.2 FTA modes

When the carrier concentration increases, to quantify, the analyze the $FTA_{x(1/2)}$ modes (frequency range $\sim 190\text{-}210\text{ cm}^{-1}$ in case of 4H-SiC) will be done. This part of Raman spectra is presented in Fig.5. 10.

Accompanying the pure electronic effect which gives rise of continuum band, a clear shift and change in the Raman shape of the $FTA_{(1/2)}$ modes appear when the Al concentration increases higher than few 10^{17} cm^{-3} . The situation complicates and clear interference effects manifest between the continuum of electronic transitions and the FTA modes as these interferences arise because of the coupling in the Raman transitions matrix between the virtual electron-hole pair and the phonon states. More information about interference effect are given in chapter III. For each sample one can see two peaks FTA_+ and FTA_- .

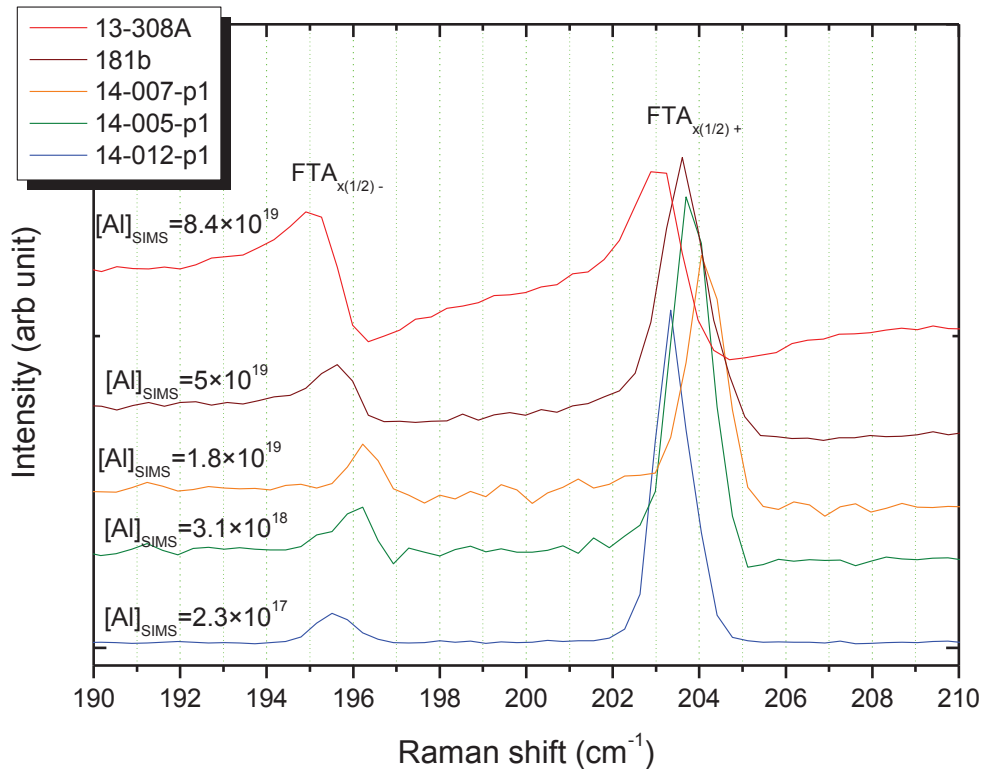


Fig.5. 10: Example of FTA modes of Raman spectra for several of investigated samples with aluminum concentration ranging from 2.3×10^{16} up to $8.4 \times 10^{19}\text{ cm}^{-3}$.

In order to quantify the aluminum concentration for p-type 4H-SiC using FTA modes we need to use, the intensity of the FTA modes introduced in chapter 3 (equation 3.22) with three Fano-parameters per mode.

Since for n-type 4H&6H-SiC the calibration curves have been already established and one can find them in the literature [9], for p-type 4H-SiC there is very little information and so far no calibration curve exist.

A series of electrical measurement on the same samples was done to obtain the carrier concentration in order to establish a new calibration curve for p type on 4H-SiC samples.

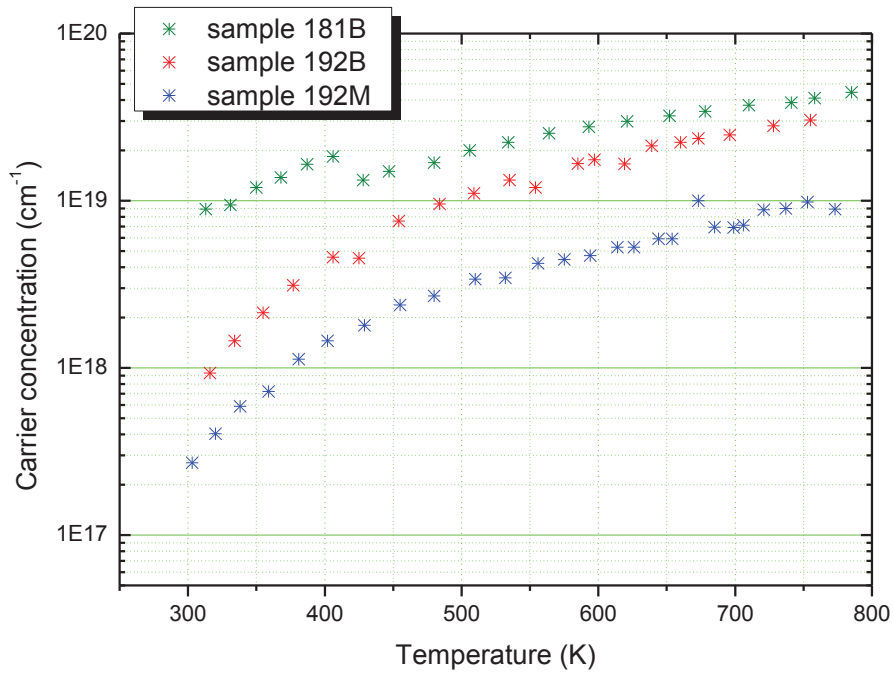
5.4 Carrier concentration by electrical measurements

The electrical measurements were done using standard DC methods on fourteen samples. The resistivity was measured in the Van der Pauw configuration using for the Hall Effect measurements a magnetic field of 1 Tesla. Since, in room temperature not all contain of aluminum is activated (especially for the low doped samples) in order to determine entire amount of acceptors the measurement as a function of temperature were performed. All samples were measured in temperature range 300K up to 800K. To investigate the temperature dependence, we used a furnace fitted with a quartz tube enabling to control the outer helium atmosphere. The temperature was measured using Pt100 resistor and stabilized within 0.3 K accuracy. The detailed description of the method and the experimental setup are presented in annex 3.

Since the donor concentration for all samples is negligible low one can estimate than in our cases $N_a - N_d$ is equal N_a .

An example of electrical measurement is shown in Fig.5. 11 a) and b). The carrier concentration (Fig.5. 11 a)) and mobility (Fig.5. 11 b)) are plotted as a function of temperature for three differently doped samples. With increasing the temperature the amount of activated aluminum increases and reaches the maximum at about 800K. In room temperature the carrier concentration is about to 1.5 order of magnitude lower than in the 800K. In the other hand the mobility decreases, when temperature increases.

a)



b)

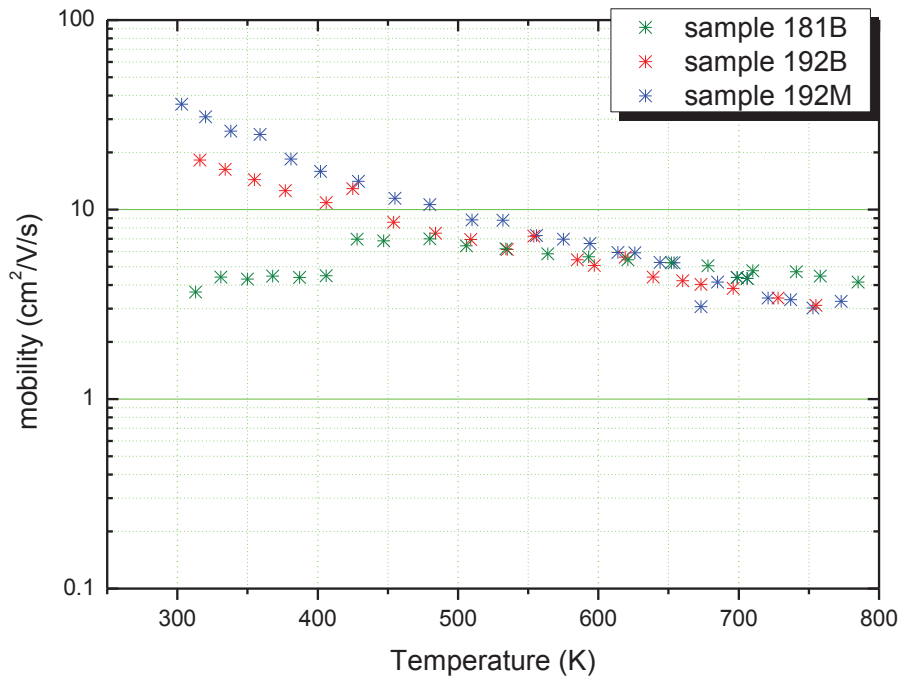


Fig.5. 11: a) Carrier concentration and b) mobility measured by Hall Effect as a function of temperature for three different samples.

The results of electrical measurements for several samples are summarized in Tab.5. 5 For samples with low carrier concentration (lower than few 10^{17}cm^{-3}) the evaluation of free carrier concentration was not possible.

SAMPLE	HALL EFFECT, N_A (CM^{-3})
175C	Al free
14-012	
14-015	
13-331	
14-003	$3 \times 10^{17}_{(\text{DL})}$
192M	2.7×10^{17}
192C	8.2×10^{17}
14-004	6.4×10^{17}
14-005	9.5×10^{17}
192B	8.7×10^{17}
14-007	2.5×10^{18}
181M	1.8×10^{18}
181B	8.5×10^{18}
12-308C	1.5×10^{19}
12-308D	1.8×10^{18}
12-308B	2.7×10^{18}
12-308E	2.8×10^{19}
12-308A	5.6×10^{19}
14-009	

Tab.5. 5: Carrier concentration values of investigated samples evaluated by Hall Effect measurements.

5.5 Calibration curve for p-type 4H-SiC.

Using Fano-formula, with three parameters per mode, we could successively fit all FTA modes profiles in the carrier concentration range few 10^{17} up to $4 \times 10^{19} \text{ cm}^{-3}$. These characteristics parameters are related to the Raman matrix element and the hole concentration. Two examples of the fit obtained on two samples with different Al concentration are shown on the Fig.5. 12. In the boxes are shown the Fano-parameters obtained due to the fit. Clear difference in term of shape is visible, also one can notice that the values of the parameters are different. The peaks position Ω (cm^{-1}) were found due to low doped samples, where the Fano-interference effect does not occur.

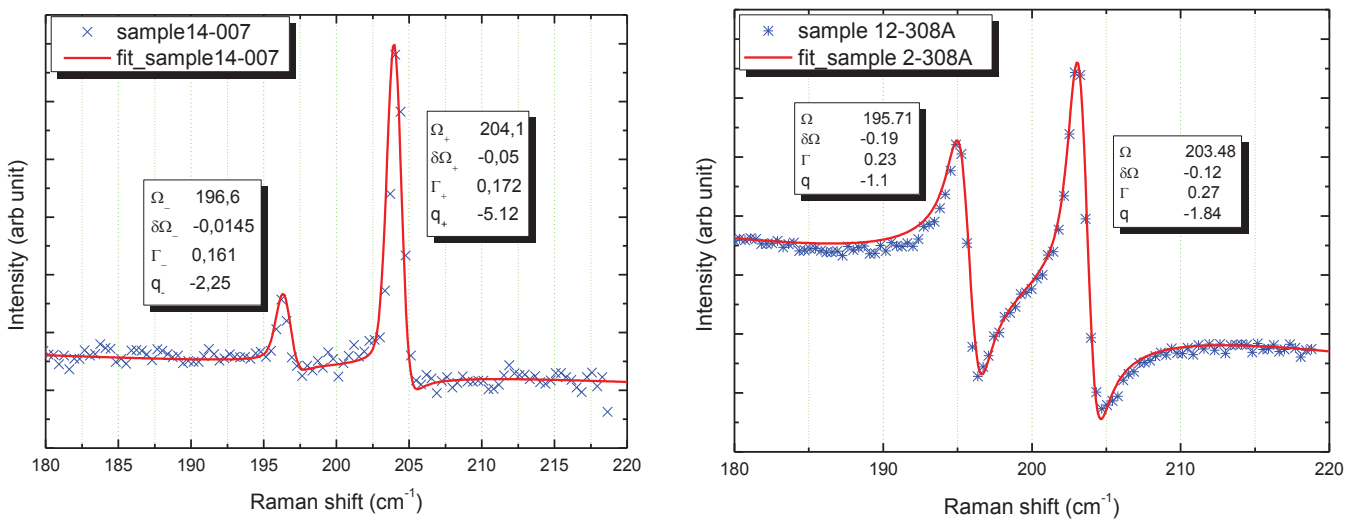
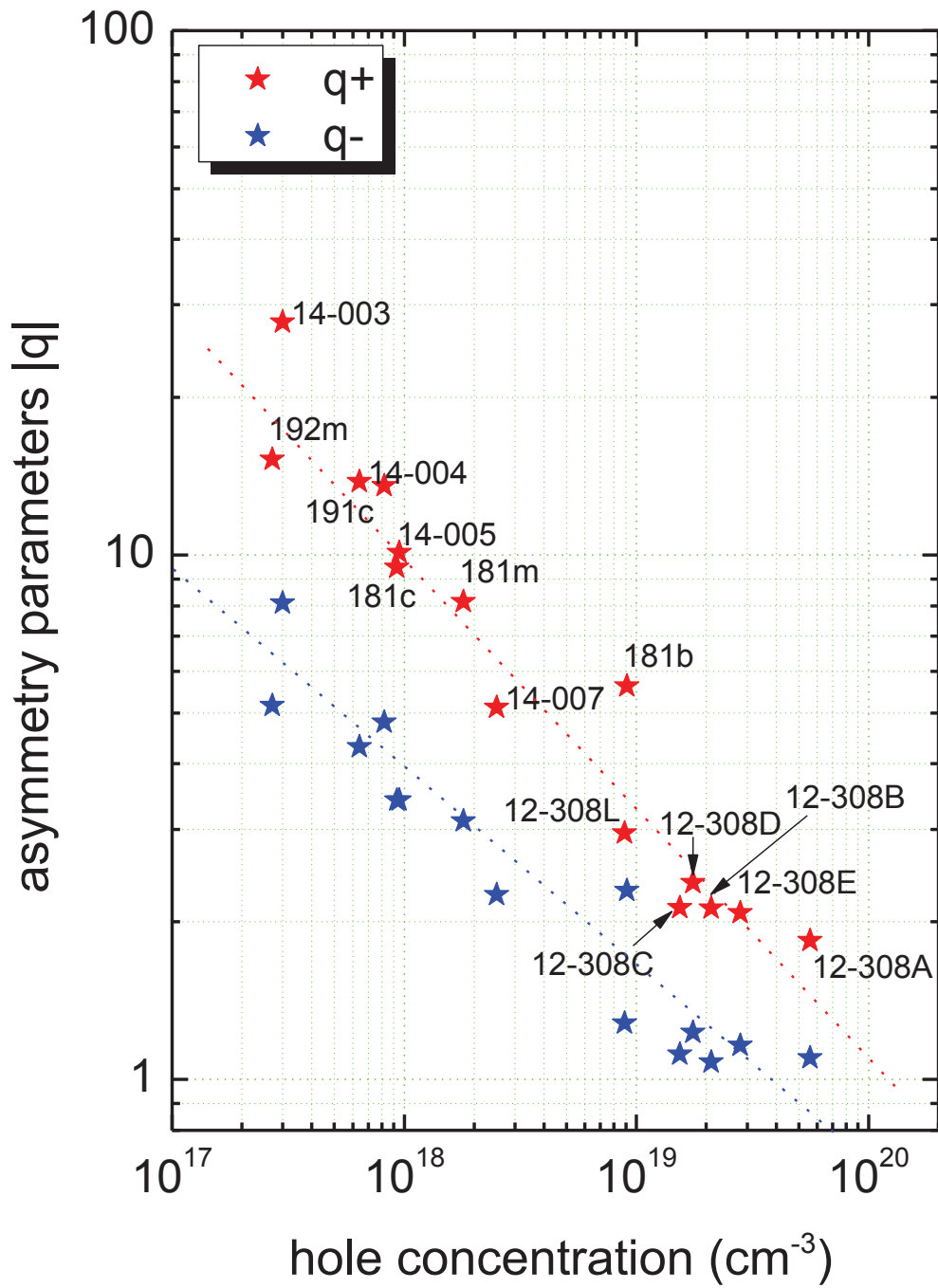


Fig.5. 12: Example of theoretical fit using Fano-formula for two samples with different carrier concentrations.

Fig.5. 13 presents the absolute value of asymmetry a) and broadening b) parameters as a function of hole concentration. The linear correlation has been found for both cases: asymmetry and broadening parameter. Along with increasing the carrier concentration, the absolute value of asymmetry parameters decrease for both q_+ and q_- . In the other hand the broadening parameter increases linearly with increasing carrier doping. Both parameters can be used to determine carrier concentration in p-type 4H-SiC in a quite wide range from few 10^{17} up to few 10^{19} cm^{-3} . Nonetheless it seems than the asymmetry parameters is much more suitable to use in lower range i.e. from few 10^{17} up to about 10^{19} cm^{-3} and for higher concentration range the broadening parameter Γ is more appropriate to determine carrier concentration. Similar trend of asymmetry and broadening parameters was observed for n-type 4H-SiC (see chapter 4).

a)



b)

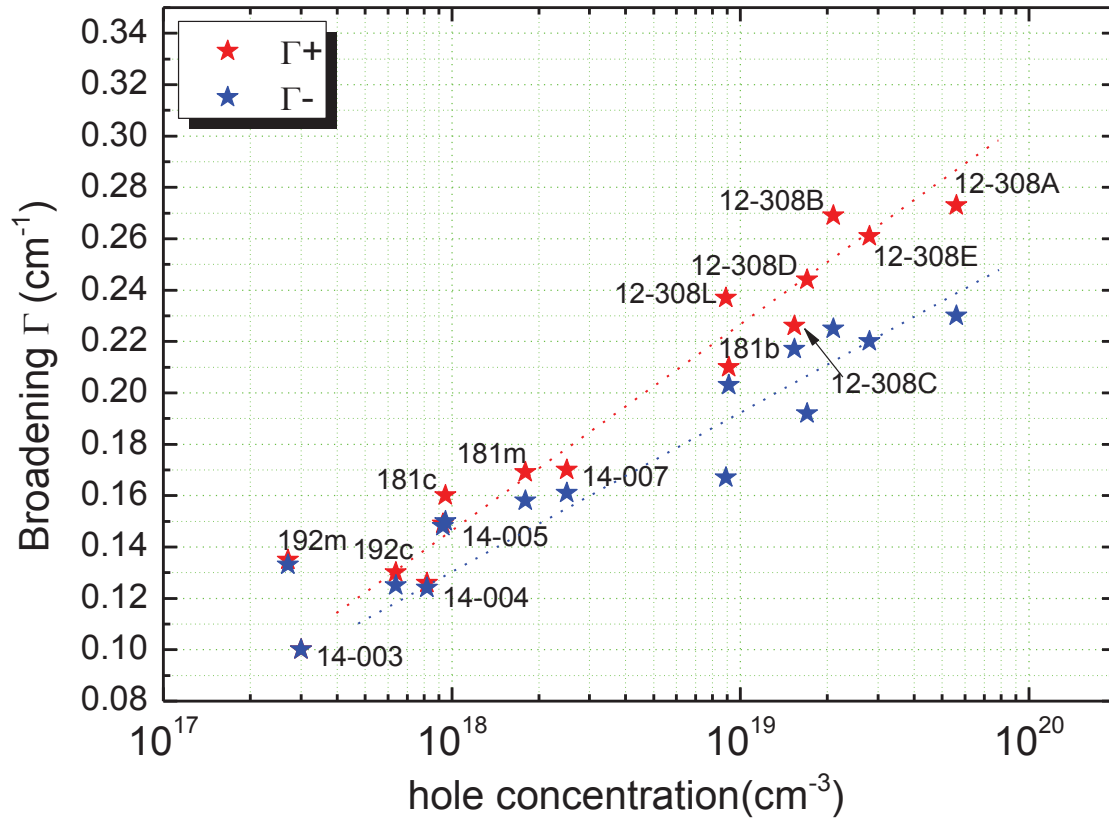


Fig.5. 13: The Fano-parameters as a function of hole concentration, a) asymmetry parameters, b) broadening parameters. Red and blue dotted lines are guide for eyes for q and Γ of FTA+ and FTA- line respectively.

Tab.5. 6 summarizes the aluminum/carrier concentration values evaluated using different methods. We could determine the Al concentration for 17 samples using SIMS measurements, and carrier concentration for 14 samples using Hall Effect measurements. LTPL allowed us to determine the doping level for 7 samples, this method is especially useful for low doped samples.

Sample	SIMS (cm ⁻³)		Hall effect (cm ⁻³)	LTPL (cm ⁻³)
	N	Al		
175C	≤10 ¹⁷ (DL)	Al-free		<10 ¹³
14-012	≤10 ¹⁷ (DL)	2.3×10 ¹⁶		8.2×10 ¹⁵
14-015	≤10 ¹⁷ (DL)	6.2×10 ¹⁶		2.8×10 ¹⁶
13-331	<DL	1.4×10 ¹⁷		~2×10 ¹⁷
14-003	<DL	9.1×10 ¹⁷	3×10 ¹⁷ _(DL)	9.1×10 ¹⁷
192C	≤2×10 ¹⁷	2 ×10 ¹⁸	2.7×10 ¹⁷	
192M	≤2×10 ¹⁷	4×10 ¹⁸	8.2×10 ¹⁷	
14-004	<DL	3.1×10 ¹⁸	6.4×10 ¹⁷	1.06×10 ¹⁹
14-005	<DL	6.8×10 ¹⁸	9.5×10 ¹⁷	1.22×10 ¹⁹
192B	≤10 ¹⁷	10 ¹⁹	8.7×10 ¹⁷	
14-007	<DL	1.7×10 ¹⁹	2.5×10 ¹⁸	1.4×10 ¹⁹
181M	<DL	2.3×10 ¹⁹	1.8×10 ¹⁸	
181B	<DL	5×10 ¹⁹	8.5×10 ¹⁸	
12-308C	<DL	6.2×10 ¹⁹	1.5×10 ¹⁹	
12-308D	<DL	6.4×10 ¹⁹	1.8×10 ¹⁸	
12-308B	<DL	7.1×10 ¹⁹	2.7×10 ¹⁸	
12-308E	<DL	7.1×10 ¹⁹	2.8×10 ¹⁹	
12-308A	<DL	8.4×10 ¹⁹	5.6×10 ¹⁹	

Tab.5. 6 : Summary of doping concentration values evaluated using different methods.

Both spectroscopic methods can be used to evaluate doping level in a non-destructive way. Nonetheless, both LTPL and Raman have their limitation. Fig.5. 14 shows the domain where the specific methods can be applied in order to determine aluminum/carrier concentration. Red color shows the range of usability of LTPL and blue corresponds to Raman. LTPL is more useful to evaluate Al concentration for low doped samples up to few 10¹⁷ cm⁻³ using ratio of intensity Al₀/Q₀. It can be also used in range from about 10¹⁸ to about 10¹⁹ cm⁻³ using FWHM of Al₀ line as a parameter. In the other hand Raman spectra and calibration curve that we made, allow us to evaluate carrier concentration in range few 10¹⁷cm⁻³ up to about 10²⁰cm⁻³. Combining LTPL and Raman one can evaluates the Al/carrier concentration in 4H-SiC in a very large range from ~10¹⁵ to ~10²⁰ cm⁻³. Notice that evaluation of doping in range 2×10¹⁷ to ~10¹⁸ cm⁻³, shown as black circle in Fig.5. 14 is not always possible using LTPL or Raman.

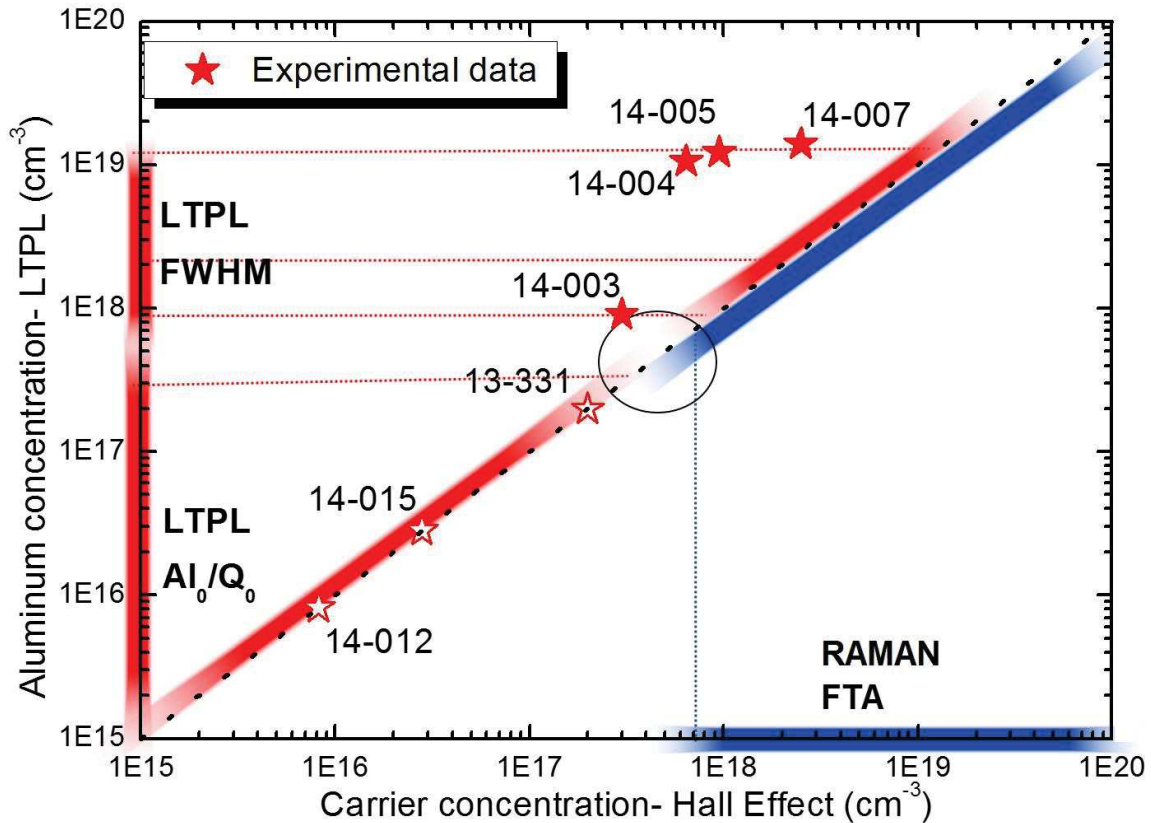


Fig.5. 14: Comparison between aluminum and carrier concentration determined by LTPL and Hall Effect measurements in Al doped 4H-SiC materials. Red stars are the value determined in this work (empty stars are the value obtained only by PL). Red color corresponds to the range of utility of PL method to determine doping level and blue to Raman.

5.6 Application for mapping of 2' wafer

In this section we propose to use previous results to quantify hole carriers concentrations in highly Al-doped 4H-SiC 2' inch wafers. Based on the analysis of Raman spectra, and more precisely focusing on the change of the $FTA_{x(1/2)}$ mode. This method is non-destructive, contactless and then allows the mapping of full wafers. Thus, this method completes the range of optical techniques and to quantify the p or n carriers concentration in 4H-SiC material, from low to high doping level.

A 2' inch high p-doped 4H-SiC sample was investigated. The sample was made by Chemical Vapor Deposition (CVD) on the 4H-SiC 8° off axis substrate. The inhomogeneity of the layer was intentionally achieved by using a non-rotated substrate's support. On whole wafer 34 Raman spectra were collected each 0.75 cm on the 2' inch sample. The Fano analysis of the

each spectrum was done. Using the asymmetry parameter correlated to the calibration curve Fig.5. 13 a) we obtain the mapping of the doping concentration presented in Fig.5. 15. The variation of hole concentration is in range 2.6×10^{18} up to $6.0 \times 10^{19} \text{cm}^{-3}$ with an average value about $2.4 \times 10^{19} \text{cm}^{-3}$. The advantage of this method is to measure even bigger samples than 2" without contactless and damage them. Note that the distribution of the doping level on the Fig.5. 15 was obtained by linear interpolation of the values. The average errors of interpolation were estimated to be about 16%.

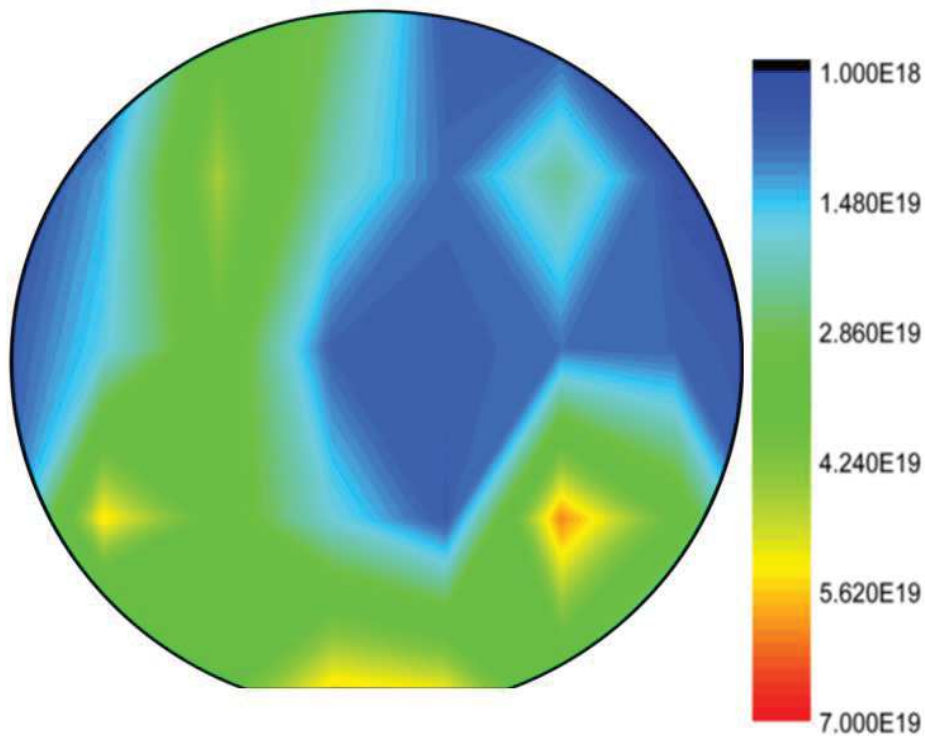


Fig.5. 15: p-doping mapping of the 2 inch wafers obtained by analyze of the Raman spectra

Due to the mapping shown in Fig.5. 15 one can see the distribution and the possible behavior of the TMA flow. This can be helpful to improve the CVD growth process and extend the knowledge about specific CVD setup. The TMA flow was applied from the flat side of the wafer. One may notice a very high concentration (marked by yellow and red colors) close to the flat edge as well as in both side. In the middle of the sample though we noticed the lowest value.

Using computer program "Gwyddion" we could evaluate the percentage of doping concentration. We found that about 36% of wafer contains less than $1.4 \times 10^{19} \text{cm}^{-3}$. About 57% of wafer ranging from about $1.5 \times 10^{19} \text{cm}^{-3}$ to about $5 \times 10^{19} \text{cm}^{-3}$. And finally we found that less than 7% contain more than $5 \times 10^{19} \text{cm}^{-3}$.

5.7 Conclusion

In this chapter LTPL and micro-Raman spectroscopies were used to investigate the p type doping in 4H-SiC epilayer.

As already said, the LTPL spectroscopy is the only one optical method that can give unambiguously the information about compensation and the polarity of the layer. This could be also the mean to determine the nitrogen and aluminum contain for several samples. Nevertheless, in case of high doped samples (with Al_{SIMS} content from higher than 10^{18} cm^{-3}), strong presence of the N- Al_{DAP} lines do not enable us to determine the aluminum concentration using PL. The undoubted advantage of the LTPL spectroscopy is the fact that it allows us to quantify the doping level for very low doped samples, what is not always possible by using others methods like Raman or electrical measurements. In the other hand to investigate near band edge energy range of SiC polytypes the measurements have to be done in low temperature ($\sim 4\text{K}$) what makes this method complicated and time consuming.

On the other hand, micro-Raman spectroscopy is a powerful tool to investigate different aspects of SiC: from polytype and crystal quality verification to electrical proprieties (carrier concentration and mobility) [5]. Another advantage is the fact that Raman measurements can be done in room temperature and the size of the sample in practice is unlimited. The investigation of LOPC and FTA modes were done. In contrary to n-type 4H-SiC material, we have demonstrated that LOPC mode is not suitable to investigate the p-type doping level. Thus, we focused on the FTA modes. Using Fano-formula with three parameters per mode we could successfully fit all Raman spectra in low frequency range. Correlating carrier concentration determined by electrical measurements and Fano-parameters, new calibration curves for p-type 4H-SiC were worked out. The linear correlation for asymmetry and broadening parameters as a function of carrier concentration were found. We showed that it's possible to determine the carrier concentration using the Raman spectra.

Despite the fact, that both technics can provide similar information about the crystal one may consider them as a complementary techniques rather than competitive. Indeed, for low doped samples the only way to determine the doping content is to use LTPL. However, for high doped samples the best way seems to be the investigation of FTA modes of Raman spectra.

Bibliography

- [1] J. Camassel, S. Juillaguet, M. Zielinski, C. Balloud, *Chem. Vap. Deposition*, vol. 12, p. 549, 2006.
- [2] C. Balloud, «Méthodes de caractérisation optique de SiC,» PhD thesis, p. 152, 2005.
- [3] H. Peyre, J. Sun, J. Guelfucci, S. Juillaguet, J. Hassan, A. Henry, S. Contreras, P. Brosselard, J. Camassel, *Materials Science Forum*, vol. 711, p. 164-168, 2012.
- [4] R. Berseman, M. Jouanne, M. Balkanski, In *Proc. 11th Intern. Conf. Physics of semiconductors*, Warsaw, p. 1181, 1972.
- [5] S. Nakashima, H. Harima, «Raman Investigation of SiC Polytypes,» *Phys. Stat. Sol*, vol. 39, p. 162, 1997.
- [6] D. Mills, R. Wallis, E. Burstein, In *Light Scattering in Solids*, Paris, 1971.
- [7] G. Wright, M. Baalkanski, *Mat. Res. Bull*, vol. 6, p. 1097, 1971.
- [8] F. Cerdeira, T. A. Fjedly, M. Cardona, *Phys. Rev. B*, vol. 8, p. 4734, 1973.
- [9] T. Mitani, S. Nakashima, *J. Appl. Phys*, vol. 043514 , p. 112, 2012.

General conclusions

The objective of this work was to investigate physical and electrical properties of 4H-SiC focusing on the evaluation of the doping / carrier concentration using non-destructive and contactless methods for n and p type. This work was done in the framework of the NetFISiC European project. The investigated samples were grown by CVD growth techniques by NOVASIC, one of the partners of the NetFISiC project. The techniques used to study the samples were Secondary Ion Mass Spectroscopy (SIMS), Low Temperature Photoluminescence (LTPL) spectroscopy, micro-Raman spectroscopy, and Hall Effect. All measurements were done in the laboratory Charles Coulomb at Université Montpellier 2.

In Chapter 1 some basic information have been given, which concern the structural and physical properties of SiC. Emphasis was given on the hexagonal 4H polytype.

In Chapter 2 the experimental techniques and experimental conditions used for samples characterisation (SIMS, PL and Raman) have been given.

In Chapter 3 the theoretical approach of evaluation of carrier concentration in n- and p-type 4H-SiC using Raman spectroscopy is done. Focusing on the optical part of Raman spectra, we studied the differences on the LOPC mode related to the type of carrier. Clear correlation between the LOPC and carrier concentration was found for n-type 4H-SiC. An important point was that, the LOPC mode's shape is almost independent of the mobility for low electrons concentration, whereas for the high electron concentration the LOPC mode exhibits a strong dependence with the mobility. However no significant change of the position of the LOPC line was observed in case of p-type. Therefore to evaluate the carrier concentration the optical part of Raman spectra is useful only in case of n-type material.

In the second part we focused on the acoustic range. The model of Fano-interference effect was described for n-type 4H-SiC and then extended for p-type SiC. The influence of Fano-parameters on the shape of the FTA line was studied. We have shown that the asymmetry parameter q does not influence the position of the peak. On the other hand, when the broadening Γ parameter increase the line is getting broader and the maximum of the peak position changes. Finally we applied this fit model to few experimental spectra.

In Chapter 4 we proposed to study, in n-type 4H-SiC samples, the nitrogen concentration using LTPL and carrier concentration using μ -Raman measurements.

At first, in each sample the nitrogen concentration values were checked by SIMS measurements. It is well known that LTPL spectroscopy can be used to evaluate quantitatively the nitrogen concentration in 4H-SiC. Focusing on the near band edge observed by LTPL, a clear signature of 4H-SiC was noticed. Using three calibration curves from the literature for three different concentration ranges we successfully determined the nitrogen concentration for investigated samples. A good agreement with the results

obtained by SIMS was found. Nonetheless we pointed out some interesting issues. According to calibration curves, the evaluation of nitrogen doping should be possible in ranges 2×10^{14} up to $2 \times 10^{19} \text{ cm}^{-3}$. However, in practice we noticed that around 10^{16} and 10^{18} cm^{-3} (i.e. in the transition regions of the abacuses) the evaluation of nitrogen concentration is not always possible.

In this work we used μ -Raman mainly to evaluate the carrier concentration. The investigation was done focusing on two parts of Raman spectra. First we investigated optical part. As expected, clear correlation between $\text{FLO}_{x(0)}$ and carrier concentration was found in case of n-type 4H-SiC. Increasing carrier concentration, shift to higher energy and broadening of this line were noticed. Using the calibration curves of FWHM and Raman shift of LOPC mode as a function of carrier concentration, we estimated values of carrier concentration for three of five of investigated samples. Although the calibration curves cover the carrier concentration range from $\sim 2 \times 10^{16}$ up to $\sim 2 \times 10^{19} \text{ cm}^{-3}$, we showed that, in real, one can use these calibration curves in narrower range $\sim 4 \times 10^{16}$ up to $\sim 9 \times 10^{17} \text{ cm}^{-3}$ because LOPC line vanishes rapidly for higher concentration. We also pointed out that, the $\text{FLO}_{x(0)}$ line can be distorted by contribution from the substrate especially for thin and / or low doped epilayer.

To evaluate the carrier concentration higher than $\sim 9 \times 10^{17} \text{ cm}^{-3}$, the low energy (acoustic) part of Raman spectra was used, where we focused on FTA_{\pm} modes. Indeed, changes of the position and the shape of these lines as a function of nitrogen concentration were noticed. The FTA_{\pm} lines on the experimental spectra were successfully fitted by the model of Fano-interference effect. For each fit three adjustable parameters per mode were used. First noticed that the distance $\Delta\omega$ between the FTA_{+} and FTA_{-} decreases for the carrier concentration higher than few 10^{18} cm^{-3} . The asymmetric parameter q is negative and $|q|$ decreases as the distortion in the FTA mode increases. Finally the broadening parameter Γ increases when increasing carrier concentration. Using calibration curves from the literature corresponding to Fano-parameters as a function of carrier concentration we are able to evaluate the carrier concentration for high doped samples in the range about 2×10^{18} up to about 10^{20} cm^{-3} . When evaluating the carrier concentration by this method, the errors were found to be lower than 7% Γ parameter and 16% for q parameter.

Finally we compared the values of nitrogen and carrier concentration obtained by LTPL and Raman measurements, respectively. LTPL has a big advantage over others methods because beside doping evaluation can provide information about compensation and can be used to determine the impurities species. The nitrogen concentration can be evaluated using LTPL spectra and three different calibration curves for three different doping ranges from 10^{15} up to 10^{19} cm^{-3} . Raman spectroscopy does not provide any information about possible compensation. Using optical and acoustic part of Raman spectra the evaluation of carrier concentration is possible in range $\sim 4 \times 10^{16}$ up to $\sim 9 \times 10^{17} \text{ cm}^{-3}$ and about 10^{18} up to about 10^{20} cm^{-3} .

In the chapter V the evaluation of aluminum/carrier concentration in p-type 4H-SiC was done. Using SIMS measurements the aluminum concentration was determined and the nitrogen concentration was checked. Then we focused on non-destructive methods. From LTPL experiment, the evaluation of Al doping, for low doped samples (lower than 10^{18} cm^{-3}), was done using calibration curve from literature and the ratio of intensity of Al_0/Q_0 lines. We pointed out that, when evaluating aluminum concentration using calibration curve and intensity ratio, the nitrogen concentration has to be taken into the consideration. For samples with Al concentration higher than few 10^{18} cm^{-3} the $\text{DAP}_{\text{N-Al}}$ is strongly pronounced. In this case since we do not observe Q_0 line to evaluate the Al doping level the FWHM of Al_0 line and calibration curve were used in the range $\sim 10^{18}$ up to $\sim 10^{19} \text{ cm}^{-3}$. Compare to SIMS measurements a good agreement was found for Al concentration lower than 10^{18} cm^{-3} .

Next, the Raman measurements were used to evaluate the carrier concentration. We investigated first the optical part of Raman spectra. But no clear correlation to the carrier concentration was found. This behavior differs clearly to the case of n type. The only parameter that could be related to the carrier concentration seemed to be FWHM. Moreover, we pointed out also that the contribution from the substrate, in case of low doped relatively thin epilayers, can be seen as an additional large peak in optical range. Since $\text{FLO}_{\text{x}(0)}$ line for thin and / or low doped samples can be distorted by contribution from the substrate as an additional peak or broadening of FLO line we decided to focus on low energy part. Clear Fano-interference effect was noticed for samples with $[\text{Al}]_{\text{SIMS}}$ higher than about 10^{18} cm^{-3} . The carrier concentration was measured by Hall effect for several samples. Then all FTA_{\pm} modes were fitted using mentioned before Fano-formula. We obtained a new calibration curves for p-type combining Fano parameters with carrier concentration obtained by electrical measurements. The linear correlation has been found for both cases asymmetry and broadening parameter. Along with increasing the carrier concentration the absolute value of asymmetry parameters decreases. In the other hand the broadening parameter increases when increasing the carrier concentration. Both calibration curves can be used to determine the carrier concentration in p-type 4H-SiC in range few 10^{17} up to about 10^{20} cm^{-3} .

Finally, the comparison between two spectroscopic techniques was done. We conclude that in order to evaluate the aluminum / carrier concentration level in p-type 4H-SiC in a range $\sim 10^{15}$ to $\sim 10^{18} \text{ cm}^{-3}$ both LTPL and Raman have to be used together. We also found that the evaluation of nitrogen / carrier concentration in range 2×10^{17} to $\sim 10^{18} \text{ cm}^{-3}$ is not always possible using neither PL nor Raman.

At the end, we proposed to apply this method to evaluate the distribution of carrier concentration on a 2' wafer. A mapping of Raman measurements have been done on the 2'inch wafer. Using the "homemade" calibration curve, we were able to find out the carrier concentration in a non-destructive way for p-type 4H-SiC wafer. Big advantage of this

method is that it is non-destructive with no special sample preparation needs and practically no limitation in terms of size of sample.

In this work, we demonstrated that non-destructive and contactless methods like LTPL and Raman spectroscopies are good ways to evaluate doping / carrier concentration in n- or p-type 4H-SiC in a wide range. We check the validity of the existing calibration curve of LTPL and Raman for both n- and p-type comparing the evaluated values with SIMS results. The limitation of each of the method was indicated and discussed. Finally we conclude that presented methods: LTPL and Raman are complementary and in order to evaluate doping / carrier concentration in range $\sim 10^{15}$ up to $\sim 10^{20}$ cm^{-3} both methods have to be used in common. Finally we make the calibration curve for high doped p-type 4H-SiC combining Fano-parameters and carrier concentration and demonstrated that the calibration curve could be used to obtain a carrier concentration mapping on 2 inch wafers.

Annex 1: Evaluation of doping in 4H-SiC by photoluminescence

Nitrogen content evaluation- theoretical approach

There are two possible ways for it to recombine (radiatively or non-radiatively) for the travelling free exciton in a low doped semiconductor:

- by thermalizing and recombining or,
- being trapped by a neutral impurity and then recombining (again radiatively or non-radiatively).

In second case the time-dependent concentration of free excitons obeys the basic rate equation:

$$\frac{dn_{FE}}{dt} = g_{FE} - \left(\frac{1}{\tau_{FE}^r} + \frac{1}{\tau_{FE}^{nr}} \right) n_{FE} - t_{RX} \quad (A.1)$$

Here: t_{RX} is a transfer term ($\text{cm}^{-3}\cdot\text{s}^{-1}$) that accounts for all possible (extrinsic) relaxation mechanisms toward one (or more) radiative (residual-impurity related) low energy state(s).

When the free exciton is trapped to a neutral donor beforehand recombination then a new four particle complex appears. This new particle complex is called neutral and consists of the nucleus, two electrons and one hole. The concentration of the bound excitons n_{DX} versus time is given by the following equation:

$$\frac{dn_{DX}}{dt} = t_{DX} - \left(\frac{1}{\tau_{DX}^r} + \frac{1}{\tau_{DX}^{nr}} \right) n_{DX} \quad (A.2)$$

where t_{DX} is the reduced transfer rate from t_{RX} and τ_{DX}^r and τ_{DX}^{nr} are the radiative and non-radiative lifetimes of the bound excitons respectively. In SiC the main donor impurity is assumed to be nitrogen that in low temperature can act as neutral donors to bound excitons. The transfer rate in equation (A.2) can be considered as a generation rate of bound excitons coming from the trapping (reduction) of free excitons. So this term depends in two basic terms:

- the concentration of free excitons,
- the probability of finding a neutral donor atom inside the Carbon sites of the SiC matrix ($[N]/[C]$) multiplied by the scattering frequency of the free excitons (f_{FE}). This term can be expressed as:

$$t_{DX} = f_{FE} n_{FE} \frac{[N]}{[C]} \quad (A.3)$$

In expression (A.3) the $f_{FE}/[C]$ is nothing more than a capture rate constant that can be written as B_{FE} ($\text{cm}^3 \cdot \text{s}^{-1}$). If equations (A.1) and (A.2) are considered in steady state conditions then they give:

$$\frac{dn_{FE}}{dt} = 0 \quad \text{and} \quad \frac{dn_{DX}}{dt} = 0 \quad (\text{A.4})$$

The luminescent intensity (in our case the LPTL intensity) of the free excitons and bound excitons is given by:

$$I_{FE} = \frac{n_{FE}}{\tau_{FE}^r} \quad \text{and} \quad I_{DX} = \frac{n_{DX}}{\tau_{DX}^r} \quad (\text{A.5})$$

For impurity concentrations simply I_{FE} transitions appear due to intrinsic material parameters. Once the impurity concentrations increases and after a certain level the I_{DX} increases progressively whereas the I_{FE} increases. The threshold of N impurities for 4H-SiC is 10^{13} to 10^{14} cm^{-3} [1]. On increasing N further, the transfer becomes complete and, provided both exciton features have similar decay times, I_{DX} finishes with intensity similar to I_{FE} . In order to probe further the dimensionless ratio of I_{DX}/I_{FE} is taken. By using the above equations:

$$\frac{I_{DX}}{I_{FE}} \approx f_{FE} \frac{\tau_{DX}^{nr} \tau_{FE}^r}{\tau_{DX}^r} \frac{[N]}{[C]} \quad (\text{A.6})$$

By this equation it is possible to define the dimensionless parameter:

$$A_1 = f_{FE} \frac{\tau_{DX}^{nr} \tau_{FE}^r}{\tau_{DX}^r} \quad (\text{A.7})$$

Since in SiC, C is a matrix element and has a more or less steady value, it can be incorporated in equation (A.7) and transform equation (A.6) for SiC and N impurities into:

$$[N] = A_2^{-1} \frac{I_{DX}}{I_{FE}} \quad (\text{A.8})$$

For 4H-SiC, due to the large unit cell, there are 24 optically active phonon modes instead of 4 in Si. These couple in different ways with all, free or bound, zero-phonon wave-functions that results in 24 different phonon replicas per zero phonon line (ZPL) with 24 different intensities [2]. Also there are two ZPLs associated with the radiative recombination of FEs bound to a given series of neutral donor (or acceptor) species. For nitrogen they are noted in the literature as P_0 and Q_0 , and refer, as it has been mentioned before, to the hexagonal and cubic lattice sites, respectively. Altogether, this results in approximately 1250 possible (independent) combinations of $I_{DX} - E_{\text{phonon}}/I_{FE} - E_{\text{phonon}}$ lines. From these lines only the ones corresponding to the most intense components are usually considered.

It has been reported in the literature by Ivanov et.al. [3] and Camassel et al. [1] that equation (A.8) works really well in hexagonal SiC polytypes. He demonstrated with a series of 4H- and 6H-SiC that the intensity ratio I_{Q_0}/I_{FE-77} scales linearly in a log-log scale. A diagram demonstrating from reference [1] is shown in Fig.A.1.

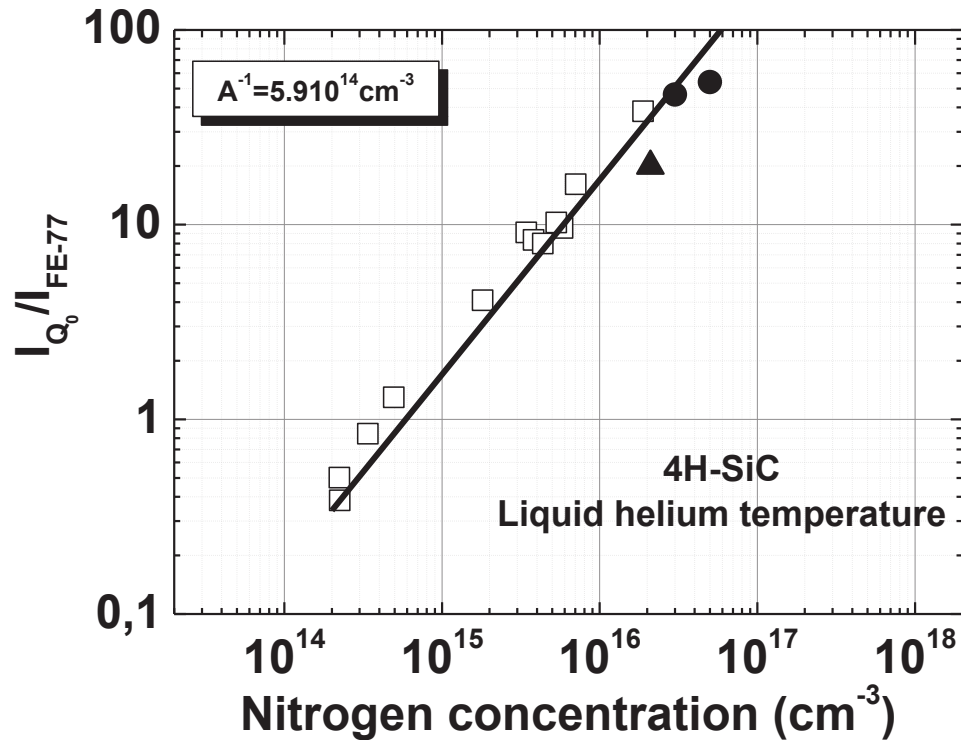


Fig.A.1: Experimental values of the intensity ratio I_{Q_0}/I_{FE-77} in 4H-SiC plotted versus nitrogen concentration. The open squares are experimental data obtained from the [3]. The full symbols are experimental results obtained from [1] using C-V (dots) and SIMS (triangle) measurements to determine the residual donor concentration. The solid line is a least mean square fit. The value of the final slope ($5.9 \times 10^{14} \text{ cm}^{-3}$) is very close to the one ($5.2 \times 10^{14} \text{ cm}^{-3}$) found in the literature [3].

As the doping concentration increases the P_{77} line disappears (high N concentration) and there only left parameters that can be observed is the broadening and shifting of the Q_0 . This was studied by Forsberg et al. [4] and comes from the change in scattering frequency of excitons when the doping concentration increases. In the case of higher nitrogen concentration (higher than few 10^{16} cm^{-3}) there is no more intrinsic transition. In the other hand we can observe the variation of the relative intensity of the lines P_{77} vs. Q_0 . In general for the nitrogen concentration lower than 10^{17} cm^{-3} the P_{77} line is more intense than the Q_0 line. Nevertheless from the N concentration's value of about 10^{17} cm^{-3} the P_{77} line is getting less intense and the Q_0 line is starting to dominate the spectrum. A schematic representation for this case can be seen in Fig.A.2. The values for 6H-SiC are coming from the work of reference [5], while the values for 4H-SiC are coming from references [6] and [1]. The solid lines are calculated using the equation:

$$\frac{(I_{DX})_C}{(I_{DX})_H} = R_0 + R_1[N] + R_2[N]^2 \quad (\text{A.9})$$

The values for R_0 , R_1 and R_2 are listed in Tab. A.1 for 4H- and 6H-SiC.

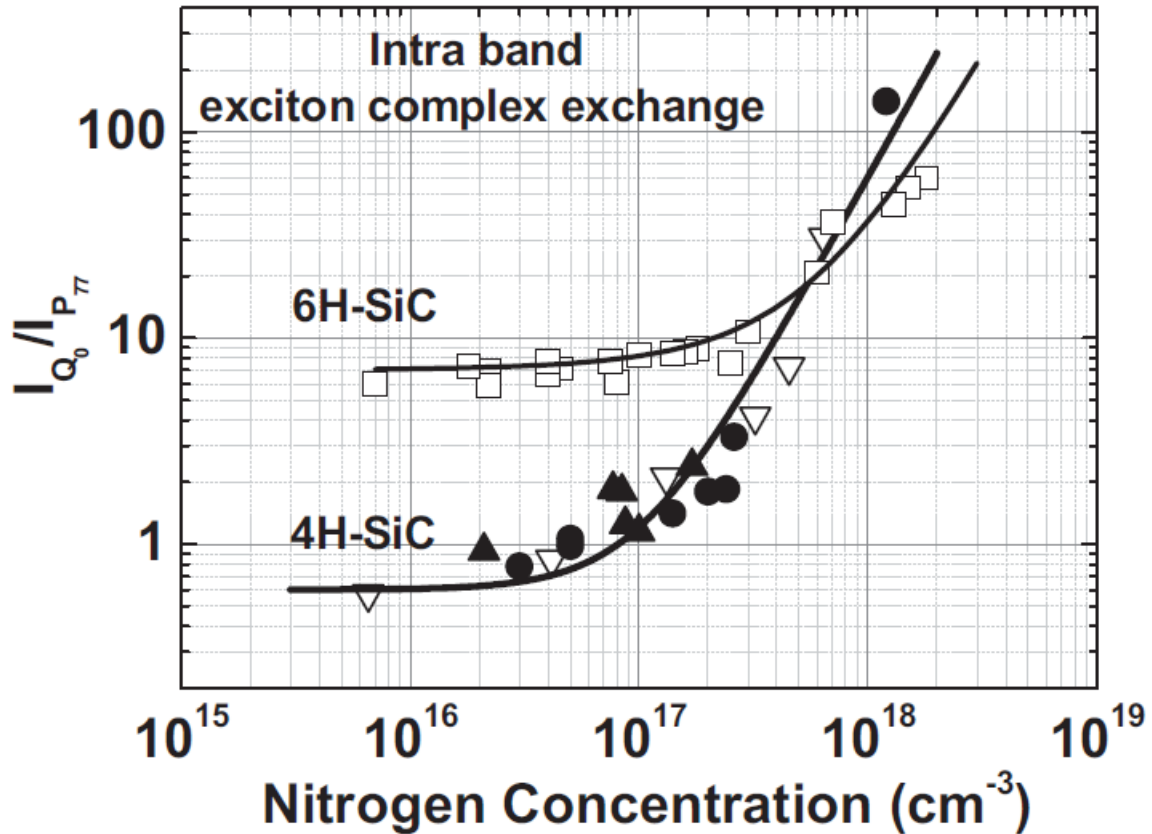


Fig.A.2: Intra-bound exciton complex exchanges observed in the case of 4H-SiC (lower curve) and 6H-SiC (upper curve). The solid lines are for demonstration purposes only. Each was fitted using Eq. (A.9) using the parameter values listed in Tab.A.1. Full symbols are experimental data from [1] for 4H-SiC. C-V (dots) and SIMS (triangle) measurements were used to deduce the residual donor concentration. Open inverse triangles are from [6]. Open squares are taken from [5].

Polytype	R_0	R_1 [cm^3]	R_2 [cm^6]
4H-SiC	0.7	3×10^{-18}	5×10^{-35}
6H-SiC	6.5	1×10^{-17}	2×10^{-35}

Tab. A.1: List of parameters used in Eq. (A.9) to draw the lines shown in Fig.A.2.

Finally for the concentration higher than few 10^{18} cm^{-3} only the recombination related to the nitrogen in the cubic site is visible, and we can observe the shift to the lower energy and broadening of the Q_0 line as is shown in figure Fig.A. 3. It has been shown that these two parameters: the energetic position and the Full Half Way Maximum (FWHM) of the Q_0 line can be used to determine the concentration of nitrogen [5], [6]. Fig.A. 3 and Fig.A.4 show the FWHM and the energy position shift of the Q_0 line respectively versus the concentration of the nitrogen density. The covered concentration values are between few 10^{16} up to $2 \times 10^{19} \text{ cm}^{-3}$.

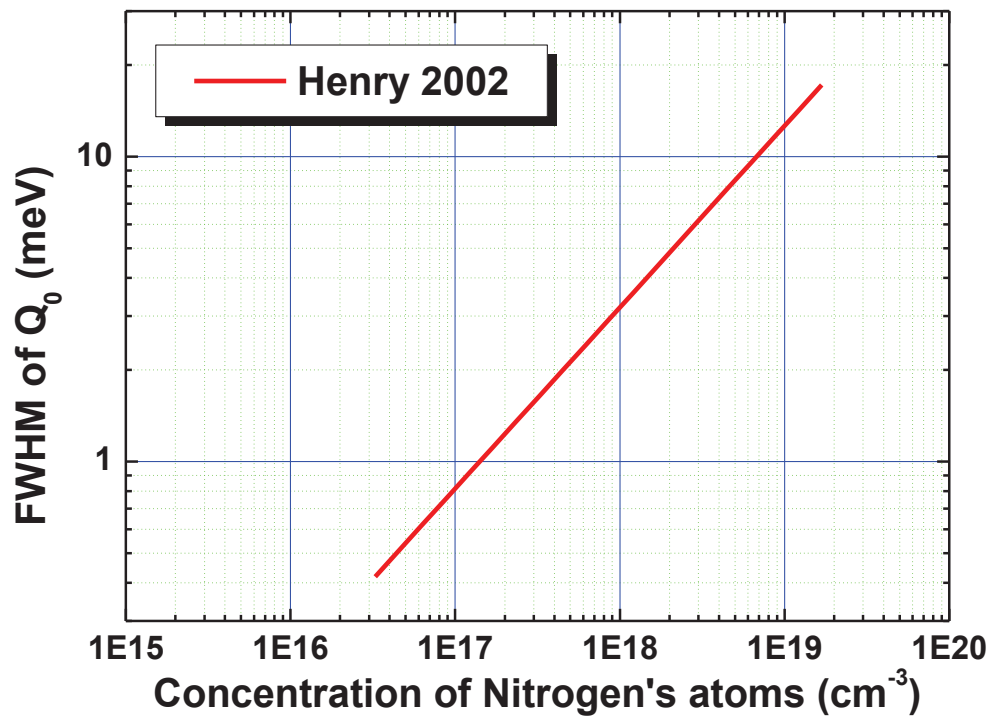


Fig.A. 3 Full Half Way Maximum (WHWM) of the Q_0 line as a function of the density of the nitrogen atoms [6]

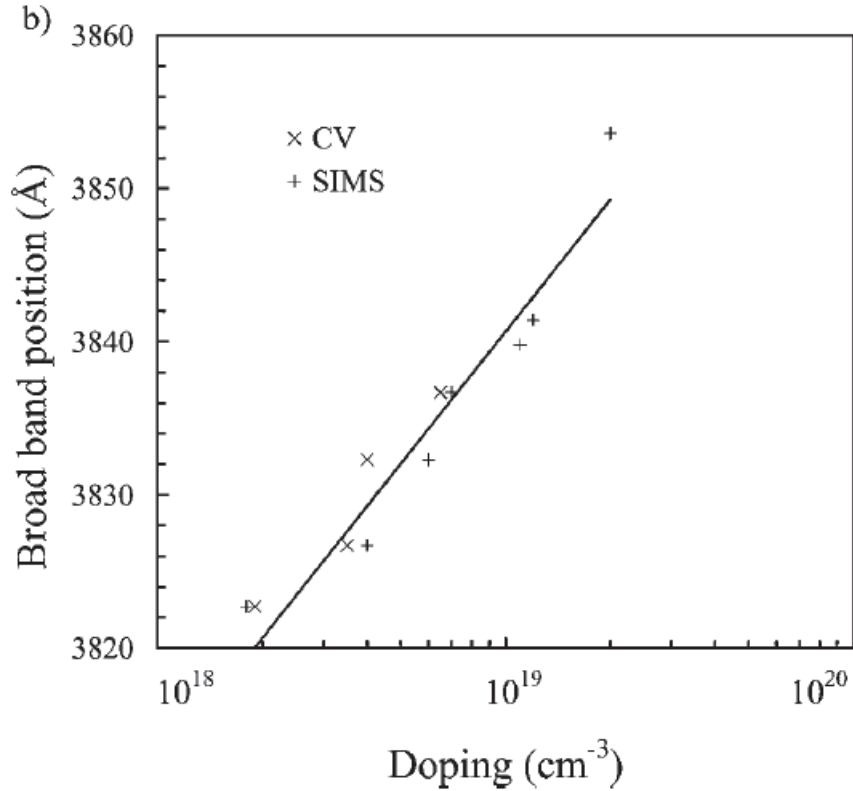


Fig.A.4. The energy position shift of the broad band observed in n-type heavily doped layer as a function of the net carrier concentration obtained by CV or nitrogen atomic concentration as determined by SIMS [8].

Aluminum contain evaluation- theoretical approach

The other common impurity that appears in SiC is aluminum. This is an acceptor type impurity and it can also trap an exciton that can recombine radiatively. Since there is usually N impurities along with the Al impurities the different recombinations that can occur can be given by the equations:

$$\frac{dn_{FE}}{dt} = g_{FE} - \left(\frac{1}{\tau_{FE}^r} + \frac{1}{\tau_{FE}^{nr}} \right) n_{FE} - f_{FE} n_{FE} \frac{[N]}{N_C} - f_{FE} n_{FE} \frac{[Al]}{Al_{Si}} \quad (A.10)$$

$$\frac{dn_{DX}}{dt} = f_{FE} n_{FE} \frac{[N]}{N_C} - \left(\frac{1}{\tau_{DX}^r} + \frac{1}{\tau_{DX}^{nr}} \right) n_{DX} \quad (A.11)$$

$$\frac{dn_{AX}}{dt} = f_{FE} n_{FE} \frac{[Al]}{Al_{Si}} - \left(\frac{1}{\tau_{AX}^r} + \frac{1}{\tau_{AX}^{nr}} \right) n_{AX} \quad (A.12)$$

where τ_{AX}^r and τ_{AX}^{nr} are the radiative and nonradiative lifetimes of the neutral acceptor n_{AX} is the density of excitons trapped by the neutral acceptor and $[Al]$ and Al_{Si} are the concentration of the neutral acceptors and the Al substitutional, respectively.

When reaching equilibrium, equations (A.10), (A.11) and (A.12) are equal with zero. Then the luminescence intensity of the free and trapped excitons can be given by:

$$I_{FE} = \frac{n_{FE}}{\tau_{FE}^r}, I_{DX} = \frac{n_{DX}}{\tau_{DX}^r}, I_{AX} = \frac{n_{AX}}{\tau_{AX}^r} \quad (A.13)$$

Again it is considered that $\tau^{nr} < \tau^r$ and from this it can be derived that:

$$\frac{I_{AX}}{I_{DX}} = \frac{\tau_{DX}^r \tau_{AX}^{nr}}{\tau_{DX}^{nr} \tau_{AX}^r} \frac{[Al]}{[N]} \frac{N_C}{Al_{Si}} \quad (A.14)$$

From this expression the ratio of N_C/Al_{Si} can be taken as equal to unity since there is the same number of substitutional sites of C by N atoms as there are of Si by Al atoms. This expression can be also simplified if the ratio of radiative and non radiative lifetimes is considered a constant. Then equation (A.14) takes becomes:

$$\frac{I_{AX}}{I_{DX}} = A \frac{[Al]}{[N]} \quad (A.15)$$

where $A = \frac{\tau_{DX}^r \tau_{AX}^{nr}}{\tau_{DX}^{nr} \tau_{AX}^r} \approx 100$.

When the Al doping is not very high (between 10^{14} and $3 \times 10^{16} \text{ cm}^{-2}$) and the N doping is low enough as not to appear Donor Acceptor pair (DAP) transitions it is possible to calculate the Al concentration by an equation of the type:

$$R_X = A_X \cdot [Al]^n \quad (A.16)$$

with $A_X = A/[N]$, n theoretically equal to 1 and $R_X = R_0 = I_{AX}/I_{DX}$. It can be seen that in order to calculate it is needed to now the intensity of the N atoms as well as their concentration.

When the Al concentration and N is high enough that DAP transitions appear, they must be taken into account otherwise the value for Al is incorrect. This happens because the probability an exciton trapped and recombining radiatively by a DAP transition is higher than a neutral acceptor since it requires less energy. In this case equation (A.16) takes the form:

$$\log R = \frac{\log R_0 + \log R_{DAP}}{2} \quad (A.17)$$

where $R_0 = I_{AX}/I_{DX}$ and $R_{DAP} = I_{DAP}/I_{DX}$. It can be seen that if $R_{DAP} = 0$ equation (A.17) reverts to equation (A.16). In both cases the evaluation of Al impurities is given by:

$$R = A_X \cdot [Al] \quad (A.18)$$

A key point is that, due to the normalizing all data to the intensity of the Q_0 line, the residual nitrogen concentration should *not* vary from sample to sample. Of course, changing the residual N concentration (i.e. changing the growth conditions or growth facility) should not change the slope parameter, but, simply, shift the ratio. This is exemplified in Fig.A. 5 [1] for three different residual nitrogen concentrations: 1.5×10^{15} , 1.5×10^{17} and $1.5 \times 10^{19} \text{ cm}^{-3}$, respectively. This ratio are plotted (on a log-log scale) versus Al concentration obtained from independent SIMS measurements. The reasonable linear behavior shows that all Al atoms detected by SIMS act as electrically active impurities.

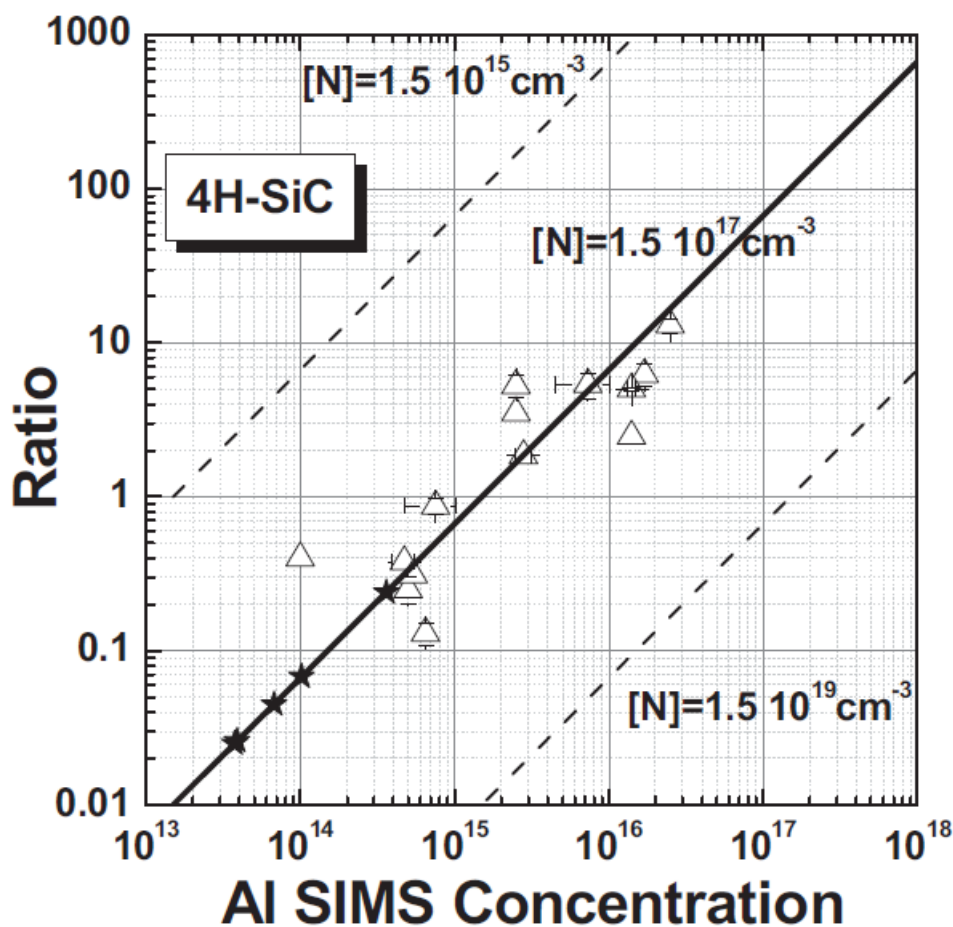


Fig.A. 5: Log-log plot of the integrated ratio calculated from experimental LTPL data versus aluminum concentration determined by SIMS. The open triangles represent experimental values of the ratio $R_0 = Al_0/Q_0$. They were used to compute the solid line, which corresponds to an average nitrogen concentration level of $\sim 1.5 \times 10^{17} \text{ cm}^{-3}$. The broken lines have been shifted assuming a lower and higher nitrogen compensation level, respectively. Typical values are $1.5 \times 10^{15} \text{ cm}^{-3}$ and $1.5 \times 10^{19} \text{ cm}^{-3}$ for the upper and lower line, respectively. The stars are extrapolated values, below the SIMS detection limit [1].

Bibliography

- [1] J. Camassel, S. Juillaguet, M. Zielinski, C. Balloud, *Chem. Vap. Deposition*, vol. 12, p. 549-556, 2006.
- [2] M. Lax, *Phys. Rev.*, vol. 119, p. 1502, 1960.
- [3] I. G. Ivanov, C. Hallin, A. Henry, O. Kordina, E. Janzen, *J. Appl. Phys.*, vol. 80, p. 3504, 1996.
- [4] U. Forsberg, A. Henry, M. K. Linnarsson, E. Janzen, *Mater. Sci. Forum*, vol. 619, p. 338-342, 2000.
- [5] R. Weingärtner, A. Albrecht, P. J. Wellmann, A. Winnacker, *Mater. Sci. Forum*, p. 433-436, 2003.
- [6] A. Henry et al., *Mat. Science Forum*, Vols. 1, p. 593, 2002.
- [7] U. Forsberg, A. Henry et al., *Mat. Science Forum*, Vols. 1, p. 619, 2000.
- [8] A. Henry, U. Forsberg, M. K. Linnarsson, E. Janzen, *Physica Scripta*, vol. 72, p. 254-257, 2005.

Annex 2: Polytype identification, homogeneity and crystal quality investigation by LTPL& Raman for n and p-type 4H-SiC

2.1 n-type samples

2.1.1 LTPL investigation

Due to the different band gap as well as the difference in the stacking order, each polytype has unique and clear PL signature.

As the extended unit cells of 4H-SiC crystals consist of 8 atoms, this result in a number of inequivalent substitutional sites within the silicon and carbon sublattices. An example of Near Band Edge (NBE), corresponding to the high energy part of the LTPL spectra taken in 5 different points of sample 13-007, is presented in Fig.A.2.1. Two lines labelled P_0 and Q_0 associated to an exciton bound to nitrogen in hexagonal and cubic site, respectively are visible. Thus we conclude the sample is 4H-SiC. Since SiC is an indirect band gap semiconductor, crystal momentum needs to be released when an exciton recombines. In the case of a band exciton, the momentum can be taken up either by lattice phonons or by the binding center itself. The phonon replicas labeled as P_x and Q_x in Fig A.2.1 are due to the former process.

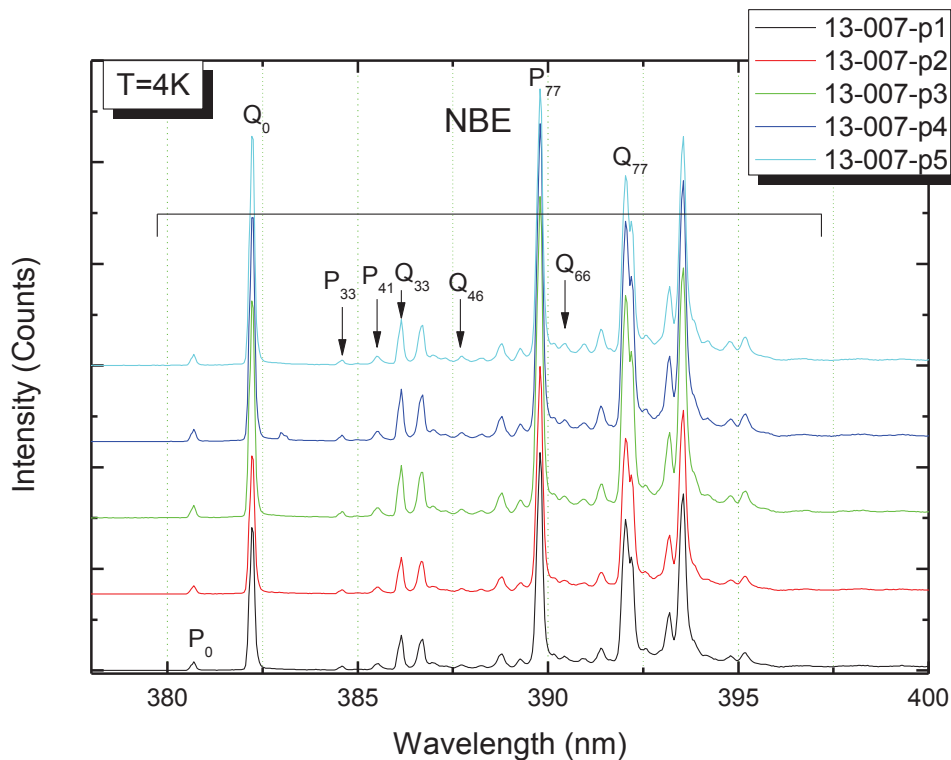


Fig.A.2.1: Near Band Edge range of low temperature photoluminescence spectrum collected at 4K on the sample 13-007 on 5 different spots on the samples.

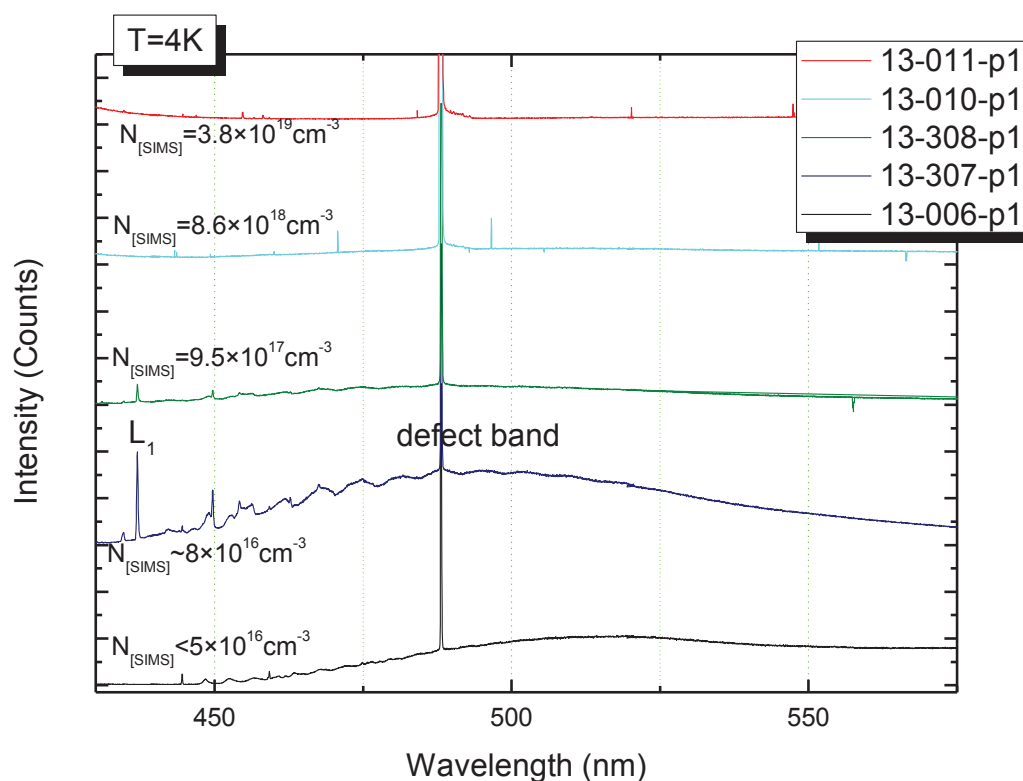


Fig. A.2.2: Zoom on range 425-575nm of PL spectra taken at 4K. A broad band assigned as defect band appears.

For sample 13-006, 13-007, 13-008 a broad band in range 450-550nm appears see Fig. A.2.2. Ellison et al. observed similar broad line for low doped samples and assigned this line to N deep B DAP line [1], but this could be also related to some defects bands. In our samples, the presence of boron is not possible and we assigned this band to a defect. One of the possible explanations of this band might be the defects in the substrate-epilayer interface. Morphological features of a non-ideal surface might explain some defects appearing in the epilayer (see chapter 1). Most of these features appear to be manifestations of non-optimal step flow during epilayer growth arising from substrate defects, non-ideal substrate surface finish, contamination, and/or unoptimized epitaxial growth conditions [2]. The propagation of the defects can extend up to a few μm into the epilayer and can be observed by PL in two cases: for very thin epilayers or very low doped epilayers. In general, the penetration depth of the laser beam strongly depends on the doping concentration. For extremely low doped and pure samples ($\sim 10^{14}\text{cm}^{-3}$) the penetration depth of the laser beam when using a high energy excitation line such as the 244 nm line of a frequency doubled laser in 2K temperature can extend according to A. Henry et al. up to $16\mu\text{m}$ [3], while for high doped samples due to strong absorption it's less than a few μm . In the other hand W.

Choyke et al. [4] claim that in case of 4H-SiC the absorption coefficient in room temperature is in range $2 \times 10^4 \text{cm}^{-1}$ for 244nm lase thus the penetration depth cannot exceeds $8 \mu\text{m}$. Nonetheless it has been observed that a broad band in NBE region from the substrate appears in LTPL spectra taken on low doped epilayers deposited on heavily doped substrates. Fig.A.2.3 illustrates the 4H-SiC samples with marked broad line assigned as a contribution from the substrate. One can notice the P_0 and Q_0 lines related to the 4H-SiC polytype and a broad line centered at 384nm. The spectrum was taken on the sample with low doping level (lower than 10^{16}cm^{-3}) the thickness of the layer is thickness about $6 \mu\text{m}$.

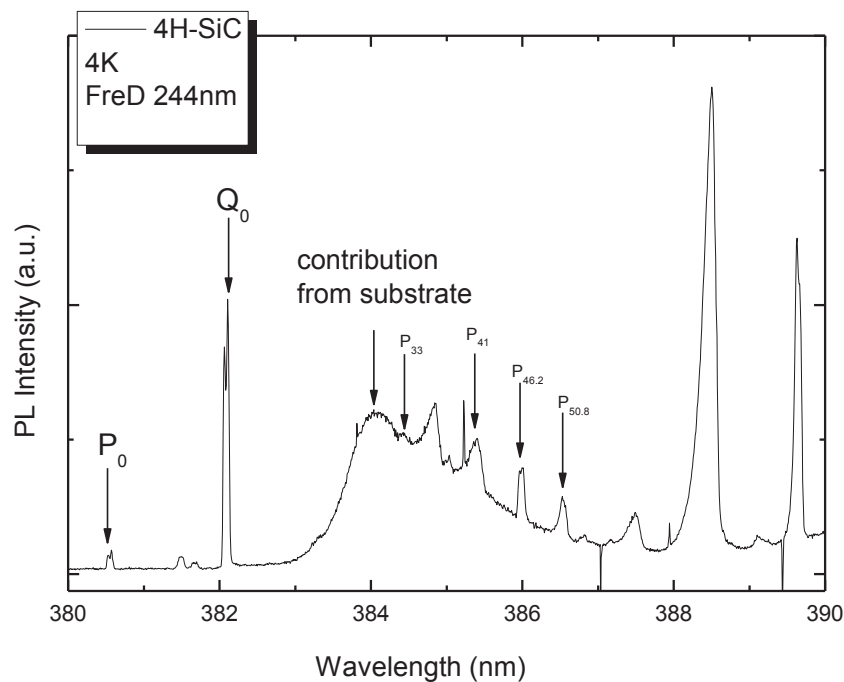


Fig.A.2.3 Example of LTPL spectra taken on low doped 4H-SiC sample, clear contribution from the substrate is visible.

In our case since one cannot see any contribution from the substrate we might estimate the penetration depth being less than the thickness of the epilayer because no feature related to the substrate are visible on the spectra. Thus for low doped samples 13-006,7&8 the broad band can be assigned as defects related to the interface. When the doping level increases from sample to sample, the penetration depth is getting lower and as a results this broad band is less pronounced. For high doped sample, though, since the penetration depth does not exceed few of μm we do not observe this defects band. Further investigation is necessary to clarify the nature of this broad band.

To check the homogeneity, LTPL measurements were performed in several different points on each of the sample (see example of sample 13-007, Fig.A.2.1). No significant differences were observed between the different spectra. This leads us to conclude that, the rotation of the substrate during the growth process is a good way to achieve the homogeneous layer. The investigation was done for all samples in a similar way by comparison of the collected spectra. All layers are very homogenous.

2.1.2 Micro Raman

As was mentioned previously the Raman spectroscopy allows to easily identify the polytype in case of SiC material. The FTA and/or FTO bands are used to determine the polytype.

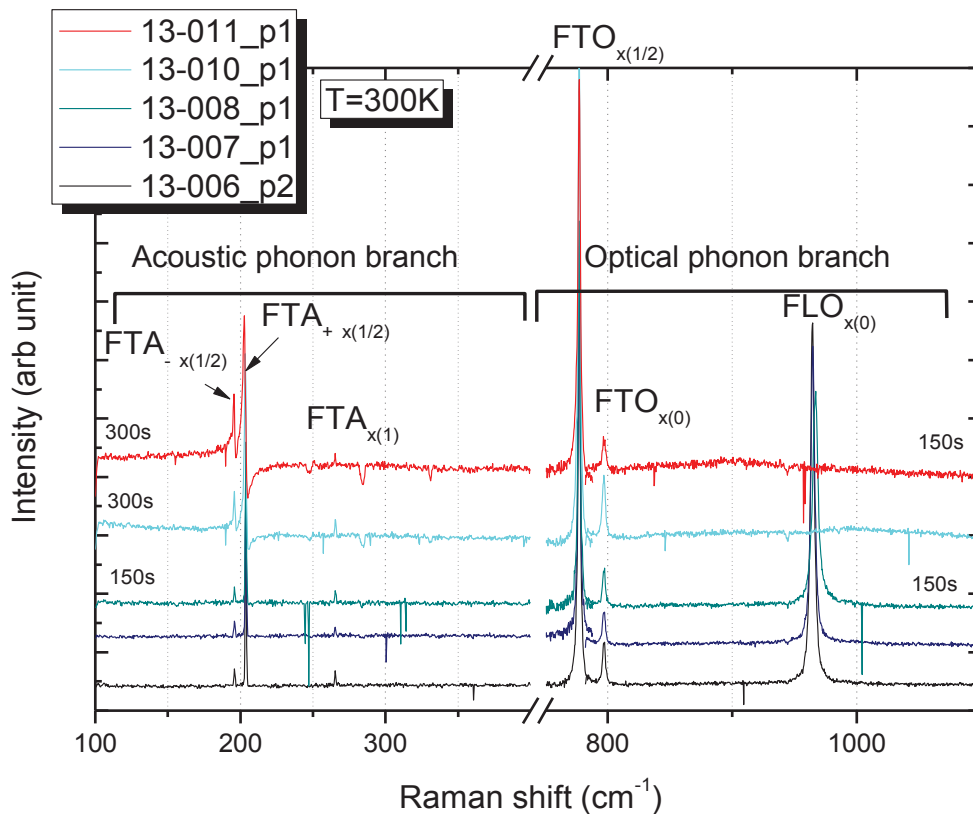


Fig.A.2. 4: Full range Raman spectra collected at room temperature in the middle of the investigated samples with marked phonon position.

One can clearly state, due to the position of the peak of the optic modes- $FTO_{x(1/2)}$ and the acoustic phonon modes $FTA_{x(1/2)}$ that all the investigated samples are 4H-SiC (see Fig.A.2.4). We do not observe any additional peaks which could be related to another polytype so one can conclude that the epilayers are pure 4H-SiC.

Raman spectra are also often used to investigate stacking disorder of SiC. Raman bands for SiC crystals containing stacking disorders broaden and become distorted. This feature in general is clearly observed for the FTA modes. For heavily disordered crystals one finds a broad background which partly reflects the density of phonon states. In our case no distortion of the Folded Transvers Acoustic (FTA) or Folded Transvers Optic (FTO) modes lines is noticed. Although, we could see some defects-related issues from PL, the Raman spectra do not show any defects.

2.2 p-type samples

2.2.1 Optical microscopy investigation

After growth process the surface of several p-type samples (see chapter 5) samples was investigated using standard optical microscopy. The measurements were done in CHREA laboratory by R. Arvinte. This allows us to see the quality of the surface and the effect of the aluminum contain increasing on these. The Fig.A. 5 a), b) and c) show the optical images for three samples with low (14-012), medium (14-005) and high (14-009) aluminum contain respectively.

a)



Doping level on Al_[SIMS] $2.3 \times 10^{16} \text{cm}^{-3}$
Sample 14-012
Magnification x20



Doping level on Al_[SIMS] $3.1 \times 10^{18} \text{cm}^{-3}$
Sample 14-005
Magnification x20

c)



Doping level on Al_[SIMS] $7.6 \times 10^{19} \text{cm}^{-3}$
Sample 14-009
Magnification x20

Fig.A. 2.5: Optical image of samples surface for a) 14-012, b) 14-005, c) 14-009.

The surfaces of the samples 14-012 & 14-005 with Al concentration determined by SIMS measurement 2.3×10^{16} and $3.1 \times 10^{18} \text{cm}^{-3}$ respectively do not show significant differences. The surface seems to be rather smooth without any defects. In the other hand the sample 14-009 containing the highest value of aluminum differs drastically. The surface is very rough and one may notice oblique stretches. One hypothesis is, that the high doping level of aluminum influences significantly the crystal quality of SiC and creates defects. Sample 14-009 will be discussed in more detailed way in the last section of this annex.

2.2.2 LTPL

The examples of LTPL spectra for four samples with different Al doping concentration are presented in Fig.A.2.6 a) and zoom on the NBE range in Fig.A.2.6 b). At the bottom the spectrum of Al free sample. At first in the low frequency range (NBE) of spectra (see Fig.A.2.6 b)) we have typical structure of 4H-SiC (see chapter 3). NBE range differs from samples to sample. This difference is related to different Al contain. A large peak called DAP (Donor Acceptor Pair) appears in the range 400-450nm more or less intense depending on the sample. From the position of this line is also possible to identify the polytype of SiC (see chapter 2). In our case the DAP line well corresponds to 4H-SiC with nitrogen as donor and Al as acceptor. The DAP lines increase significantly as the compensation is strong (higher than few 10^{18}cm^{-3} Fig.A.3.6 a)). It is worth to notice that the acquisition time for high doped samples is much longer than in the cases of the low doped samples. Apparently adding the aluminum atoms to the crystal lattice causes defects which in turns decreases the luminescence. One may also explaining decrease of intensity of PL spectra by the fact that the surface of the layers with higher contain of aluminum is more rough resulting strong dispersion or high doping creates non-radiative defects.

We can notice another large peak in range 450-600nm assigned as defects band as well as a sharp line L_1 clearly visible in case of sample 14-012. The sharp L_1 emission lines are followed by characteristic phonon-assisted structures (range 450-480nm) [5]. This feature was observed in all polytypes after various kinds of particle bombardment or irradiation [5], [6], [7], [8] and it was also observed in as-grown material after quenching and epitaxial layers grown by chemical vapor deposition [7], [8]. This defect in SiC, responsible for sharp emission lines in the low temperature photoluminescence spectra, is the so-called $D1$ center [9]. The appearance of the $D1$ defect related to the L_1 emission lines in irradiated as well as as-grown material suggests its native nature [8]. The defect complex is formed by vacancies, antisites and/or interstitials introduced by the damage, or for thermodynamical reasons. The proprieties of $D1$ center in 4H-SiC by LTPL measurements were performed by T. Egilsson et al. [10], [11] and has been explained by exciton recombination at an isoelectronic center. Thus the broad band in 450-550nm seeing on the spectra is assigned to be caused by $D1$ defect.

One may suppose that this defects lays in the substrate-epilayer interface. With increasing the aluminum contain the penetration depth of the laser beam decreases and as a results this defect band is less intense or does not appears at all. For all low doped samples the DAP line is very similar in the intensity to the low doped sample(sample 14-012) and typical for 4H-SiC NBE lines (P_0 , Q_0) are visible Nonetheless the ratios of intensity Al_0/Q_0 are different from sample to sample and varied with the Al concentration.

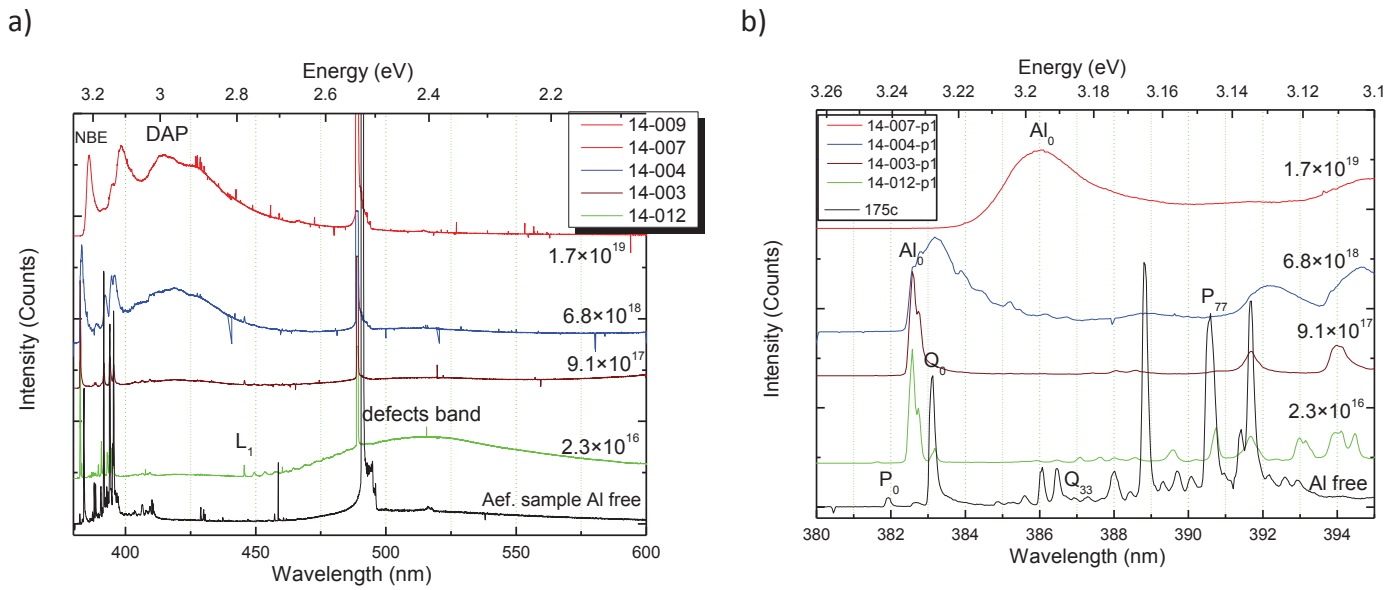


Fig.A.2.6: LTPL spectra taken at 4K on four samples with different aluminum conrtion compared to Al free sample. Zoom in Range 380-395nm four samples with different Al concentration compared to the Al free samples (on the bottom).

The homogeneity was verified for each sample. We noted that the spectra corresponding to the different points are very similar. This is an indicator suggesting that the investigated layers are homogeneous.

2.2.3 Micro-Raman

The example of Raman spectra for two samples 14-012- low doped and 14-007- high doped are shown in figure *Fig.A.2.7* and *Fig.A.2.16* respectively. In the inserts zoom on optic and acoustic range of Raman spectra is shown. By looking on the position of the FLO and FTA line we confirm that the layers are 4H-SiC.

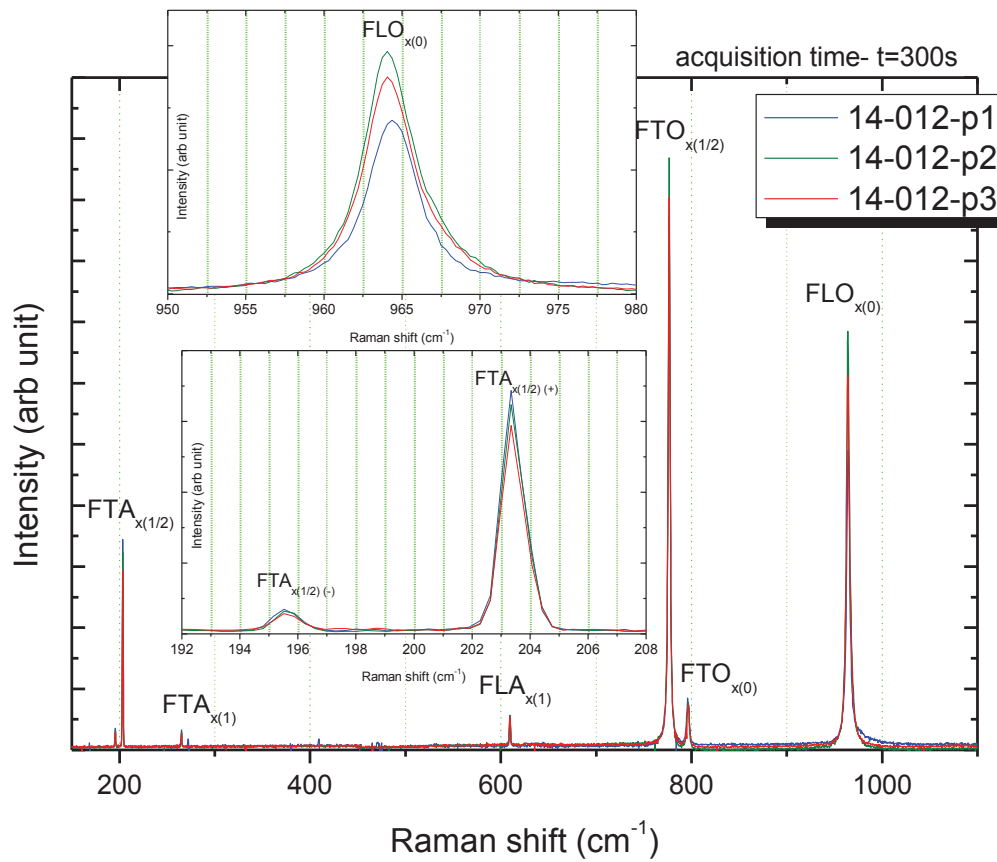


Fig.A.2.7: Raman spectra taken on sample 14-012 on three different positions (insert- zoom on optic- on the top, and acoustic- on the bottom, part of spectra).

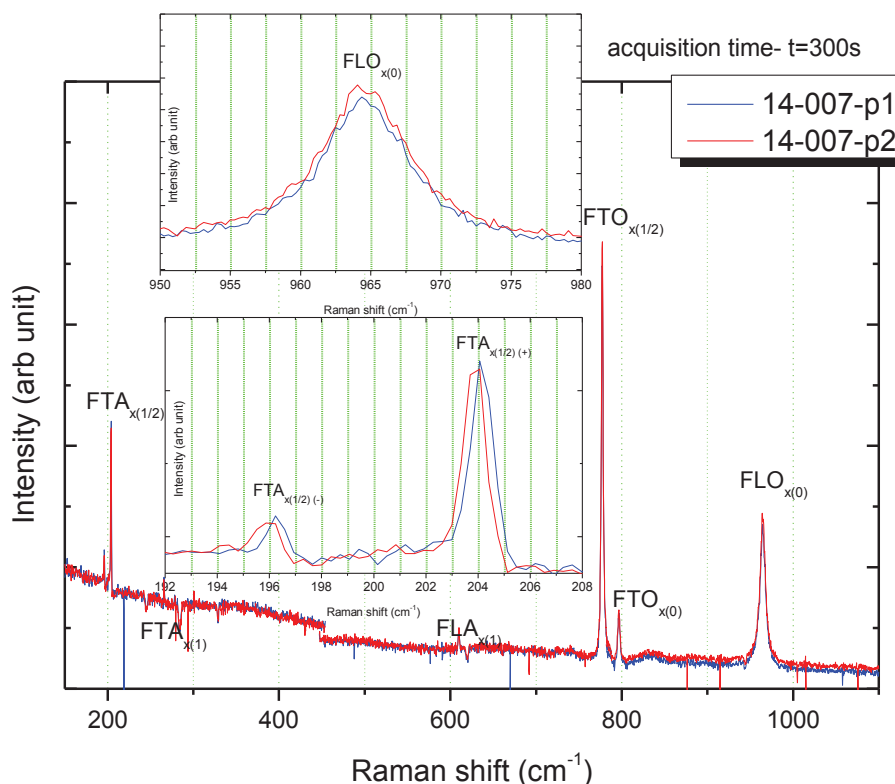


Fig.A.2.16: Raman spectra taken on the sample 14-007 on two different positions (insert-zoom on optic and acoustic part of spectra).

All spectra of sample 14-012 and 14-007 are similar in terms of the shape and the position of the peaks. Thus one may state that the layer is homogeneous. No distortion of the acoustic or optic lines, suggests of good crystal quality. Similar investigation was done for all samples. We found that the layers are homogeneous and of good quality.

2.3 Sample 14-009

Fig.A.2.9 presents the LTPL spectra for sample 14-009 which differs significantly from presented previously. No clear signature of any polytype due to NBE was noticed. One may only state what polytype is that looking on the range 400-450nm. In this range a broad line most probably corresponding to the 4H-SiC DAP. Despite that, we can see that the spectra of p1 & p2 are quite similar in terms of shape. For point 1 & 2 a broad peak centered in 600nm could be assigned to the 3C-SiC DAP, what is quite unusual. Although according to Knippenberg [12] and Inomata et al. [13], which suggested stability diagrams for SiC

polytypes as a function of temperature, the occurring of 3C-SiC is likely in very wide range of temperature it was shown that aluminum stabilizes the 4H structure [14] and, since this primary observation, other investigations have noted the same effect [15], [16]. The same stabilizing effect is also attributed to boron [17]. On the other hand, electron-donors, like nitrogen and phosphorus, seem to stabilize cubic SiC [12]. Nonetheless in this case the growth conditions and SIMS measurements indicate that sample 14-009 should contain high value of Al ($>5 \times 10^{19}$). On the other hand, the Raman spectra obtained on this samples see figure A.2.9 no shown the presence of 3C-SiC. Taking into the consideration this fact most probably this broad peak in range 550-650nm is caused by some defects. To find out about the nature of this defect further investigation is needed. Spectrum corresponding to p3 differs from the two others. Again we can see a large peak in the range 400-450nm which could be assigned as 4H-SiC DAP, nonetheless this spectrum is dominated by one broad line centered in position 525nm. Thus regarding the issue of homogeneity of the layer, one may state that in this case some differences occur. There is no possible way thought, using only LTPL spectra, to conclude whether the layer is inhomogeneous in term of aluminum doping

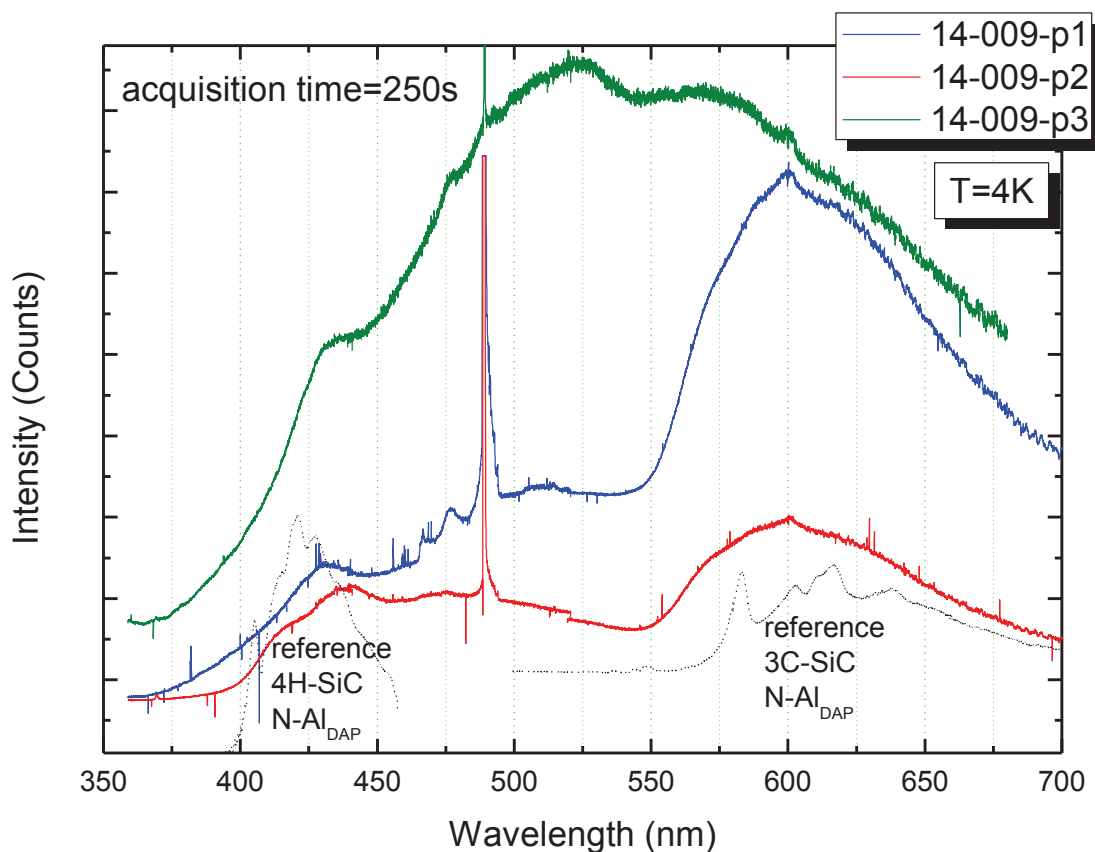
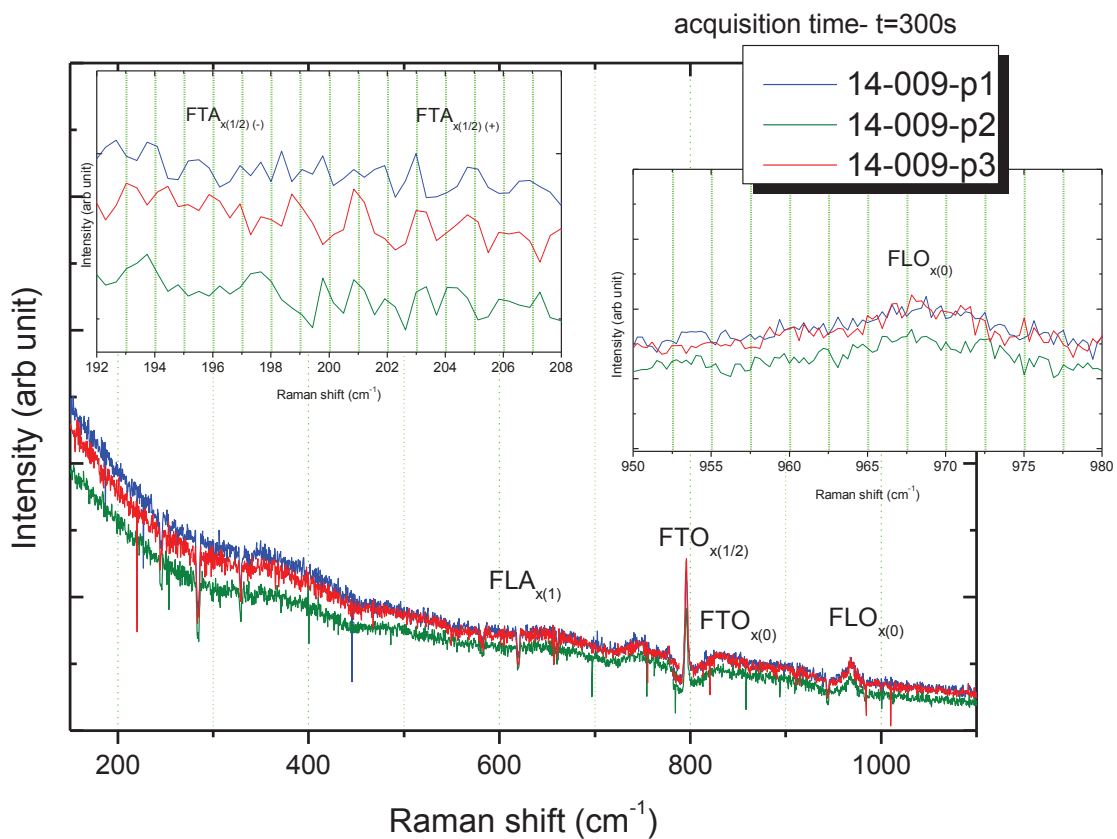


Fig.A.2.9: LTPL spectra of sample 14-009 taken at 4K on three different points, in the insert the NBE range of the spectra with marked phonons position.

Looking on the spectra of sample 14-009 one may conclude that such a high doping influences the lattice of the SiC and may cause various defects. As a results of that the LTPL are very low in term of intensity and the acquisition time to collect the spectra is very long, about 250s. This mean that the epilayer contain a lot of non radiatve defects which kill the LTPL.

Also Raman investigation revealed that sample 14-009 with the highest Al doping concentration differs significantly from others. Raman spectra of sample 14-009 is presented in A.2.10, one may notice four peaks labeled as $FLA_{x(1)}$, $FTO_{x(1/2)}$, $FTO_{x(0)}$ and $FLO_{x(0)}$ suggesting that investigated layers is 4H-SiC. In the high frequency region an intense continuum band appears, what suggests high doping concentration. The line's shape as it was mentioned before can be used as an indication of crystal quality. In this case we observe strong distortion of the peaks, broadening and change of the shape what can suggest presence of defects in the crystal.



A.2.10: Raman spectra taken on the sample 14-009 on three different positions (insert- zoom on optic and acoustic part of spectra).

Bibliography

- [1] Ellison and e. al., *Mat Science Forum*, pp. 264-268, 1998.
- [2] Cree, "Silicon Carbide: Physical Electronic Properties.," [Online]. Available: http://www.cree.com/Products/sic_index.asp.
- [3] A. Henry and e. al., *Materials Science and Engineering* , vol. 62, pp. 234-238, 1999.
- [4] W.Choyke, M. H. and G. Pensel, *Silicon Carbide Recent Major Advances*, Springer Berlin, 2003.
- [5] W. J. Choyke and L. Patrick, *Phys. Rev. B* 4, p. 1842, 1971.
- [6] V. V. Makarov, *Sov. Phys. Solid State*, vol. 13, p. 1944, 1972.
- [7] L. Patrick and W. J. Choyke, *Phys. Rev. B*, vol. 5, p. 3254, 1972.
- [8] C. Haberstroh, R. Helbig and R. A. Stein, *J. Appl. Phys*, vol. 76, p. 509, 1994.
- [9] J. Schneider and K. Maier, *Physica B*, vol. 199, p. 185, 1993.
- [10] T. Egilsson, J. P. Bergman, I. G. Ivanov, A. Henry and E. Janzen, *Phys. Rev. B*, vol. 1956, p. 59, 1999.
- [11] T. Egilsson, A. Henry, I. G. Ivanov, J. L. Lindstrom and E. Janzen, *Phys. Rev B*, vol. 59, p. 8008, 1999.
- [12] W. Knippenberg and F. Philips, *Research Reports*, vol. 18, pp. 161-274, 1963.
- [13] Y. Inomata, A. Inona, M. Mitomo, H. Sudzuki and 7. (. 3.-3. Yogyo-Kyokai-Shi, *Reserche Reports*, vol. 76, pp. 313-319, 1698.
- [14] D. Lundqvist, *Acta Chem. Scand*, vol. 2, p. 177, 1948.
- [15] J. M. Bind, *Mat. Res. Bull.*, vol. 13, pp. 91-96, 1978.
- [16] K. A. Schwetz and A. Lipp, *Proc. 10th Symp. On the Science of Ceramics, Edited by H. Hausner, Deutsche Keram. Ges.*, pp. 149-158, 1980.
- [17] S. Martin, *Aspects of Hot-Pressing of Silicon Carbide, Ph.D. Thesis, University of Cambridge*, 1980.

Annex 3: Carrier concentration evaluation by electrical measurements

The electrical measurements have been done to determine the electrical parameters of the samples: the resistivity by a Van der Pauw method, and the carrier concentration by the Hall Effect measurement. The experiments have been carried out as a function of temperatures in the range 300-800 K. The sample with the dimensions of about 6×6mm² was used. Contacts in the van der Pauw geometry (see the Fig.B.1) were realized by vacuum evaporation of nickel dots, and the samples were bonded with gold wires to a ceramic support. The electrical connections between the support and the sample holder were realized with gold wires fixed by conducting silver paste. Before the resistivity and Hall measurements, the ohmicity of the samples were checked by the V(I) characteristics.

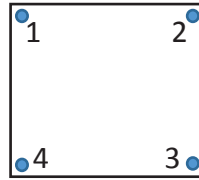


Fig.B.1: The electrical contacts in van der Pauw configuration

3.1 Resistivity measurement by Van der Pauw methods :

For resistivity measurements, a voltage is applied to flow current along one side of the sample and the voltage along the opposite side, is measured. The Van der Pauw voltages were measured for four contacts configurations respectively and for +I, -I and I=0.

The resistances were:

$$R_{12,43} = \frac{V_{43}}{I_{12}} \quad R_{23,14} = \frac{V_{14}}{I_{23}} \quad R_{34,21} = \frac{V_{21}}{I_{34}} \quad R_{41,32} = \frac{V_{32}}{I_{41}}$$

The sample resistivity in this case is done by the following expression:

$$\rho = \frac{\pi d}{\ln(2)} \left(\frac{R_{12,43} + R_{23,14} + R_{34,21} + R_{41,32}}{4} \right)$$

where d is the thickness of the sample.

3.2 Hall Effect measurement

The Hall Effect can be observed when the combination of a magnetic field perpendicular to the sample and a current along the sample create a transverse voltage perpendicular to both the field and the current. For Hall Effect measurements in Van Der Pauw configuration, a voltage is applied to flow current between the contacts placed at diagonally opposite corners and the Hall voltage V_H is measured between two other contacts. In our experiments the V_H voltages were measured respectively for both contacts configurations and for +I, -I and the average Hall voltage was calculated from each of the two diagonal sets of contacts. In the case of the conduction by one type of carriers, the Hall voltage can be written as [1]:

$$V_H = \frac{A_H r_H}{q n d} I B$$

Where A_H is the anisotropic factor, r_H the Hall scattering factor, d the thickness of the sample (in our case the thickness epilayer), I the electrical current passes through the sample and B the magnetic field and n the carrier concentration.

The Hall scattering factor depends of the carrier scattering mechanism and usually it is approximated by unity. However it should be noticed that this approximation overestimates the Hall scattering factor, involving one systematic overestimation of the doping level determined by Hall Effect.

The Hall Effect can be also defined by the Hall coefficient K_H [2], [3]:

$$K_H = \frac{V_H}{IB} = \frac{1}{q n_H d}$$

where n_H is the hall density of carrier.

From both, resistivity ρ and Hall Effect K_H measurements the Hall mobility can be calculated as :

$$\mu_H = \frac{dK_H}{\rho}$$

3.3 Experimental Set-up

The measurements of resistivity and Hall coefficient were performed using the van der Pauw DC method. For Hall-effect measurements a magnetic field of 1 T was applied. For the high temperature measurements the sample holder was placed inside the furnace in a quartz tube along with the system used to change the annealing atmosphere. The helium gas was used as neutral atmosphere. Temperatures of up to 800 K were measured with a platinum Pt resistor and controlled with a precision better than 0.5 K.

A basic resistivity and Hall Effect measurement set-up has included the following components:

- A bipolar, constant-current source: Model Keithley 6220
- A high input impedance, Low-Noise voltmeter: Model Keithley 2010
- A switch matrix (scanner) to eliminate the need for manual connections/disconnections between probe contacts: Model Keithley 7001
- Source Measure Unit for precise temperature measurements through the platinum Pt resistor: Model Keithley 2611
- An electromagnet with power unit capable of generating magnetic field up to 1 T: Model Brucker 55 A
- High temperature furnace with stabilized power unit: home-made, based on Eurotherm Model 2404.
- The PC computer with the GPIB interface to control the experimental set-up and to collect the experimental data.

Bibliography

[1] W.zawadzki, *Adv. Phys.*, vol. 23, p. 435, 1974.

[2] W. Neil et N. D. Mermin, *Solid State Physics*, Philadelphia, 1976.

[3] C. Kittel, *Introduction to Solid State Physics*, 6th edition, 1986: John Wiley & Sons.

Résumé en français

Ce travail porte sur la caractérisation optique d'échantillons de 4H-SiC. Les échantillons étudiés ont été répartis en deux groupes : type-n et type-p. La croissance des épitaxies a été réalisée par CVD technique utilisant horizontal, paroi chaude, chauffée par résistance, en utilisant de l'hydrogène comme gaz porteur silane et/propane en tant que précurseurs de Si/C respectivement. Pour atteindre différents dopages : N₂ pour le n-type et TMA pour de type p ont été utilisés. Les échantillons ont été étudiés par photoluminescence, micro-Raman and spectroscopies de masse d'ions secondaires. Pour les échantillons de type-p mesures d'effet Hall ont été utilisés pour déterminer la concentration de porteurs. Avec l'aide de ces techniques, il a été possible de déterminer le niveau de dopage dans une très large gamme pour les deux types. Les deux spectroscopies : Raman et LTPL peut donner des informations sur la concentration, polytype, qualité du cristal et concentration de porteurs, mais seulement LTPL fournit des informations sur la compensation et est indispensable de définir la polarité. Pour les échantillons faiblement dopés les meilleures façons de déterminer le niveau de dopage semble être des mesures LTPL. Pour les échantillons fortement dopés on a remarqué l'avantage de Raman, qui permet de déterminer la concentration en porteurs jusqu'à 10²⁰cm⁻³. Enfin en utilisant les mesures électriques et de Fano-paramètres obtenus grâce à micro-Raman, nous avons fait la courbe d'étalonnage pour type p 4H-SiC.

Summary

The main topic of this thesis is the optical characterization of 4H-SiC samples. The samples were divided in 2 groups: type-n doped with nitrogen and type-p doped with aluminum. Samples were grown by CVD method performed in a horizontal, hot wall, resistively heated, using hydrogen as a carrier gas and silane/propane as Si/C precursors respectively. To achieve different doping N₂ for n-type and TMA for p-type were used. The samples were studied by three different spectroscopies techniques: low temperature photoluminescence, micro-Raman and secondary ion mass spectroscopies. For p-type samples Hall effect measurements were used to determine carrier concentration. With the help of this techniques it was possible to determine doping level in a very large range for both types. Both LTPL and Raman spectroscopy can give information about the polytype, crystal quality and carrier concentration but only LTPL provides information about compensation and is indispensable to define the polarity. For low doped samples since the LOPC & FTA modes of Raman spectra do not exhibit any significant changes the best ways seems to be LTPL measurements. For the highest doped samples notice the advantage of Raman which allows to determine the carrier concentration up to 10²⁰cm⁻³. Finally due to electrical measurements and Fano-parameters obtained due to micro-Raman spectra we made calibration curve for p-type 4H-SiC.
